PhD Thesis in Applied Mathematics

Università degli Studi dell'Insubria

Dipartimento di Scienza e Alta Tecnologia

Université de Bordeaux

Institut de Mathématiques and Inria Bordeaux Sud-Ouest team Memphis

Numerical methods for all-speed flows in fluid-dynamics and non-linear elasticity

Author:
Emanuela ABBATE

Supervisors:
Prof. Gabriella PUPPO
Prof. Angelo IOLLO

Examining Committee:

Dr. Sebastiano BOSCARINO	Assistant Professor	University of Catania
Prof. Christophe CHALONS	Professor	University of Versailles
Prof. Angelo IOLLO	Professor	University of Bordeaux
Dr. Raphael LOUBÈRE	Senior Research Scientist	University of Bordeaux, CNRS
Prof. Giovanni NALDI	Professor	University of Milano
Prof. Gabriella PUPPO	Professor	University of Insubria
Prof. Giovanni RUSSO	Professor	University of Catania

Numerical methods for all-speed flows in fluid-dynamics and non-linear elasticity

Abstract

In this thesis we are concerned with the numerical simulation of compressible materials flows, including gases, liquids and elastic solids. These materials are described by a monolithic Eulerian model of conservation laws, closed by an hyperelastic state law that includes the different behaviours of the considered materials. A novel implicit relaxation scheme to solve compressible flows at all speeds is proposed, with Mach numbers ranging from very small to the order of unity. The scheme is general and has the same formulation for all the considered materials, since a direct dependence on the state law is avoided via the relaxation. It is based on a fully implicit time discretization, easily implemented thanks to the linearity of the transport operator in the relaxation system. The spatial discretization is obtained by a combination of upwind and centered schemes in order to recover the correct numerical viscosity in different Mach regimes. The scheme is validated with one and two dimensional simulations of fluid flows and of deformations of compressible solids. We exploit the domain discretization through Cartesian grids, allowing for massively parallel computations (HPC) that drastically reduce the computational times on 2D test cases. Moreover, the scheme is adapted to the resolution on adaptive grids based on quadtrees, implementing adaptive mesh refinement techinques. The last part of the thesis is devoted to the numerical simulation of heterogeneous multi-material flows. A novel sharp interface method is proposed, with the derivation of implicit equilibrium conditions. The aim of the implicit framework is the solution of weakly compressible and low Mach flows, thus the proposed multi-material conditions are coupled with the implicit relaxation scheme that is solved in the bulk of the flow.

Key words

Compressible flows, Eulerian elasticity, low Mach limit, all-speed schemes, finite volumes, relaxation, Cartesian grids, multi-material flows, immersed boundaries

---

Metodi numerici per flussi multi-regime in fluidodinamica ed elasticità non lineare

Riassunto

Questa tesi è dedicata allo sviluppo di metodi numerici per la simulazione di flussi di materiali comprimibili, sia fluidi che solidi elastici. Tutti i materiali considerati sono descritti con lo stesso modello euleriano di leggi di conservazione, che è chiuso da una legge di stato iperelastica, in cui vengono descritti i differenti comportamenti dei materiali. Abbiamo derivato un nuovo schema implicito di rilassamento in grado di risolvere flussi comprimibili in regimi diversi, con numeri di Mach che variano da molto piccoli all'ordine uno. Lo schema ha una formulazione sufficientemente generale che, tremite il rilassamento, permette di non dipendere direttamente dalla legge di stato e dunque dal materiale considerato. È basato su una integrazione in tempo completamente implicita, che viene facilmente implementata grazie alla linearità dell'operatore di trasporto del sistema di rilassamento. La discretizzazione in spazio èdata dalla combinazione di schemi upwind e centrati, con l'obiettivo di ottenere la corretta viscosità numerica nei diversi regimi di Mach. L'utilizzo di griglie cartesiane per i casi bidimensionali si adatta facilmente alla parallelizzazione del codice, riducendo drasticamente i tempi computazionali. Inoltre, lo

schema è stato adattato alla sua soluzione su griglie adattive basate su quadtrees, per implementare l'adattività di griglia tramite criteri di entropia. L'ultima parte della tesi è dedicata alla simulazione di flussi multi-materiale in domini eterogenei. Abbiamo proposto un nuovo metodo a interfaccia "sharp", derivando le condizioni di equilibrio in implicito. Questo ha come obiettivo la soluzione di interfacce fisiche in regimi debolmente comprimibili e low Mach, per questo le condizioni multi-materiali sono accoppiate allo schema implicito di rilassamento, che viene risolto lontano dalle interfacce.

Parole chiave

flussi comprimibili, elasticità euleriana, limite low Mach, schemi multi-regime, volumi finiti, rilassamento, griglie cartesiane, flussi multi-materiale, frontiere immerse

---

Méthodes numériques pour des écoulements multi-régimes en fluidodynamique et élasticité non-linéaire

Résumé

Dans cette thèse on s'intéresse à la simulation numérique d'écoulements des matériaux compressibles, voir fluides et solides élastiques. Les matériaux considérés sont décrits avec un modèle monolithique eulérian, fermé avec une loi d'état hyperélastique qui considère les différents comportéments des matériaux. On propose un nouveau schéma de relaxation qui résout les écoulements compressibles dans des différents régimes, avec des nombres de Mach très petits jusqu'à l'ordre 1. Le schéma a une formulation générale qui est la même pour tous le matériaux considérés, parce que il ne dépend pas directement de la loi d'état. Il se base sur une discrétization complétement implicite, facile à implémenter grâce à la linearité de l'opérateur de transport du système de relaxation. La discrétization en éspace est donnée par la combinaison de flux upwind et centrés, pour retrouver la correcte viscosité numérique dans les différents régimes. L'utilisation de mailles cartésiennes pour les cas 2D s'adapte bien à une parallélisation massive, qui permet de réduire drastiquement le temps de calcul. De plus, le schéma a été adapté pour la résolution sur des mailles quadtree, pour implémenter l'adaptivité de la maille avec des critères entropiques. La dernière partie de la thèse concerne la simulation numérique d'écoulements multi-matériaux. On a proposé une nouvelle méthode d'interface "sharp", en dérivant les conditions d'équilibre en implicite. L'objectif est la résolution d'interfaces physiques dans des régimes faiblement compressibles et avec un nombre de Mach faible, donc les conditions multi-matériaux sont couplées au schéma implicite de relaxation.

Mots clés

écoulements compressibles, élasticité eulerienne, limite bas Mach, schémas multi-regimes, volumes finis, relaxation, maillage cartésien, écoulements multi-materiaux, frontières immergées

Ai miei genitori, Sergio e Giovanna

"Così tra questa immensità s'annega il pensier mio:
E il naufragar m'è dolce in questo mare"
G. Leopardi

"Our imagination is stretched to the utmost, not as in fiction, to imagine things which are not
really there, but just to comprehend those things which are there"
R. Feynman

"Dans la vie, rien n'est à craindre, tout est à comprendre"
M. Skłodowska Curie

Acknowledgments

First of all, I would like to warmly thank my two advisors, Gabriella Puppo and Angelo Iollo. They made this joint PhD project possible and they never stopped supporting and helping me. In these three years they have taught me a lot, always communicating me their passion for research, making me grow scientifically but also as a person.

A thank-you goes to Florian Bernard, who has always found some time to answer my questions and to help me when nothing was working. I'd like to thank also Matteo Semplice, with whom I have discussed several times about my work, receiving great advises. I am also grateful to Riccardo Sacco, who was the first contact with my advisors and my first teacher.

I would like to thank my reviewers, Giovanni Russo and Christophe Chalons, for accepting to read and review my work and for their useful insights and suggestions. Thanks to all the other members of the jury, for taking the time to come to Como.

The greatest thank-you goes to my parents, to whom this thesis is dedicated. It is thanks to them that I am reaching this achievement, because they have always supported me in every possible way, especially believing in me every day. I thank them for their unconditional love and because they were the first ones to teach me curiosity, scientific interest, my principles and my beliefs. I am also grateful to my brother Stefano, with whom we are able to fight and after five minutes laugh. I thank him for always finding some time for me and for giving me help or advice whenever I asked him "mathematical" questions and doubts.

I'd like to thank my colleagues in Bordeaux, the Memphis and Monc teams. Especially, thanks to Alice and Federico, for their friendship that I am sure will last and for sharing breaks, anxieties and laughs. Also thanks to Claire, for the girls chitchat and the french-italian exchanges. I am also grateful to all the PhD students in Como, with whom I shared the office, the lunches and the aperitivi. In particular, I'd like to thank Isabella, because we have been able to help and encourage each other from day one.

Another thank-you is for all my friends, that are now scattered in Milan, Bordeaux and all over the world, especially to Eleonora and Silvia.

And then, I would like to deeply thank Gabriele, who is by my side when we are close and when we are apart, always sharing every moment of our lives. I thank him for the laughs and the discussions, for his love, for always pushing me in believing in myself and for putting up with me in my worst days. Thanks for walking with me up here and for continuing on this road, holding hands and enjoying every step.

Contents

CONTENTS

Introduction

Context and scope of the study

In the propagation of flows of particles of different compressible materials, complex and non stationary phenomena are generated. The complexity often arises due to the local stiffness of the involved media, affecting the speed of the different waves travelling inside the materials. Difficulties may also come from the geometry of the physical problem and from interfaces separating the different materials.

Multi-material flows are ubiquitous in nature, with several applications such as fluid-structure interactions, multiphase flows and impacts. These problems are often hard to be resolved with traditional approaches, both theoretically and experimentally. Moreover, experiments in a laboratory may be extremely hard to perform and also very expensive. Thus, the accurate and efficient simulation of those experiments is of paramount importance to reduce the costs and also the environmental impact in several industrial fields and applications. The numerical study of phenomena involving different materials requires an efficient mathematical modelling and the construction of suitable numerical methods. The physical modelling and the numerical computation of multi-material flows is therefore an active research field, due to the intrinsic difficulty in applying standard multi-physics approaches. The main goal of the present thesis is to perform numerical simulations involving both fluid-structure interaction problems and deformations of elastic materials. To this end, we aim at proposing robust numerical methods to approximate flows and waves propagating inside compressible fluids and elastic solids.

In particular, numerical difficulties can occur when treating the simulation of waves propagating at very different speeds. Several physical systems are affected by drastic changes of the sound speed. Such large variations may be due to geometrical effects or to the heterogeneity of the considered media. For example, air-water systems are characterized by density ratios of three orders of magnitude and by a sound speed ratio of about five orders. Acoustic and elastic waves in heterogeneous solid materials may travel at very different speeds, depending on the local stiffness of the medium. Impacts at low speed, such as crash tests, consist in a deformation wave which is extremely slow with respect to the fast acoustic waves occurring when the "crash" happens. The accurate numerical simulation of all these phenomena requires the construction of numerical schemes that are able to deal with those different regimes. Standard explicit codes for the simulation of compressible flows may fail in accurately approximating fluid flows or solid deformations at low speed and moreover they would require an enormous computational effort due to intrinsic stability constraints. The derivation of *all-speed* solvers is motivated by all the above mentioned reasons. In general, the purpose of an all-speed scheme is to handle both the compressible regime (i.e. local Mach number of order unity) and the incompressible one (i.e.

very small local Mach number). Moreover, the different behaviours characterizing gases, liquids and solids require a numerical method that is robust and also general enough to deal with the heterogeneity of the considered phenomena. This means that suitable numerical methods to solve such problems should not significantly change their structure when switching from a medium to another one.

A very important aspect to be accounted for when performing numerical simulations is related to the computational effort. The massive parallelization of the codes allows for a refined resolution of the simulation results, without the need of enormous computational times. Therefore, the derivation of the numerical methods has to be carried out in the perspective of an implementation on HPC architectures.

Numerical methods

In this thesis, we aim at proposing robust numerical methods that are designed to solve flows of different compressible materials and at different speeds. In order to do that, the different materials are described within the same mathematical model. The media are different only through their specific state law. In particular, we are concerned with the simulation of fluids (gases and liquids) and of solids that can be deformed under non-linear elasticity laws. We consider materials that are compressible (especially weakly compressible), non viscous and non miscible.

The mathematical model is based on the standard laws of conservation of mass, of momentum and of energy. Those are the same equations that characterize the standard compressible Euler system. The description of the solid deformations is possible thanks to the notion of backward characteristics, coherently with the chosen Eulerian framework. The backward characteristics are functions that associate the position of a material point in the deformed configuration to its position in the initial configuration, thus "recording" the deformations. Fluids are treated with a very general state law that allows to model both gases and liquids, thanks to the presence of coefficients that are characteristic of each medium. Solids are described with a non-linear elastic Hook's law.

The main purpose is to build numerical methods that are able to solve this Eulerian model in different regimes, that is to say also for slow flow speeds and in presence of small (or slow) deformations. The low Mach limit in a solid is observed when the acoustic and elastic waves occurring in the deformation phenomenon are consistently faster with respect to the deformation wave itself. When approaching the low Mach limit, the standard explicit-upwind schemes may fail for two main reasons: the exceedingly large numerical viscosity and the extremely small time step imposed by stability requirements. Several numerical schemes have been derived in literature to solve gas and fluid dynamics problems at all speeds. The majority of these schemes depends directly on the specific state law, for example in choosing the splitting of the time discretization the EOS terms are divided into fast and slow scales. In the present work, our aim is to design numerical methods that are independent of the considered material and preserve their structure when dealing with different state laws. With this in mind, we adopt a relaxation technique that approximates the original problem in the limit of a small relaxation time. The main reason for this choice is due to the fact that the fluxes are relaxed at the continuous level, obtaining a linear transport operator and avoiding a dependence of

the spatial derivatives on the EOS. This implies that complex solvers such as Riemann solvers are not required and thus implicit time integrators can be easily adopted. The use of a fully implicit time discretization is twofold: on one hand, the choice of the time step is not dictated by stability reasons anymore, thus avoiding the increase of the computational time in the slow regimes. On the other hand, centered discretizations of the gradients may be adopted without getting stability problems, decreasing the numerical viscosity when the Mach number tends to zero. The proposed scheme is asymptotic preserving, namely it provides a consistent and stable discretization of the incompressible limit system.

The second topic of the thesis concerns the numerical treatment of the physical interfaces separating two materials. In order to solve multi-material flows, a numerical method to approximate the multi-material interface is needed. We propose a sharp treatment of the interface, namely we consider it to have zero width. In order to solve the problem for compressible and weakly compressible multi-material flows, equilibrium conditions are derived in an implicit framework and are exploited with the proposed all-speed scheme.

A traditional approach to simulate multi-material flows consists in employing unstructured grids that adapt to the interface geometry. This means that the grid deforms itself with the flows. A major drawback of this technique is related to the fact that every time grid cells are too much distorted, the domain has to be re-meshed. In order to avoid this inconvenience, we consider a Cartesian mesh, which is easy to be generated. Also the numerical discretization of the equations is simplified and less expensive, since it is easily parallelizable. Of course, in this case the interface is immersed in the grid. Hence, a method to track the interface position has to be included to perform multi-material simulations.

Organization of the thesis

The thesis is organized as follows. The *first chapter* is devoted to the presentation of a mathematical model for the description of flows of different compressible materials. Both fluids and elastic solids are described in the Eulerian framework, with the same system of conservation laws. As a first step, the Euler system of gas-dynamics is introduced as a particular case. Then, a Eulerian model is introduced, which we will call "monolithic" model since it contains the flow equations together with continuous deformations. A general constitutive law is adopted to close the system, with the aim of describing gases, liquids and non-linear elastic solids at the same time. The general formulation of the speed of the waves is reported and the wave pattern is analyzed. The model is presented in two dimensions and in the last section a 1D version is derived.

The *second chapter* is devoted to the low Mach limit theory. As a first step, the standard study on the Euler equations is carried out, with their non-dimensionalization and asymptotic analysis. Then, this theory is extended to the monolithic Eulerian system of the first chapter, thus allowing us to analyze the low Mach regime also in compressible solids. Two different Mach numbers and two different low Mach regimes are introduced. In the last part of the chapter, we revise the problems related to the numerical solution of low Mach flows with standard compressible codes. The main techniques proposed in literature to handle the low Mach regimes are briefly presented. Then, the novel relaxation all-speed scheme is introduced, by explaining the reason for adopting a relaxation method and the need of a fully implicit time integration for

the solution of the proposed Eulerian model in the low Mach regime.

In the *third chapter*, the novel relaxation all-speed scheme is derived and analyzed in detail for one dimensional problems. The numerical properties of the scheme are studied and several numerical tests are presented in order to validate the scheme, mainly exploiting two lines: the nozzle flow test with a convergence analysis and also tests concerning material waves propagation inside different materials. The scheme proves to be precise in the approximation of low Mach regimes and also of fully compressible flows. Then, in *chapter IV* the scheme is extended to solve two dimensional low Mach flows and a proof of the asymptotic preserving property of the scheme is proposed. The computational effort is reduced thanks to the parallelization of the code. Both the mesh generation procedure and the linear system resolution are described. In the second part of the chapter, we introduce the use of hierarchical Cartesian grids based on quadtrees. These structures allow us to recursively adapt the grid (adaptive mesh refinement) in order to reduce the number of degrees of freedom in regions of smooth flows, by preserving the accuracy where the main phenomena occur.

Chapter V is devoted to multi-material problems, with a review of the existing models to treat physical interfaces, including diffused and sharp interface models. After this review, a novel numerical method for moving walls and physical interfaces is derived. The method is coupled with the implicit relaxation scheme, with ad-hoc modifications. The scheme proposed in the first part of the thesis is thus extended to multi-material problems, in order to solve multi-material weakly compressible flows. In this chapter, the proposed "immersed boundary" framework is validated on one dimensional problems, showing that the interface is kept sharp even after long times for fluid/fluid, solid/fluid and solid/solid interactions.

In *chapter VI*, the multi-material model is extended to the simulation of 2D multi-material problems. This is done by rewriting the multi-material equilibrium conditions to two dimensions and by introducing a level set function to track the interface. Some preliminary test cases are presented, in order to validate fluid/fluid and solid/fluid interactions at different speeds.

Chapter I

An Eulerian model for non-linear elasticity

This chapter is devoted to the presentation of a monolithic Eulerian model that describes both fluids and elastic solids with the same system of equations [61]. We suppose that the described materials are compressible, non-viscous and that they can be subject to large deformations. The mechanics of the continuous media is based on conservation of mass, momentum and total energy. Every material is governed by its own equation of state. Specifically, compressible solids follow the non-linear elasticity state law. The model is fully written in the Eulerian framework, thanks to the introduction of backward characteristics to record the deformation. The Eulerian approach to model hyperelastic materials has been the focus of the works of Plohr and Sharp [102, 103], Miller and Collela [92], Cottet et al. [41], Gavrilyuk et al. [53], Barton et al. [13, 14], Peshkov and Romenski [99, 49] and Iollo et al. [62, 44, 1].

We firstly draw a brief revision of the Euler equations for gas and fluid dynamics. In the second part of the chapter, we introduce the chosen Eulerian model for non-linear elasticity in two dimensions. The general hyperelastic state law is introduced and the different behaviors that are modeled are detailed. The computation of the characteristic speeds of the system and the wave pattern are also presented.

I.1   The Euler equations

There exist two main methods for the description of continuous media: the Lagrangian method, which consists in following the material points of a continuum in their movement in time, and the Eulerian method, which consists in looking at the quantities of interest at a geometrical point in space at every time.

Let $\Omega_0 \in \mathbb{R}^2$ be the reference or initial configuration of a continuum medium. This initial domain is transformed at time $t \in \mathbb{R}^+$ in the deformed configuration $\Omega_t = X(\Omega_0, t)$, where $X : \mathbb{R}^2 \times \mathbb{R}^+ \to \mathbb{R}^2$ is the coordinate transformation occurred under the flow. Let $\mathbf{u} : \mathbb{R}^2 \times \mathbb{R}^+ \to \mathbb{R}^2$ be the velocity field, such that $\mathbf{u}(X, t) = \partial_t X$. The Lagrangian formalism consists in writing the main quantities referring to the initial domain Ω_0, whereas the Eulerian formalism corresponds to use the variables in the configuration Ω_t.

Let $f = f(x, t)$ be a function $f : (\mathbb{R}^2, \mathbb{R}) \to \mathbb{R}$ that represents a quantity transported by

the flow. In order to relate the Eulerian and the Lagrangian formulations, we report here the Reynolds formula for volumes:

$$\frac{d}{dt}\left(\int_{\Omega_t} f(x,t)\,dx\right) = \int_{\Omega_t} \left(\partial_t f + \nabla_x \cdot (f\mathbf{u})\,dx\right). \tag{I.1}$$

By noting $\frac{D}{Dt}$ the material derivative, we can then relate the Lagrangian and Eulerian frameworks in the following way:

$$\frac{Df}{Dt} = \partial_t f + \mathbf{u} \cdot \nabla_x f.$$

The state of a continuous medium is in general characterized by its mass, its pressure, its velocity and its internal energy. Fluids are in general described within the Eulerian framework and the compressible Euler equations describe the flow of a perfect fluid. In what follows, we derive these conservation equations with the use of the Reynolds formula (I.1) and then we introduce the equation of state (EOS) for fluids in order to close the system.

I.1.1 Conservation equations

For the derivation of the conservation Euler equations in this section, the reader can refer to the books of Leveque [80] and of Whitham [129] and references therein. We now briefly derive the conservation system with the use of the Reynolds formula (I.1).

The continuity equation, which is the mass conservation equation, states the fact that the variation in time of the mass is zero in a control volume Ω_t. Let ρ be the mass per units of volume (namely the density). By integrating the variation in time of the density over Ω_t, we have that

$$\frac{d}{dt}\left(\int_{\Omega_t} \rho(x,t)\,dx\right) = 0,$$

which becomes, with the use of the Reynolds formula (I.1)

$$\frac{d}{dt}\left(\int_{\Omega_t} \rho(x,t)\,dx\right) = \int_{\Omega_t} \left(\partial_t \rho + \nabla_x \cdot (\rho\mathbf{u})\right)dx = 0.$$

Since this relation holds for every volume of fluid Ω_t, we easily get the continuity equation

$$\partial_t \rho + \nabla_x \cdot (\rho\mathbf{u}) = 0. \tag{I.2}$$

For the conservation of momentum, we apply the fundamental principle of dynamics to a volume of fluid Ω_t. This states that the variation of momentum is equal to the sum of external forces applied to the system. Letting $f_v(x,t)$ be the external volume forces per units of volume and $\sigma(x,t)\,\mathbf{n}(x,t)$ the surface forces, we get

$$\frac{d}{dt}\left(\int_{\Omega_t} \rho(x,t)\,\mathbf{u}(x,t)\,dx\right) = \int_{\partial\Omega_t} \sigma(x,t)\,\mathbf{n}(x,t)\,ds + \int_{\Omega_t} f_v(x,t)\,dx.$$

This gives a balance law where the external and surface forces enter in the right hand side as sources. For simplicity, we now suppose that $f_v(x,t) = 0$ and that the fluid is non-viscous, namely $\sigma = -p\mathbf{I}$. After applying (I.1), we get the conservation law of momentum

$$\partial_t(\rho\mathbf{u}) + \nabla_x \cdot (\rho\mathbf{u} \otimes \mathbf{u} + p\mathbf{I}) = 0. \tag{I.3}$$

Let e be the total energy per unit mass, which is given by the sum of the kinetic energy and the internal energy per unit mass ϵ:

$$e = \frac{1}{2}|\mathbf{u}|^2 + \epsilon. \tag{I.4}$$

We here apply the first thermodynamics principle, which states that the variation of total energy is equal to the quantity of energy exchanged with the exterior medium as heat and work. For the Euler equations, the heat transfer is negligible (adiabatic case), thus we get:

$$\frac{d}{dt}\left(\int_{\Omega_t} \rho\,(x,t)\,e\,(x,t)\,dx\right) = \int_{\partial\Omega_t} \sigma\,(x,t)\,\mathbf{n}\,(x,t)\cdot\mathbf{u}\,(x,t)\,ds + \int_{\Omega_t} f_v\,(x,t)\cdot\mathbf{u}\,(x,t)\,dx.$$

We adopt the same hypothesis as before on the external and surface forces, i. e. $f_v\,(x,t) = 0$ and $\sigma = -p\mathbf{I}$. Applying the Reynolds formula (I.1), we obtain the conservation law for the energy:

$$\partial_t\,(\rho e) + \nabla_x\cdot\left((\rho e + p)\,\mathbf{u}\right) = 0. \tag{I.5}$$

The compressible Euler equations for fluid dynamics are then (I.2)-(I.3)-(I.5):

$$\begin{cases} \partial_t\rho + \nabla_x\cdot(\rho\mathbf{u}) = 0 \\ \partial_t\,(\rho\mathbf{u}) + \nabla_x\cdot(\rho\mathbf{u}\otimes\mathbf{u} + p\mathbf{I}) = 0 \\ \partial_t\,(\rho e) + \nabla_x\cdot\left((\rho e + p)\,\mathbf{u}\right) = 0. \end{cases} \tag{I.6}$$

Letting $x = (x_1, x_2)$ be the coordinates in the canonical basis of $\mathbb{R}^2$, $\mathbf{u} = (u_1, u_2)$ the velocity components, system (I.6) may be rewritten in a compact form in the following way:

$$\partial_t\boldsymbol{\psi} + \partial_{x_1}\mathbf{F}\,(\boldsymbol{\psi}) + \partial_{x_2}\mathbf{G}\,(\boldsymbol{\psi}) = 0, \tag{I.7}$$

where we have adopted the directional splitting of the flux function. The conservation variables and the fluxes along the two directions read as follows:

$$\boldsymbol{\psi} = \begin{bmatrix} \rho \\ \rho u_1 \\ \rho u_2 \\ \rho e \end{bmatrix}, \quad \mathbf{F}\,(\boldsymbol{\psi}) = \begin{bmatrix} \rho u_1 \\ \rho u_1^2 + p \\ \rho u_1 u_2 \\ (\rho e + p)\,u_1 \end{bmatrix}, \quad \mathbf{G}\,(\boldsymbol{\psi}) = \begin{bmatrix} \rho u_2 \\ \rho u_1 u_2 \\ \rho u_2^2 + p \\ (\rho e + p)\,u_2 \end{bmatrix}. \tag{I.8}$$

I.1.2 Equation of state for fluids

In order to close system (I.6), one needs to prescribe a state law for the internal energy ϵ present in (I.4). In the case of fluids, this can be done with thermodynamics considerations. The first principle of thermodynamics states that the variation of internal energy is equal to the quantity of energy exchanged with the exterior medium as heat and work, namely, when $\mathbf{u} = 0$:

$$de = d\epsilon = \delta Q + \delta W.$$

Writing the heat as $\delta Q = Tds$, where T is the temperature and s is the entropy, and the work as $\delta W = -pdV = p/\rho^2 d\rho$, where $V = 1/\rho$ is the volume, we get

$$de = d\epsilon = Tds + \frac{p}{\rho^2}d\rho.$$

We consider the following general law for the internal energy as function of the density and the entropy:

$$e\left(\rho, s\right) = \frac{\kappa\left(s\right)}{\gamma - 1}\left(\frac{1}{\rho} - b\right)^{1-\gamma} - a\rho + \frac{p_\infty}{\rho}, \tag{I.9}$$

where $\gamma = c_p/c_v$ is the polytropic constant, $\kappa\left(s\right) = exp\left(\left(s - s_0\right)/c_v\right)$ with s_0 reference entropy, a and b are the coefficients of a real gases model (Van der Waals model) and p_∞ is a constant describing the intermolecular interaction, typical of rarefied gases. Therefore, thanks to the last relations temperature and pressure can be derived as follows

$$\begin{cases} T\left(\rho, s\right) = \left.\frac{\partial e}{\partial s}\right|_{\rho=const} = \frac{\kappa\left(s\right)}{c_v\left(\gamma - 1\right)}\left(\frac{1}{\rho} - b\right)^{1-\gamma} \\ p\left(\rho, s\right) = \rho^2\left.\frac{\partial e}{\partial \rho}\right|_{s=const} = \kappa\left(s\right)\left(\frac{1}{\rho} - b\right)^{-\gamma} - a\rho^2 - p_\infty. \end{cases} \tag{I.10}$$

Then from relations (I.10) and (I.9), one can write the energy and the pressure as functions of ρ and T as

$$\begin{cases} e\left(\rho, T\right) = c_v T - a\rho + \frac{p_\infty}{\rho} \\ p\left(\rho, T\right) = \frac{\rho\left(\gamma - 1\right)c_v T}{1 - b\rho} - a\rho^2 - p_\infty. \end{cases} \tag{I.11}$$

With the reported expressions and with specific choices of the coefficients a, b, p_∞, we recover some well-known expressions for specific gas models.

Perfect gas

The model for perfect gases describes gases where the particles do not interact with each other and where their size is negligible with respect to the intermolecular distances. This is a good approximation of real gases under specific conditions of low pressure and high temperature. We get the perfect gas state law by taking $a = b = p_\infty = 0$ in (I.9). The expression of the internal energy of a perfect gas reads as follows:

$$\epsilon\left(\rho, s\right) = \frac{\kappa\left(s\right)\rho^{\gamma-1}}{\left(\gamma - 1\right)}.$$

This in turn gives the following expressions for pressure and temperature, calculated from (I.10):

$$T\left(\rho, s\right) = \frac{\kappa\left(s\right)}{c_v\left(\gamma - 1\right)}\rho^{\gamma-1}, \qquad p\left(\rho, s\right) = \kappa\left(s\right)\rho^\gamma.$$

Using the energy and pressure formulations as functions of ρ and T in (I.11), we have

$$\epsilon\left(\rho, p\right) = \frac{p}{\rho\left(\gamma - 1\right)}, \qquad p = \rho R T.$$

where $R = c_p - c_v$ is the specific constant for perfect gases.

Stiffened gas

The law describing rarefied gases is able to model fluids that are weakly compressible, such as water and liquids in general. This property is accounted for in the model with the constant p_∞,

that includes the intermolecular forces. By taking $a = b = 0$, we obtain the following law for rarefied gases:

$$e\left(\rho, s\right) = \frac{\kappa\left(s\right)\rho^{\gamma-1}}{\left(\gamma - 1\right)} + \frac{p_\infty}{\rho}. \tag{I.12}$$

This gives the following expressions for pressure and temperature, calculated from (I.10):

$$T\left(\rho, s\right) = \frac{\kappa\left(s\right)}{c_v\left(\gamma - 1\right)}\rho^{\gamma-1}, \qquad p\left(\rho, s\right) = \kappa\left(s\right)\rho^\gamma - p_\infty.$$

Using the energy and pressure formulations as functions of ρ and T in (I.11), we have

$$\epsilon\left(\rho, p\right) = \frac{p + \gamma p_\infty}{\rho\left(\gamma - 1\right)}, \qquad p = \rho R T - p_\infty.$$

I.2 Eulerian model for compressible elasticity

We now introduce the Eulerian model for elasticity, whose resolution is one of objects of this thesis. More details of the derivation can be found in the original works of Godunov [60, 61]. We firstly introduce the description of the deformation of continuous media. Then the system of conservation equations is derived, with the hyperelastic general state law and the stress tensor formulations.

I.2.1 Deformations: forward and backward characteristics

The conventional approach for describing large deformations is the Lagrangian formalism. Starting from the notation briefly introduced in Sec. I.1, let $\Omega_0 \in \mathbb{R}^2$ be the reference, or initial, configuration of the continuum. This configuration, at time t, is transformed in a deformed configuration $\Omega_t \in \mathbb{R}^2$. In order to describe the evolution of the continuum in the Lagrangian framework, we define the *forward characteristics* X (see Fig. I.1) as the position $x \in \Omega_t$ at time t of a material point that initially was in position $\xi \in \Omega_0$, i.e.:

$$\begin{aligned} X : \Omega_0 \times [0, T] &\to \Omega_t \\ (\xi, t) &\to x = X\left(\xi, t\right). \end{aligned} \tag{I.13}$$

In the case of smooth flow, these characteristics represent a bijective and bicontinuous transformation. They "record" the history of the deformations of the solid until time t.

The velocity field $\mathbf{u}$ on the deformed configuration is defined as

$$\begin{aligned} u : \Omega_t \times [0, T] &\to \mathbb{R}^2 \\ (x, t) &\mapsto \mathbf{u}\left(x, t\right). \end{aligned} \tag{I.14}$$

This velocity field can be related with the forward characteristics in the following way:

$$\begin{cases} \partial_t X\left(\xi, t\right) = \mathbf{u}\left(X\left(\xi, t\right), t\right) \\ X\left(\xi, 0\right) = \xi, \qquad \xi \in \Omega_0. \end{cases} \tag{I.15}$$
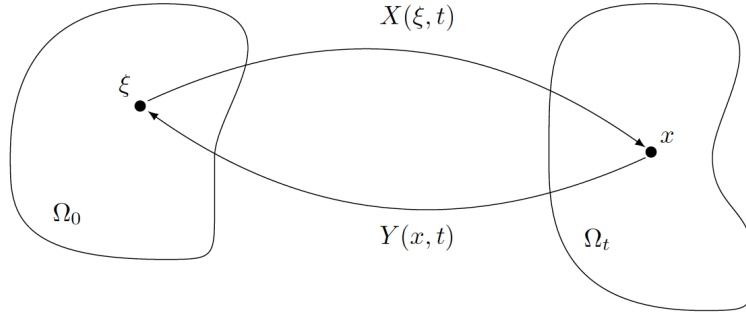
Figure I.1: Forward and backward characteristics.

The Eulerian framework, instead, is based on the deformed configuration. Hence, we introduce the *backward characteristics*, which allow to describe the deformation of a continuum in the configuration at time t:

$$Y : \Omega_t \times [0, T] \to \Omega_0$$
$$(x, t) \mapsto Y(x, t) \tag{I.16}$$

These functions "record" the position in the initial configuration Ω_0 of a material point, which is located in $x \in \Omega_t$ at time t (see Fig. I.1).

Since the transformation X (I.13) is bijective, we can rewrite function (I.16) as $Y = X^{-1}$. This way, forward and backward characteristics can be related in the following way:

$$X(Y(x, t), t) = x, \qquad Y(X(\xi, t), t) = \xi. \tag{I.17}$$

By deriving one of these two relations with respect to time t, we get the Eulerian equivalent of the Lagrangian equation (I.15) on the velocity field (I.14). The new relation takes the form of a transport equation on the backward characteristics, as follows:

$$\begin{cases} \partial_t Y(x, t) + \mathbf{u}(x, t) \cdot \nabla_x Y(x, t) = 0 \\ Y(x, 0) = x, \qquad x \in \Omega_t. \end{cases} \tag{I.18}$$

Moreover, the derivation of the first relation in (I.17) with respect to x and of the second with respect to ξ gives the following relation

$$F := [\nabla_\xi X(\xi, t)] = [\nabla_x Y(x, t)]^{-1}, \tag{I.19}$$

where we have introduced tensor F, which is defined as the gradient of the deformation in the Lagrangian framework. Relation (I.19) is helpful to express in the Eulerian framework (i. e. in the deformed configuration) all quantities that in the Lagrangian formulation depend on $[\nabla_\xi X(\xi, t)]$. For example, the conservation of mass in the Lagrangian formulation reads

$$\rho(X(\xi, t), t) \det([\nabla_\xi X(\xi, t)]) = \rho(\xi, 0).$$

In the Eulerian framework we can rewrite it in the following way:

$$\rho(x, t) = \det([\nabla_x Y(x, t)]) \rho(Y(x, t), 0). \tag{I.20}$$

I.2.2 Conservation equations

In this section we report the system of conservation equations that models fluids and hyperelastic solids in the Eulerian framework. The model is written in the deformed configuration Ω_t, adopting the Eulerian framework not only as classically done for fluids, but also for solids. The equations describing the evolution of elastic solids are the conservation of mass, of momentum and energy as for fluids (see Section I.1 for the explicit derivation). We consider the external volume forces applied to the considered material, i.e. $f_v(x,t) = 0$ equal to zero and we also consider the full stress tensor σ.

Moreover, a law for the description of the deformation has to be added: this is done with the introduction of equations of transport of the backward characteristics, introduced in the section above. The gradient of the deformation in the Eulerian framework can be computed via the gradient of the backward characteristic functions $Y(x,t)$ defined in (I.16). Since the stress tensors have a direct dependence on $[\nabla_x Y]$, the gradient of (I.18) is taken as a governing equation.

This way, we get the following conservative form of the equations of a general medium in the deformed configuration:

$$\begin{cases} \partial_t \rho + \nabla_x \cdot (\rho \mathbf{u}) = 0 \\ \partial_t (\rho \mathbf{u}) + \nabla_x \cdot (\rho \mathbf{u} \otimes \mathbf{u} - \sigma) = 0 \\ \partial_t ([\nabla_x Y]) + \nabla_x (\mathbf{u} \cdot [\nabla_x Y]) = 0 \\ \partial_t (\rho e) + \nabla_x \cdot (\rho e \mathbf{u} - \sigma^T \mathbf{u}) = 0, \end{cases} \tag{I.21}$$

where some fluxes of the third equation are zero, as it will be clearly shown by expression (I.34).

The third equation on the gradient of the deformation is useful only for solid phases. However, since our aim is to have a scheme which is able to solve flows of all different compressible materials, this equation will be solved in the whole domain. We also point out that this equation is redundant with the mass conservation equation, due to relation (I.20).

As usual, in order to close system (I.21), a specific equation of state needs to be prescribed.

I.2.3 Equation of state: hyperelasticity

In this section we describe the general equation of state that we adopt to close system (I.21). This state law includes different behaviours and is able to describe fluids and hyperelastic solids at the same time. For more details on the derivation we refer to [60, 41].

In an elastic medium described in the Lagrangian framework, the internal energy per unit volume W (density of energy) is a function of the strain tensor $[\nabla_\xi X]$ and of the entropy s. Thus we can write the elastic energy $\mathcal{E}$ in the following way:

$$\mathcal{E} = \int_{\Omega_0} W\left([\nabla_\xi X(\xi,t)], s(X(\xi,t),t)\right) d\xi. \tag{I.22}$$

By denoting ϵ the internal energy per unit mass, we have that W and ϵ are related in the following way: $W = \rho_0 \epsilon$, ρ_0 being the initial density. Thanks to this, we can write the elastic energy (I.22) also in the deformed configuration Ω_t in the Eulerian framework with the change of variables $\xi = Y(x,t)$, obtaining:

$$\mathcal{E} = \int_{\Omega_t} W\left([\nabla_x Y]^{-1}(x,t), s(x,t)\right) \det(\nabla_x Y(x,t)) \, dx.$$

The considered potential W has to be Galilean invariant, i. e. invariant for any reference system, and isotropic, i. e. with the same behavior in all directions. It can be proved that the material is Galilean invariant if, and only if, W is expressed as a function of the entropy and of the invariants of the right Cauchy-Green tensor (for the details see [38]). This tensor is defined as $C = F^T F = [\nabla_\xi X]^T [\nabla_\xi X]$, where F is the gradient of the deformation defined in (I.19). Tensor C possesses the same invariants of the left Cauchy-Green tensor, which is in turn defined in the following way:

$$B = FF^T = [\nabla_\xi X][\nabla_\xi X]^T = [\nabla_x Y]^{-1} [\nabla_x Y]^{-T}. \tag{I.23}$$

The two dimensional invariants considered in literature are the determinant $\det(\cdot)$ and the trace $\mathrm{tr}(\cdot)$.

We also assume that W is the sum of two different terms:

- a term depending on volume variation and entropy, which can be noted as W_{vol};

- a term accounting for isochoric deformation, which can be noted as W_{iso}. In general the term relative to an isochoric transformation may also depend on the entropy. However, in the present work we limit the discussion to materials where the isochoric term is independent of the entropy, as for example metals.

Consequently, the internal energy can be decomposed in the following way [68]:

$$\begin{aligned}
\epsilon &= \epsilon_{vol}\left(\rho\left(X\left(\xi,t\right),t\right), s\left(X\left(\xi,t\right),t\right)\right) + \epsilon_{iso}\left(\mathrm{tr}\left(\overline{B}\left(\xi,t\right)\right)\right) \\
&= \epsilon_{vol}\left(\rho\left(x,t\right), s\left(x,t\right)\right) + \epsilon_{iso}\left(\mathrm{tr}\left(\overline{B}\left(x,t\right)\right)\right).
\end{aligned} \tag{I.24}$$

Here again we have the two different contributions:

- ϵ_{vol} is the purely volumetric contribution to the energy associated to the deformation (depending on the volume and on the entropy s) and it is the so called "hydrodynamic part";

- ϵ_{iso} is the purely isochoric (volume preserving) contribution and it is relative to elastic deformations at constant volume, such as shear deformations.

In (I.24), $\overline{B}$ is the normalized Cauchy stress tensor (I.23), which is computed in two dimensions in the following way:

$$\overline{B} = \frac{B}{J}, \qquad J = \det\left([\nabla_x Y]\right)^{-1}. \tag{I.25}$$

For the sake of clarity, we here explicitly write the gradient of the backward deformation in 2D and its inverse

$$[\nabla_x Y] = \begin{bmatrix} Y^1_{,1} & Y^1_{,2} \\ Y^2_{,1} & Y^2_{,2} \end{bmatrix}, \qquad [\nabla_x Y]^{-1} = \frac{1}{Y^1_{,1}Y^2_{,2} - Y^2_{,1}Y^1_{,2}} \begin{bmatrix} Y^2_{,2} & -Y^1_{,2} \\ -Y^2_{,1} & Y^1_{,1} \end{bmatrix}, \tag{I.26}$$

and then we have $J = \left(Y^1_{,1}Y^2_{,2} - Y^2_{,1}Y^1_{,2}\right)^{-1}$. Here the superscript ^{i} indicates the component of Y and the subscript $_{,j}$ stands for the direction along which the derivative is calculated, namely the notation is the following:

$$Y^i_{,j} = \frac{\partial Y^i}{\partial x_j}.$$

Consequently, the Cauchy-Green tensor reads

$$\overline{B} = \frac{1}{Y_{,1}^1 Y_{,2}^2 - Y_{,1}^2 Y_{,2}^1} \begin{bmatrix} \left(Y_{,2}^1\right)^2 + \left(Y_{,2}^2\right)^2 & -\left(Y_{,1}^2 Y_{,2}^2 + Y_{,2}^1 Y_{,1}^1\right) \\ -\left(Y_{,1}^2 Y_{,2}^2 + Y_{,2}^1 Y_{,1}^1\right) & \left(Y_{,1}^2\right)^2 + \left(Y_{,1}^1\right)^2 \end{bmatrix}. \tag{I.27}$$

The matrix $\overline{B}$ is symmetric and its determinant is equal to 1. This explains the fact that $\overline{B}$ accounts for the isochoric deformations.

Let us now focus on the two terms of relation (I.24). The hydrodynamic behavior is described with the general Van der Waals state law introduced in Section I.1.2, which includes the perfect gas and the stiffened gas behavior. We can then write the volumetric contribution in the following way:

$$\epsilon_{vol}\left(\rho, s\right) = \frac{\kappa\left(s\right)}{\gamma - 1}\left(\frac{1}{\rho} - b\right)^{1-\gamma} - a\rho + \frac{p_\infty}{\rho}.$$

For the isochoric contribution, we choose the following neo-hookean elastic law

$$\epsilon_{iso}\left(\overline{B}\right) = \frac{\chi}{\rho_0}\left(\text{tr}\overline{B} - 2\right),$$

where χ is the shear elastic modulus specific of the considered material.

Thus, the general constitutive law is able to describe gases, fluids and elastic solids at the same time and reads as follows [62, 44]

$$\epsilon\left(\rho, s, [\nabla_x Y]\right) = \underbrace{\frac{\kappa\left(s\right)}{\gamma - 1}\left(\frac{1}{\rho} - b\right)^{1-\gamma} - a\rho + \frac{p_\infty}{\rho}}_{\text{general gas}} + \underbrace{\frac{\chi}{\rho}\left(\text{tr}\overline{B} - 2\right)}_{\text{neohookean solid}}. \tag{I.28}$$

The energy function (I.28) includes different physical behaviors:

1. the first term describes an isoentropic compression, which induces an increase of internal energy (a and b correspond to the van der Waals parameters);

2. the p_∞ term accounts for the physical effect that the energy has to increase when the density is reduced. This term models the intermolecular forces that are present in liquids and solids;

3. the last term describes the variation of energy in a neohookean elastic solid due to elastic deformations. This term accounts for finite deformations. For larger deformations more complex models such as the Mooney-Rivlin or the Ogden models are needed. Without loosing in generality, we stick to a neohookean model as it leads to simpler expressions in the following developments.

As shown in Table I.1, classical models are obtained by specific choices of the coefficients.

I.2.4 Stress tensor

By definition, the Piola-Kirchhoff stress tensor can be written as the derivative of $\epsilon\left([\nabla_\xi X\left(\xi, t\right), s\left(X, t\right)]\right)$ with respect to the first variable at fixed entropy, namely

$$\mathcal{T}\left(\xi, t\right) = \rho_0 \left.\frac{\partial \epsilon}{\partial\left[\nabla_\xi X\right]}\right|_{s=const}. \tag{I.29}$$

Material	γ	a	b	p_∞	χ
		$[\mathrm{Pa\,m^6/Kg^2}]$	$[\mathrm{m^3/Kg}]$	$[\mathrm{Pa}]$	$[\mathrm{Pa}]$
Perfect biatomic gas	1.4	0	0	0	0
Van der Waals gas	1.4	5	10^{-3}	0	0
Stiffened gas (water)	4.4	0	0	$6.8 \cdot 10^8$	0
Elastic solid (copper)	4.22	0	0	$3.42 \cdot 10^{10}$	$5 \cdot 10^{10}$

Table I.1: Typical parameters for different materials.

This definition allows to compute $\mathcal{T}(\xi, t)$ in the case of a general internal energy. Moreover, the Piola-Kirchhoff stress tensor is related to the Cauchy stress tensor $\sigma(x, t)$ by the Piola transformation, which reads as follows [68]

$$\mathcal{T}(\xi, t) = \sigma\left(X\left(\xi, t\right), t\right) Cof\left(\left[\nabla_\xi X\left(\xi, t\right)\right]\right), \tag{I.30}$$

where the cofactor matrix is defined by $Cof(A) = \det(A) A^{-T}$. Thus, from the Piola-Kirchhoff tensor, the Cauchy tensor is easily computed via relation (I.30) in the following way:

$$\sigma(x, t) = \frac{\tau(\xi, t)}{\det\left(\left[\nabla_\xi X\right]\right)\left[\nabla_\xi X\right]^{-T}} = \frac{\tau\left(Y\left(x, t\right), t\right)}{\det\left(\left[\nabla_x Y\right]\right)^{-1}\left[\nabla_x Y\right]^T}$$
$$= \frac{\rho_0 \det\left(\left[\nabla_x Y\right]\right)}{\left[\nabla_x Y\right]^T}\left.\frac{\partial \epsilon}{\partial\left(\left[\nabla_x Y\right]^{-1}\right)}\right|_{s=const} = \frac{\rho}{\left[\nabla_x Y\right]^T}\left.\frac{\partial \epsilon}{\partial\left(\left[\nabla_x Y\right]^{-1}\right)}\right|_{s=const}$$

Here we have used in the second equality the change of variables $\xi = Y(x, t)$ and relation (I.17). For the third equality, the definition of τ (I.29) is plugged in, where the derivative with respect to $[\nabla_\xi X]$ is equivalent to the derivative with respect to $[\nabla_x Y]$. For the last equality, relation (I.20) is employed.

With this latter expression, we are now able to compute σ in the case of constitutive law (I.24). The resulting Cauchy stress tensor is the following (see [68] for the detailed derivation):

$$\sigma(x, t) = -\rho^2 \left.\frac{\partial \epsilon_{vol}}{\partial \rho}\right|_{s=const}(\rho, s) + 2J^{-1}\epsilon'_{iso}\left(\mathrm{tr}\left(\overline{B}\right)\right)\left(\overline{B} - \frac{\mathrm{tr}\left(\overline{B}\right)}{2}I\right). \tag{I.31}$$

Then, the general expression of the Cauchy stress tensor σ is obtained from (I.28) and (I.31) in the following way

$$\begin{cases} \sigma\left(\rho, s, \left[\nabla_x Y\right]\right) = -p\left(\rho, s\right)\mathbf{I} + 2\chi J^{-1}\left(\overline{B} - \frac{\mathrm{tr}\overline{B}}{2}\mathbf{I}\right) \\ p\left(\rho, s\right) = -p_\infty - a\rho^2 + k\left(s\right)\left(\frac{1}{\rho} - b\right)^{-\gamma}. \end{cases} \tag{I.32}$$

Here the matrix $\mathbf{I}$ is the identity. In two dimensions σ can be explicitly written as follows:

$$\sigma = \begin{bmatrix} \sigma^{11} & \sigma^{12} \\ \sigma^{21} & \sigma^{22} \end{bmatrix} =$$

$$-p\left(\rho, s\right)\mathbf{I} + \chi \begin{bmatrix} \left(Y_{,2}^2\right)^2 + \left(Y_{,2}^1\right)^2 - \left(Y_{,1}^1\right)^2 - \left(Y_{,1}^2\right)^2 & -2\left(Y_{,1}^1 Y_{,2}^1 + Y_{,1}^2 Y_{,2}^2\right) \\ -2\left(Y_{,1}^1 Y_{,2}^1 + Y_{,1}^2 Y_{,2}^2\right) & -\left(Y_{,2}^2\right)^2 - \left(Y_{,2}^1\right)^2 + \left(Y_{,1}^1\right)^2 + \left(Y_{,1}^2\right)^2 \end{bmatrix}.$$

σ^{11} and σ^{22} are the normal components of the tensor along directions x_1 and x_2 and they can be decomposed in an acoustic part (given by the pressure function) and an elastic part, whereas $\sigma^{12} = \sigma^{21}$ are the tangential components, related to shear. The tangential component of the stress tensor is only elastic. We remark that σ is a symmetric tensor. It is evident that by setting $a = b = 0$ and $\chi = p_\infty = 0$ the perfect gas state law is recovered.

Letting $x = (x_1, x_2)$ be the coordinates in the canonical basis of $\mathbb{R}^2$, $\mathbf{u} = (u_1, u_2)$ the velocity components, system (I.21) can be rewritten in the compact form

$$\partial_t \psi + \partial_{x_1} \mathbf{F}(\psi) + \partial_{x_2} \mathbf{G}(\psi) = 0, \tag{I.33}$$

where we have adopted the directional splitting of the flux function. The conservation variables and the fluxes along the two directions read as follows:

$$\psi = \begin{bmatrix} \rho \\ \rho u_1 \\ \rho u_2 \\ Y_{,1}^1 \\ Y_{,1}^2 \\ Y_{,2}^1 \\ Y_{,2}^2 \\ \rho e \end{bmatrix}, \quad \mathbf{F}(\psi) = \begin{bmatrix} \rho u_1 \\ \rho u_1^2 - \sigma^{11} \\ \rho u_1 u_2 - \sigma^{21} \\ u_1 Y_{,1}^1 + u_2 Y_{,2}^1 \\ u_1 Y_{,1}^2 + u_2 Y_{,2}^2 \\ 0 \\ 0 \\ (\rho e - \sigma^{11}) u_1 - \sigma^{21} u_2 \end{bmatrix}, \quad \mathbf{G}(\psi) = \begin{bmatrix} \rho u_2 \\ \rho u_1 u_2 - \sigma^{12} \\ \rho u_2^2 - \sigma^{22} \\ 0 \\ 0 \\ u_1 Y_{,1}^1 + u_2 Y_{,2}^1 \\ u_1 Y_{,1}^2 + u_2 Y_{,2}^2 \\ (\rho e - \sigma^{22}) u_2 - \sigma^{12} u_2 \end{bmatrix}. \tag{I.34}$$

I.2.5 Wave speeds

The computation of the characteristic speeds of system (I.21) closed by state law (I.28) is detailed in previous works for 2D and 3D conservation systems [62, 44]. Here we report the computation in two dimensions.

By considering smooth flow, the entropy is transported along the characteristics, i. e. the following equation holds:

$$\partial_t s + \mathbf{u} \cdot \nabla_x s = 0. \tag{I.35}$$

We adopt the directional splitting (I.33)-(I.34). The wave velocities are locally defined by infinitesimal variations of the conservative variables ψ. Therefore, the energy equation can be replaced by equation (I.35). The system is closed by the constitutive law (I.28). Due to this, the stress tensor σ is defined as a non-linear function of the conservative variables, as reported in expression (I.32).

For the sake of simplicity, we consider variations only along the x_1 direction. We can then re-write the system in the quasi-linear form as follows:

$$\partial_t \psi + \tilde{F}'(\psi) \partial_{x_1} \psi = 0,$$

where $\tilde{F}'(\psi)$ is the Jacobian of the flux $\tilde{F}$. The flux $\tilde{F}$ is the same as the flux $\mathbf{F}$ defined in (I.34), except for the last component which is substituted by the entropy equation (I.35) that is

already in quasi-linear form. Thus, the Jacobian of the flux $\tilde{F}(\psi)$ has the following formulation:

$$\tilde{F}'(\psi) = \begin{bmatrix} 0 & 1 & 0 & 0 & 0 & 0 \\ -u_1^2 & 2u_1 & 0 & -\sigma_{,1}^{11} & -\sigma_{,2}^{11} & -\sigma_{,s}^{11} \\ -u_1 u_2 & u_2 & u_1 & -\sigma_{,1}^{21} & -\sigma_{,2}^{21} & -\sigma_{,s}^{21} \\ -\frac{u_1 Y_{,1}^1 + u_2 Y_{,2}^1}{\rho} & \frac{Y_{,1}^1}{\rho} & \frac{Y_{,2}^1}{\rho} & u_1 & 0 & 0 \\ -\frac{u_1 Y_{,1}^2 + u_2 Y_{,2}^2}{\rho} & \frac{Y_{,1}^2}{\rho} & \frac{Y_{,2}^2}{\rho} & 0 & u_2 & 0 \\ 0 & 0 & 0 & 0 & 0 & u_1 \end{bmatrix}, \tag{I.36}$$

where we are using the following notation

$$\sigma_{,i}^{jk} = \frac{\partial \sigma^{jk}}{\partial Y_{,1}^i}, \quad \sigma_{,s}^{jk} = \frac{\partial \sigma^{jk}}{\partial s}.$$

The wave speeds correspond to the eigenvalues of the matrix $\tilde{F}'(\psi)$ in (I.36).

In order to compute the eigenvalues of matrix (I.36), we define the tensor Σ as

$$\Sigma = [\nabla_Y \sigma] [\nabla_x Y] = \begin{bmatrix} \sigma_{,1}^{11} & \sigma_{,2}^{11} \\ \sigma_{,1}^{21} & \sigma_{,2}^{21} \end{bmatrix} \begin{bmatrix} Y_{,1}^1 & Y_{,2}^1 \\ Y_{,1}^2 & Y_{,2}^2 \end{bmatrix}.$$

Thus, the characteristic polynomial of the Jacobian (I.36) can be written in the following way:

$$P(\lambda) = \frac{(\lambda - u_1)^2}{\rho^2} \left[\left((\lambda - u_1)^2 \rho \right)^2 - tr(-\Sigma)(\lambda - u_1)^2 \rho + \det(-\Sigma) \right].$$

The set of the eigenvalues is then easily computed by taking the roots of $P(\lambda)$:

$$\Lambda = \{u_1, u_1, u_1 \pm \sqrt{\frac{\alpha_1}{\rho}}, u_1 \pm \sqrt{\frac{\alpha_2}{\rho}}\}, \tag{I.37}$$

where α_1 and α_2 are the eigenvalues of $-\Sigma$, namely the roots of the polynomial

$$X^2 - tr(\Sigma) X + \det(\Sigma) = 0.$$

The conditions of hyperbolicity for the system along direction x_1 are thus $\alpha_1 > 0$ and $\alpha_2 > 0$.

The eigenvalues may also be written with following general expression [62]:

$$\Lambda = \left\{ u_1, u_1, u_1 \pm \sqrt{\frac{\mathcal{A}_1 \pm \sqrt{\mathcal{A}_2}}{\rho}} \right\}. \tag{I.38}$$

In order to get this formulation, one has to substitute the state law (I.28) inside the Jacobian (I.36). Then, α_1 and α_2 take the following expressions:

$$\alpha_1 = \mathcal{A}_1 + \sqrt{\mathcal{A}_2} \text{ and } \alpha_2 = \mathcal{A}_1 - \sqrt{\mathcal{A}_2},$$

$$\begin{cases} \mathcal{A}_1 = \frac{\rho c^2}{2} + \chi(\alpha + \beta) \\ \mathcal{A}_2 = \left(\frac{\rho c^2}{2} + \chi(\alpha - \beta) \right)^2 + 4\chi^2 \delta^2, \end{cases}$$
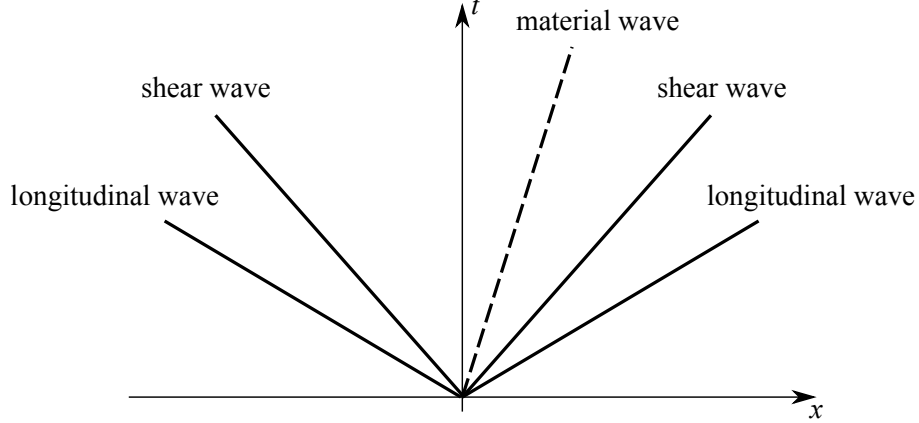
Figure I.2: Wave structure with 5 waves. The material wave is dotted and corresponds to a contact discontinuity.

where c is the sound speed defined as

$$c^2 = \left.\frac{\partial p}{\partial \rho}\right|_{s=const} = \frac{\gamma\left(p + a\rho^2 + p_\infty\right)}{\rho\left(1 - \rho b\right)} - 2a\rho \tag{I.39}$$

and where we also have introduced the notation

$$\begin{cases} \alpha = \left(Y_{,1}^1\right)^2 + \left(Y_{,1}^2\right)^2 \\ \beta = \left(Y_{,2}^1\right)^2 + \left(Y_{,2}^2\right)^2 \\ \delta = Y_{,1}^1 Y_{,2}^1 + Y_{,1}^2 Y_{,2}^2. \end{cases} \tag{I.40}$$

This way, the roots α_1 and α_2 in (I.37) are positive values if $\chi \geq 0$ and $c^2 > 0$. These conditions are always verified, thus the eigenvalues (I.37) are real numbers and the wave speed are well defined. The hyperbolicity of the conservation system is always verified.

With six eigenvalues, two of which are identical, we get a Riemann problem with five waves. This Riemann problem wave structure is constituted by

1. two *longitudinal waves* relative to the normal stress, with speed

$$\lambda_{1,5} = u_1 \pm \sqrt{c^2/2 + \chi/\rho\left(\alpha + \beta\right) + 1/\rho\sqrt{\left(\rho c^2/2 + \chi\left(\alpha - \beta\right)\right)^2 + 4\chi^2\delta^2}}; \tag{I.41}$$

2. two *shear waves* relative to the tangential stress, with speed

$$\lambda_{2,4} = u_1 \pm \sqrt{c^2/2 + \chi/\rho\left(\alpha + \beta\right) - 1/\rho\sqrt{\left(\rho c^2/2 + \chi\left(\alpha - \beta\right)\right)^2 + 4\chi^2\delta^2}}; \tag{I.42}$$

3. one *material wave* with speed $\lambda_3 = u_1$, namely the flow velocity.

In (I.41)-(I.42) we are using the notation introduced in (I.40). It is clear that longitudinal waves are always faster than shear waves. The wave pattern is illustrated in Fig. I.2.

In the case of a fluid, the shear modulus is zero $\chi = 0$. Thus the coefficients $\mathcal{A}_1$ and $\mathcal{A}_2$ inside (I.38) get the following simplified expression: $\mathcal{A}_1 = \rho c^2/2$ and $\mathcal{A}_2 = \mathcal{A}_1^2$. The set of eigenvalues (I.37) of the Jacobian matrix then reduces to

$$\Lambda = \{u_1, u_1 \pm c\}, \tag{I.43}$$

namely we get the standard three wave speeds of fluid dynamics: two acoustic waves related to compression and one material wave.

I.2.6 One dimensional problem formulation

In this section, we focus on the variations only along direction x_1, thus considering the problem in one dimension. Deformations are still considered in both the two directions, but the derivatives along x_2 are set equal to zero. Tensor $[\nabla_x Y]$ reduces to

$$[\nabla_x Y] = \begin{bmatrix} Y^1_{,1} & 0 \\ Y^2_{,1} & 1 \end{bmatrix}.$$

The problem can be further simplified, since $\rho(x,t) = \det([\nabla_x Y](x,t)) \rho_0(x)$, where ρ_0 is the initial density. Thanks to this, the equation on $Y^1_{,1}$ is equivalent to conservation of mass and thus redundant, having $Y^1_{,1} = \rho/\rho_0$.

In this framework, the Cauchy stress tensor (I.32) has the following two non-zero components, which are the normal and the tangential stress respectively:

$$\sigma^{11} = -p(\rho,s) + 2\chi J^{-1}\left(\overline{B}^{11} - \frac{\mathrm{tr}\overline{B}}{2}\right) = -p(\rho,s) + \chi\left(1 - \left(Y^2_{,1}\right)^2 - (\rho/\rho_0)^2\right)$$

$$\sigma^{21} = 2\chi J^{-1}\overline{B}^{21} = -2\chi Y^2_{,1}.$$

The σ^{11} component is responsible for deformations along direction x_1, such as elongations or compressions. These deformations may be acoustic or elastic or a combination of the two, as it is clear by analyzing the expressions of the stress tensor component. Indeed, σ^{11} is given by the sum of the pressure function, which is the acoustic part, and of a function of the elastic deformation. The σ^{21} component is instead only elastic and it produces shear deformations along direction x_2. The five waves are those analyzed in the previous section (see Fig. I.2).

We can then write the following compact form for the 1D Eulerian model:

$$\partial_t \boldsymbol{\psi} + \partial_{x_1} \mathbf{F}(\boldsymbol{\psi}) = 0, \tag{I.44}$$

where the vector of conservative variables and the vector of fluxes are both in $\mathbb{R}^5$ and read

$$\boldsymbol{\psi} = \begin{bmatrix} \rho \\ \rho u_1 \\ \rho u_2 \\ Y^2_{,1} \\ \rho e \end{bmatrix}, \quad \mathbf{F}(\boldsymbol{\psi}) = \begin{bmatrix} \rho u_1 \\ \rho u_1^2 - \sigma^{11} \\ \rho u_1 u_2 - \sigma^{21} \\ u_1 Y^2_{,1} + u_2 \\ (\rho e - \sigma^{11})u_1 - \sigma^{21}u_2 \end{bmatrix}.$$

This compact formulation will be our starting point for the analysis of the low Mach limits that can occur inside elastic solids. This will be the main topic of the next chapter. Moreover, the novel all-speed scheme presented in Chapter III will be derived on this one dimensional formulation. The extension of the scheme to two dimensional problems (with the solution of the full 2D conservation system (I.21)) will be carried out in Chapter IV.

The aim of the present thesis is indeed the solution of the Eulerian model illustrated in this chapter, with a numerical method that is built to handle the low Mach regime and the fully compressible regime at the same time. The goal is to have an all-speed scheme that does not depend on the specific state law but is able to solve flows of gases, liquids and solids with the same structure.

Chapter II

The low Mach regime

This chapter is devoted to the analysis of the low Mach limits in fluid dynamics and continuum mechanics and to the numerical problems that can occur in the low Mach regime.

As a first step, we briefly revise the standard low Mach limit theory for fluid dynamics problems, specifically for the Euler equations. Then, we extend this theory to the full Eulerian system presented in Chapter I, namely we introduce the low Mach regime in elastic solids. In general, the low Mach regime occurs when material waves travel with a speed that is consistently lower with respect to a subset of the remaining waves. In the case of fluids, it means that the flow motion is consistently slower than the acoustic waves. In the case of an elastic solid, the deformation wave is slower than the longitudinal compression waves and/or slower than the shear isochoric waves.

In the second part of the chapter, we focus on the main numerical difficulties that are encountered when using standard compressible codes to solve the low Mach regime. We briefly present different numerical schemes that have been proposed in literature to solve low Mach fluid flows (*low Mach* solvers) and also schemes to solve the fully compressible and the low Mach regimes with the same code (*all-speeds* solvers). As part of this latter category, a novel all-speed relaxation scheme is introduced, for the solution of the full Eulerian system. The scheme will be derived and analyzed in detail in Chapter III.

II.1   The low Mach limit for the Euler equations

In this section, we carry out an analysis of the low Mach regime in fluid dynamics. The low Mach limit of the Euler equations has been extensively studied in literature, starting from the seminal works by Klainerman and Majda [74, 75]. Several other works and reviews on the low Mach limits of the continuous Euler system may be found in literature on both the isentropic system (see for example the works of Métivier and Schochet [91, 113] and the work of Degond et al. [45]) and non-isentropic system (see for example the work of Dellacherie [46] and the works of Guillard and Viozat [65] and of Klein [76], where the behavior of Godunov-type schemes is also analyzed). In most of these papers, to the analysis of the continuous Euler system, a derivation of numerical schemes possessing the correct asymptotics follows (the numerical schemes proposed in literature to solve low Mach flows will be presented in Section II.3).

Here, we focus on the general non-isentropic Euler system. We begin by introducing the

non-dimensional compressible Euler system and then we analyze its asymptotics when the Mach number tends to zero. We thus derive the incompressible limit system and study the propagation of acoustic waves at small Mach numbers.

II.1.1 Non-dimensional Euler system

The first step toward the study of the behavior of compressible flows in the low Mach regime consists in writing the Euler system in its non-dimensional (or scaled) formulation. Each quantity, such as density, velocity and pressure, is decomposed into a product of a reference value (denoted with the subscript $*$) and a dimensionless number (denoted with $\widehat{\cdot}$), e.g. $\rho = \rho^* \widehat{\rho}$ is the decomposition of the density. The reference value is a "scaling" factor and it should always be chosen in such a way that the dimensionless value is of order one. In this spirit, the following non-dimensional variables are introduced:

$$\widehat{\rho} = \frac{\rho}{\rho^*}, \qquad \widehat{\mathbf{u}} = \frac{\mathbf{u}}{u^*},$$

$$\widehat{x} = \frac{x}{x^*}, \qquad \widehat{t} = \frac{t}{t^*} = \frac{t u^*}{x^*}, \tag{II.1}$$

$$\widehat{p} = \frac{p}{p^*} = \frac{p}{\rho^* (c^*)^2}, \qquad \widehat{(\rho e)} = \frac{\rho e}{\rho^* (c^*)^2}.$$

In the scaling of the pressure, we have defined the reference pressure p^* with the reference sound speed $c^* = \sqrt{p^*/\rho^*}$ (for the general definition of the speed of sound see (I.39)). The same scaling through the reference sound speed is adopted for the total energy ρe, which is defined in (I.4): since it is given by the sum of a kinetic part and an internal part, we choose to scale it on the internal part, which is proportional to the pressure.

Definitions (II.1) can be substituted inside the standard Euler system (I.6) and the non-dimensional formulation is easily derived. After some simple algebraic manipulations, most of the reference quantities cancel out, leading to the non-dimensional Euler system (from now on, we omit the hat notation $\widehat{\cdot}$ for the sake of simplicity):

$$\begin{cases} \partial_t \rho + \operatorname{div}(\rho \mathbf{u}) = 0 & \text{(II.2)} \\[2mm] \partial_t (\rho \mathbf{u}) + \operatorname{div}(\rho \mathbf{u} \otimes \mathbf{u}) + \frac{1}{M^2} \nabla p = 0 & \text{(II.3)} \\[2mm] \partial_t (\rho e) + \operatorname{div}((\rho e + p)\, \mathbf{u}) = 0. & \text{(II.4)} \end{cases}$$

We can observe that the non-dimensional Euler system depends only on a single, non-dimensional reference quantity. This is the reference Mach number, which is defined as the ratio between the reference flow velocity and the reference sound speed as follows:

$$M = \frac{u^*}{c^*}. \tag{II.5}$$

The non-dimensional state law reads

$$p = (\gamma - 1) \left[\rho e - \frac{M^2}{2} \rho |\mathbf{u}|^2 \right]. \tag{II.6}$$

In this procedure, the scaling of the energy introduced in relation (II.1) allows to non-dimensionalize the equation of state separately from the three conservation laws, as it is done in several works, such as [65, 40].

Alternatively, one could scale the total energy in a different way, i. e. by taking into account the two components in the scaling: then the kinetic part is non-dimensionalized with the reference flow velocity u^* and the internal part with the non-dimensional sound speed c^*. Thus, the energy equation (II.4) is re-written by substituting the expression of the total energy inside it, as follows

$$\partial_t \left(\frac{1}{2} \rho |\mathbf{u}|^2 + \frac{p}{\gamma - 1} \right) + \text{div} \left(\left(\frac{1}{2} \rho |\mathbf{u}|^2 + \frac{\gamma}{\gamma - 1} p \right) \cdot \mathbf{u} \right) = 0. \tag{II.7}$$

In the scaled formulation, with the splitting of kinetic and internal part, (II.7) becomes

$$\frac{1}{2} \partial_t \left(\rho |\mathbf{u}|^2 \right) + \frac{1}{M^2 (\gamma - 1)} \partial_t p + \frac{1}{2} \text{div} \left(\rho |\mathbf{u}|^2 \cdot u \right) + \frac{\gamma}{M^2 (\gamma - 1)} \text{div} (p\mathbf{u}) = 0. \tag{II.8}$$

This last expression helps in distinguishing the two different time scales also in the energy equation.

II.1.2   Low Mach number asymptotics

In what follows, the asymptotic behavior of the compressible Euler equations in the limit of zero Mach number is analyzed, by mostly following the work by Guillard and Viozat [65]. We focus on the scaled system (II.2)-(II.3)-(II.4). An expansion of the non-dimensional equations in terms of the Mach number is performed, i.e. the non-dimensional density, velocity, pressure and energy are written in the following way:

$$\begin{aligned}
\rho &= \rho_0 + M \rho_1 + M^2 \rho_2 + \mathcal{O}\left(M^3 \right) \\
\mathbf{u} &= \mathbf{u}_0 + M \mathbf{u}_1 + M^2 \mathbf{u}_2 + \mathcal{O}\left(M^3 \right) \\
(\rho e) &= (\rho e)_0 + M (\rho e)_1 + M^2 (\rho e)_2 + \mathcal{O}\left(M^3 \right) \\
p &= p_0 + M p_1 + M^2 p_2 + \mathcal{O}\left(M^3 \right).
\end{aligned} \tag{II.9}$$

The terms of zeroth order (subscript $\cdot_0$) represent the zero Mach number limit. Expressions (II.9) are thus inserted into the non-dimensional Euler system (II.2)-(II.3)-(II.4) with the non-dimensional EOS (II.6) and terms with equal power of M are collected, obtaining :

- order $\mathcal{O}\left(1/M^2 \right)$:

$$\nabla p_0 = 0 \tag{II.10}$$

- order $\mathcal{O}\left(1/M \right)$:

$$\nabla p_1 = 0 \tag{II.11}$$

- order $\mathcal{O}\left(1 \right)$:

$$\begin{cases}
\partial_t \rho_0 + \nabla \cdot (\rho_0 \mathbf{u}_0) = 0 & \text{(II.12)} \\
\partial_t (\rho_0 \mathbf{u}_0) + \nabla \cdot (\rho_0 \mathbf{u}_0 \otimes \mathbf{u}_0) + \nabla p_2 = 0 & \text{(II.13)} \\
\partial_t (\rho e)_0 + \nabla \cdot ((\rho e)_0 \mathbf{u}_0 + p_0 \mathbf{u}_0) = 0, & \text{(II.14)}
\end{cases}$$

with the first order of the state law

$$p_0 = (\gamma - 1) (\rho e)_0. \tag{II.15}$$

Relations (II.10) and (II.11) demonstrate that the pressure is constant in space up to fluctuations of order M^2. Hence we can write the following pressure asymptotic:

$$p\left(x,t\right) = P_0\left(t\right) + M^2 p_2\left(x,t\right), \tag{II.16}$$

where $P_0\left(t\right)$ is a thermodynamic pressure constant in space. This means that in the low Mach regime, namely when $M \to 0$, the pressure is almost constant in space.

In presence of open boundaries, the thermodynamic pressure P_0 is imposed to be equal to the exterior pressure P_{ext}. For the sake of simplicity, we assume that the exterior pressure does not change in time. Under these conditions on the boundaries, P_0 is constant in both space and time, since we have that

$$\frac{dP_{ext}}{dt} = \frac{dP_0}{dt} = 0.$$

Therefore, from the first order state law (II.15), we deduce that also the energy is constant in space and time, since it is proportional to the thermodynamic pressure P_0, getting

$$\partial_t\left(\rho e\right)_0 = \nabla\left(\rho e\right)_0 = 0.$$

This last fact can be used inside the first order conservation of energy (II.14), which can be re-written and degenerates as follows

$$\partial_t\left(\rho e\right)_0 + \mathbf{u}_0\nabla\left(\rho e\right)_0 + \left(\rho e\right)_0\nabla\cdot\mathbf{u}_0 + p_0\nabla\cdot\mathbf{u}_0 + u_0\nabla p_0$$
$$= \left(\rho e\right)_0\nabla\cdot\mathbf{u}_0 = 0.$$

giving the incompressibility constraint $\nabla\cdot\mathbf{u}_0 = 0$.

Introducing this constraint into the continuity equation (II.12), we get the following expression

$$\partial_t\rho_0 + \rho_0\nabla\cdot\mathbf{u}_0 + \mathbf{u}_0\nabla\cdot\rho_0$$
$$= \partial_t\rho_0 + \mathbf{u}_0\nabla\cdot\rho_0 = 0,$$

namely the material derivative of the density is zero $\frac{D\rho}{Dt} = 0$. This means that the density is constant along a trajectory of any fluid element. Therefore, when the incompressibility constraint is respected, in the case where the initial density of the fluid is constant in space, the density of the fluid is constant in time and space, i. e. $\rho_0 = $ const.

II.1.2.1 Incompressible Euler equations

With the study of the asymptotics carried out above, the first order $\mathcal{O}\left(1\right)$ system (II.12)-(II.13)-(II.14) reduces to the *incompressible* Euler system in its non-dimensional form. This system reads as follows

$$\begin{cases} \rho_0 = \text{const} & \text{(II.17)} \\ \rho_0\left(\partial_t\mathbf{u}_0 + \left(\mathbf{u}_0\cdot\nabla\right)\mathbf{u}_0\right) + \nabla p_2 = 0 & \text{(II.18)} \\ \nabla\cdot\mathbf{u}_0 = 0. & \text{(II.19)} \end{cases}$$

This is the zero Mach number limit of the compressible Euler system. The name "incompressible" originates from the fact that the density of a fluid element cannot change, as it is advected with the flow (the material derivative of the density is zero and thus the density is constant).

Moreover, we stress the fact that the asymptotic behavior of the pressure field is now known though relation (II.16). This relation states that the pressure fluctuations scale with the square of the Mach number, as the solution of the compressible Euler equations convergences to the solution of the incompressible equations. An explicit equation for the pressure can be obtained by taking the divergence of the incompressible momentum equation (II.18), in the following way:

$$\nabla \cdot \left[\rho_0 \left(\partial_t \mathbf{u}_0 + (\mathbf{u}_0 \cdot \nabla) \mathbf{u}_0 \right) \right] + \triangle p_2 = 0.$$

Using the fact that $\nabla \cdot \mathbf{u}_0 = 0$, the time derivative is eliminated and we get that the pressure satisfies the following equation:

$$
\begin{aligned}
-\triangle p_2 &= \rho \nabla \cdot (\mathbf{u}_0 \cdot \nabla \mathbf{u}_0) \\
&= \rho \, \mathrm{tr} \left(\nabla \mathbf{u}_0 \right)^2,
\end{aligned}
\tag{II.20}
$$

where we have re-written the divergence $\nabla \cdot (\mathbf{u}_0 \cdot \nabla \mathbf{u}_0)$ as the trace of the gradient of $\mathbf{u}_0$ after some algebraic manipulations. Observing equation (II.20), it is clear that the pressure in the incompressible limit satisfies an elliptic problem. This problem expresses the instantaneous propagation of pressure information throughout the entire domain in incompressible flows. The fact that the pressure propagates instantaneously throughout the entire domain will have very important consequences on the numerical method, as we will see in Section II.3.

We also point out that the energy in an incompressible flow is constant in space and time $\rho e = \mathrm{const}$ thanks to EOS at first order (II.15), which states that the total energy is proportional to the pressure.

II.1.2.2 Acoustic waves

The incompressible Euler equations (II.17)-(II.18)-(II.19) do not describe acoustic waves, since they do not permit density fluctuations at all. However, it is evident from everyday physics that stationary fluids at small Mach number support the propagation of acoustic waves. In order to show this fact, let us consider a fluid at rest (i. e. $u_0 = 0$) with constant density ρ_0 and constant pressure p_0. For the sake of simplicity, we focus on a one dimensional problem. We can express small variations from this rest state in the following way:

$$\rho = \rho_0 + M \rho_1, \quad p = p_0 + M p_1, \quad u = M u_1, \tag{II.21}$$

where $M \ll 1$ and where we are considering scaled variables, but we loose the $\widehat{\cdot}$ for simplicity, as done in the previous section.

We study the evolution of these small variations by plugging them into the scaled continuity and momentum Euler equations (II.2)-(II.3) in one dimension. We keep only terms up to order $\mathcal{O}(M)$, getting the following continuity and momentum equations:

$$
\begin{cases}
\partial_t \rho_1 + \rho_0 \partial_x u_1 = 0 & \text{(II.22)} \\[2mm]
\rho_0 \partial_t u_1 + \dfrac{1}{M^2} \partial_x p_1 = 0. & \text{(II.23)}
\end{cases}
$$

Here we have used the fact that ρ_0 and p_0 are constant in space and thus all spatial derivatives involving these quantities cancel out.

We now take the time derivative of the continuity equation (II.22) and get

$$\partial_{tt}\rho_1 + \rho_0 \partial_t \partial_x u_1 = 0, \tag{II.24}$$

and also the spatial derivative of the momentum equation (II.23), getting

$$\rho_0 \partial_x \partial_t u_1 + \frac{1}{M^2}\partial_{xx}p_1 = 0.$$

In this latter equation, the two derivatives of the first term may be exchanged due to continuity, therefore an expression for the term $\partial_t \partial_x u_1$ is easily obtained. This expression can be used inside equation (II.24), which is thus rewritten in the following way:

$$\partial_{tt}\rho_1 - \frac{1}{M^2}\partial_{xx}p_1 = 0. \tag{II.25}$$

Considering isentropic flow for simplicity, i. e. the energy equation is not solved, we express the pressure fluctuations as density fluctuations, under the hypothesis of an adiabatic thermodynamic process. By recognizing the definition of the non-dimensional speed of sound c, the following expression for the pressure is obtained

$$p_1 = \left.\frac{\partial p}{\partial \rho}\right|_{s=const} \rho_1 = c^2\rho_1.$$

This can be used to rewrite equation (II.25) in the following way:

$$\partial_{tt}\rho_1 - \frac{c^2}{M^2}\partial_{xx}\rho_1 = 0.$$

This is clearly a linear wave equation. Therefore, it is evident that sound waves that can propagate forward and backwards at speed $\pm c/M$ are present.

The above analysis has shown that the Euler system allows for the propagation of sound waves with arbitrarily small velocity fluctuations, which means that these waves may propagate at arbitrarily small Mach numbers. Moreover, the relative velocity fluctuations have the same order of the pressure fluctuations. Therefore, sound waves may be recognized by the fact that pressure fluctuations scale linearly with the reference Mach number (see relation (II.21)).

Dellacherie [46] and also Schochet [112] have proved that as the Mach number is decreased, compressible Euler equations permit two distinct solutions in the low Mach number regime:

1. nearly *incompressible* flows, as described in Section II.1.2.1 with the derivation of the incompressible Euler system;

2. *acoustic waves* propagating with arbitrarily small velocity fluctuations, as described just above.

The incompressible solution may be used as a criterium to check the good quality of a numerical scheme that has to be accurate in the low Mach limit. When setting up an incompressible flow as initial condition for the compressible Euler equations, the solutions should stay in the incompressible regime. This means that a scheme should maintain this property and an incompressible solution should be recovered at all times. In this case, the pressure fluctuations of the flow have to scale with M^2, as reported in relation (II.16).

If instead we are in the second case, i. e. acoustic waves propagate, pressure fluctuations have to decrease as the Mach number of the flow is decreased with a linear dependence.

II.2 The low Mach limit in elastic solids

In this section, we analyze the low Mach regime in compressible elastic solids. As a first step, we perform the non-dimensionalization of the monolithic Eulerian model introduced in Chapter I for the simulation of compressible materials. Then, we extend to solids the concept of low Mach regime, that has been presented in the previous section for fluids. We have recently proposed this analysis in [1, 3].

II.2.1 Non-dimensionalization

For simplicity of notation, we here consider the case of the one-dimensional formulation (I.44) and we also take $a = b = 0$ (namely Van der Waals gases are not analyzed in this section).

As a first step, we introduce the two following speeds:

- the *speed of sound*, which is computed in the standard way obtaining

$$c\left(\rho, s, \nabla_x Y\right) = \sqrt{\left.\frac{\partial p}{\partial \rho}\right|_{s=const}} = \sqrt{\gamma k\left(s\right) \rho^{\gamma-1}} = \sqrt{\frac{\gamma}{\rho}\left(p + p_\infty\right)}. \qquad (II.26)$$

- an "*isochoric elastic speed*", which is here defined in the following way:

$$u_{iso} = \sqrt{\frac{2\chi}{\rho}}. \qquad (II.27)$$

With the two speeds defined above, two different scales can be distinguished. They are helpful in the non-dimensionalization of the Eulerian system, since on these two speeds, two different "Mach numbers" can be defined as follows:

- the classical *acoustic Mach number*, which is the ratio between the acoustic speed and the advective velocity, defined as

$$M = \frac{u_1}{c}; \qquad (II.28)$$

- an *isochoric Mach number*, which is the ratio between the isochoric speed (II.27) and the advective velocity, defined as

$$M_\chi = \frac{u_1}{u_{iso}} = \sqrt{\frac{\rho u_1^2}{2\chi}}. \qquad (II.29)$$

As done for the standard case of the Euler system with relations (II.1), every variable has to be decomposed into a product of a reference value (denoted by the subscript *) with a dimensionless number (denoted with $\widehat{\cdot}$). Also in this case, we keep using the sound speed (II.26) to scale the pressure. Then, a reference elastic modulus χ^* is introduced in order to scale the dimensional shear modulus and a reference velocity u^* is used to scale both u_1 and u_2. We also draw the attention of the reader on the fact that overall the stress tensor σ has the same units of a pressure (Pascal $Pa = kg/\left(ms^2\right)$) and that the gradient of the deformation $[\nabla_x Y]$ is non-dimensional (Y is a length and ∇_x is the reciprocal of a length). In the end, only the

following non-dimensional variables differ from the standard Euler case (II.1):

$$
\widehat{u_1} = \frac{u_1}{u^*} \quad \widehat{u_2} = \frac{u_2}{u^*}
$$
$$
\widehat{p} = \frac{p}{p^*} = \frac{p}{\rho^* \left(c^*\right)^2}
$$
$$
\widehat{\chi} = \frac{\chi}{\chi^*} = \frac{\chi}{\rho^* \left(u_{el}^*\right)^2}.
$$

(II.30)

By using the definitions of the two Mach numbers (II.28) and (II.29), we get the following formulation of the non-dimensional Eulerian system (for simplicity of notation we loose the hat $\widehat{\cdot}$ on the non-dimensional variables):

$$
\begin{cases}
\partial_t \rho + \partial_x \left(\rho u_1\right) = 0 \\[2mm]
\partial_t \left(\rho u_1\right) + \partial_x \left(\rho u_1^2\right) + \dfrac{\partial_x p}{M^2} - \dfrac{\chi}{2} \dfrac{\partial_x \left(1 - \left(Y_{,1}^2\right)^2 - (\rho/\rho_0)^2\right)}{M_\chi^2} = 0 \\[4mm]
\partial_t \left(\rho u_2\right) + \partial_x \left(\rho u_1 u_2\right) + \chi \dfrac{\partial_x Y_{,1}^2}{M_\chi^2} = 0 \\[4mm]
\partial_t \left(Y_{,1}^2\right) + \partial_x \left(u_1 Y_{,1}^2 + u_2\right) = 0 \\[3mm]
\partial_t \left(\dfrac{1}{2}\rho u^2 + \dfrac{p + \gamma p_\infty}{M^2 \left(\gamma - 1\right)} + \dfrac{\chi \left(tr\overline{B} - 2\right)}{2M_\chi^2}\right) + \partial_x \left(\dfrac{1}{2}\rho |u|^3 + \dfrac{\gamma \left(p + \gamma p_\infty\right)}{M^2 \left(\gamma - 1\right)} u_1\right) + \\[4mm]
\dfrac{\chi}{2M_\chi^2}\partial_x \left[\left(tr\overline{B} - 2 - \chi \left(1 - \left(Y_{,1}^2\right)^2 - (\rho/\rho_0)^2\right)\right) u_1 + 2\chi Y_{,1}^2 u_2\right] = 0.
\end{cases}
$$

(II.31)

The non-dimensional system shows that three different scales can be distinguished:

1. the *advective scale*, with u_1 as the characteristic speed. This scale is given by the spatial derivatives (gradients in 2D) of the velocity field **u**. This scale corresponds to the material wave speed, namely the flow velocity and/or the deformation velocity;

2. the *acoustic scale*, with the sound speed c as the characteristic speed. This is represented by the spatial gradient of the acoustic parts of the stress tensor σ, i. e. by the pressure function $p(\rho, s)$. The pressure gradients are divided by M^2, thus these terms become predominant in the system (low acoustic Mach limit $M \to 0$);

3. the *isochoric scale*, with the elastic speed u_{el} defined in (II.27) as the characteristic speed. This scale is represented by the elastic parts of the stress tensor σ, which is a function of the gradient of the backward characteristics $[\nabla Y]$. This represents the elastic deformation and is proportional to the shear elastic modulus χ. The gradients of the elastic deformation are divided by M_χ^2 and then they become predominant in the case of small elastic Mach numbers (low elastic Mach limit $M_\chi \to 0$).

II.2.2   Low Mach limits and wave speeds

For gas dynamics problems, the stiffness in the system when the Mach number goes to zero is given by the pressure gradients. These terms are of the order $\mathcal{O}\left(1/M^2\right)$, namely they tend to infinity if $M \to 0$.

In the monolithic Eulerian model, the non-dimensional formulation (II.31) shows that if at least one between M and M_χ tends to zero, the gradients of the Cauchy stress tensor σ introduce stiffness in the system. The gradient of the pressure part of σ is of the order $\mathcal{O}\left(1/M^2\right)$. Thus, its behavior is exactly the same observed for gas dynamics problems. The gradient of the elastic part of σ (the one depending on $\overline{B}$ and $[\nabla_x Y]$) is of the order $\mathcal{O}\left(1/M_\chi^2\right)$. Therefore, when $M \to 0$ is verified, the stiffness is only due to the pressure gradients. Instead, when $M_\chi \simeq M \to 0$, the stiffness is due to both the pressure gradients and the elastic deformation gradients, since it is always verified that $M \le M_\chi$.

The low Mach limit for a solid deformation can be seen as a *slow or small deformation*. In this case, one can approximate the gradient of the deformation as the identity matrix $[\nabla Y] \simeq I$. As described in Sec. I.2.5, the five eigenvalues of the 1D formulation correspond to the following five different waves: two longitudinal waves, which are always the fastest, two shear waves and one material wave.

According to notation (I.40), in the 1D formulation we have $\delta = Y_{,1}^2$. Then, in the case of a small deformation, we can set $\delta \simeq 0$. Moreover, we get $\alpha = \beta = 1$. With this "small deformation approximation", the expressions of the wave speeds simplify and we have that

1. longitudinal waves still consist in both a compression and an elastic contribution, since relation (I.41) becomes

$$\lambda_{1,5} = u_1 \pm \sqrt{c^2 + 2\frac{\chi}{\rho}}; \tag{II.32}$$

2. shear waves reduce to only the isochoric contribution proportional to χ. The compression part in (I.42) cancels out and this expression becomes

$$\lambda_{2,4} = u_1 \pm \sqrt{2\frac{\chi}{\rho}}. \tag{II.33}$$

Therefore, in the small deformation limit, the speeds of transverse waves coincide with the classical theory of linear elasticity.

Two different "low Mach" regimes are then distinguished:

1. *acoustic and shear low Mach regime*: $M \ll 1$ and $M_\chi \ll 1$. In this regime, both the pressure gradients and the elastic deformations through the gradients of $[\nabla_x Y]$ become predominant in the non-dimensional formulation (II.31). The acoustic and the isochoric scales are consistently faster than the advective scale.

   This regime can be observed only in materials that are characterized by $\mathcal{O}\left(p_\infty\right) \simeq \mathcal{O}\left(\chi\right)$. An example of elastic material where this limit can occur is copper, whose parameters are $p_\infty = 3.42 \cdot 10^{10}$ and $\chi = 5 \cdot 10^{10}$. By definition of the sound speed (II.26) and of the elastic speed (II.27), with this configuration we get $c \simeq u_{iso}$ and then $\mathcal{O}\left(M\right) \simeq \mathcal{O}\left(M_\chi\right)$. Thus, comparing the wave speeds (II.32) and (II.33), it is easily observed that $\mathcal{O}\left(\lambda_{1,5}\right) \simeq \mathcal{O}\left(\lambda_{2,4}\right)$. This means that both longitudinal and shear waves are consistently faster than the material wave, as illustrated in Fig. II.1(a);

2. *acoustic only low Mach regime*: $M \ll 1$ and $M \ll M_\chi$. In this regime, the pressure gradient is the only predominant term in the non-dimensional system (II.31), with the
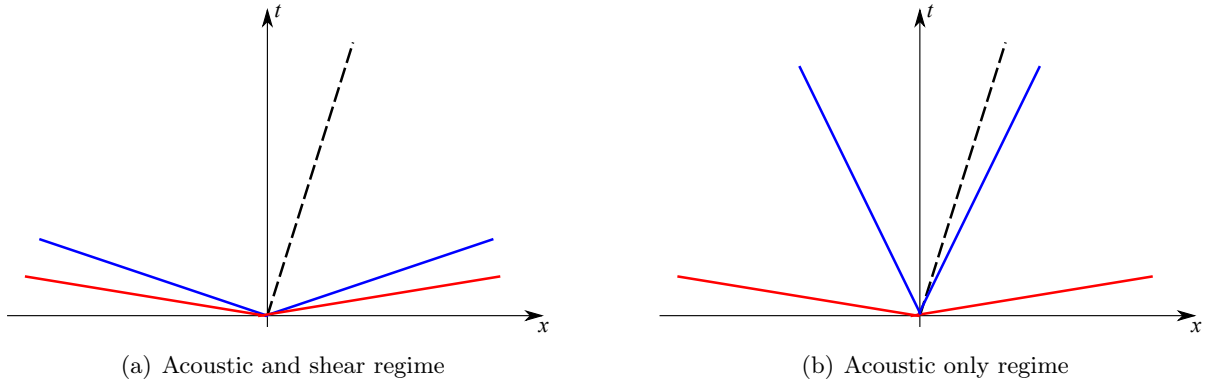
(a) Acoustic and shear regime   (b) Acoustic only regime

Figure II.1: Wave patterns for the two different regimes: acoustic and shear low Mach regime on the left and acoustic only low Mach regime on the right. Longitudinal waves in red, shear waves in blue, material wave in dotted black.

order $\mathcal{O}\left(1/M^2\right)$. The acoustic scale is consistently faster with respect to both the advective and isochoric scales.

This regime can be instead observed only in materials characterized by $p_\infty \gg \chi$, such as rubber. This means that the sound speed is consistently higher than the flow velocity but also than the elastic speed, namely $c \gg |u_1|$ and $c \gg u_{iso}$. Comparing the eigenvalues formulations (II.32) and (II.33), we observe that $\lambda_{1,5} \gg \lambda_{2,4}$, namely longitudinal waves are consistently faster than all the other waves, as illustrated in Fig. II.1(b).

For the considered Eulerian model, the low Mach regime is encoutered when having a low acoustic Mach number, as for the Euler system for perfect gases. In this limit, there are cases when also the isochoric Mach number is low (of the order of the Mach number), thus introducing additional stiffness to the problem. There are also cases when the isochoric Mach number is larger then the acoustic Mach number, thus no further stiffness is added by the elastic part.

II.3   Numerical methods for low Mach flows

In the previous sections, we have shown how compressible flow equations reduce to incompressible equations when the Mach number tends to zero. However, in numerical simulations, it is very difficult to shift from compressible equations to incompressible ones in the regions where the Mach number becomes very small.

Specific numerical problems arise when solving low Mach number flows with standard compressible Godunov-type schemes (for the general Godunov theory see the books of Leveque [80] and Toro [124] and references therein). On one hand, the upwind discretization provides an excessive numerical viscosity on the slow waves when the Mach number becomes small, as detailed in the seminal work of Guillard and Viozat [65, 64] and in the more recent analysis of Dellacherie [46]. In [64], the authors perform an extensive analysis using expansions in terms of the reference Mach number of Riemann problems solved with Godunov-like methods at the cell interfaces. In the case of the Euler equations, an upwind Godunov-like scheme on a Cartesian grid leads to pressure fluctuations of order $\mathcal{O}(M)$, while in the continuous case the pressure fluctuations

are of order $\mathcal{O}\left(M^2\right)$ (see system (II.2)). Therefore, it is clear that incompressible solutions cannot be maintained by Godunov-like methods, since they scale with $\mathcal{O}\left(M^2\right)$ as detailed in Sec. II.1.2.1.

In the works of Dellacherie and collaborators [46, 47], the importance of centering pressure gradients in the limit of small Mach numbers has been addressed. A centered discretization is able to limit the excessive numerical viscosity on any mesh when simulating a low Mach flow with the Euler system. Referring to the monolithic Eulerian model that we want to solve in the present study, the excess of viscosity is observed in the stress tensor fluctuations. These fluctuations describe both the acoustic compression and the elastic deformation.

The second important issue in adopting standard explicit-upwind methods for low Mach flows is due to the enforcement of the CFL stability condition. This condition limits the time step with the space step divided by the fastest wave speed. Thus, the time step of compressible codes becomes extremely small as the incompressible regime gets closer, requiring an increasingly large computational time. Indeed, for the Euler system we have that the fastest speed is given by $\lambda_{max} = u \pm c$, u being the flow velocity and c the sound speed as usual. Therefore, we get the following restriction on the time step:

$$\Delta t \leq \frac{\Delta x}{\lambda_{max}} = \frac{\Delta x}{max|u \pm c|} = M \frac{\Delta x}{max|u\left(M \pm 1\right)|}. \tag{II.34}$$

It is evident that the time step is roughly proportional to the Mach number M and is dramatically reduced when M is small. This is the direct consequence of the instantaneous propagation of the pressure described by equation (II.20), that may require a change from a spatially explicit to a spatially implicit problem.

A variety of different methods have been developed to overcome these problems and to solve flows in the low Mach regime. In most applications, it is desirable to build a scheme that is able to accurately solve different regimes at the same time. Hence, in literature different "all-speed" schemes have been proposed, with the purpose of solving compressible flows by handling both the fully compressible regime with a local Mach number of order one and the incompressible regime. A first category of schemes designed to solve low Mach flows consists in applying preconditioning methodologies to fully implicit time discretizations. A second track consists in splitting fast and slow scales in different ways, sometimes by focusing on the pressure equation, with the idea of adapting classical incompressible schemes to the compressible case. In the next sections both approaches are described.

II.3.1 Preconditioning methods

The preconditioning approach consists in resorting to implicit time discretizations. This way, the acoustic CFL constraint is not necessary for stability reasons and the use of larger time steps is possible. However, a naive implementation of implicit schemes to solve the Euler system may present two different problems. First, usual upwind discretizations such as Godunov-type methods are usually based on exact or approximate Riemann solvers and thus are highly non-linear. The non-linearity of the numerical solver consistently increases the difficulty of implementation of a fully implicit method. The other problem is related to the fact that the implicit version of standard upwind schemes introduces the usual excessive numerical dissipation on the slow waves in low Mach regimes. This results in a poor accuracy of the numerical solutions.

In order to cure the problem of the large numerical viscosity, preconditioning techniques have been designed in literature. The behaviour of different fully implicit schemes with preconditioning techinques are investigated in the work of Viozat [128]. The early "artificial compressibility" technique of Chorin [37] was introduced to solve the incompressible Navier-Stokes equations for steady state solutions. The idea was one of the first preconditioning techniques and it consists in curing the inconsistent scaling behavior of numerical flux functions of Godunov-like schemes: the upwind artificial viscosity terms are modified by multiplication with preconditioning matrices.

Other examples can be found in the works of Turkel [125, 126], where the authors mainly introduce a modification of the absolute value of the Roe matrix with a suitable preconditioner that at low Mach numbers avoids excessive numerical diffusion of the upwind discretization. This is done on the computation of steady state solutions, namely when $\partial_t \psi = 0$, where ψ is the state vector of conservative variables. The time dependence is anyway retained and used to march the system to a steady state in an iterative process. The stiffness of the system at low Mach numbers can thus be reduced by multiplying the time derivative of the state vector with a suitable invertible matrix $\mathbf{P}$ as $\mathbf{P}^{-1}\partial_t \psi$. This modification leaves the steady state solution unchanged since the time derivative vanishes and is only used for the numerical solution process. In one dimension, the following system is numerically solved:

$$\mathbf{P}^{-1}\partial_t \psi + \partial_x \mathbf{F}(\psi) = 0 \quad \Longrightarrow \quad \partial_t \psi + \mathbf{P}\partial_x \mathbf{F}(\psi) = 0.$$

The matrix $\mathbf{P}$ is constructed to reduce the stiffness of the system at low Mach numbers by equalizing the eigenvalues of the modified flux Jacobian $\mathbf{P}\partial_x \mathbf{F}(\psi)$.

This techinque has inspired more recent implicit methods that decrease the numerical diffusion of upwind schemes at low Mach numbers (see for example the works of Li et al. [84], Van Leer et al. [127] and Klingenberg et al. [12]). However, the main problem of this technique is related to the difficulty in handling the non-linearities of classical upwind discretizations (e.g. approximate Riemann solvers) inside the employed fully implicit schemes.

II.3.2   Splitting of scales and pressure equation methods

Other works propose a different approach which is based on the decoupling of fast and slow scales. The main idea consists in adapting classical incompressible schemes to compressible flows, most of the times by focusing on the pressure equations. Starting from the early works of Klainerman and Majda [74, 75], several techniques among these have been explicitly designed to treat *low Mach* number regimes, since they are derived on low Mach number asymptotics. In [76] Klein proposes an operator splitting into a convection system for mass and momentum, which should be solved with an explicit-upwind method. Then, a momentum/energy balance has to be discretized by a semi-implicit scheme in order to account for its mixed hyperbolic/elliptic nature. This way, the leading order contributions of the pressure are solved explicitly and the lower orders implicitly.

However, several physical systems are effected by drastic changes of the sound speed. These large variations may be due to geometrical effects or to the heterogeneity of the media. The relevance for the construction of effective *all Mach* number solvers is then the ability of an accurate simulation of wave propagation in heterogeneous materials without the small time step restriction typical of explicit schemes. With this motivation, several different all-speed schemes

have been derived in literature for gas and fluid dynamics. In this direction, Fedkiw et al. [79] have adopted a pressure stabilization technique that allows to go beyond the classical CFL restriction, by solving an advection-diffusion equation for the pressure.

Similar schemes may be derived following the Asymptotic Preserving (AP) methodology. A scheme for compressible Euler equations is AP if its lower order expansion is a consistent and stable discretization of the incompressible limit. Moreover, its stability condition on Δt has to be independent of the Mach number, with a Courant number only related to the slow characteristic speeds: this is usually possible due to implicit-explicit (IMEX) time integration. If the acoustic waves are integrated implicitly and only the material wave explicitly, then the stability constraint has to be enforced on the material velocity and not on the sound speed. This way, the dependence of Δt on the Mach number shown by relation (II.34) for explicit schemes is avoided.

Examples of AP all-speed schemes based on the solution of an equation for the pressure can be found in the works of Degond et al. [45, 40]. Their main idea consists in introducing pressure gradient-type terms inside the momentum equation, allowing the splitting of the fast and the slow scales. Letting $\Delta t = t_{n+1} - t_n$ be the time stepping in the discretization, the authors propose the following integration in time of the scaled Euler system in [40]:

$$
\begin{cases}
\rho^{n+1} - \rho^n + \Delta t \nabla \cdot (\rho \mathbf{u})^n = 0 \\
(\rho \mathbf{u})^{n+1} - (\rho \mathbf{u})^n + \Delta t \nabla \cdot (\rho^n \mathbf{u}^n \otimes \mathbf{u}^n + \alpha p^n) + \frac{1 - \alpha M^2}{M^2} \nabla p^{n+1} = 0 \\
W^{n+1} - W^n + \Delta t \nabla \cdot \left(\left(e^n + \frac{p^n}{\rho^n} (\rho \mathbf{u})^{n+1} \right) \right) = 0
\end{cases}
\tag{II.35}
$$

Here the auxiliary variable $W = \rho e$ is split as follows: $W^{n+1} = \rho^{n+1} \epsilon^{n+1} + 1/2 M^2 \rho^n |\mathbf{u}^n|^2$: this means that the time discretization of the total energy W splits into an implicit evaluation of the internal energy ϵ, and in an explicit evaluation of the kinetic energy. The parameter α is a tuning parameter which satisfies $\alpha \in [0; 1/M^2]$. The spatial discretization consists in an upwind scheme on unstructured grids of all the spatial derivatives except for the term $(1 - \alpha M^2) / M^2 \nabla p^{n+1}$. This term is centered without affecting the stability of the full scheme, since the gradient is taken in implicit. It can be noticed that taking $\alpha = 0$ corresponds to full pressure upwinding in the proposed spatial discretization. In practice, the solution of the system consists in recovering the density ρ^{n+1} by solving the conservation of mass in (II.35). Then, an elliptic equation for the pressure is solved. This elliptic equation is built by re-writing the momentum equation and plugging it inside the energy equation. This way one gets

$$
W^{n+1} - \Delta t^2 \frac{1 - \alpha M^2}{M^2} \nabla \cdot \left(\left(e^n + \frac{p^n}{\rho^n} \right) \nabla p^{n+1} \right) = \Phi \left(\rho^n, (\rho \mathbf{u})^n, W^n \right),
\tag{II.36}
$$

where the right hand side is an explicit function of the density, the momentum and the total energy. It is evident that equation (II.36) is non linear and that its solution depends on the chosen state law. The solution is obtained with a Newton iteration.

Another strtegy is proposed by Chalons et al. in [32, 31], where an all-speed scheme based on the decoupling between acoustic and transport phenomena is proposed. The authors introduce a two step algorithm with an implicit update for the acoustic step and an explicit march in time for the transport step. This splitting is equivalent to a Lagrange-projection method. Moreover,

for the acoustic system a Suliciu relaxation is performed by introducing a surrogate pressure. In the relaxed system the characteristic fields are linearly degenerate, which allows to solve analytically the Riemann problem. This scheme has been recently extended to solve two-phase flows in [33].

Another all-speed scheme has been recently proposed by Russo et al. in [22], where also a proof of the AP property is detailed. This scheme is once again based on an IMEX time integration that treats acoustic waves implicitly and material waves explicitly. However, the space discretization is performed on a Nessyahu-Tadmor staggered grid, that guarantees a central discretization and a second order reconstruction. This avoids the need for Riemann solvers and reduces the excess of numerical diffusion at low Mach numbers.

Other AP schemes based on similar pressure-splitting approaches can be found in the works of Noelle et al. [96], of Dimarco et al. [48] and of Jin et al. [66].

II.3.3   Relaxation all-speed scheme

In this thesis, we are interested in the numerical simulation of compressible and low Mach flows not only in fluid dynamics but also in elastic solids. Thus, our aim is the construction of an all-speed scheme, which is able to accurately approximate waves propagating inside heterogeneous compressible materials.

The monolithic Eulerian model introduced in Chapter I is a system of conservation laws which is the same for all considered compressible materials. The EOS includes all the different behaviors that need to be considered. Thus, the goal is to derive a scheme that works in the same manner for gases, liquids and solids, namely that does not strictly depend on the specific state law. A pressure-splitting approach as the ones described in Section II.3.2 would directly involve the equation of state, in order to analyze and separate the scales. The presence of the stress tensor σ consistently increases the difficulty of a "stress-splitting", since σ is composed by acoustic and elastic parts. Moreover, we have shown in Section II.2.1 that three different scales are present and that two different limits may occur. This further complicates the splitting, which should take into account the two possible limits in building the time integration.

To overcome all the difficulties discussed above, we propose a scheme that is based on the relaxation technique that was firstly introduced by Jin and Xin in [71]. With this method, the fluxes are relaxed at the continuous level and a linear transport operator is obtained. This avoids a direct dependence of the spatial derivatives on the specific EOS. Moreover, thanks to this, the use of Riemann solvers is not necessary and fully implicit time integrators can be easily implemented. The fully implicit time discretization allows to get rid of demanding acoustic CFL constraints when the low Mach limit is reached.

The spatial discretization of the proposed scheme is obtained by a combination of upwind and centered schemes, in order to recover the correct numerical viscosity at low Mach number but also to avoid spurious oscillations in the fully compressible regime. The detailed derivation and the study of the numerical properties of this scheme are the object of Chapter III and of the two papers [1, 2] in one dimension. The two dimensional extension and a proof of the asymptotic preserving property are then presented in Chapter IV.

II.4   Preliminary conclusions

In this chapter, the low Mach limits that can occur in elastic solids have been characterized, after the standard analysis for the Euler equations for gas-dynamics. Two different behaviors have been identified, namely an acoustic and an acoustic-elastic low Mach limit.

The numerical difficulties that are faced when using standard compressible codes to solve the low Mach regime have been analyzed. Then, we have briefly described some techniques proposed in literature to cure these problems. These schemes have been specifically derived for the solution of fluid-dynamics problems and their extension to the elastic case is not straightforward.

Since the aim of the present work is the solution of the low Mach regime in different compressible materials (gases, liquids and elastic solids), a general scheme which is independent of the state law is needed. In this sense, an all-speed scheme based on the relaxation technique is proposed. This scheme possesses the correct numerical viscosity at different speeds and its detailed derivation and validation will be the object of Chapters III and IV.

Chapter III

An all-speed relaxation scheme

This chapter is devoted to the derivation and validation of a novel implicit relaxation scheme that is able to solve the Eulerian model of Chapter I at all speeds. The scheme has the same formulation for all materials and it accurately approximates flows in the fully compressible regime and also in the low Mach limits presented in Chapter II.

We adopt the relaxation method intoduced by Jin and Xin in [71] due to its simplicity and generality. With this approach, the resulting relaxation system is linear except for a lower order source. The linearity of the advective operator is fundamental to easily implement a fully implicit scheme. In this framework, demanding acoustic constraints on the time step can be avoided. For the spatial discretization, both centered and upwind schemes are introduced. The centered discretization is needed to recover the correct limit on the stress tensor gradients when the Mach number tends to zero. The upwind discretization, on the other hand, introduces enough numerical viscosity when solving regimes with Mach number of order one. Hence, a convex combination of the two methods is adopted, based on the local Mach number of the flow.

In the present chapter, we focus on one dimensional problems. The scheme is validated on the nozzle problem and on material waves propagating inside different materials. A comparison with the results obtained with a standard explicit-upwind relaxation scheme is performed, with the aim of showing that the proposed scheme accuracy is superior in the low Mach regime.

III.1   The relaxation method

The resolution of the low Mach regime is difficult due to the stiffness of the Cauchy stress tensor gradients (see Chapter II) and due to the high velocities of acoustic and shear waves. The general state law is highly non-linear and our goal is to build a scheme which has the same formulation for all the considered compressible materials, without a direct dependence on the state law. To allow for an efficient and robust numerical procedure, we adopt a relaxation approach.

The study of the hyperbolic systems with stiff relaxation terms goes back to the seminal works by Liu [86] and by Levermore et al. [35] and the introduction of relaxation approximations for hyperbolic systems of conservation law was firstly apporached in the work of Jin and Xin [71]. With this relaxation procedure, the entire original system is modified and approximated by a larger linear system with a stiff source. The special structure of the new system enables the use of underresolved stable discretizations, avoiding complex solvers. This procedure has triggered

the development of a variety of relaxation schemes, for example the ones proposed in the works of Russo et al. [26, 20, 19], of Naldi and Pareschi [95] and of Leveque et al. [81].

A different relaxation approximation has been proposed in the work of Suliciu [118], where the idea is to modify only the pressure law in the original compressible Euler equations, since it contains all the genuine nonlinearities. This amounts to enlarging the original system of only one equation. This work has inspired the derivation of relaxation schemes in the works of Chalons, Coquel et al. [39, 29, 30, 9] and of Bouchut et al. [24, 25]. In this framework, nonlinear terms are still present in the transport operator (e. g. in the momentum equation spatial derivatives). Thus, the discretization process introduces nonlinearities outside of the diagonals.

In the present work, we adopt the Jin-Xin approach [71, 28], where the whole fluxes are approximated by relaxation variables. A linear hyperbolic relaxation system is build, which approximates the original system (I.44) with a small dissipative correction. Thanks to the linearity of the advection terms, the spatial derivatives do not depend anymore on the state law. Numerical schemes can then be derived without a direct dependence on the EOS of each considered material. Moreover, the numerical solution does not require the introduction of sophisticated solvers, allowing for a simpler implementation of fully implicit time discretizations. The only nonlinear terms appear in the right hand side of the relaxation system. This implies that in the discretization process only diagonal terms are interested by the need of a linearization.

III.1.1 The Jin-Xin relaxation

Here we describe the Jin-Xin relaxation method for 1D problems, since in the present chapter we derive a numerical scheme for the solution of the one dimensional model (I.44). A relaxation variables vector with the same dimensions of the conservative variables vector has to be introduced. Thus, in the case of system (I.44), we introduce $\mathbf{v} \in \mathbb{R}^5$, since we have $\boldsymbol{\psi} \in \mathbb{R}^5$. The relaxation system takes the following formulation:

$$\begin{cases} \partial_t \boldsymbol{\psi} + \partial_x \mathbf{v} = 0 \\ \partial_t \mathbf{v} + \mathbf{A} \partial_x \boldsymbol{\psi} = \dfrac{1}{\eta} \left(\mathbf{F}(\boldsymbol{\psi}) - \mathbf{v} \right), \quad \eta > 0, \end{cases} \tag{III.1}$$

where $\mathbf{A} = diag\{a_i\}$, $i = 1, .., 5$ is a positive diagonal matrix.

We apply the so-called Chapman-Enskog expansion of the variables for small η [34]:

$$\begin{cases} \boldsymbol{\psi} = \boldsymbol{\psi}_0 + \eta \boldsymbol{\psi}_1 + \eta^2 \boldsymbol{\psi}_2 + ... \\ \mathbf{v} = \mathbf{v}_0 + \eta \mathbf{v}_1 + \eta^2 \mathbf{v}_2 + ... \end{cases}$$

in order to asses the behavior of system (III.1) at different orders. At leading order (small relaxation limit), the original system is recovered, with the relaxation variables equal to the fluxes:

$$\begin{cases} \mathbf{v} = \mathbf{F}(\boldsymbol{\psi}) \\ \partial_t \boldsymbol{\psi} + \partial_x \mathbf{F}(\boldsymbol{\psi}) = 0. \end{cases} \tag{III.2}$$

Thus, in a first order approximation, $\mathbf{v} = \mathbf{F}(\boldsymbol{\psi}) + \eta \mathbf{v}_1$. The state satisfying (III.2) is called local equilibrium. Using this in the second equation of the relaxation system and developing, we get

the following expression for the first order:

$$\mathbf{v} = \mathbf{F}(\boldsymbol{\psi}) - \eta\partial_t\mathbf{F}(\boldsymbol{\psi}) - \eta\mathbf{A}\partial_x\boldsymbol{\psi}$$
$$= \mathbf{F}(\boldsymbol{\psi}) - \eta\left(-\mathbf{F}'(\boldsymbol{\psi})\partial_x\mathbf{F}(\boldsymbol{\psi}) + \mathbf{A}\partial_x\boldsymbol{\psi}\right)$$
$$= \mathbf{F}(\boldsymbol{\psi}) - \eta\left(\mathbf{A}\partial_x\boldsymbol{\psi} - \mathbf{F}'(\boldsymbol{\psi})^2\partial_x\boldsymbol{\psi}\right)$$
$$= \mathbf{F}(\boldsymbol{\psi}) - \eta\left(\mathbf{A} - \mathbf{F}'(\boldsymbol{\psi})^2\right)\partial_x\boldsymbol{\psi} = \mathbf{v}_0 + \eta\mathbf{v}_1,$$

where $\mathbf{F}'(\boldsymbol{\psi})$ is the Jacobian matrix of the flux function. The first order approximation we get is the following:

$$\begin{cases} \mathbf{v} = \eta\left(\mathbf{A} - \mathbf{F}'(\boldsymbol{\psi})^2\right)\partial_x\boldsymbol{\psi} \\ \partial_t\boldsymbol{\psi} + \partial_x\mathbf{F}(\boldsymbol{\psi}) = \eta\partial_x\left(\left(\mathbf{A} - \mathbf{F}'(\boldsymbol{\psi})^2\right)\partial_x\boldsymbol{\psi}\right), \end{cases} \tag{III.3}$$

where $\mathbf{F}'(\boldsymbol{\psi})$ is the Jacobian matrix of the flux function. In order to ensure the dissipative nature of system (III.3), it is necessary to respect the Liu *subcharacteristic condition* [86, 129]

$$\mathbf{A} - \mathbf{F}'(\boldsymbol{\psi})^2 \geq 0 \quad \forall\boldsymbol{\psi} \tag{III.4}$$

when building the relaxation system. For $\boldsymbol{\psi}$ varying in a bounded domain, this condition is satisfied by choosing $\mathbf{A} = diag\{a_i\}$, $i = 1,..,5$ sufficiently large. The construction of the relaxation matrix $\mathbf{A}$ is detailed in Sec. III.1.1.1.

Initial and boundary conditions have to be imposed in a way that initial and boundary layers are not introduced [71]. Thus, these conditions need to be consistent with the equilibrium state (III.2). Letting $\partial\Omega$ be the boundary of a domain Ω, if $\boldsymbol{\psi}|_{\partial\Omega}$ is given, then $\mathbf{v}|_{\partial\Omega} = \mathbf{F}(\boldsymbol{\psi}|_{\partial\Omega})$ is set. Similarly for homogeneous Neumann boundary conditions $\partial_n\boldsymbol{\psi}|_{\partial\Omega} = 0$, we have the same condition for relaxation variables

$$\partial_n\mathbf{v} = \mathbf{F}'(\boldsymbol{\psi})\partial_n\boldsymbol{\psi} = 0 \text{ on } \partial\Omega. \tag{III.5}$$

Different kinds of boundary conditions can be imposed in a similar manner.

The relaxation approach can be extended to multi-dimensional problems, as described in [71]. The method consists in a "dimension-by-dimension" relaxation of the fluxes, which allows to reduce the problem complexity. The two dimensional version of relaxation schemes will be the object of Chapter IV.

III.1.1.1 The relaxation matrix

The relaxation matrix $\mathbf{A}$ is diagonal and it is built by imposing the subcharacteristic condition (III.4). The wave speeds of the relaxation system are the following

$$\mu_j = \pm\sqrt{a_i}, \;\; i = 1,..5, \;\; j = 1,..10. \tag{III.6}$$

Condition (III.4) states that the eigenvalues λ_i of the original system need to lie between the eigenvalues μ_j of the relaxation system.On the other hand, the CFL constraint has to be enforced on the speeds (III.6) of the relaxation system. Therefore, the smallest $\mathbf{A}$ satisfying (III.4) is needed.

In the present work, we avoid the easy choice $\mathbf{A} = a\mathbf{I}$, a being a constant, in order to have distinct eigenvalues (III.6). This means reproducing all the wave speeds of the original system. In particular, we construct $\mathbf{A}$ by a-priori estimating the wave speeds λ_i of each specific problem. Then, we take the maximum over the domain for every speed: $\mathbf{A} \simeq \mathbf{\Lambda}_{max}^2$, where $\mathbf{\Lambda}_{max} = diag\{max_x \lambda_i\}$. The jacobian of the flux can be diagonalized as $\mathbf{F}'(\boldsymbol{\psi})^2 = \mathbf{R}\mathbf{\Lambda}^2\mathbf{R}^{-1}$, where $\mathbf{R}$ is the matrix of the right eigenvectors and $\mathbf{\Lambda} = diag\{\lambda_i\}$. This way, the first order correction derived in Eq. (III.3) becomes

$$\partial_t \boldsymbol{\psi} + \partial_x \mathbf{F}(\boldsymbol{\psi}) \simeq \eta \left(\mathbf{\Lambda}_{max}^2 - \mathbf{R}\mathbf{\Lambda}^2\mathbf{R}^{-1}\right) \partial_{xx}\boldsymbol{\psi}.$$

The matrix $\mathbf{\Lambda}_{max}^2 - \mathbf{R}\mathbf{\Lambda}^2\mathbf{R}^{-1}$ is positive definite, thus the subcharacteristic condition is respected. Moreover, we can control and limit the diffusion of the relaxation by approximating all the original waves.

The a-priori estimation of the eigenvalues can be easily performed, since the sound speed and the elastic coefficients of the most common materials are well-known. The explicit formula for the eigenvalues is given in Section I.2.5.

III.2 Numerical schemes

System (III.1) is discretized with finite volumes on a Cartesian mesh. For one dimensional problems, let $\Delta x = x_{i+1/2} - x_{i-1/2}$ be the grid spacing and $\Delta t = t_{n+1} - t_n$ the time stepping. $\mathbf{w}_i^n$ denotes the approximate cell average of a quantity $\mathbf{w}$ in the cell $\left[x_{i-1/2}, x_{i+1/2}\right]$ at time t_n and $\mathbf{w}_{i+1/2}^n$ denotes the approximate point value of $\mathbf{w}$ in $x = x_{i+1/2}$ and at $t = t_n$.

For the discussion of the numerical schemes it is convenient to treat the spatial discretization and the time discretization separately, as in the method of lines. With this approach, we briefly revisit the standard explicit relaxation scheme of [71]. Then, we present our novel implicit relaxation scheme, designed with the aim of solving problems with Mach numbers ranging from very small to order of unity. We point out that in deriving the numerical scheme only the acoustic Mach number M is used, because it is always lower than M_χ.

III.2.1 Standard explicit relaxation scheme

Jin and Xin propose a scheme where the space derivatives are explicit and only the stiff source relaxation term is implicit [71]. This discretization falls in the IMEX schemes class, which are specifically designed for problems where a stiff part is present and are widely used for relaxation systems (see, for example, the seminal work of Pareschi and Russo [98], the works of Russo and Boscarino [20, 21], the work of Cavalli et al. [27] and references therein).

At first order, the relaxation system is discretized in time as follows:

$$\begin{cases} \dfrac{\boldsymbol{\psi}^{n+1} - \boldsymbol{\psi}^n}{\Delta t} + \partial_x \mathbf{v}^n = 0 \\ \dfrac{\mathbf{v}^{n+1} - \mathbf{v}^n}{\Delta t} + \mathbf{A}\partial_x \boldsymbol{\psi}^n = \dfrac{1}{\eta}\left(\mathbf{F}\left(\boldsymbol{\psi}^{n+1}\right) - \mathbf{v}^{n+1}\right). \end{cases} \qquad \text{(III.7)}$$

The solution can be approached in a sequential manner: the unknowns $\boldsymbol{\psi}^{n+1}$ are calculated by solving the first equation and then are put inside the stiff source term to compute $\mathbf{v}^{n+1}$.

This means that at every time step the relaxation variables $\mathbf{v}^{n+1}$ are projected on the fluxes $\mathbf{F}\left(\boldsymbol{\psi}^{n+1}\right)$. At second order, we adopt the IMEX scheme proposed in [98] (Butcher tableau of Table III.1).

(a) Explicit				(b) Implicit		
0	0			γ	0	
1	0			$1 - 2\gamma$	γ	
1/2	1/2			1/2	1/2	

Table III.1: Butcher tableau of the IMEX scheme proposed in [98], $\gamma = 1 - 1/\sqrt{2}$.

III.2.1.1   Upwind spatial discretization

In general, the spatial discretization for system (III.1) reads

$$
\begin{cases}
\partial_t \boldsymbol{\psi}_i + \dfrac{\mathbf{v}_{i+1/2} - \mathbf{v}_{i-1/2}}{\Delta x} = 0 \\
\partial_t \mathbf{v}_i + \mathbf{A}\dfrac{\boldsymbol{\psi}_{i+1/2} - \boldsymbol{\psi}_{i-1/2}}{\Delta x} = \dfrac{1}{\eta}\left(\mathbf{F}\left(\boldsymbol{\psi}_i\right) - \mathbf{v}_i\right).
\end{cases}
\tag{III.8}
$$

For sufficiently accurate space discretizations, this approximation has an accuracy of $\mathcal{O}\left(\Delta x^2\right)$, because the flux is averaged in the following way:

$$
\mathbf{F}\left(\boldsymbol{\psi}_i\right) = \mathbf{F}\left(\frac{1}{\Delta x}\int_{x_{i-1/2}}^{x_{i+1/2}} \boldsymbol{\psi}\,dx\right) = \frac{1}{\Delta x}\int_{x_{i-1/2}}^{x_{i+1/2}} \mathbf{F}\left(\boldsymbol{\psi}\right)dx + \mathcal{O}\left(\Delta x^2\right) = \mathbf{F}_i + \mathcal{O}\left(\Delta x^2\right).
$$

The variables at the interfaces $x_{i+1/2}$ inside (III.8) have to be computed with an "ad hoc" stable scheme. For an explicit time stepping, a possible choice leading to a stable scheme is the upwind discretization.

We build the upwind scheme as in [71]. System (III.1) has two characteristic variables $\mathbf{v} \pm \mathbf{A}^{1/2}\boldsymbol{\psi}$, travelling at the frozen speeds $\pm\mathbf{A}^{1/2}$. The upwind spatial approximation is applied to the linear system on the two characteristic variables, obtaining the interface values as follows:

$$
\begin{cases}
\boldsymbol{\psi}_{i+1/2} = \frac{1}{2}\left(\boldsymbol{\psi}_{i+1} + \boldsymbol{\psi}_i\right) - \frac{1}{2}\mathbf{A}^{-1/2}\left(\mathbf{v}_{i+1} - \mathbf{v}_i\right) \\
\mathbf{v}_{i+1/2} = \frac{1}{2}\left(\mathbf{v}_{i+1} + \mathbf{v}_i\right) - \frac{1}{2}\mathbf{A}^{1/2}\left(\boldsymbol{\psi}_{i+1} - \boldsymbol{\psi}_i\right).
\end{cases}
\tag{III.9}
$$

Plugging this into discretization (III.8) gives the first order upwind approximation:

$$
\begin{cases}
\dfrac{\mathbf{v}_{i+1/2} - \mathbf{v}_{i-1/2}}{\Delta x} = \dfrac{1}{2\Delta x}\left(\mathbf{v}_{i+1} - \mathbf{v}_{i-1}\right) - \dfrac{\mathbf{A}^{1/2}}{2\Delta x}\left(\boldsymbol{\psi}_{i+1} - 2\boldsymbol{\psi}_i + \boldsymbol{\psi}_{i-1}\right) \\
\dfrac{\boldsymbol{\psi}_{i+1/2} - \boldsymbol{\psi}_{i-1/2}}{\Delta x} = \dfrac{1}{2\Delta x}\left(\boldsymbol{\psi}_{i+1} - \boldsymbol{\psi}_{i-1}\right) - \dfrac{\mathbf{A}^{-1/2}}{2\Delta x}\left(\mathbf{v}_{i+1} - 2\mathbf{v}_i + \mathbf{v}_{i-1}\right).
\end{cases}
\tag{III.10}
$$

For a second order approximation, a Van Leer MUSCL (Monotonic Upstream-Centered Scheme for Conservation Laws) scheme is employed.

The presented upwind discretization is classically used in explicit relaxation schemes. The explicit-upwind relaxation scheme is stable provided that the stability CFL condition on the fastest wave (acoustic CFL) is verified [71].

III.2.2   Implicit relaxation scheme

We propose a fully implicit relaxation scheme, with the goal of getting rid of acoustic CFL constraints. The linearity of the spatial derivatives in the relaxation system allows for a straightforward use of implicit time discretizations.

The implicit time discretization at first order is a simple backward Euler scheme and reads:

$$\begin{cases} \dfrac{\boldsymbol{\psi}^{n+1} - \boldsymbol{\psi}^n}{\Delta t} + \partial_x \mathbf{v}^{n+1} = 0 \\ \dfrac{\mathbf{v}^{n+1} - \mathbf{v}^n}{\Delta t} + \mathbf{A}\partial_x \boldsymbol{\psi}^{n+1} = \dfrac{1}{\eta}\left(\mathbf{F}\left(\boldsymbol{\psi}^{n+1}\right) - \mathbf{v}^{n+1} \right). \end{cases} \tag{III.11}$$

For a second order implicit approximation, a BDF (Backward Differentiation Formula) of second order is adopted.

The treatment of the non-linear fluxes $\mathbf{F}(\boldsymbol{\psi})$ is dealt with applying one iteration of the Newton's method, namely the fluxes are approximated with a Taylor expansion in the following way:

$$\mathbf{F}\left(\boldsymbol{\psi}^{n+1}\right) = \mathbf{F}\left(\boldsymbol{\psi}^{n}\right) + \mathbf{F}'\left(\boldsymbol{\psi}^{n}\right)\left(\boldsymbol{\psi}^{n+1} - \boldsymbol{\psi}^{n}\right). \tag{III.12}$$

$\mathbf{F}'\left(\boldsymbol{\psi}^{n}\right)$ is the Jacobian of the flux and can be computed analytically. For system (I.44) it reads

$$\mathbf{F}'\left(\psi\right) = \begin{bmatrix} 0 & 1 & 0 & 0 & 0 \\ -u_1^2 - \sigma_{,\psi_1}^{11} & 2u_1 - \sigma_{,\psi_2}^{11} & -\sigma_{,\psi_3}^{11} & -\sigma_{,\psi_4}^{11} & -\sigma_{,\psi_5}^{11} \\ -u_1 u_2 & u_2 & u_1 & 2\chi & 0 \\ \dfrac{u_1 Y_{,1}^2 + u_2}{\rho} & \dfrac{Y_{,1}^2}{\rho} & \dfrac{1}{\rho} & u_1 & 0 \\ \dfrac{-Eu_1 + \sigma^{11}u_1}{\rho} - u_1\sigma_{,\psi_1}^{11} + \dfrac{\sigma^{21}u_2}{\rho} & \dfrac{E - \sigma^{11}}{\rho} - u_1\sigma_{,\psi_2}^{11} & -u_1\sigma_{,\psi_3}^{11} - \dfrac{\sigma^{21}}{\rho} & -\sigma_{,\psi_4}^{11}u_1 + 2\chi u_2 & u_1\left(1 - \sigma_{,\psi_5}^{11}\right) \end{bmatrix}, \tag{III.13}$$

where $\sigma_{,\psi_i}^{jk}$ stands for the derivative of the ^{jk}, $j,k = 1,2$ component of the tensor σ with respect to the conservative variable ψ_i, $i = 1,..5$. In deriving (III.13), we have used the fact that $\sigma_{,\psi_1}^{21} = \sigma_{,\psi_2}^{21} = \sigma_{,\psi_3}^{21} = \sigma_{,\psi_5}^{21} = 0$ and $\sigma_{,\psi_4}^{21} = -2\chi$. The derivatives of σ^{11} have the following expressions:

$$\sigma_{,\psi_1}^{11} = -\left(\gamma - 1\right)\left(\frac{1}{2}\left(u_1^2 + u_2^2\right) - \frac{2\chi\rho}{\rho_0^2} + \frac{2\chi}{\rho_0} \right) - \frac{2\chi\rho}{\rho_0^2},$$

$$\sigma_{,\psi_2}^{11} = \left(\gamma - 1\right)u_1, \qquad\qquad \sigma_{,\psi_3}^{11} = \left(\gamma - 1\right)u_2,$$

$$\sigma_{,\psi_4}^{11} = \left(\gamma - 1\right)2\chi Y_{,1}^2 - 2\chi Y_{,1}^2, \qquad \sigma_{,\psi_5}^{11} = -\left(\gamma - 1\right).$$

III.2.2.1   Centered spatial discretization

As described in Section II.3, it has been proved that upwind spatial discretizations present an excessive numerical viscosity when approximating low Mach phenomena [65, 46]. In the case of the Euler equations, these discretizations lead to pressure fluctuations of order $\mathcal{O}\left(M\right)$, while in the continuous case the pressure fluctuations are of order $\mathcal{O}\left(M^2\right)$ (see system (II.31)). Instead, centered spatial discretizations of the pressure gradient in the Euler equations avoid the excess of viscosity on any mesh when dealing with low Mach regimes [46, 47]. In the adopted Eulerian model, this corresponds to centering the stiff parts of σ in the non-dimensional system (II.31).

A centered discretization of the spatial derivatives can be employed without stability problems in the implicit scheme just introduced. The interface values inside (III.8) are computed as follows:

$$\begin{cases} \boldsymbol{\psi}_{i+1/2} = \frac{1}{2}\left(\boldsymbol{\psi}_{i+1} + \boldsymbol{\psi}_i\right) \\ \mathbf{v}_{i+1/2} = \frac{1}{2}\left(\mathbf{v}_{i+1} + \mathbf{v}_i\right). \end{cases} \tag{III.14}$$

Then, the centered implicit scheme reads

$$\begin{cases} \dfrac{\boldsymbol{\psi}_i^{n+1} - \boldsymbol{\psi}_i^n}{\Delta t} + \dfrac{\mathbf{v}_{i+1}^{n+1} - \mathbf{v}_{i-1}^{n+1}}{2\Delta x} = 0 \\ \dfrac{\mathbf{v}_i^{n+1} - \mathbf{v}_i^n}{\Delta t} + \mathbf{A}\dfrac{\boldsymbol{\psi}_{i+1}^{n+1} - \boldsymbol{\psi}_{i-1}^{n+1}}{2\Delta x} = \dfrac{1}{\eta}\left(\mathbf{F}\left(\boldsymbol{\psi}_i^{n+1}\right) - \mathbf{v}_i^{n+1}\right). \end{cases} \tag{III.15}$$

This scheme possesses the following zero relaxation limit $\eta \to 0^+$:

$$\frac{\boldsymbol{\psi}_i^{n+1} - \boldsymbol{\psi}_i^n}{\Delta t} + \frac{\mathbf{F}\left(\boldsymbol{\psi}_{i+1}^{n+1}\right) - \mathbf{F}\left(\boldsymbol{\psi}_{i-1}^{n+1}\right)}{2\Delta x} = 0, \tag{III.16}$$

which is a consistent and unconditionally stable discretization of system (I.44). Unconditional stability is easily proven for linear advection with the Von Neumann stability analysis [67]. Therefore, scheme (III.15) is unconditionally stable, namely a stability condition on the time step is not required. Moreover, by centering the whole fluxes, also the gradient of σ is centered. Hence, the accuracy in space of scheme (III.16) does not depend on the Mach number.

III.2.2.2 All-speed spatial discretization

The centered approximation (III.15) accurately solves low Mach flows, because the correct Mach number order on the stress tensor gradients is respected by the scheme. Nevertheless, we aim at deriving an all-speed scheme. When solving problems at high velocities (Mach number of order one or more), the centered discretization does not provide enough numerical viscosity, thus spurious numerical oscillations can arise. In this spirit, an all-speed spatial discretization is introduced, through a convex combination of the upwind and centered schemes described in Secs. III.2.1.1-III.2.2.1. The combination is based on the local Mach number of the specific flow.

Let h be a generic variable. For the sake of simplicity, we introduce the notation $\mathbf{D}\left(\partial_x h\right) \simeq \partial_x h$, $\mathbf{D}\left(\partial_x h\right)$ being the numerical discretization of the spatial derivative of h. The main idea of the scheme consists in defining the hybrid all-speed discretization $\mathbf{D}\left(\partial_x h\right)_{hyb}$ as follows:

$$\mathbf{D}\left(\partial_x h\right)_{hyb} = f\left(M_{loc}\right)\mathbf{D}\left(\partial_x h\right)_{upw} + \left(1 - f\left(M_{loc}\right)\right)\mathbf{D}\left(\partial_x h\right)_{cent}, \tag{III.17}$$

where $\mathbf{D}\left(\partial_x h\right)_{upw}$ is the upwind spatial discretization (III.10) and $\mathbf{D}\left(\partial_x h\right)_{cent}$ is the centered one. M_{loc} is the local Mach number, which can be computed on the numerical solution at the previous time step. The function $f\left(M_{loc}\right)$ has to meet the criterion $0 \leq f\left(M_{loc}\right) \leq 1$. Two different f are adopted:

- minimum function: $f\left(M_{loc}\right) = \min\{1, M_{loc}\}$

- arcotangent function: $f\left(M_{loc}\right) = \dfrac{\arctan\left(M_{loc}\right)}{\pi/2}$.

The two choices for f have proved to be equivalent in the numerical results.

The hybrid all-speed spatial discretization reads:

$$\begin{cases} \mathbf{D}\left(\partial_x \mathbf{v}\right)_{hyb} = \dfrac{1}{2\Delta x}\left(\mathbf{v}_{i+1} - \mathbf{v}_{i-1}\right) - \dfrac{f\left(M_{loc}\right)}{2\Delta x}\mathbf{A}^{1/2}\left(\boldsymbol{\psi}_{i+1} - 2\boldsymbol{\psi}_i + \boldsymbol{\psi}_{i-1}\right) \\ \mathbf{D}\left(\partial_x \boldsymbol{\psi}\right)_{hyb} = \dfrac{1}{2\Delta x}\left(\boldsymbol{\psi}_{i+1} - \boldsymbol{\psi}_{i-1}\right) - \dfrac{f\left(M_{loc}\right)}{2\Delta x}\mathbf{A}^{-1/2}\left(\mathbf{v}_{i+1} - 2\mathbf{v}_i + \mathbf{v}_{i-1}\right). \end{cases} \tag{III.18}$$

We underline the fact that combination (III.17) essentially produces a centered finite difference scheme. An upwind numerical viscosity is introduced inside the scheme when the Mach number is not close to zero. This is shown by analyzing relation (III.18). The centered scheme is second order accurate, therefore for low Mach flows the convex combination keeps the same accuracy. In the case of smooth solutions, the slopes can be calculated without the introduction of non-linear limiters. In presence of discontinuities, the non-linear slope limiters could be computed with a predictor-corrector approach.

The relaxation all-speed scheme is thus derived. The all-speed spatial discretization (III.18) is adopted with the implicit time discretization (III.11), having:

$$\begin{cases} \dfrac{\boldsymbol{\psi}^{n+1} - \boldsymbol{\psi}^n}{\Delta t} + \dfrac{1}{2\Delta x}\left(\mathbf{v}_{i+1}^{n+1} - \mathbf{v}_{i-1}^{n+1}\right) - \dfrac{f\left(M_{loc}\right)\mathbf{A}^{1/2}}{2\Delta x}\left(\boldsymbol{\psi}_{i+1}^{n+1} - 2\boldsymbol{\psi}_i^{n+1} + \boldsymbol{\psi}_{i-1}^{n+1}\right) = 0 \\ \dfrac{\mathbf{v}^{n+1} - \mathbf{v}^n}{\Delta t} + \dfrac{\mathbf{A}}{2\Delta x}\left(\boldsymbol{\psi}_{i+1}^{n+1} - \boldsymbol{\psi}_{i-1}^{n+1}\right) - \dfrac{f\left(M_{loc}\right)\mathbf{A}^{1/2}}{2\Delta x}\left(\mathbf{v}_{i+1}^{n+1} - 2\mathbf{v}_i^{n+1} + \mathbf{v}_{i-1}^{n+1}\right) = \\ \qquad\qquad\qquad\qquad\qquad\qquad\qquad\qquad \dfrac{1}{\eta}\left(\mathbf{F}\left(\boldsymbol{\psi}^{n+1}\right) - \mathbf{v}^{n+1}\right). \end{cases} \tag{III.19}$$

This scheme will be referred to as "all-speed implicit relaxation scheme" in what follows.

III.2.2.3 Linear system structure

Linearization (III.12) introduces a coupling among all the equations. Thus, the following linear system has to be solved:

$$\begin{cases} \mathbf{M}\boldsymbol{\Psi}^{n+1} + \mathbf{N}\mathbf{V}^{n+1} = \mathbf{r} \\ \mathbf{P}\boldsymbol{\Psi}^{n+1} + \mathbf{Q}\mathbf{V}^{n+1} = \mathbf{s}, \end{cases} \tag{III.20}$$

where $\boldsymbol{\Psi}^{n+1}$ and $\mathbf{V}^{n+1}$ are the vectors containing the grid point values of the five conservative and of the five relaxation variables respectively. The matrices structure comes from the spatial discretization defined in Sec. III.2.2.2. With our linearization, the implicit stiff source produces additional terms only on the diagonals of the blocks. A constant term proportional to $1/\eta$ appears on the diagonal of $\mathbf{Q}$ and the Taylor expansion introduces terms on the diagonals of the sub-blocks of $\mathbf{P}$. Therefore the computational effort in the inversion algorithms is not excessively increased.

We consider the case of a 1D problem on a uniform mesh. At first order, the blocks $\mathbf{M}$, $\mathbf{N}$ and $\mathbf{Q}$ are tridiagonal. Then the inverse of $\mathbf{M}$ can be computed with a direct solver thanks to its structure. System (III.20) can be split into two linear systems that are solved sequentially by calculating $\mathbf{V}^{n+1}$ and then $\boldsymbol{\Psi}^{n+1}$ in the following way:

$$\begin{cases} \mathbf{V}^{n+1} = \left(\mathbf{Q} - \mathbf{P}\mathbf{M}^{-1}\mathbf{N}\right)^{-1}\left(\mathbf{s} - \mathbf{P}\mathbf{M}^{-1}\mathbf{r}\right) \\ \boldsymbol{\Psi}^{n+1} = \mathbf{M}^{-1}\left(\mathbf{r} - \mathbf{N}\mathbf{V}^{n+1}\right). \end{cases}$$

III.2.3 CFL conditions

Among the wave speeds (III.6), let $\mu_{max} = \sqrt{a_{max}} \geq max|\lambda_1|$, λ_1 being the speed of the longitudinal waves (I.41) and $\mu_{mat} = \sqrt{a_{mat}} \geq max|\lambda_3| = max|u_1|$. We define two different CFL conditions that can be enforced to choose the time step.

Definition III.2.1 *The acoustic Courant number is defined on the speed of the fastest wave as $\nu_{ac} = \mu_{max}\Delta t/\Delta x$. An acoustic CFL condition is enforced by setting $\nu_{ac} \leq 1$.*

Definition III.2.2 *The material Courant number is defined on the speed of the material wave as $\nu_{mat} = \mu_{mat}\Delta t/\Delta x$. A material CFL condition is enforced by setting $\nu_{mat} \leq 1$.*

Remark 1 *For system (I.44), taking $\mu_{max} \simeq |u_1 + c + u_{iso}|$ (approximation of the longitudinal speed (I.41)) we get*

$$\nu_{ac} \simeq \frac{\Delta t}{\Delta x}|u_1|\left(1 + \frac{1}{M} + \frac{1}{M_\chi}\right) \simeq \nu_{mat}\left(1 + \frac{1}{M} + \frac{1}{M_\chi}\right). \tag{III.21}$$

For the Euler equations (namely $\chi = 0$ and no deformation), taking $\mu_{max} \simeq |u_1 + c|$ we get

$$\nu_{ac} \simeq \frac{\Delta t}{\Delta x}|u_1|\left(1 + \frac{1}{M}\right) \simeq \nu_{mat}\left(1 + \frac{1}{M}\right). \tag{III.22}$$

For standard explicit schemes as the ones of Sec. III.2.1, an acoustic CFL condition is needed for stability. As shown by expressions (III.21)-(III.22), this constraint provides an extremely small Δt when $M \to 0$.

The implicit scheme (III.19), instead, is stable without a CFL constraint. Nevertheless, Δt has to be chosen according to the required accuracy. Thus, a material CFL condition is recommended in order to reproduce the propagation of material waves. Since the material CFL does not depend on the speed of the fast waves, these waves are not captured in the low Mach limit.

III.2.4 Numerical viscosity

We study the numerical viscosity by applying the "modified equation" method [80] to schemes at first order on linear transport for a generic variable u. As it is well-known in literature [80], we get the modified equation

$$\partial_t u + \mu \partial_x u = D \partial_{xx} u, \tag{III.23}$$

where μ is the speed of the wave (for system (III.1) is defined in (III.6)) and D is the diffusion coefficient. This latter coefficient takes takes different formulations according to the chosen numerical scheme:

- for the explicit-upwind scheme it can be written as follows:

$$D_{expl-upw} = \mu\frac{\Delta x}{2} - \mu^2\frac{\Delta t}{2} = (1 - \nu)\frac{\mu\Delta x}{2}, \tag{III.24}$$

where ν is the Courant number, which needs to be acoustic to have stability;

- for the implicit-upwind scheme it can be written as follows:

$$D_{impl-upw} = \mu \frac{\Delta x}{2} + \mu^2 \frac{\Delta t}{2} = (1 - \nu) \frac{\mu \Delta x}{2}; \qquad \text{(III.25)}$$

- for the implicit-centered scheme it can be written as follows:

$$D_{impl-cent} = \mu^2 \frac{\Delta t}{2} = \frac{\mu \Delta x}{2} \frac{\mu \Delta t}{\Delta x} = \nu \frac{\mu \Delta x}{2}. \qquad \text{(III.26)}$$

The three diffusion coefficients are of the same order and for $\nu = \nu_{ac} \lesssim 1$ the implicit-upwind scheme has the highest diffusion and the explicit-upwind scheme the lowest.

The accuracy in approximating the different waves depends on the chosen Δt due to numerical viscosity. With our novel implicit scheme, a material CFL is enforced. For gas flows, the diffusion coefficient for the centered spatial discretization (III.26) on material waves becomes:

$$D_{mat} = \frac{\mu_{mat} \Delta x}{2} \frac{\mu_{mat} \Delta t}{\Delta x} \simeq \frac{|u_1| \Delta x}{2} \nu_{mat}. \qquad \text{(III.27)}$$

This formulation explains how the scheme is accurate on material waves also when enforcing material CFL constraints on Δt, namely the accuracy is not reduced by a large time step.

Instead, on acoustic waves, the diffusion coefficient (III.26) reads as follows:

$$D_{ac} = \frac{\mu_{max} \Delta x}{2} \frac{\mu_{max} \Delta t}{\Delta x} \simeq \frac{|u_1 + c| \Delta x}{2} \nu_{ac} \simeq \frac{|u_1 + c| \Delta x}{2} \nu_{mat} \left(1 + \frac{1}{M} \right), \qquad \text{(III.28)}$$

where we have used relation (III.22) for the last equality. In the limit $M \to 0$, the numerical diffusion of the scheme becomes large on acoustic waves when a material CFL condition is used (large Δt). However, in low Mach flows applications, acoustic waves carry a small amount of energy, thus the low accuracy in their approximation can be acceptable. If accuracy on these waves is needed, acoustic CFL constraints on Δt can be applied.

We remind the reader that also the relaxation method itself introduces a viscosity in the hyperbolic system, due to the first order correction derived in equation (III.3). However, as explained in Sec. III.1.1.1, the relaxation matrix is build in a way that this additional viscosity is limited as much as possible.

III.3   Numerical results

In this section, the all-speed implicit relaxation scheme (III.19) is validated at all speeds. We show and discuss several tests by carrying out a thorough comparison with the results of the standard relaxation scheme of Sec. III.2.1 (for simplicity of notation, we refer to this scheme as "explicit"). In all computations the relaxation parameter is $\eta = 10^{-8}$ and $\mathbf{A}$ is built as explained in Sec. III.1.1.1.

We first present steady test cases on the Euler equations (flow in a nozzle) with perfect and stiffened gas state laws. Then, we study the propagation of material waves in compressible media, with the simulation of the full Eulerian model introduced in Chapter I.
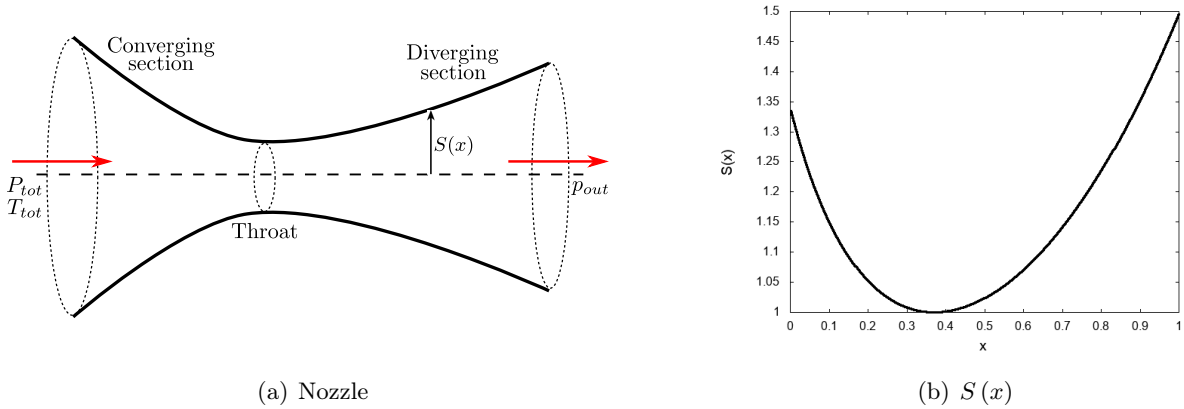
(a) Nozzle

(b) $S(x)$

Figure III.1: Left: Laval nozzle general sketch. Right: geometry of the simulated nozzle.

III.3.1 The Laval nozzle flow

The Laval nozzle is a converging-diverging duct. It is widely used for achieving steady supersonic flows in a variety of systems such as rocket motors and wind tunnels. The sketch of a nozzle is drawn in Fig. III.1(a).

Given the geometry, the flow in the nozzle is three-dimensional. The simplest analytic model for compressible flow in a Laval nozzle is the quasi one-dimensional duct flow approximation [16]:

$$\begin{cases} \partial_t(S\rho) + \partial_x(S\rho u) = 0 \\ \partial_t(S\rho u) + \partial_x\left(S\left(\rho u^2 + p\right)\right) = p\partial_x S \\ \partial_t(S\rho e) + \partial_x(Su(\rho e + p)) = 0. \end{cases} \tag{III.29}$$

The quasi one-dimensional assumption consists in taking the cross sectional area as a smooth function of the axial coordinate, $S = S(x)$. Hence, all flow variables are functions of the axial coordinate and not of the other coordinates. After a few manipulations, system (III.29) can be rearranged in such a way that the Euler system is obtained, with a non linear source depending on the fluxes:

$$\begin{cases} \partial_t\rho + \partial_x(\rho u) = -\rho u \dfrac{\partial_x S}{S} \\ \partial_t(\rho u) + \partial_x\left(\rho u^2 + p\right) = -\rho u^2 \dfrac{\partial_x S}{S} \\ \partial_t(\rho e) + \partial_x(u(\rho e + p)) = -u(\rho e + p)\dfrac{\partial_x S}{S}. \end{cases} \tag{III.30}$$

Formulations (III.29)-(III.30) are equivalent and both conservative because the cross section $S(x)$ of the nozzle is a smooth function of x. System (III.30) can be rewritten in the general framework (I.44) with no deformation and with an additional a non-linear source depending on the cross section.

We simulate perfect gas and stiffened gas (water) flows through a Laval nozzle. Steady state is reached evolving system (III.30) in time until the difference of the solution between two consecutive time steps gets under a certain tolerance (this tolerance is usually taken of order 10^{-9}). All the nozzle results are obtained with 512 grid points unless otherwise stated and on the computational domain $[0, 1]$. For all computations, we use the function $S(x)$ plotted in Fig. III.1(b).

III.3.1.1   Perfect gas nozzle flow

The case of a perfect gas nozzle flow is considered. At the inlet the total pressure (which is given by the Bernoulli principle) and temperature are imposed $P_{tot} = 1$Pa and $T_{tot} = 1$K. At the outlet, a certain pressure p_{out} has to be imposed and determines the regime of the nozzle. We study two different configurations:

- *test 1*: $p_{out} = 0.9$Pa. The flow is subsonic, with a Mach number varying in the range $M \in [0.45; 0.7]$;

- *test 2*: $p_{out} = 0.99999$Pa. The flow is subsonic, with a low Mach number in the range $M \in [4; 9] \cdot 10^{-3}$.

We remark that the pressure and temperature values imposed for these configurations are chosen in the spirit of having suitable validation tests of the scheme in different regimes.

In both cases, for the explicit relaxation scheme the results are obtained by enforcing acoustic CFL conditions: $\nu_{ac} = 0.9$ at first order and $\nu_{ac} = 0.4$ at second order. For the implicit scheme, instead, the constraint is not required and the presented results are obtained with $\nu_{ac} = 100$.

The results of *test 1* are presented in Fig. III.2. Here we compare the velocity, pressure and density profiles obtained with the standard relaxation scheme of Sec. III.2.1 (left column) and with the novel implicit scheme (right column). The simulated flow is subsonic, with a Mach number close to one. The two schemes produce very similar results. The convergence analysis for this test (see Fig. III.4(a)) shows that the implicit scheme is more precise than the explicit scheme at order one. Nevertheless, at second order, the precision is the same for the two schemes.

Test 2 is a low Mach flow simulation. The quantities of interest are presented in Fig. III.3, where again the comparison between the results of the two schemes is carried out. The density and pressure profiles obtained with the explicit scheme at first order are shifted with respect to the exact solution and they present some oscillations at the boundaries. This is due to the excessive numerical viscosity produced the upwind spatial discretization in this regime. On the contrary, the implicit relaxation scheme is able to overcome these problems: the pressure and the density curves are superimposed to the exact ones, due to convex combination (III.17) which produces an "almost-fully-centered" discretization in presence of low Mach regimes.

The convergence analysis of Fig. III.4(b) confirms these observations. The implicit all-speed scheme is more precise if compared to the explicit scheme, at both first and second order. This is due to the adopted all-speed spatial discretization (III.18), which provides the correct numerical viscosity also when solving low Mach flows. The two proposed tests prove that the novel implicit scheme can provide very accurate solutions in different regimes. The computational effort of the two schemes for the case of 512 grid points is compared in Table III.2. The implicit scheme is more expensive mainly because of the simple direct linear solver used. The CPU time could be reduced by employing preconditioned iterative methods. On the other hand, techniques such as local time stepping and multigrid (see for example [121, 70]) could accelerate the convergence of the explicit scheme for the specific nozzle application. However, these results show that the numerical error on the low Mach solution is reduced of a factor of 10 with the implicit scheme for a given number of grid points.
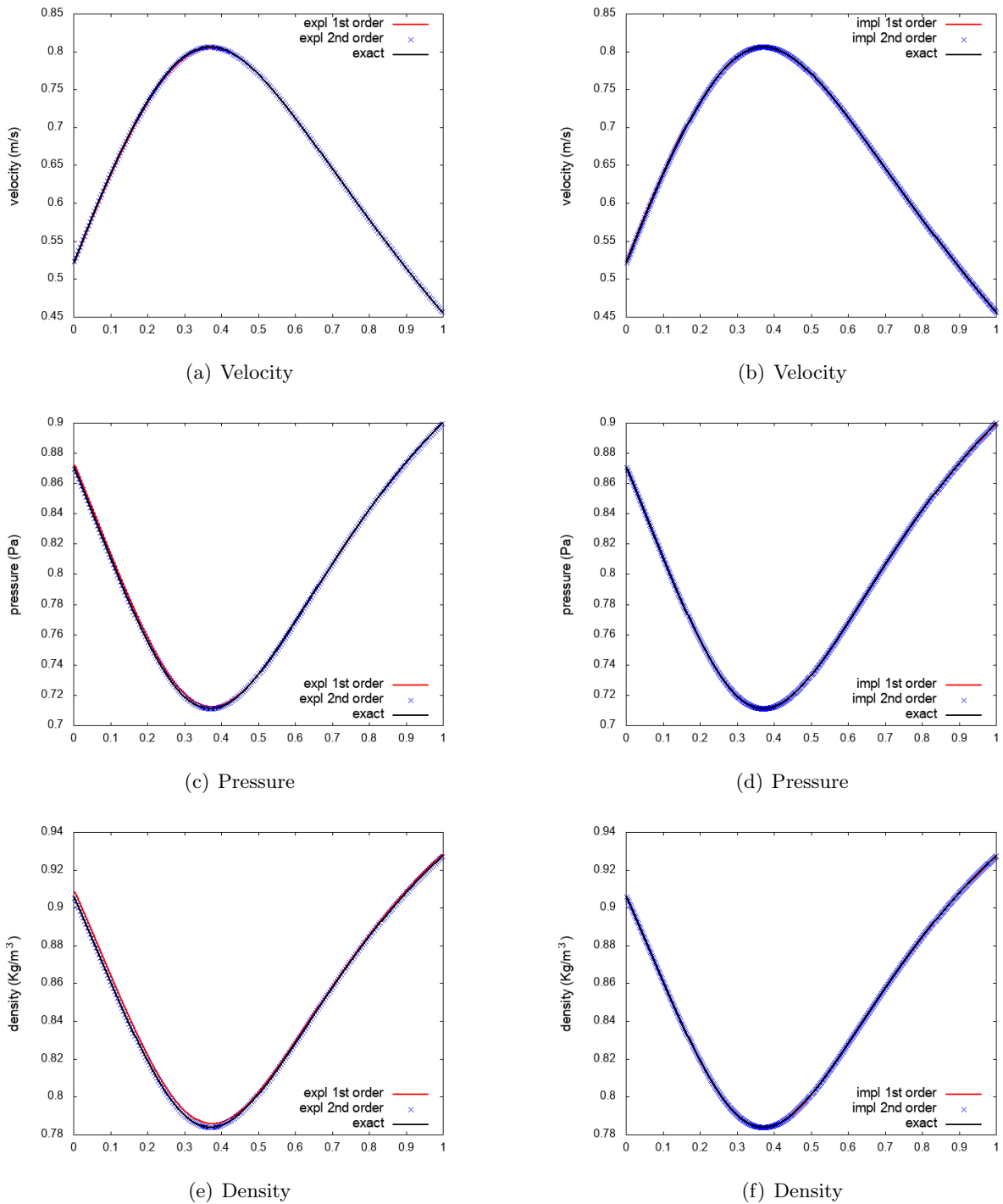
Figure III.2: Perfect gas nozzle flow *test 1*: velocity, pressure and density. Left column: explicit relaxation scheme. Right column: implicit relaxation scheme.

On the other hand, for a given error, the CPU time required by the explicit scheme is much larger than the CPU time of the implicit scheme to reach the same accuracy on the solution. The comparison of computational times, grid points and iterations needed by the two schemes to reach the steady state are shown in Table III.3. We obtain the correct numerical solution
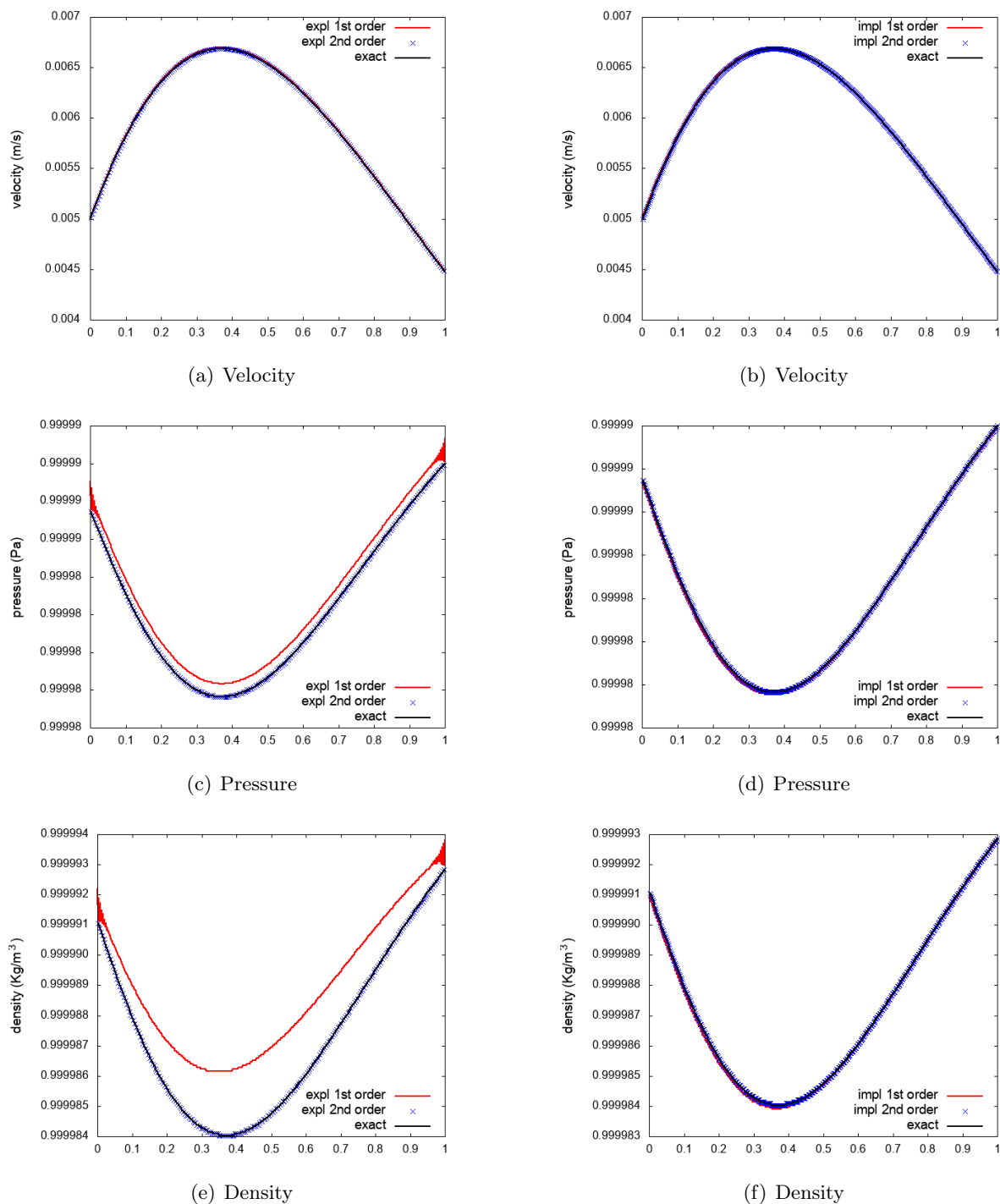
(a) Velocity

(b) Velocity

(c) Pressure

(d) Pressure

(e) Density

(f) Density

Figure III.3: Perfect gas nozzle flow *test 2*: velocity, pressure and density. Left column: explicit relaxation scheme. Right column: implicit relaxation scheme.

with the explicit relaxation scheme only when employing extremely refined grids. Consequently, the computational times increase enormously. We remark that for the computation of the steady state solution, the time dependent problem is solved as an iterative method (such as the Richardson method) until steady state is reached. Therefore, the number of iterations needed
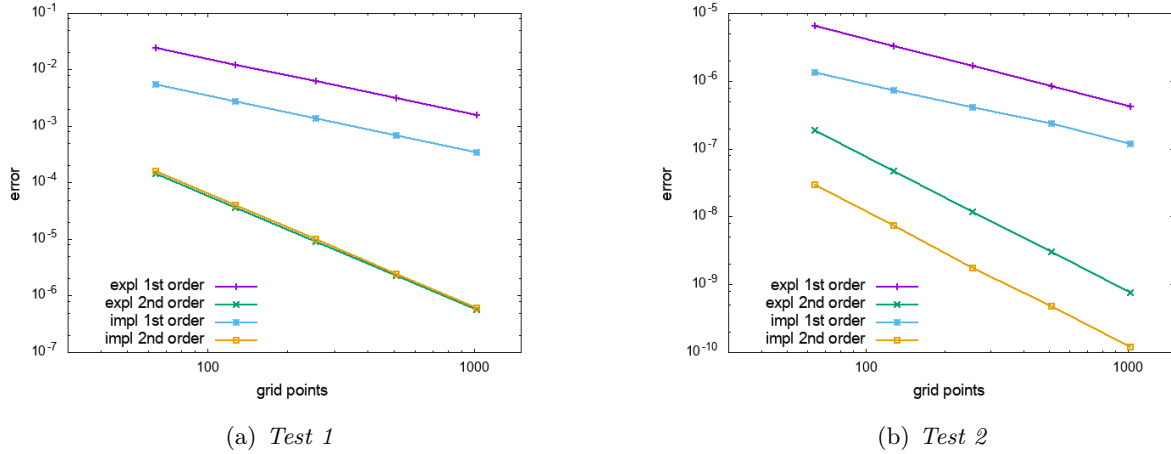
(a) *Test 1* (b) *Test 2*

Figure III.4: Perfect gas nozzle flow: L_∞ numerical error on pressure. Left panel: gas nozzle flow *test 1*. Right panel: gas nozzle flow *test 2*.

(a) Test 1

	Explicit-upwind	Implicit all-speed
error	$2.75{\cdot}10^{-3}$	$6.75{\cdot}10^{-4}$
CPU time	15	712
iterations	22667	79

(b) Test 2

	Explicit-upwind	Implicit all-speed
error	$1.64{\cdot}10^{-6}$	$1.95{\cdot}10^{-7}$
CPU time	78.3	552
iterations	113914	51

Table III.2: Comparison of numerical error, CPU time and iterations needed to reach convergence for 512 grid points with the two schemes.

to converge corresponds to the number of time steps.

(a) Error $\simeq 7.9 \cdot 10^{-7}$

	Explicit-upwind	Implicit all-speed
grid points	2950	128
CPU time	353.1	8.1
iterations	135402	48

(b) Error $\simeq 3.8 \cdot 10^{-7}$

	Explicit-upwind	Implicit all-speed
grid points	9000	256
CPU time	3464.5	64.8
iterations	448809	58

Table III.3: Comparison of computational time and iterations needed by the two relaxation schemes to reach the same precision at steady state for test 2 (low Mach flow).

III.3.1.2   Stiffened gas nozzle flow

(a) Velocity

(b) Velocity

(c) Pressure
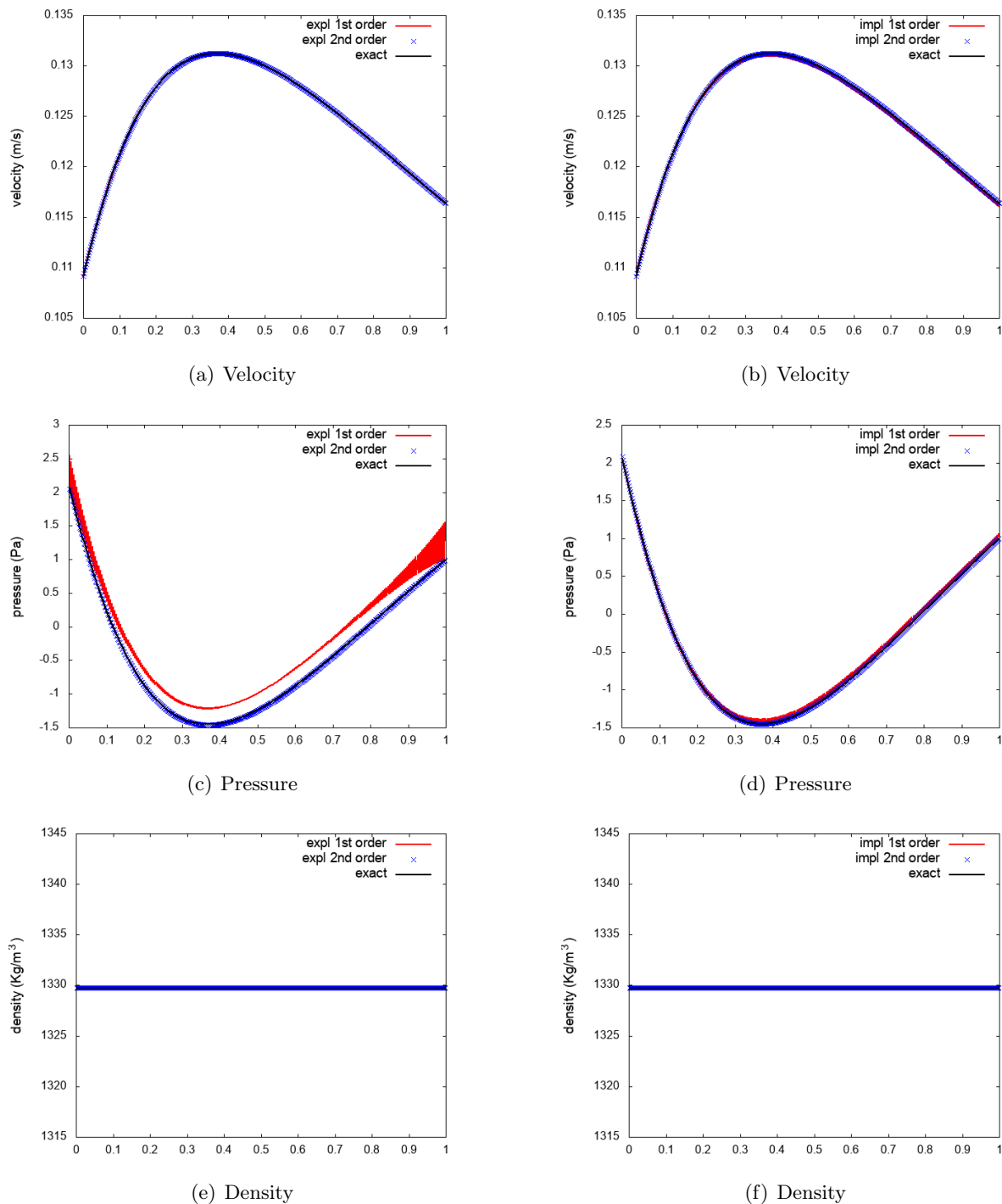
(d) Pressure

(e) Density

(f) Density

Figure III.5: Water nozzle flow: velocity, pressure and density. Left column: explicit relaxation scheme. Right column: implicit relaxation scheme.

With the state law of a stiffened gas, we simulate a water flow inside a Laval nozzle. The flow is low Mach and almost incompressible, due to the presence of the p_∞ term in the state law. For this simulation, we impose at the inlet $P_{tot} = 10$Pa and $T_{tot} = 280$K, at the outlet

$p_{out} = 1\mathrm{Pa}$. The Mach number varies in the interval $M \in [7.26; 8.67] \cdot 10^{-5}$ approximately inside the nozzle.

In Fig. III.5, the profiles of the density, pressure and velocity obtained with the two schemes are compared with the exact solution. Once again, the oscillations and the shift from the exact solution that can be observed in Fig. III.5(c) are due to the excessive numerical viscosity of the upwind discretization. The novel implicit relaxation scheme improves the precision of the solution thanks to the hybrid spatial discretization (III.18).
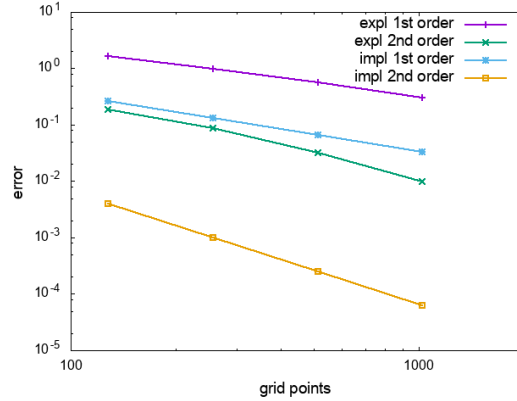

Figure III.6: Water nozzle flow: L_∞ numerical error on pressure.

The convergence analysis is carried out in Fig. III.6. The implicit scheme is always more precise with respect to the explicit one. The convergence rates are the correct ones. In the computations of this test case, the acoustic CFL for the explicit scheme is $\nu_{ac} = 0.4$ at first and second order and for the implicit scheme is $\nu_{ac} = 100$ at first and second order.

Laval nozzle flow: the exact solution in the subsonic regime

All the presented numerical results are compared with the exact solution. We are interested in computing the exact solution for the subsonic regime, namely we expect that no shock will form inside the nozzle. In this case, the solution of the quasi 1D problem can be easily computed with the use of thermodynamics.

We recall that for a perfect gas the enthalpy has the following expression:

$$h = \epsilon + \frac{p}{\rho} = c_p T.$$

Since the energy is conserved, for any two points x_1 and x_2, it holds

$$c_p T_1 + \frac{u_1^2}{2} = c_p T_2 + \frac{u_2^2}{2}$$

and the following ratio between temperatures at different locations is obtained:

$$\frac{T_2}{T_1} = \frac{1 + \frac{u_1^2}{2c_p T_1}}{1 + \frac{u_2^2}{2c_p T_2}} = \frac{1 + \frac{\gamma-1}{2}M_1^2}{1 + \frac{\gamma-1}{2}M_2^2}. \tag{III.31}$$

Here, we have used the definition of Mach number $M = u/a$ and the expression for the sound speed $c = \sqrt{\gamma R T}$ to rewrite

$$\frac{u^2}{2 c_p T} = \frac{u^2}{2 \gamma R T} \frac{\gamma R}{c_p} = \frac{\gamma - 1}{2} M^2.$$

The law of perfect gases states $p = \rho R T$ and the conservation of entropy gives

$$\frac{T_2}{T_1} = \frac{p_2}{p_1} \frac{\rho_1}{\rho_2} = \left(\frac{\rho_2}{\rho_1} \right)^{\gamma - 1} = \left(\frac{p_2}{p_1} \right)^{\frac{\gamma - 1}{\gamma}}. \tag{III.32}$$

Thus, the following pressure ratio is easily recovered:

$$\frac{p_2}{p_1} = \left(\frac{1 + \frac{\gamma - 1}{2} M_1^2}{1 + \frac{\gamma - 1}{2} M_2^2} \right)^{\frac{\gamma - 1}{\gamma}}. \tag{III.33}$$

This last expression can be used to compute the Mach number at the outflow of the nozzle, since p_{out} and P_{tot} are known:

$$M_{out} = \sqrt{\frac{2}{\gamma - 1} \left(\left(\frac{P_{tot}}{p_{out}} \right)^{\frac{\gamma - 1}{\gamma}} - 1 \right)}.$$

The ratio between the area of the nozzle $A(x)$ at different coordinates x_1 and x_2 is computed in the following way:

$$\frac{A_2}{A_1} = \frac{M_1}{M_2} \sqrt{\left(\frac{1 + \frac{\gamma - 1}{2} M_2^2}{1 + \frac{\gamma - 1}{2} M_1^2} \right)^{\frac{\gamma + 1}{\gamma - 1}}}, \tag{III.34}$$

where M_1 and M_2 are the Mach numbers computed at x_1 and x_2. This expression comes from the ratio of mass flow rates at different locations (see for its derivation [15]). Since the Mach number at the outflow is known, we can reconstruct the Mach number $M(x)$ for every point inside the nozzle by solving relation (III.34) with $x_2 = x_{out}$ and $x_1 = x$. In order to find the zero of this expression we employ a Newton method.

All other quantities can now be calculated, starting from the pressure by using relation (III.33) with $p_2 = p(x)$ and $p_1 = P_{tot}$ (having then $M_1 = 0$). Then the temperature $T(x)$ is easily recovered from (III.31) and the sound speed $c(x) = \sqrt{\gamma R T}$ and the flow velocity $u(x) = M(x) c(x)$.

The solution in a water nozzle consists always in a subsonic (almost incompressible) flow, due to the stiffness of the state law with the p_∞ term. Therefore, the exact solution is computed by following the same thermodynamic procedure we introduced for the subsonic solution with a perfect gas, with some changes due to the different state law.

The enthalpy now takes the following expression:

$$h = \epsilon + \frac{p}{\rho} = c_v T + \frac{p_\infty}{\rho} + (\gamma - 1) c_v T - \frac{p_\infty}{\rho},$$

where we have used the internal energy formulation (I.12) for a stiffened gas. Nevertheless, after the same computations we did in the case of a perfect gas, we obtain the same ratio between temperatures at different locations (III.31). What changes is the relation with the pressure, having now:

$$\frac{T_2}{T_1} = \frac{p_2 + p_\infty}{\rho_2} \frac{\rho_1}{p_1 + p_\infty} = \left(\frac{\rho_2}{\rho_1} \right)^{\gamma - 1} = \left(\frac{p_2 + p_\infty}{p_1 + p_\infty} \right)^{\frac{\gamma - 1}{\gamma}}, \tag{III.35}$$

where we have used the expression (I.12) for the pressure and again the fact that the flow is isentropic. Everything else follows from this: the expression for the outflow Mach number becomes

$$M_{out} = \sqrt{\frac{2}{\gamma - 1} \left(\left(\frac{P_{tot} + p_\infty}{p_{out} + p_\infty} \right)^{\frac{\gamma - 1}{\gamma}} - 1 \right)}.$$

Then the other expressions follow directly.

III.3.2 Simulation of material waves

We now address the simulation of propagating material waves by solving different Riemann problems in pipes filled with perfect gases, water and hyperelastic solids in different regimes (Table III.4). The results are obtained with the explicit relaxation scheme and the novel implicit scheme at first order in all tests.

Initial conditions and parameters are listed in Table III.5, where L is the length of the tube and x_0 is the initial position of the contact discontinuity. The discontinuous initial conditions are smoothed with an arcotangent function in order to overcome the problem of the computation of non-linear flux limiters on the discontinuity.

Test	Material	Regime	γ	p_∞ (Pa)	χ (Pa)
1	perfect gas	$M \simeq 0.9$	1.4	0	0
2	perfect gas	$M \simeq 6 \cdot 10^{-3}$	1.4	0	0
3	water	$M \simeq 2.5 \cdot 10^{-3}$	4.4	$6.8 \cdot 10^8$	0
4	copper	$M \simeq M_\chi \simeq \mathcal{O}\left(10^{-3}\right)$	4.22	$3.42 \cdot 10^{10}$	$5 \cdot 10^{10}$
5	hyperelastic solid	$M \simeq 3 \cdot 10^{-3}, M_\chi \simeq 0.15$	4.4	$6.8 \cdot 10^8$	$8 \cdot 10^5$

Table III.4: Parameters for the material waves test cases: materials and regime on the contact wave.

Test	L (m)	x_0 (m)	t_{end} (s)	ρ_L (Kg/m^3)	ρ_R (Kg/m^3)	$u_{1,L}$ (m/s)	$u_{1,R}$ (m/s)	$u_{2,L}$ (m/s)	$u_{2,R}$ (m/s)	p_L (Pa)	p_R (Pa)
1	1	0.5	0.1644	1	0.125	0	0	0	0	1	0.1
2	1	0.5	0.25	1	1	0	0.008	0	0	0.4	0.399
2.1	400	200	150	1	1	0	0.008	0	0	0.4	0.399
3	1	0.5	10^{-4}	10^3	10^3	0	15	0	0	10^8	$0.98 \cdot 10^8$
3.1	400	200	0.095	10^3	10^3	0	15	0	0	10^8	$0.98 \cdot 10^8$
4	2	1	$6 \cdot 10^{-5}$	$8.9 \cdot 10^3$	$8.9 \cdot 10^3$	0	0	0	100	10^9	10^5
4.1	500	250	0.04	$8.9 \cdot 10^3$	$8.9 \cdot 10^3$	0	0	0	100	10^9	10^5
5	100	50	0.016	$1 \cdot 10^3$	$1 \cdot 10^3$	0	10	0	40	10^8	$0.98 \cdot 10^8$

Table III.5: Parameters for the material waves test cases: initial state.

For all test cases we use homogeneous Neumann boundary conditions, namely we impose $\frac{\partial \psi}{\partial \mathbf{n}}\big|_{x=0} = \frac{\partial \psi}{\partial \mathbf{n}}\big|_{x=L} = 0$ ($\mathbf{n}$ being the outward normal to the boundary) on the conservative variables. Since $\frac{\partial \mathbf{v}}{\partial \mathbf{n}} = \mathbf{F}'(\psi) \frac{\partial \psi}{\partial \mathbf{n}}$, on the relaxation variables we impose $\frac{\partial \mathbf{v}}{\partial \mathbf{n}}\big|_{x=0} = \frac{\partial \mathbf{v}}{\partial \mathbf{n}}\big|_{x=L} = 0$.
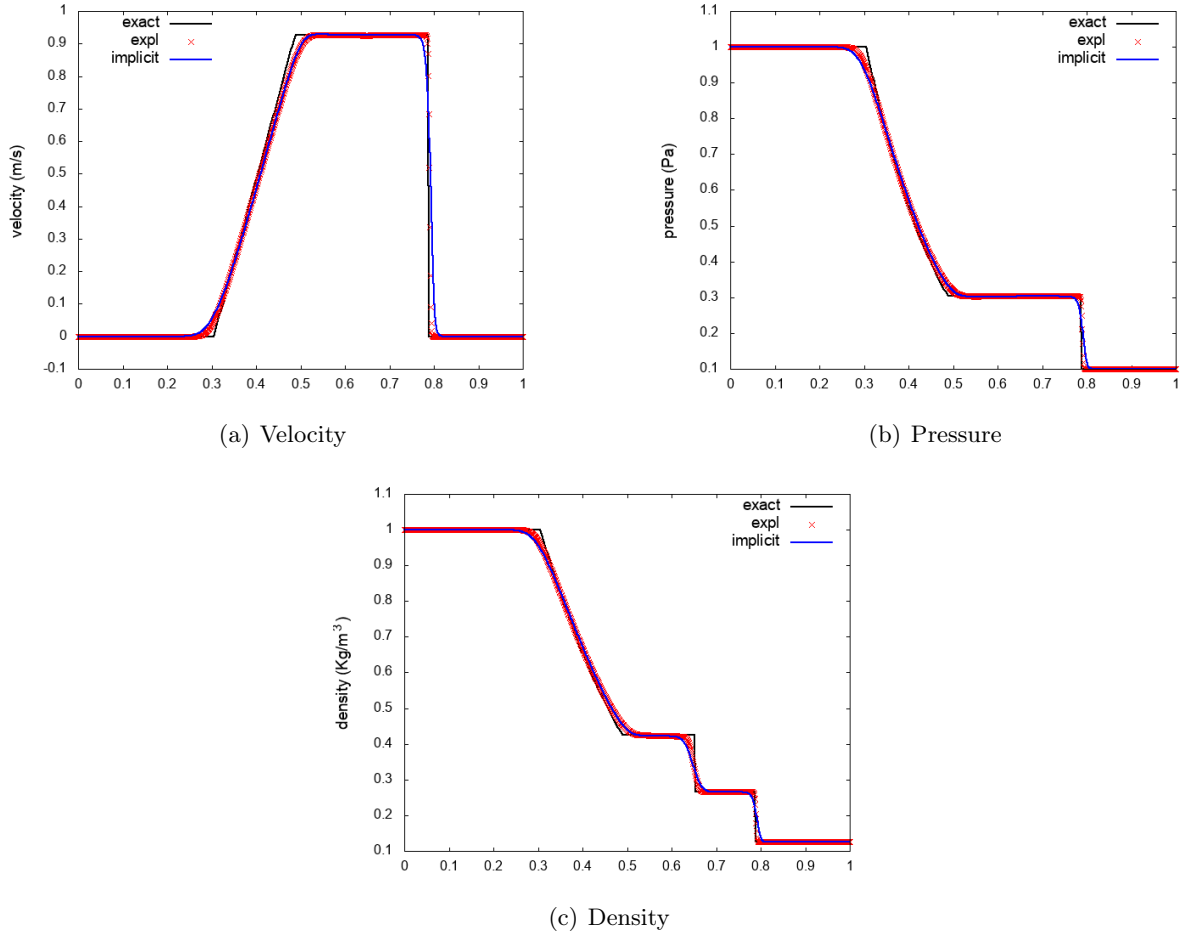
(a) Velocity

(b) Pressure

(c) Density

Figure III.7: *Test 1*: Sod shock tube with perfect gas (1000 grid points).

III.3.2.1 Perfect gas

Test 1 is a Sod shock tube filled with a biatomic perfect gas. The flow is accelerated, characterized by an expansion wave, a contact discontinuity and a shock. The Mach number on the contact wave is $M \simeq 0.9$. The profiles obtained with the explicit and the implicit relaxation schemes are similar, as shown by Fig. III.7. Both schemes provide results in good agreement with the exact solution, are oscillation free and have the correct shock strength and speed. The explicit relaxation scheme is solved with $\nu_{ac} = 0.4$. For the implicit scheme we impose $\nu_{mat} = 0.3$, corresponding to $\nu_{ac} = 0.9$, since the sound speed and the flow velocity are of the same order.

Test 2 is a perfect gas low Mach flow, with $M \simeq 6 \cdot 10^{-3}$ on the contact wave. In the tube, a small pressure ratio and a small velocity on the right are imposed. The gas is expanded in both directions and the contact wave moves very slowly (this test is proposed in the book of Toro [124]).

In Fig. III.8 we show the influence of the time step on the density profile computed with the implicit scheme. The contact wave is always kept sharp thanks to spatial discretization (III.18). The numerical viscosity on this wave does not increase when taking a larger time step, as shown by relation (III.27). All the three waves are accurately reproduced when an acoustic
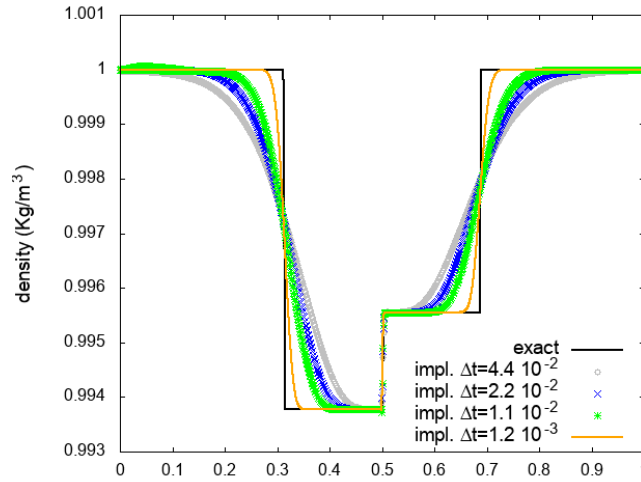
Figure III.8: Density profiles for different time steps of the implicit scheme for *test 2* (1000 grid points). CFL constraints: $\Delta t = 4.4 \cdot 10^{-2}$ given by $\nu_{mat} = 0.4$, $\Delta t = 2.2 \cdot 10^{-2}$ by $\nu_{mat} = 0.2$, $\Delta t = 1.1 \cdot 10^{-2}$ by $\nu_{mat} = 0.1$, $\Delta t = 1.2 \cdot 10^{-3}$ by $\nu_{ac} = 0.9$.
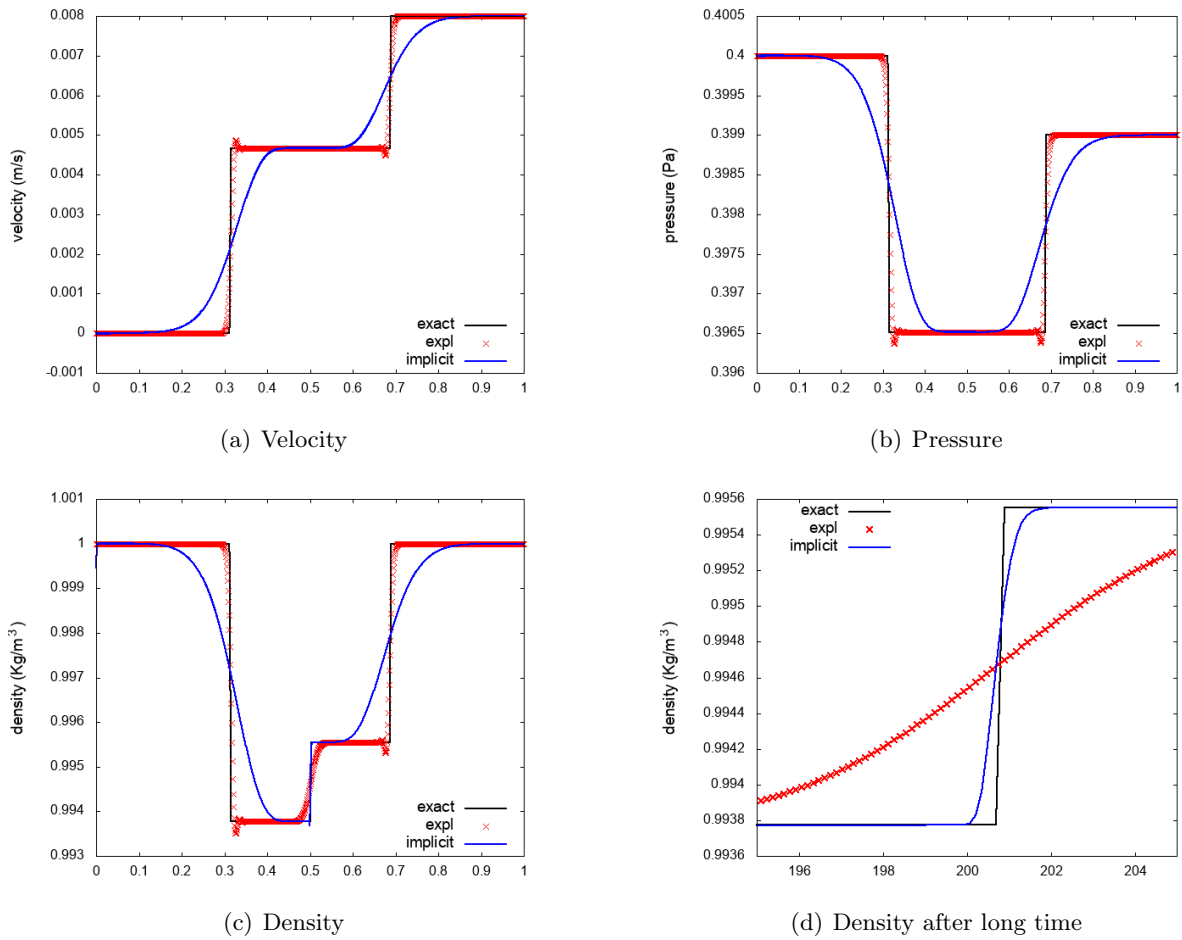

(a) Velocity

(b) Pressure

(c) Density

(d) Density after long time

Figure III.9: *Test 2*: Low Mach tube with perfect gas (1000 grid points). Panel (d): zoom on the material wave obtained for *test 2.1* (4000 grid points).

constraint $\nu_{ac} = 0.9$ is enforced. With a grid spacing $\Delta x = 10^{-3}$, this condition gives a small time step $\Delta t = 1.2 \cdot 10^{-3}$s (orange line), thus producing long computational times. Material CFL conditions $\nu_{mat} = 0.1$, $\nu_{mat} = 0.2$ and $\nu_{mat} = 0.4$ reduce the computational time, since they give $\Delta t = 1.1 \cdot 10^{-2}$ (green line), $\Delta t = 2.2 \cdot 10^{-2}$ (blue line) and $\Delta t = 4.4 \cdot 10^{-2}$ (grey line) respectively. The acoustic waves are smoothed due to the numerical diffusion (III.28).

The time step of the implicit scheme is not imposed by stability issues, but has to be chosen accordingly to the accuracy needed on the acoustic waves. If the focus is the approximation of material waves, a material CFL condition can be adopted in order to reduce the computational time. If instead a good resolution of fast waves is needed, the use of an acoustic CFL is recommended.

In Figs. III.9(a)-III.9(b)-III.9(c) we compare velocity, pressure and density obtained by the implicit scheme with $\nu_{mat} = 0.2$, giving $\Delta t = 2.2 \cdot 10^{-2}$ (blue line) and by the explicit scheme, giving $\Delta t = 5.3 \cdot 10^{-4}$ (red line). This latter condition gives . After 0.25s, the contact discontinuity has only moved from $x_0 = 0.5$m to $x_0 = 0.501$m, namely it has crossed 1 cell for a grid spacing $\Delta x = 10^{-3}$. The implicit scheme is consistently more accurate than the explicit scheme in the approximation of the contact wave.

The ability of the scheme in capturing travelling waves is then tested with a simulation for longer times (*test 2.1* in Table III.5). In Fig. III.9(d) we show a zoom on the contact wave in a tube of length $L = 400$m. After 150s the contact discontinuity has moved from $x_0 = 200$m to $x_0 = 200.71$m, namely it has crossed 7 cells for the employed grid spacing $\Delta x = 10^{-1}$. The explicit relaxation scheme is completely smoothing the contact discontinuity. It is evident that the implicit scheme is superior in capturing the travelling material wave.

III.3.2.2 Stiffened gas

Test 3 simulates a water flow in a pipe where a very small pressure ratio is imposed. The Mach number on the contact wave is $M \simeq 2.5 \cdot 10^{-3}$. In Figs. III.10(a)-III.10(b)-III.10(c), the explicit scheme presents some small oscillations on the rarefactions due to the stiffness of the problem. These results are obtained with $\nu_{ac} = 0.4$ having $\Delta t = 2.14 \cdot 10^{-7}$s on a grid of 1000 points. The results of the implicit scheme are obtained with a material CFL $\nu_{mat} = 0.15$, which gives a time step $\Delta t = 9.4 \cdot 10^{-6}$s for the chosen grid. The contact discontinuity is kept sharp and has the correct speed. As expected, the acoustic waves are smoothed due to the large time step. In these results the contact wave has moved from $x_0 = 0.5$ to $x_0 = 0.5008$m, which means that on the chosen grid it has not even crossed one cell yet.

The density profile in Fig. III.10(d) is computed after long times (*test 3.1*: tube of $L = 400$m). At time $t = 0.095$s the contact wave has moved from $x_0 = 200$m to $x_0 = 200.76$m, namely it has crossed 8 cells for a grid spacing $\Delta x = 10^{-1}$. The explicit relaxation scheme is not reproducing the travelling material wave. Instead, the position and the velocity of the wave are captured by the implicit scheme, even if there is not a perfect superimposition due to the stiffness of the problem.
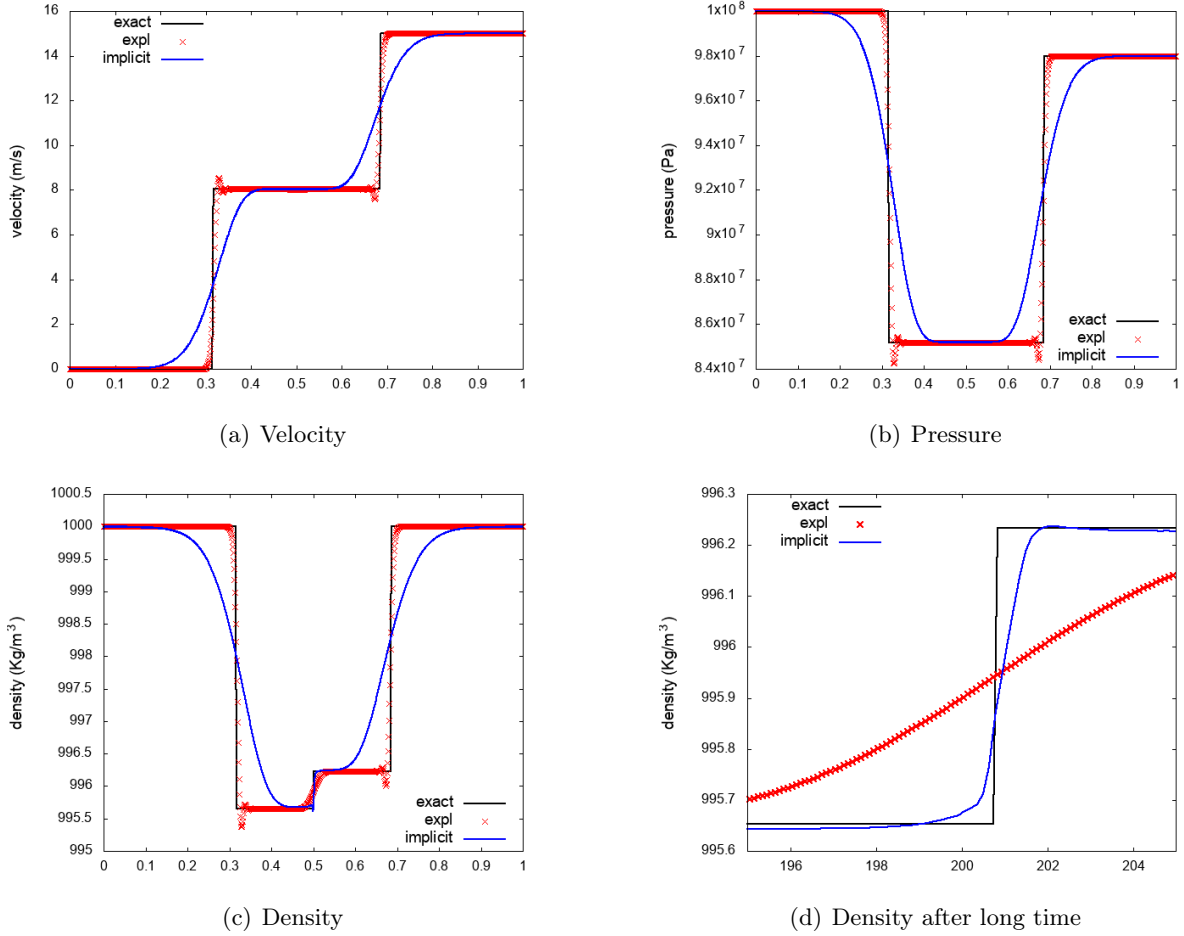
(a) Velocity

(b) Pressure

(c) Density

(d) Density after long time

Figure III.10: *Test 3*: tube with water (1000 grid points). Panel (d): zoom on the material wave profile obtained for *test 3.1* (4000 grid points).

III.3.2.3 Hyperelastic solids

The scheme is tested on the deformation of hyperelastic solids. The 1D system (I.44) is fully simulated and the isochoric and the volumetric contributions in the state law (I.28) are both present. *Test 4* simulates the deformation of a pipe of length $L = 2$m filled with copper (see Tables III.4 and III.5 for parameters and initial conditions). Copper is at rest and at higher pressure on the left part. A tangential velocity discontinuity is imposed, so five waves appear. On the contact wave, the acoustic Mach number is $M \simeq 2.6 \cdot 10^{-3}$ and the elastic Mach number is $M_\chi \simeq 3.15 \cdot 10^{-3}$. Since the two numbers are of the same order, this test is representative of the *"shear and acoustic low Mach limit"* case, due to intrinsic copper properties $p_\infty \simeq \chi \simeq \mathcal{O}\left(10^{10}\right)$.

In Fig. III.11 we compare the density and pressure profiles obtained with the implicit scheme for different time steps. All five different waves can be distinguished when the time step is acoustic (black line): the fastest waves are those relative to the normal stress, the middle one is the material wave, and the two intermediate waves are those relative to the tangential (shear) stress. The time step chosen for this simulation is $\Delta t = 1.7 \cdot 10^{-7}$, given by enforcing $\nu_{ac} = 0.9$. The other results of the implicit scheme are obtained with $\nu_{mat} = 0.15$, giving $\Delta t = 8.3 \cdot 10^{-6}$
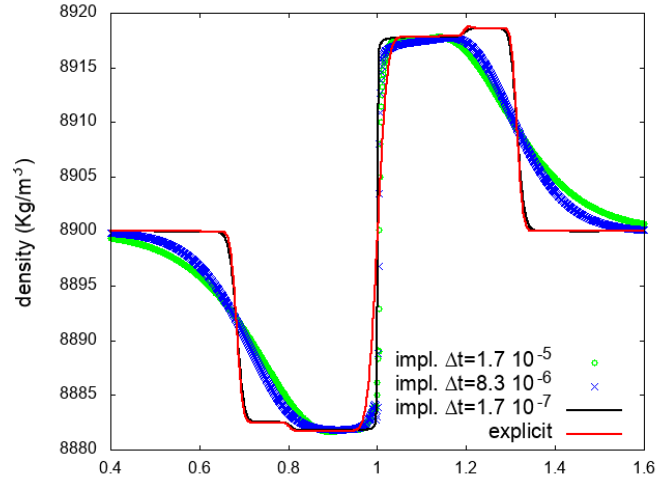
(a) Density
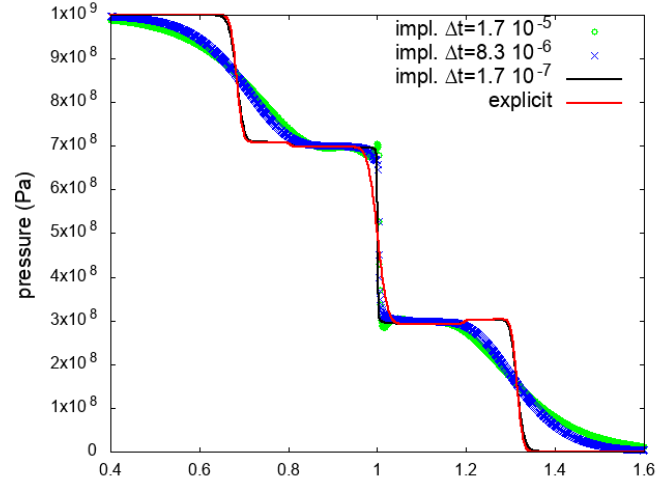
(b) Pressure

Figure III.11: Density and pressure profiles for different time steps of the implicit scheme for *test 4* (2000 grid points on the domain $[0, 2]$). CFL constraints: $\Delta t = 1.7 \cdot 10^{-5}$ given by $\nu_{mat} = 0.3$, $\Delta t = 8.3 \cdot 10^{-6}$ by $\nu_{mat} = 0.15$, $\Delta t = 1.7 \cdot 10^{-7}$ by $\nu_{ac} = 0.9$.

(blue line) and $\nu_{mat} = 0.3$, giving $\Delta t = 1.7 \cdot 10^{-5}$ (green line). With these latter constraints, the number of time steps and, consequently, computational times are reduced. Longitudinal and shear waves are smoothed due to numerical diffusion (III.28). Nevertheless, for every choice of Δt, the implicit scheme keeps sharp the material wave, reproducing it more accurately than the explicit scheme. The results of the explicit scheme are calculated with $\nu_{ac} = 0.4$ giving $\Delta t = 8.7 \cdot 10^{-8}$ (red line). In Fig. III.12 we compare the other fields computed by the two schemes. For the implicit scheme, here we use $\nu_{mat} = 0.15$. After $6 \cdot 10^{-5}$s the contact wave has moved from $x_0 = 1$m to $x_0 = 1.001$m, not even crossing one cell with the grid spacing $\Delta x = 10^{-3}$.

We simulate the same problem for longer times (*test 4.1*). At time $t = 0.04$s, the discontinuity has moved from $x_0 = 250$m to $x_0 = 250.65$m in a tube of length $L = 500$m. The results in

(a) Normal velocity

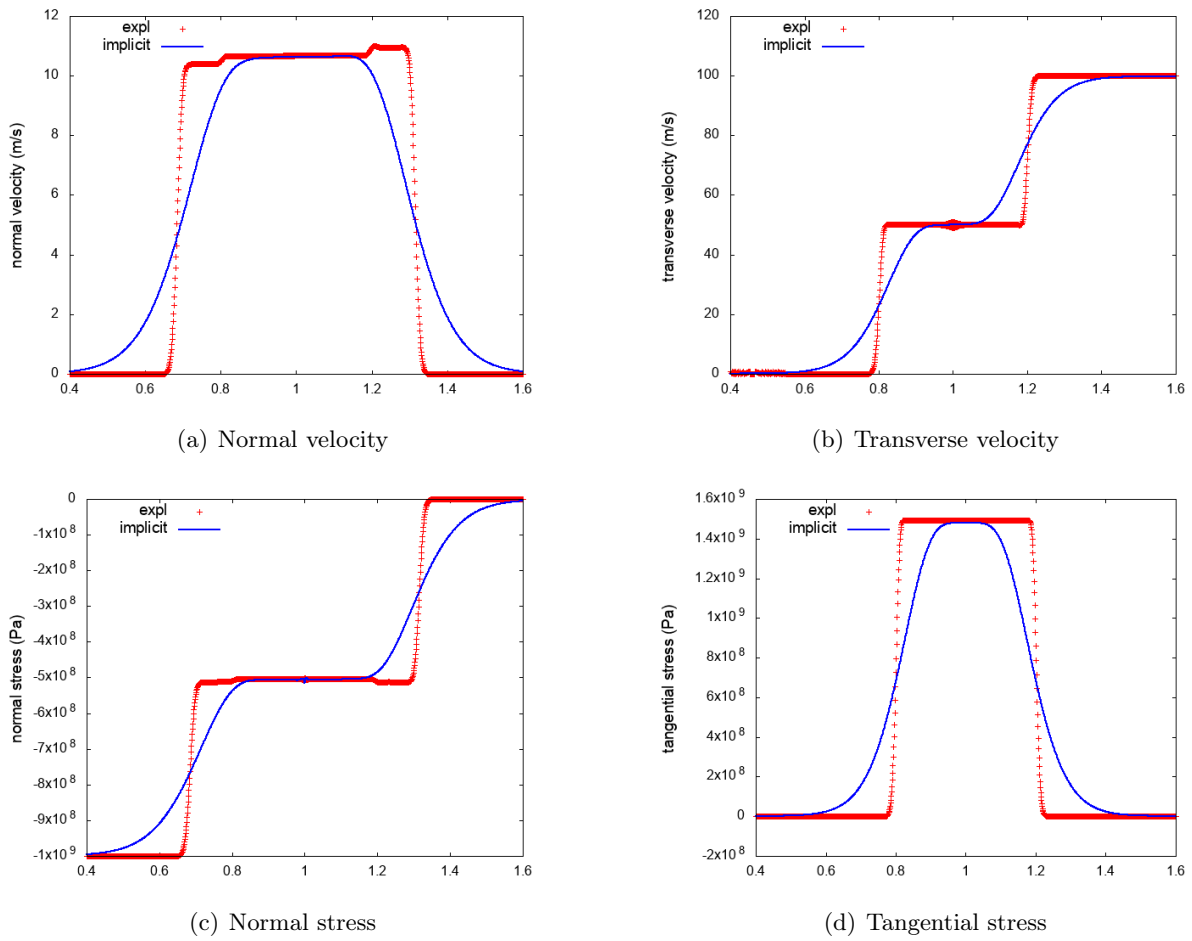(b) Transverse velocity

(c) Normal stress

(d) Tangential stress

Figure III.12: *Test 4*: tube with copper (2000 grid points on the domain $[0, 2]$).

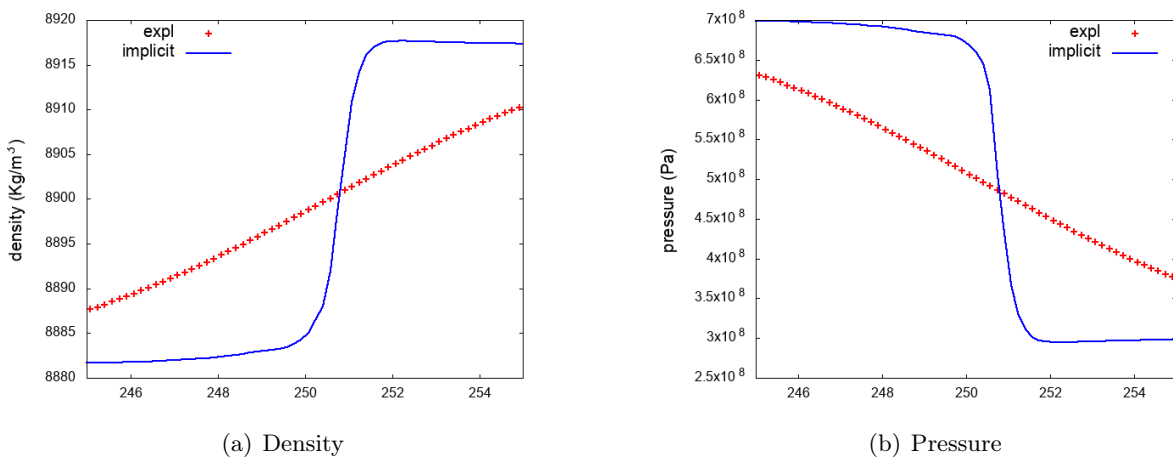(a) Density

(b) Pressure

Figure III.13: *Test 4.1*: density and pressure for long times (4000 grid points on the domain $[0, 500]$).

Fig. III.13 confirm that the implicit scheme is accurately capturing the travelling material wave, instead the explicit scheme is not reproducing this wave anymore.

As a last peculiar case, we approach the *"only acoustic low Mach limit"*. *Test 5* simulates

the deformation of an hyperelastic material characterized by $p_\infty = \mathcal{O}\left(10^8\right) \gg \chi = \mathcal{O}\left(10^5\right)$ (for the material parameters and the initial conditions see Tables III.4 and III.5). These parameters were specifically chosen to obtain this particular regime. The two Mach numbers on the contact wave are then $M \simeq 3 \cdot 10^{-3}$ and $M_\chi \simeq 0.15$. By imposing a tangential velocity on the right, two slow shear waves arise. The material and the shear waves are almost stationary, whereas the longitudinal waves are extremely fast due to the the stiff p_∞ term.

(a) Transverse velocity
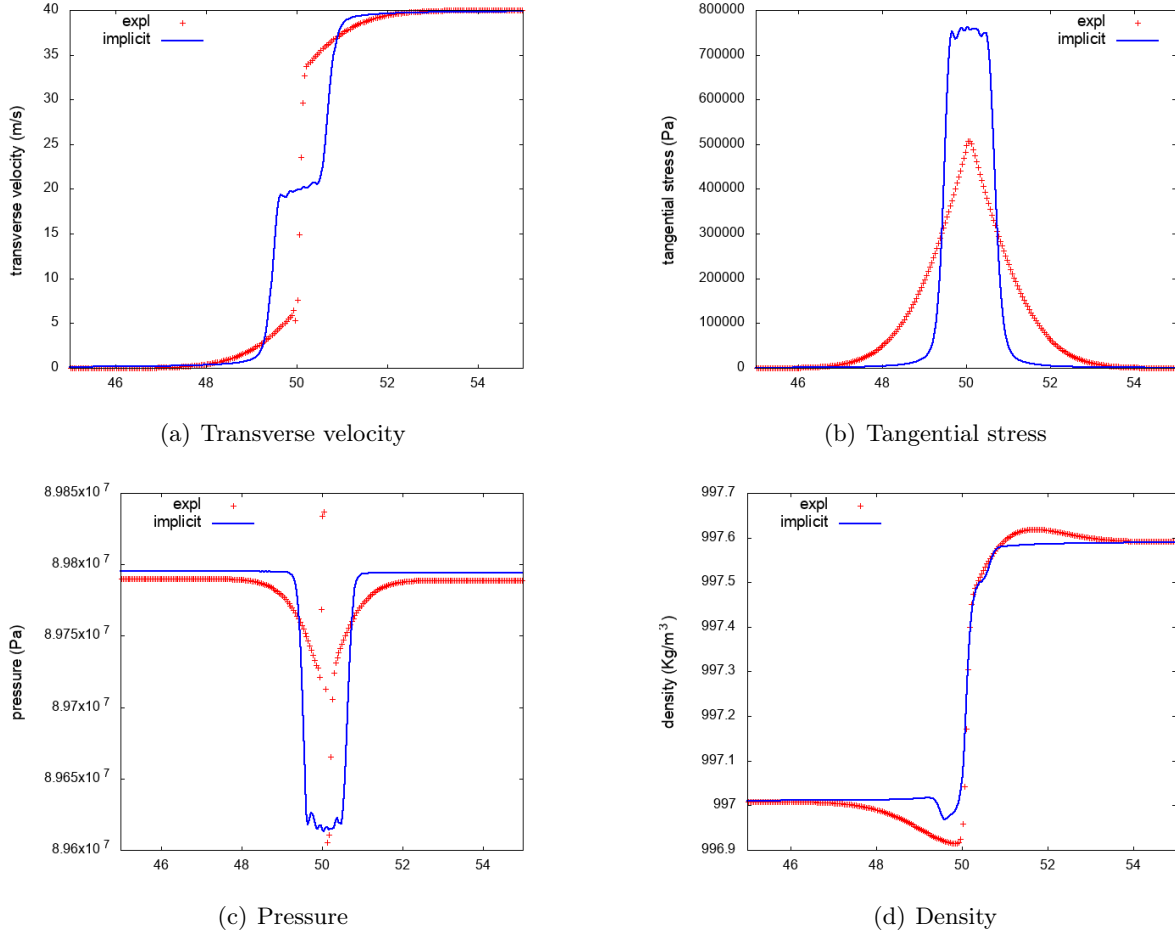
(b) Tangential stress

(c) Pressure

(d) Density

Figure III.14: *Test 5*: transverse velocity, tangential stress, pressure and density (2500 grid points). Zoom on the center of the full domain.

The ability of the implicit scheme in reproducing the slow waves is proven in Fig. III.14. Here we show the main profiles in the central region of the domain. By observing the transverse velocity, the tangential stress and the pressure, it is clear that the implicit scheme is superior in capturing the shape and the speed of the shear waves, even if small amplitude oscillations are present. The explicit scheme, instead, does not resolve them. In the density profile obtained by the implicit scheme, the presence of the three slow waves is recognizable, whereas the explicit scheme does not make a distinction (Fig. III.14(d)).

For the explicit scheme, we employ $\nu_{ac} = 0.4$, giving $\Delta t = 6.89 \cdot 10^{-6}$s on a grid spacing $\Delta x = 4 \cdot 10^{-2}$. The results of the implicit scheme are obtained with a time step $\Delta t = 2.325 \cdot 10^{-4}$s, which is around 300 times bigger than the explicit Δt. A small time step is here needed due to

the presence of three slow waves, which remain very close to each other. In order to limit the oscillations Δt could be further reduced.

III.4   Preliminary conclusions

In this chapter we have proposed a novel all-speed relaxation scheme for the numerical simulation of compressible materials. The scheme has proved to be accurate for one dimensional cases, in the computation of steady state solutions and also in the approximation of material waves for different Mach regimes. The correct numerical viscosity is recovered at all speeds, as shown by the nozzle flow tests.

The scheme is simple and general, since it is the same for compressible flows in gases, liquids and hyperelastic solids, without any need of adaptation to a specific state law. The tests on the propagation of material waves have shown a consistent improvement in the approximation of material waves at slow velocity with respect to standard explicit-upwind schemes. The two low Mach limits introduced in Chapter II have been successfully solved.

In the next chapter, the scheme is extended for the solution of two dimensional problems on Cartesian grids.

Chapter IV

Low Mach flows in two dimensions

In this chapter we extend the all-speed relaxation scheme to the solution of two dimensional problems. The extension is performed by adopting the multi-dimensional Jin-Xin relaxation, which relaxes the non-linear fluxes "direction by direction". The all-speed scheme is asymptotic preserving (AP) and a proof of this property is proposed.

Two dimensional simulations require a large amount of computational time, due to the implicit time integration and to the increased number of variables introduced with the relaxation. As a first step, we decrese the computational time by proposing a parallelization of the code. The parallel code is implemented in the MPI paradigm, with a partitioning of the computational domain into sub-domains. Every sub-domain is assigned to one of the threads involved in the computation. Our code is based on the Bitpit library [50] for mesh generation and on the PETSc library [11] for the numerical linear algebra algorithms. The two dimensional scheme is validated on Cartesian uniform grids, with the classical Gresho vortex test case and with the approximation of travelling material waves.

In the second part of the chapter, the discretization is carried out on adaptive octree meshes. The number of degrees of freedom is consistently reduced where smooth behaviour is expected, but a local increase of accuracy is possible in specific areas of interest. The adaptive mesh refinement (AMR) is pivoted by an entropy based criterion [104, 105], which is here adapted to compute the numerical entropy of the relaxation all-speed scheme.

IV.1   Two dimensional all-speed relaxation scheme

We extend to two dimensional problems the all-speed relaxation scheme introduced in Chapter III and in [1, 2]. The scheme is built for the solution of the full two dimensional Eulerian model introduced in Chapter I with the system of conservation laws (I.21) closed by the hyperelastic state law (I.24).

We consider the compact formulation in $m = 2$ dimensions (I.33)-(I.34) where we have the vector of conservative variables $\boldsymbol{\psi} \in \mathbb{R}^n$ and the fluxes along the two directions $\mathbf{F}(\boldsymbol{\psi})$, $\mathbf{G}(\boldsymbol{\psi}) \in \mathbb{R}^n$, with $n = 8$. This is a $n \times n$ system with $(x, t) \in (\mathbb{R}^2, \mathbb{R}^+)$, where $x = (x_1, x_2)$ as in the notation introduced in Chapter I. In order to construct the corresponding relaxation system, two vectors containing the relaxation variables $\mathbf{v} \in \mathbb{R}^n$ and $\mathbf{w} \in \mathbb{R}^n$ in the two directions are introduced, in order to linearize the fluxes $\mathbf{F}(\boldsymbol{\psi})$ and $\mathbf{G}(\boldsymbol{\psi})$ respectively. The resulting system

of dimension $n \times (m+1)$ reads as follows:

$$
\begin{cases}
\partial_t \boldsymbol{\psi} + \partial_{x_1} \mathbf{v} + \partial_{x_2} \mathbf{w} = 0 \\
\partial_t \mathbf{v} + \mathbf{A}_1 \partial_{x_1} \boldsymbol{\psi} = \dfrac{1}{\eta} \left(\mathbf{F} \left(\boldsymbol{\psi} \right) - \mathbf{v} \right) \\
\partial_t \mathbf{w} + \mathbf{A}_2 \partial_{x_2} \boldsymbol{\psi} = \dfrac{1}{\eta} \left(\mathbf{G} \left(\boldsymbol{\psi} \right) - \mathbf{w} \right).
\end{cases}
\tag{IV.1}
$$

We remark that the relaxation is performed *direction by direction*, namely the equations on the relaxation variables are one dimensional problems.

The relaxation matrices $\mathbf{A}_1$ and $\mathbf{A}_2$ are chosen with the subcharacteristic condition [86, 129]:

$$
\mathbf{A}_1 - \mathbf{F}' \left(\boldsymbol{\psi} \right)^2 \geq 0 \text{ and } \mathbf{A}_2 - \mathbf{G}' \left(\boldsymbol{\psi} \right)^2 \geq 0 \quad \forall \boldsymbol{\psi}.
\tag{IV.2}
$$

More details on the construction of the relaxation matrices are given in Chapter III.

IV.1.1   Implicit time discretization

We propose a fully implicit relaxation scheme, with the goal of getting rid of acoustic CFL constraints. The linearity of the spatial derivatives in the relaxation system allows for a straightforward use of implicit time discretizations. The implicit time discretization at first order is a simple backward Euler scheme and reads:

$$
\begin{cases}
\dfrac{\boldsymbol{\psi}^{n+1} - \boldsymbol{\psi}^n}{\Delta t} + \partial_{x_1} \mathbf{v}^{n+1} + \partial_{x_2} \mathbf{w}^{n+1} = 0 \\
\dfrac{\mathbf{v}^{n+1} - \mathbf{v}^n}{\Delta t} + \mathbf{A}_1 \partial_{x_1} \boldsymbol{\psi}^{n+1} = \dfrac{1}{\eta} \left(\mathbf{F} \left(\boldsymbol{\psi}^{n+1} \right) - \mathbf{v}^{n+1} \right) \\
\dfrac{\mathbf{w}^{n+1} - \mathbf{w}^n}{\Delta t} + \mathbf{A}_2 \partial_{x_2} \boldsymbol{\psi}^{n+1} = \dfrac{1}{\eta} \left(\mathbf{G} \left(\boldsymbol{\psi}^{n+1} \right) - \mathbf{w}^{n+1} \right)
\end{cases}
\tag{IV.3}
$$

As in in the 1D version of the scheme, the non-linear fluxes $\mathbf{F} \left(\boldsymbol{\psi} \right)$ and $\mathbf{G} \left(\boldsymbol{\psi} \right)$ are solved with one iteration of the Newton's method. The resulting approximation consists in the following Taylor expansions:

$$
\begin{aligned}
\mathbf{F} \left(\boldsymbol{\psi}^{n+1} \right) &\simeq \mathbf{F} \left(\boldsymbol{\psi}^n \right) + \mathbf{F}' \left(\boldsymbol{\psi}^n \right) \left(\boldsymbol{\psi}^{n+1} - \boldsymbol{\psi}^n \right) \\
\mathbf{G} \left(\boldsymbol{\psi}^{n+1} \right) &\simeq \mathbf{G} \left(\boldsymbol{\psi}^n \right) + \mathbf{G}' \left(\boldsymbol{\psi}^n \right) \left(\boldsymbol{\psi}^{n+1} - \boldsymbol{\psi}^n \right).
\end{aligned}
\tag{IV.4}
$$

$\mathbf{F}' \left(\boldsymbol{\psi}^n \right)$ and $\mathbf{G}' \left(\boldsymbol{\psi}^n \right)$ are the Jacobian of the fluxes in the two directions and can be computed

analytically. Here we report the analytical formulation of the jacobians:

$$
\mathbf{F'}(\boldsymbol{\psi}) =
\begin{bmatrix}
0 & 1 & 0 & 0 \\
-u_1^2 - \sigma^{11}_{,\psi_1} & 2u_1 - \sigma^{11}_{,\psi_2} & -\sigma^{11}_{,\psi_3} & -\sigma^{11}_{,\psi_4} \\
-u_1 u_2 - \sigma^{21}_{,\psi_1} & u_2 - \sigma^{21}_{,\psi_2} & u_1 - \sigma^{21}_{,\psi_3} & -\sigma^{21}_{,\psi_4} \\
-\dfrac{u_1 Y^1_{,1} + u_2 Y^1_{,2}}{\rho} & \dfrac{Y^1_{,1}}{\rho} & \dfrac{Y^1_{,2}}{\rho} & u_1 \\
-\dfrac{u_1 Y^2_{,1} + u_2 Y^2_{,2}}{\rho} & \dfrac{Y^2_{,1}}{\rho} & \dfrac{Y^2_{,2}}{\rho} & 0 \\
0 & 0 & 0 & 0 \\
0 & 0 & 0 & 0 \\
\dfrac{-Eu_1 + \sigma^{11}u_1}{\rho} - u_1\sigma^{11}_{,\psi_1} + \dfrac{\sigma^{21}u_2}{\rho} & \dfrac{E - \sigma^{11}}{\rho} - u_1\sigma^{11}_{,\psi_2} & -u_1\sigma^{11}_{,\psi_3} - \dfrac{\sigma^{21}}{\rho} & -u_1\sigma^{11}_{,\psi_4} - u_2\sigma^{21}_{,\psi_4}
\end{bmatrix}
$$

$$
\begin{bmatrix}
0 & 0 & 0 & 0 \\
-\sigma^{11}_{,\psi_5} & -\sigma^{11}_{,\psi_6} & -\sigma^{11}_{,\psi_7} & -\sigma^{11}_{,\psi_8} \\
-\sigma^{21}_{,\psi_5} & -\sigma^{21}_{,\psi_6} & -\sigma^{21}_{,\psi_7} & 0 \\
0 & u_2 & 0 & 0 \\
u_1 & 0 & u_2 & 0 \\
0 & 0 & 0 & 0 \\
0 & 0 & 0 & 0 \\
-u_1\sigma^{11}_{,\psi_5} - u_2\sigma^{21}_{,\psi_5} & -u_1\sigma^{11}_{,\psi_6} - u_2\sigma^{21}_{,\psi_6} & -u_1\sigma^{11}_{,\psi_7} - u_2\sigma^{21}_{,\psi_7} & \left(1 - \sigma^{11}_{,\psi_8}\right)u_1
\end{bmatrix}
\tag{IV.5}
$$

$$
\mathbf{G'}(\boldsymbol{\psi}) =
\begin{bmatrix}
0 & 0 & 1 & 0 \\
-u_1 u_2 - \sigma^{12}_{,\psi_1} & u_2 - \sigma^{12}_{,\psi_2} & u_1 - \sigma^{12}_{,\psi_3} & -\sigma^{12}_{,\psi_4} \\
-u_2^2 - \sigma^{22}_{,\psi_1} & -\sigma^{22}_{,\psi_2} & 2u_2 - \sigma^{22}_{,\psi_3} & -\sigma^{22}_{,\psi_4} \\
0 & 0 & 0 & 0 \\
0 & 0 & 0 & 0 \\
-\dfrac{u_1 Y^1_{,1} + u_2 Y^1_{,2}}{\rho} & \dfrac{Y^1_{,1}}{\rho} & \dfrac{Y^1_{,2}}{\rho} & u_1 \\
-\dfrac{u_1 Y^2_{,1} + u_2 Y^2_{,2}}{\rho} & \dfrac{Y^2_{,1}}{\rho} & \dfrac{Y^2_{,2}}{\rho} & 0 \\
\dfrac{-Eu_2 + \sigma^{22}u_2}{\rho} - u_2\sigma^{22}_{,\psi_1} + \dfrac{\sigma^{12}u_1}{\rho} & -u_2\sigma^{22}_{,\psi_2} - \dfrac{\sigma^{12}}{\rho} & \dfrac{E - \sigma^{22}}{\rho} - u_2\sigma^{22}_{,\psi_3} & -u_2\sigma^{22}_{,\psi_4} - u_1\sigma^{12}_{,\psi_4}
\end{bmatrix}
$$

$$
\begin{bmatrix}
0 & 0 & 0 & 0 \\
-\sigma^{12}_{,\psi_5} & -\sigma^{12}_{,\psi_6} & -\sigma^{12}_{,\psi_7} & 0 \\
-\sigma^{22}_{,\psi_5} & -\sigma^{22}_{,\psi_6} & -\sigma^{22}_{,\psi_7} & -\sigma^{22}_{,\psi_8} \\
0 & 0 & 0 & 0 \\
0 & 0 & 0 & 0 \\
0 & u_2 & 0 & 0 \\
u_1 & 0 & u_2 & 0 \\
-u_2\sigma^{22}_{,\psi_5} - u_1\sigma^{12}_{,\psi_5} & -u_2\sigma^{22}_{,\psi_6} - u_1\sigma^{12}_{,\psi_6} & -u_2\sigma^{22}_{,\psi_7} - u_1\sigma^{12}_{,\psi_7} & \left(1 - \sigma^{22}_{,\psi_8}\right)u_2
\end{bmatrix},
\tag{IV.6}
$$

where $\sigma^{jk}_{,\psi_i}$ stands for the derivative of the ^{jk}, $j, k = 1, 2$ component of the tensor σ with respect to the conservative variable ψ_i, $i = 1, ..8$. Tensor σ is symmetric and it has been defined in

relation (I.32). Its elements have the following expressions

$$\begin{cases} \sigma^{11} = -p + \dfrac{2\chi}{J}\left(\overline{B}^{11} - \dfrac{tr\overline{B}}{2}\right) \\ \sigma^{22} = -p + \dfrac{2\chi}{J}\left(\overline{B}^{22} - \dfrac{tr\overline{B}}{2}\right) \\ \sigma^{12} = \sigma^{21} = \dfrac{2\chi}{J}\overline{B}^{12} = \dfrac{2\chi}{J}\overline{B}^{21} = -2\chi\left(Y_{,1}^2 Y_{,2}^2 + Y_{,2}^1 Y_{,1}^1\right). \end{cases}$$

In order to derive the analytical expressions of the two jacobians (IV.5)-(IV.6), the pressure can be re-written as function of the energy as follows

$$p = -\gamma p_\infty + (\gamma - 1)\left(\rho e - \frac{1}{2}\rho|\mathbf{u}|^2 - \chi\left(tr\overline{B} - 2\right)\right).$$

IV.1.2 Spatial discretization

System (IV.1) is discretized with finite volumes on a Cartesian mesh. Let Δx_l be the grid spacing in the x_l direction and $\Omega_{i,j}$ the control volume centered in the node $(i\Delta x_1, j\Delta x_2)$. The semi-discretization in space for system (IV.1) reads

$$\begin{cases} \partial_t \psi_{ij} + \dfrac{\mathbf{v}_{i+1/2,j} - \mathbf{v}_{i-1/2,j}}{\Delta x_1} + \dfrac{\mathbf{w}_{i,j+1/2} - \mathbf{w}_{i,j-1/2}}{\Delta x_2} = 0 \\ \partial_t \mathbf{v}_{ij} + \mathbf{A}_1 \dfrac{\psi_{i+1/2,j} - \psi_{i-1/2,j}}{\Delta x_1} = \dfrac{1}{\eta}\left(\mathbf{F}\left(\psi_{ij}\right) - \mathbf{v}_{ij}\right) \\ \partial_t \mathbf{w}_{ij} + \mathbf{A}_2 \dfrac{\psi_{i,j+1/2} - \psi_{i,j-1/2}}{\Delta x_2} = \dfrac{1}{\eta}\left(\mathbf{G}\left(\psi_{ij}\right) - \mathbf{w}_{ij}\right). \end{cases} \tag{IV.7}$$

The variables at the cell interfaces $x_{i+1/2,j}$ and $x_{i,j+1/2}$ inside (IV.7) have to be computed with an "ad hoc" stable scheme.

The hybrid spatial discretization (III.17) is introduced also in the 2D relaxation scheme, through a convex combination of upwind and centered schemes. As in one dimension, the upwind part is useful in order to prevent spurious oscillations developing when the Mach number is high whereas the centered part is necessary to moderate the numerical viscosity when the Mach number approaches zero. The convex combination is based on the local Mach number of the specific flow and its translation to 2D spatial discretizations is straightforward, yielding for a generic variable h

$$h_{i+1/2,j} = f\left(M_{loc}\right)\left(h_{i+1/2,j}\right)_{upw} + \left(1 - f\left(M_{loc}\right)\right)\left(h_{i+1/2,j}\right)_{cent}, \tag{IV.8}$$

where the function of the local Mach number $f\left(M_{loc}\right)$ is defined as in 1D (see Section III.2.2.2) and M_{loc} is computed at the previous time step at the numerical interface $x_{i+1/2,j}$.

The interface values along direction x_1 with the centered scheme are computed as follows:

$$\begin{cases} \left(\psi_{i+1/2,j}\right)_{cent} = \frac{1}{2}\left(\psi_{i+1,j} + \psi_{ij}\right) \\ \left(\mathbf{v}_{i+1/2,j}\right)_{cent} = \frac{1}{2}\left(\mathbf{v}_{i+1,j} + \mathbf{v}_{ij}\right). \end{cases} \tag{IV.9}$$

The upwind scheme is built as in [71], getting the following expression for the interface values along the direction x_1:

$$\begin{cases} \left(\psi_{i+1/2,j}\right)_{upw} = \frac{1}{2}\left(\psi_{i+1,j} + \psi_{ij}\right) - \frac{1}{2}\mathbf{A}_1^{-1/2}\left(\mathbf{v}_{i+1,j} - \mathbf{v}_{ij}\right) \\ \left(\mathbf{v}_{i+1/2,j}\right)_{upw} = \frac{1}{2}\left(\mathbf{v}_{i+1,j} + \mathbf{v}_{ij}\right) - \frac{1}{2}\mathbf{A}_1^{1/2}\left(\psi_{i+1,j} - \psi_{ij}\right). \end{cases} \tag{IV.10}$$

Discretizations (IV.9) and (IV.10) are thus plugged into the convex combination (IV.8) along both directions. By using the implicit time discretization (IV.3), we obtain the full 2D all-speed scheme

$$
\begin{cases}
\dfrac{\boldsymbol{\psi}_{ij}^{n+1} - \boldsymbol{\psi}_{ij}^n}{\Delta t} + \dfrac{1}{2\Delta x_1}\left(\mathbf{v}_{i+1,j}^{n+1} - \mathbf{v}_{i-1,j}^{n+1}\right) - \dfrac{f\left(M_{loc}\right)\mathbf{A}_1^{1/2}}{2\Delta x_1}\left(\boldsymbol{\psi}_{i+1,j}^{n+1} - 2\boldsymbol{\psi}_{ij}^{n+1} + \boldsymbol{\psi}_{i-1,j}^{n+1}\right) + \\[2ex]
\qquad \dfrac{1}{2\Delta x_2}\left(\mathbf{w}_{i,j+1}^{n+1} - \mathbf{w}_{i,j-1}^{n+1}\right) - \dfrac{f\left(M_{loc}\right)\mathbf{A}_2^{1/2}}{2\Delta x_2}\left(\boldsymbol{\psi}_{i,j+1}^{n+1} - 2\boldsymbol{\psi}_{ij}^{n+1} + \boldsymbol{\psi}_{i,j-1}^{n+1}\right) = 0 \\[2ex]
\dfrac{\mathbf{v}_{ij}^{n+1} - \mathbf{v}_{ij}^n}{\Delta t} + \dfrac{\mathbf{A}_1}{2\Delta x_1}\left(\boldsymbol{\psi}_{i+1,j}^{n+1} - \boldsymbol{\psi}_{i-1,j}^{n+1}\right) - \dfrac{f\left(M_{loc}\right)\mathbf{A_1}^{1/2}}{2\Delta x_1}\left(\mathbf{v}_{i+1,j}^{n+1} - 2\mathbf{v}_{ij}^{n+1} + \mathbf{v}_{i-1,j}^{n+1}\right) = \\[2ex]
\qquad\qquad\qquad\qquad\qquad\qquad \dfrac{1}{\eta}\left(\mathbf{F}\left(\boldsymbol{\psi}_{ij}^{n+1}\right) - \mathbf{v}_{ij}^{n+1}\right) \\[2ex]
\dfrac{\mathbf{w}_{ij}^{n+1} - \mathbf{w}_{ij}^n}{\Delta t} + \dfrac{\mathbf{A}_2}{2\Delta x_2}\left(\boldsymbol{\psi}_{i,j+1}^{n+1} - \boldsymbol{\psi}_{j,i-1}^{n+1}\right) - \dfrac{f\left(M_{loc}\right)\mathbf{A}_2^{1/2}}{2\Delta x_2}\left(\mathbf{w}_{i,j+1}^{n+1} - 2\mathbf{w}_{ij}^{n+1} + \mathbf{w}_{i,j-1}^{n+1}\right) = \\[2ex]
\qquad\qquad\qquad\qquad\qquad\qquad \dfrac{1}{\eta}\left(\mathbf{G}\left(\boldsymbol{\psi}_{ij}^{n+1}\right) - \mathbf{w}_{ij}^{n+1}\right).
\end{cases}
\tag{IV.11}
$$

IV.2 The asymptotic preserving property

The Asymptotic-Preserving (AP) property is defined as follows. Let us consider a continuous physical model $\mathcal{S}_M$ which involves a perturbation parameter M. In the case we are interested in, M is the acoustic Mach number and $\mathcal{S}_M$ represents the compressible Euler system (I.6) or the monolithic Eulerian model (I.21). The perturbation parameter can range from $M \simeq \mathcal{O}\left(1\right)$ to $M \ll 1$ values. We suppose that there exists a reduced system $\mathcal{S}_0$, which is the limit system of $\mathcal{S}_M$ as $M \to 0$. For example, in the case of $\mathcal{S}_M$ being the compressible Euler system, $\mathcal{S}_0$ is the incompressible one.

Then, let $\mathcal{S}_M^\Delta$ be a numerical scheme providing a consistent discretization of $\mathcal{S}_M$, with discrete time and space steps $\Delta = (\Delta t, \Delta x)$. The scheme $\mathcal{S}_M^\Delta$ is said to be AP if the two following properties are verified:

1. its stability condition is independent of M, namely the time step Δt does not depend on the Mach number of the flow;

2. as M goes to zero, there exists the limit discrete $\mathcal{S}_0^\Delta$, which provides a consistent discretization of the continuous limit system $\mathcal{S}_0$.

In Section II.3.2, a brief revision of some AP methods proposed in literature is carried out. Our aim is to show that also the implicit relaxation scheme (IV.11) is asymptotic preserving, as recently demonstrated in [3]. The scheme is fully implicit, thus unconditionally stable, as shown in Section III.2.3. Consequently, property 1 is satisfied, i. e. the stability constraint does not depend on the Mach number. We now need to show that property 2 is respected. This can be done by writing the limit discrete scheme $\mathcal{S}_0^\Delta$ as $M \to 0$ of the implicit relaxation scheme and by showing that it is consistent with the continuous limit model $\mathcal{S}_0$. For the sake of simplicity, we focus on the compressible Euler system (I.7)-(I.8), thus we consider $\mathcal{S}_0$ to be the incompressible Euler system.

In what follows, we begin with the non-dimensionalization of the scheme and then we carry out the analysis of its asymptotics. We expose the reasoning on the time semi-discrete scheme (IV.3) for readability. The extension to the full time and space discretization is straightforward.

IV.2.1 Non-dimensional implicit relaxation scheme

In deriving the non-dimensional implicit relaxation scheme, we adopt the same notation of Section II.1.1, with the non-dimensional variables (II.1). Here, we also have to scale the relaxation variables $\mathbf{v}$ and $\mathbf{w}$, which have the same physical dimensions of the fluxes $\mathbf{F}(\boldsymbol{\psi})$ and $\mathbf{G}(\boldsymbol{\psi})$ defined in (I.8). In this spirit, the following scaling is performed:

$$
\begin{aligned}
\widehat{v_1} &= \frac{v_1}{\rho^* u^*}, & \widehat{w_1} &= \frac{w_1}{\rho^* u^*}, \\[2mm]
\widehat{v_2} &= \frac{v_2}{\rho^* (c^*)^2}, & \widehat{w_2} &= \frac{w_2}{\rho^* (u^*)^2}, \\[2mm]
\widehat{v_3} &= \frac{v_3}{\rho^* (u^*)^2}, & \widehat{w_3} &= \frac{w_3}{\rho^* (c^*)^2}, \\[2mm]
\widehat{v_4} &= \frac{v_4}{\rho^* (c^*)^2 u^*}, & \widehat{w_4} &= \frac{w_4}{\rho^* (c^*)^2 u^*},
\end{aligned}
\tag{IV.12}
$$

where we have made the arbitrary choice to scale v_2 and w_3 considering the pressure as predominant and thus using the speed of sound.

We substitute definitions (II.1) and (IV.12) inside the semi-discrete relaxation scheme (IV.3), getting the following non-dimensional formulation (we omit from now on the subscript $\widehat{\cdot}$ for simplicity of notation):

1. the non-dimensional conservation of mass reads

$$
\begin{cases}
\rho^{n+1} - \rho^n + \Delta t \left(\partial_x v_1^{n+1} + \partial_y w_1^{n+1} \right) = 0 \\[2mm]
v_1^{n+1} - v_1^n + a_1 \Delta t \partial_x \rho^{n+1} = \dfrac{\Delta t}{\eta} \left((\rho u_1)^{n+1} - v_1^{n+1} \right) \\[2mm]
w_1^{n+1} - w_1^n + a_1 \Delta t \partial_y \rho^{n+1} = \dfrac{\Delta t}{\eta} \left((\rho u_2)^{n+1} - w_1^{n+1} \right).
\end{cases}
\tag{IV.13}
$$

We can rewrite this in a compact formulation, setting $\mathbf{z}_1 = [v_1, w_1]^T$. We get

$$
\begin{cases}
\rho^{n+1} - \rho^n + \Delta t \nabla \cdot \mathbf{z}_1 = 0 \\[2mm]
\mathbf{z}_1^{n+1} - \mathbf{z}_1^n + a_1 \Delta t \nabla \rho^{n+1} = \dfrac{\Delta t}{\eta} \left((\rho \mathbf{u})^{n+1} - \mathbf{z}_1^{n+1} \right).
\end{cases}
$$

2. the non-dimensional conservation of momentum is given by the two parts:

$$
\begin{cases}
(\rho u_1)^{n+1} - (\rho u_1)^n + \Delta t \left(\dfrac{\partial_x v_2^{n+1}}{M^2} + \partial_y w_2^{n+1} \right) = 0 \\[2mm]
\dfrac{v_2^{n+1} - v_2^n}{M^2} + a_2 \Delta t \partial_x (\rho u_1)^{n+1} = \dfrac{\Delta t}{\eta} \left((\rho u_1^2)^{n+1} + \dfrac{p^{n+1}}{M^2} - \dfrac{v_2^{n+1}}{M^2} \right) \\[2mm]
w_2^{n+1} - w_2^n + a_2 \Delta t \partial_y (\rho u_1)^{n+1} = \dfrac{\Delta t}{\eta} \left((\rho u_1 u_2)^{n+1} - w_2^{n+1} \right)
\end{cases}
\tag{IV.14}
$$

$$\begin{cases} (\rho u_2)^{n+1} - (\rho u_2)^n + \Delta t \left(\partial_x v_3^{n+1} + \dfrac{\partial_y w_3^{n+1}}{M^2} \right) = 0 \\ v_3^{n+1} - v_3^n + a_3 \Delta t \partial_x (\rho u_2)^{n+1} = \dfrac{\Delta t}{\eta} \left((\rho u_1 u_2)^{n+1} - v_3^{n+1} \right) \\ \dfrac{w_3^{n+1} - w_3^n}{M^2} + a_3 \Delta t \partial_x (\rho u_2)^{n+1} = \dfrac{\Delta t}{\eta} \left((\rho u_2^2)^{n+1} + \dfrac{p^{n+1}}{M^2} - \dfrac{w_3^{n+1}}{M^2} \right). \end{cases} \qquad \text{(IV.15)}$$

If the vectors $\mathbf{z}_2 = [v_2, w_2]^T$ and $\mathbf{z}_3 = [v_3, w_3]^T$ are introduced, we immediately see that their components cannot be scaled in the same way, since one depends on the sound speed and the other one on the material velocity.

3. the non-dimensional conservation of energy is given by

$$\begin{cases} (\rho e)^{n+1} - (\rho e)^n + \Delta t \left(\partial_x v_4^{n+1} + \partial_y w_4^{n+1} \right) = 0 \\ v_4^{n+1} - v_4^n + a_4 \Delta t \partial_x (\rho e)^{n+1} = \dfrac{\Delta t}{\eta} \left(\left((\rho e)^{n+1} + p^{n+1} \right) u_1^{n+1} - v_4^{n+1} \right) \\ w_4^{n+1} - w_4^n + a_4 \Delta t \partial_y (\rho e)^{n+1} = \dfrac{\Delta t}{\eta} \left(\left((\rho e)^{n+1} + p^{n+1} \right) u_2^{n+1} - w_4^{n+1} \right) \end{cases} \qquad \text{(IV.16)}$$

with the scaled state law

$$p^{n+1} = (\gamma - 1) \left((\rho e)^{n+1} - \dfrac{M^2}{2} \rho^{n+1} |\mathbf{u}|^{n+1} \right). \qquad \text{(IV.17)}$$

Introducing $\mathbf{z}_4 = [v_4, w_4]^T$, we get the compact form

$$\begin{cases} (\rho e)^{n+1} - (\rho e)^n + \Delta t \nabla \cdot \mathbf{z}_4 = 0 \\ \mathbf{z}_4^{n+1} - \mathbf{z}_4^n + a_4 \Delta t \nabla (\rho e)^{n+1} = \dfrac{\Delta t}{\eta} \left(\left((\rho e)^{n+1} + p^{n+1} \right) \mathbf{u}^{n+1} - \mathbf{z}_4^{n+1} \right). \end{cases}$$

IV.2.2 Asymptotics of the implicit relaxation scheme

In the spirit of studying the low Mach number asymptotics, we can now develop all scaled variables, i. e. both conservative and relaxation variables, in powers of the Mach number, as done in relations (II.9). Moreover, since we are dealing with a relaxation scheme, relaxation variables may be expanded also in powers of η, as in a Chapman-Enksog expansion (see Section III.1). Let us begin with the expansion of the scaled relaxation variable v_1 in powers of the Mach number, keeping η fixed. This reads as follows

$$(v_1)^{n+1} = \left(v_1^{0,0} \right)^{n+1} + M \left(v_1^{1,0} \right)^{n+1} + M^2 \left(v_1^{2,0} \right)^{n+1} + \mathcal{O} \left(M^3 \right). \qquad \text{(IV.18)}$$

Here we have introduced the notation with two superscripts, the first one indicating the order in the power of M and the second one indicating the order in the power of η (which is here always equal to zero, since we are keeping it fixed). Terms of zero-th order (superscript $\cdot^{0,0}$) represent the zero Mach number limit in the zero relaxation limit. For all other variables, the same expansion in powers of M can be performed.

We now expand relaxation variables in powers of η by keeping the Mach number fixed, in the following way

$$(v_1)^{n+1} = \left(v_1^{0,0} \right)^{n+1} + \eta \left(v_1^{0,1} \right)^{n+1} + \mathcal{O} \left(\eta^2 \right), \qquad \text{(IV.19)}$$

where terms of zero-th order (superscript $\cdot^{0,0}$) represent the zero relaxation limit. One could then combine expansions (IV.18) and (IV.19) and write the following full expansion for all relaxation variables $\mathbf{v}$ and $\mathbf{w}$ in powers of both M and η. The expansion for v_1 is the following

$$
\begin{aligned}
(v_1)^{n+1} = \left(v_1^{0,0}\right)^{n+1} &+ \eta \left(v_1^{0,1}\right)^{n+1} + M \left(\left(v_1^{1,0}\right)^{n+1} + \eta \left(v_1^{1,1}\right)^{n+1} + \mathcal{O}\left(\eta^2\right)\right) \\
&+ M^2 \left(\left(v_1^{2,0}\right)^{n+1} + \eta \left(v_1^{2,1}\right)^{n+1} + \mathcal{O}\left(\eta^2\right)\right) + \mathcal{O}\left(M^3\right).
\end{aligned}
\tag{IV.20}
$$

We need to preserve the low Mach behaviour in the expansions introduced above, hence it is required that $\eta \ll M$. This is necessary to recover the correct zero relaxation limit (i. e. $\mathbf{v} = \mathbf{F}\left(\boldsymbol{\psi}\right) + \mathcal{O}\left(\eta\right)$ and $\mathbf{w} = \mathbf{G}\left(\boldsymbol{\psi}\right) + \mathcal{O}\left(\eta\right)$ as presented in Section III.1) also in the case of $M \to 0$. More precisely, we require that $\eta < M^2$, in order to preserve the terms of order $\mathcal{O}\left(M^2\right)$ and $\mathcal{O}\left(M\right)$. These terms cannot be canceled if we want to analyze the low Mach regime.

We begin our analysis by substituting expansion (IV.18) in power of M inside the scaled relaxation scheme (IV.13)-(IV.14)-(IV.15)-(IV.16) and by collecting terms with equal power of M. We get the following results:

1. **order $\mathcal{O}_M\left(1/M^2\right)$:**

$$
\begin{cases}
\partial_x \left(v_2^{0,0}\right)^{n+1} = 0 \\
\left(v_2^{0,0}\right)^{n+1} - \left(v_2^{0,0}\right)^n = \dfrac{\Delta t}{\eta} \left(p_0^{n+1} - \left(v_2^{0,0}\right)^{n+1}\right) \\
\partial_y \left(w_3^{0,0}\right)^{n+1} = 0 \\
\left(w_3^{0,0}\right)^{n+1} - \left(w_3^{0,0}\right)^n = \dfrac{\Delta t}{\eta} \left(p_0^{n+1} - \left(w_3^{0,0}\right)^{n+1}\right).
\end{cases}
\tag{IV.21}
$$

At this point, we substitute into these equations the expansion (IV.19) in powers of η:

$$
\begin{cases}
\partial_x \left(\left(v_2^{0,0}\right)^{n+1} + \eta \left(v_2^{0,1}\right)^{n+1}\right) = 0 \\
\left(v_2^{0,0}\right)^{n+1} + \eta \left(v_2^{0,1}\right)^{n+1} - \left(v_2^{0,0}\right)^n - \eta \left(v_2^{0,1}\right)^n = \dfrac{\Delta t}{\eta} \left(p_0^{n+1} - \left(v_2^{0,0}\right)^{n+1} - \eta \left(v_2^{0,1}\right)^{n+1}\right).
\end{cases}
$$

The same holds for variable w_3. We are interested in the zero relaxation limit $\eta \to 0$, hence we have to collect the terms $\mathcal{O}_\eta\left(1/\eta\right)$ in the last equation, to obtain $\left(v_2^{0,0}\right)^{n+1} = p_0^{n+1}$ and $\left(w_3^{0,0}\right)^{n+1} = p_0^{n+1}$. These expressions are then used inside (IV.21), getting:

$$
\begin{cases}
\left(v_2^{0,0}\right)^{n+1} = p_0^{n+1} \\
\partial_x p_0^{n+1} = 0
\end{cases}
\qquad
\begin{cases}
\left(w_3^{0,0}\right)^{n+1} = p_0^{n+1} \\
\partial_y p_0^{n+1} = 0.
\end{cases}
$$

It is clear then that $\nabla p_0^{n+1} = 0$ is respected.

2. **order $\mathcal{O}_M \left(1/M \right)$:**

$$\begin{cases} \partial_x \left(v_2^{1,0} \right)^{n+1} = 0 \\ \left(v_2^{1,0} \right)^{n+1} - \left(v_2^{1,0} \right)^n = \dfrac{\Delta t}{\eta} \left(p_1^{n+1} - \left(v_2^{1,0} \right)^{n+1} \right) \\ \partial_y \left(w_3^{1,0} \right)^{n+1} = 0 \\ \left(w_3^{1,0} \right)^{n+1} - \left(w_3^1 \right)^n = \dfrac{\Delta t}{\eta} \left(p_1^{n+1} - \left(w_3^{1,0} \right)^{n+1} \right). \end{cases} \tag{IV.22}$$

As above, we insert here the expansion (IV.19) in powers of η, having:

$$\begin{cases} \partial_x \left(\left(v_2^{1,0} \right)^{n+1} + \eta \left(v_2^{1,1} \right)^{n+1} \right) = 0 \\ \left(v_2^{1,0} \right)^{n+1} + \eta \left(v_2^{1,1} \right)^{n+1} - \left(v_2^{1,0} \right)^n - \eta \left(v_2^{1,1} \right)^n = \dfrac{\Delta t}{\eta} \left(p_1^{n+1} - \left(v_2^{1,0} \right)^{n+1} - \eta \left(v_2^{1,1} \right)^{n+1} \right). \end{cases}$$

Taking the zero relaxation limit $\eta \to 0$ and collecting the terms $\mathcal{O}_\eta \left(1/\eta \right)$, we obtain the following relations:

$$\begin{cases} \left(v_2^{1,0} \right)^{n+1} = p_1^{n+1} \\ \partial_x p_1^{n+1} = 0 \end{cases} \qquad \begin{cases} \left(w_3^{1,0} \right)^{n+1} = p_1^{n+1} \\ \partial_y p_1^{n+1} = 0. \end{cases}$$

This means that $\nabla p_1^{n+1} = 0$ is respected.

3. **order $\mathcal{O}_M \left(1 \right)$:**

- for the conservation of mass we have:

$$\begin{cases} \rho_0^{n+1} - \rho_0^n + \Delta t \nabla \cdot \left(\mathbf{z}_1^{0,0} \right)^{n+1} = 0 \\ \left(\mathbf{z}_1^{0,0} \right)^{n+1} - \left(\mathbf{z}_1^{0,0} \right)^n + a_1 \Delta t \nabla \rho_0^{n+1} = \dfrac{\Delta t}{\eta} \left(\left(\rho \mathbf{u} \right)_0^{n+1} - \left(\mathbf{z}_1^{0,0} \right)^{n+1} \right). \end{cases} \tag{IV.23}$$

Once again, we can substitute into this system the expansion in powers of η and take the zero relaxation limit by collecting terms of order $\mathcal{O}_\eta \left(1/\eta \right)$, yielding

$$\begin{cases} \left(\mathbf{z}_1^{0,0} \right)^{n+1} = \left(\rho \mathbf{u} \right)_0^{n+1} \\ \rho_0^{n+1} - \rho_0^n + \Delta t \nabla \cdot \left(\rho \mathbf{u} \right)_0^{n+1} = 0. \end{cases} \tag{IV.24}$$

- for the conservation of momentum we have:

$$\begin{cases} \left(\rho u_1 \right)_0^{n+1} - \left(\rho u_1 \right)_0^n + \Delta t \left(\partial_x \left(v_2^{2,0} \right)^{n+1} + \partial_y \left(w_2^{0,0} \right)^{n+1} \right) = 0 \\ \left(v_2^{2,0} \right)^{n+1} - \left(v_2^{2,0} \right)^n + a_2 \Delta t \partial_x \left(\rho u_1 \right)_0^{n+1} = \dfrac{\Delta t}{\eta} \left(\left(\rho u_1^2 \right)_0^{n+1} + p_2^{n+1} - \left(v_2^{2,0} \right)^{n+1} \right) \\ \left(w_2^{0,0} \right)^{n+1} - \left(w_2^{0,0} \right)^n + a_2 \Delta t \partial_y \left(\rho u_1 \right)_0^{n+1} = \dfrac{\Delta t}{\eta} \left(\left(\rho u_1 u_2 \right)_0^{n+1} - \left(w_2^{0,0} \right)^{n+1} \right), \end{cases} \tag{IV.25}$$

$$\begin{cases} (\rho u_2)_0^{n+1} - (\rho u_2)_0^n + \Delta t \left(\partial_x \left(v_3^{0,0} \right)^{n+1} + \partial_y \left(w_3^{2,0} \right)^{n+1} \right) = 0 \\ \left(v_3^{0,0} \right)^{n+1} - \left(v_3^{0,0} \right)^n + a_3 \Delta t \partial_x (\rho u_2)_0^{n+1} = \frac{\Delta t}{\eta} \left((\rho u_1 u_2)_0^{n+1} - \left(v_3^{0,0} \right)^{n+1} \right) \\ \left(w_3^{2,0} \right)^{n+1} + \left(w_3^{2,0} \right)^n + a_3 \Delta t \partial_x (\rho u_2)_0^{n+1} = \frac{\Delta t}{\eta} \left(\left(\rho u_2^{2,0} \right)_0^{n+1} + p_2^{n+1} - \left(w_3^{2,0} \right)^{n+1} \right) \end{cases}$$
$$(\text{IV}.26)$$

In the expansion in powers of η, terms of order $\mathcal{O}_\eta \left(1/\eta \right)$ give expressions for $\left(v_2^{2,0} \right)^{n+1}$, $\left(v_3^{0,0} \right)^{n+1}$, $\left(w_2^{0,0} \right)^{n+1}$ and $\left(w_3^{2,0} \right)^{n+1}$. This yields

$$\begin{cases} \left(v_2^{2,0} \right)^{n+1} = \left(\rho u_1^2 \right)_0^{n+1} + p_2^{n+1} \\ \left(w_2^{0,0} \right)^{n+1} = (\rho u_1 u_2)_0^{n+1} \\ \left(v_3^{0,0} \right)^{n+1} = (\rho u_1 u_2)_0^{n+1} , \\ \left(w_3^{2,0} \right)^{n+1} = \left(\rho u_2^2 \right)_0^{n+1} + p_2^{n+1} \\ (\rho \mathbf{u})_0^{n+1} - (\rho \mathbf{u})_0^{n+1} + \Delta t \nabla \cdot (\rho_0 \mathbf{u}_0 \otimes \mathbf{u}_0)^{n+1} + \Delta t \nabla p_2^{n+1} = 0. \end{cases} \quad (\text{IV}.27)$$

- for the conservation of energy we have

$$\begin{cases} (\rho e)_0^{n+1} - (\rho e)_0^n + \Delta t \nabla \cdot \left(\mathbf{z}_4^{0,0} \right)^{n+1} = 0 \\ \left(\mathbf{z}_4^{0,0} \right)^{n+1} - \left(\mathbf{z}_4^{0,0} \right)^n + a_4 \Delta t \nabla (\rho e)_0^{n+1} = \frac{\Delta t}{\eta} \left(\left((\rho e)_0^{n+1} + p_0^{n+1} \right) \mathbf{u}_0^{n+1} - \left(\mathbf{z}_4^{0,0} \right)^{n+1} \right) . \end{cases}$$
$$(\text{IV}.28)$$

By substituting the expansion in powers of η and by taking the zero relaxation limit, we obtain

$$\begin{cases} \left(\mathbf{z}_4^{0,0} \right)^{n+1} = \left((\rho e)_0^{n+1} + p_0^{n+1} \right) u_0^{n+1} \\ (\rho e)_0^{n+1} - (\rho e)_0^{n+1} + \Delta t \nabla \cdot \left((\rho e)_0^{n+1} + p_0^{n+1} \right) \mathbf{u}_0^{n+1} \right) = 0. \end{cases} \quad (\text{IV}.29)$$

This goes with the $\mathcal{O}_M (1)$ state law

$$p_0^{n+1} = (\gamma - 1) (\rho e)_0^{n+1} . \tag{IV.30}$$

We have thus obtained the discrete limit system $\mathcal{S}_0^\Delta$ (IV.24)-(IV.27)-(IV.29) in the zero relaxation limit, that we report here for the sake of clarity:

$$\begin{cases} \rho_0^{n+1} - \rho_0^n + \Delta t \nabla \cdot (\rho \mathbf{u})_0^{n+1} = 0 \\ (\rho \mathbf{u})_0^{n+1} - (\rho \mathbf{u})_0^{n+1} + \Delta t \nabla \cdot (\rho_0 \mathbf{u}_0 \otimes \mathbf{u}_0)^{n+1} + \Delta t \nabla p_2^{n+1} = 0 \\ (\rho e)_0^{n+1} - (\rho e)_0^{n+1} + \Delta t \nabla \cdot \left((\rho e)_0^{n+1} + p_0^{n+1} \right) \mathbf{u}_0^{n+1} \right) = 0. \end{cases}$$

This system is clearly a consistent discretization of the Euler system in its incompressible limit, derived in (II.12)-(II.13)-(II.14). This means that the scheme is asymptotic preserving. Nevertheless, in what follows, we show that the incompressibility constraint $\nabla \cdot \mathbf{u}_0^{n+1} = 0$ is respected.

From (IV.24) and (IV.27), we get that

$$\begin{cases} \rho_0^{n+1} = \rho_0^n + \mathcal{O} (\Delta t) \\ \mathbf{u}_0^{n+1} = \mathbf{u}_0^n + \mathcal{O} (\Delta t) , \end{cases}$$

$$\tag{IV.31}$$
$$\tag{IV.32}$$

with Δt independent of M, as already stated. We remark that (IV.32) implies that $\nabla \cdot \mathbf{u}_0^{n+1} = \nabla \cdot \mathbf{u}_0^n + \mathcal{O}(\Delta t)$. However, even if $\nabla \cdot \mathbf{u}_0^0 = 0$, summing over all time steps we get that $\nabla \cdot \mathbf{u}_0^{n+1} = \mathcal{O}(1)$, thus we need to show directly that $\nabla \cdot \mathbf{u}_0^{n+1} = 0$, as in the continuous case (see Section II.1.2).

Relations $\nabla p_0^{n+1} = 0$ and $\nabla p_1^{n+1} = 0$ imply that p^{n+1} is constant in space up to fluctuations of order M^2. From the state law (IV.30), we get that also $(\rho e)_0^{n+1}$ is independent of space. We can rewrite the conservation of energy (IV.29) as follows:

$$(\rho e)_0^{n+1} - (\rho e)_0^n + \Delta t \left(\mathbf{u}_0^{n+1} \nabla (\rho e)_0^{n+1} + (\rho e)_0^{n+1} \nabla \cdot \mathbf{u}_0^{n+1} + \mathbf{u}_0^{n+1} \nabla p_0^{n+1} + p_0^{n+1} \nabla \cdot \mathbf{u}_0^{n+1} \right) = 0$$

which becomes, due to the previous considerations on p_0^{n+1} and $(\rho e)_0^{n+1}$:

$$(\rho e)_0^{n+1} - (\rho e)_0^n + \Delta t \left((\rho e)_0^{n+1} + p_0^{n+1} \right) \nabla \cdot \mathbf{u}_0^{n+1} = 0. \tag{IV.33}$$

We now assume that the boundary conditions are such that p_0^{n+1} is independent of n too, i. e. $p_0^{n+1} = p_0^n = ... = p_0^1 = p_0^0$ and the same for p_1^{n+1}. Of course, this means that also the energy is independent of n, namely $(\rho e)_0^{n+1} - (\rho e)_0^n = 0$. Inserting this inside equation (IV.33), one obtains directly the incompressibility constraint $\nabla \cdot \mathbf{u}_0^{n+1} = 0$.

We have thus proved that the Asymptotic Preserving property is respected, providing a consistent discretization of the incompressible model in the low Mach limit and recovering the divergence-free condition on the velocity. The fact that the scheme is AP means that it is consistent with both the compressible and the incompressible regimes.

IV.3 Parallelization on Cartesian grids

We have proposed a novel scheme which is fully implicit and it is based on the relaxation method of Jin and Xin [71]. As shown above, the number of variables of the original 2D conservation system is triplicated in the relaxation system (IV.1), due to relaxation of the fluxes along the two directions. The directional splitting of the proposed numerical method is possible since we choose to discretize the computational domain with Cartesian grids.

In the resulting method, although the equations for the relaxation variables $\mathbf{v}$ and $\mathbf{w}$ are one dimensional problems, a full linear system of large size needs to be solved at the end of the discretization process. Hence, the numerical simulation of compressible flows with the proposed numerical method proves to be computationally demanding.

A natural way to reduce the computational time is parallelization, which is useful also for memory requirements. The C++ code developed in this thesis is parallelized with the MPI paradigm. The parallelization is very efficient on Cartesian grids and this is one of the main reasons for using this type of grids. In general, the parallelization consists in a partitioning of the computational domain (and thus of the degrees of freedom) into sub-domains or blocks, without paying specific attention to the problem to solve. Every sub-domain is assigned to one of the different threads. Each thread executes the same code in its sub-domain and the specific thread does not know what is happening in the neighbouring sub-domains. The advantage of Cartesian grids consists in the fact that the partitioning of the domain is very simple and that the data required for the solution are collocated on the axis directions, due to the directional
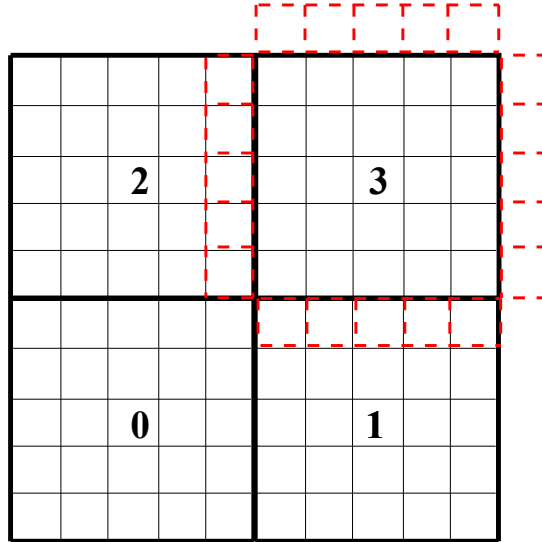
Figure IV.1: Partitioning of a 2D domain among 4 processors and ghost cells to be communicated (in red) for processor 3.

splitting of the scheme. Moreover, the communication of data among the different threads is easily performed.

Going into details, to compute the fluxes at a numerical interface that match with an interface between two sub-domains, it is necessary to communicate the data between threads and to know exactly which data are required. The data that are received from the neighbouring threads are stocked inside ghost cells. In Fig. IV.1 we illustrate an example of a 2D domain which is partitioned into 4 sub-domains. For example, the left cells of processor 3 have to know the state of the cells on the right border of processor 2. If one processor does not have neighbors on one or more sides, then the boundary conditions are applied.

Of course, one need to choose carefully the number of cells that have to be communicated. Actually, the less communications there are, the more the parallelization is effective. The width of the halo of cells to be communicated depends on the width of the stencil of the numerical scheme used to discretize the fluxes.

By considering only one direction of communication, at the interface $x_{i+1/2}$ of cell C_i, we need to compute the all-speed discretization (IV.8), which is calculated with the variables values in the cells C_i and C_{i+1}. For the full computation of the two numerical fluxes at the interfaces of cell C_i we then need a stencil of size 3 $[C_{i-1}, C_i, C_{i+1}]$. If the cell on the border of the block is cell C_i, the processor that owns C_i has to receive the data of cell C_{i+1} from its left neighbor.

IV.3.1 Mesh generation: the uniform case

We here focus on the discretization of the computational domains with uniform Cartesian grids. The grid generation is performed for all two dimensional simulations with the BitPit library [50]. This parallel C++ library is developed with the aim of performing adaptive mesh refinement. This choice is due to the fact that we will implement also a version of our numerical method on adaptive grids, in order to further reduce the computational effort of our simulations (see Section IV.5). As we will describe, the main principle of this technique consists in reducing

the number of grid cells in the regions of the domain where smooth behavior of the solution is expected.

Specifically, the Cartesian mesh of all the simulations of this chapter is generated on a squared domain, with the use of the Bitpit object "VolOctree". This object creates a discretization based on a linear quadtree structure. The detailed description of the AMR technique and of the use of Cartesian hierarchical grids will be detailed in Section IV.5. For the moment we focus on Cartesian uniform grids generated with one call of the VolOctree object and we do not apply progressive refinement.
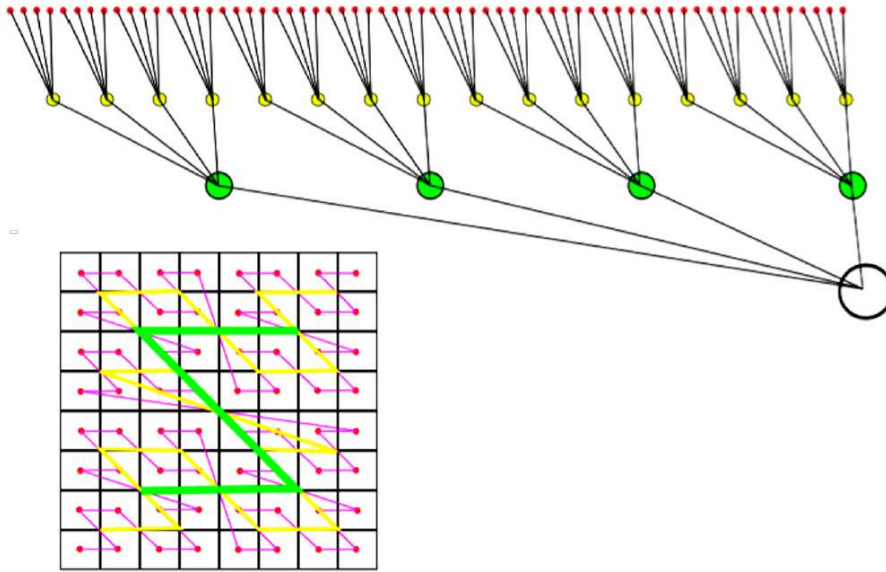
Figure IV.2: Example of a global nested Z-ordering.

We point out that, since we are using the Voloctree object also for the uniform cases, the ordering of the nodes of the computational mesh follows the so-called "Z-curve" introduced by Morton in [94]. The ordering curve is similar to a Z, as one can see in Fig. IV.2. Due to this, the matrices will not have the usual structure of advection problems due to the Z-ordering of the grid cells.

IV.3.2   The linear system

Linearization (IV.4) introduces a coupling among all the equations. Thus, the following linear system has to be solved:

$$\begin{cases} \mathbf{L}\mathbf{\Psi}^{n+1} + \mathbf{M}\mathbf{V}^{n+1} + \mathbf{N}\mathbf{W}^{n+1} = \mathbf{r} \\ \mathbf{P}\mathbf{\Psi}^{n+1} + \mathbf{Q}\mathbf{V}^{n+1} = \mathbf{s_1} \\ \mathbf{T}\mathbf{\Psi}^{n+1} + \mathbf{U}\mathbf{W}^{n+1} = \mathbf{s_2} \end{cases} \tag{IV.34}$$

where $\mathbf{\Psi}^{n+1}$, $\mathbf{V}^{n+1}$ and $\mathbf{W}^{n+1}$ are the vectors containing the grid point values of the conservative and of the relaxation variables respectively. Letting k be the number of grid nodes, we have $\mathbf{\Psi}^{n+1}, \mathbf{V}^{n+1}, \mathbf{W}^{n+1} \in \mathbb{R}^{k \times n}$, where $n = 8$ is the number of the conservative variables of the

2D Eulerian model (I.33)-(I.34). The matrices structure is given by the spatial discretization (IV.8). The linearized implicit stiff source produces additional terms only on the diagonals of the blocks. A constant term proportional to $1/\eta$ appears on the diagonals of $\mathbf{Q}$ and $\mathbf{U}$ and the Taylor expansion introduces terms on the diagonals of the sub-blocks of $\mathbf{P}$ and $\mathbf{T}$.

System (IV.34) can be re-written in a global form as follows

$$\mathbf{C}\boldsymbol{z} = \mathbf{h}, \tag{IV.35}$$

where the vector $\boldsymbol{z} \in \mathbb{R}^{n \times (2+1) \times k}$ collects all conservative and relaxation variables, namely

$$
\begin{aligned}
\boldsymbol{z} =[&\rho_0^{n+1},\ \rho_1^{n+1},\ ...,\ \rho_k^{n+1}, \\
&(\rho u_1)_0^{n+1},\ ...,\ (\rho u_1)_k^{n+1}, \\
&(\rho u_2)_0^{n+1},\ ...,\ (\rho u_2)_k^{n+1}, \\
&... \\
&(\rho e)_0^{n+1},\ ...,\ (\rho e)_k^{n+1}, \\
&(v_1)_0^{n+1},\ ...,\ (v_1)_k^{n+1}, \\
&... \\
&(v_8)_0^{n+1},\ ...,\ (v_8)_k^{n+1}, \\
&(w_1)_0^{n+1},\ ...,\ (w_1)_k^{n+1}, \\
&... \\
&(w_8)_0^{n+1},\ ...,\ (w_8)_k^{n+1}]
\end{aligned}
\tag{IV.36}
$$

The global matrix $\mathbf{C}$ of system (IV.35) has the sparsity structure depicted in Fig. IV.3, which is obtained with the VolOctree mesh in a uniform case. The structure shows that the only "truly-2D" problem is the first part of the relaxation system, namely the equations on the conservative variables. This is clear by looking at block $\mathbf{L}$. Moreover, the Z-ordering for a uniform mesh reduces the distance between the diagonal and the extra-diagonal elements with respect to a standard uniform ordering.

The second and third part of the linear system are 1D problems, because the relaxation is performed "direction-by-direction". The blocks related to the relaxation variables are built with the addition of terms on the diagonals of the sub-blocks of $\mathbf{P}$ and $\mathbf{T}$ of system (IV.34), due to the Taylor expansion.

IV.3.3   Structure in parallel

The linear algebra is dealt with the PETSc library [11] in our code. Bitpit is able to manage the parallelization of the computational mesh, but we also aim at solving the linear system (IV.35) in parallel. PETSc is able to manage the parallel solution of the linear system with iterative solvers, but we need to build a linear system that can be easily solved in a parallel way.

In the relaxation perspective, we are dealing with conservative and relaxation variables that are defined all over the computational domain. The global system (IV.35) can be solved by one process in its global formulation, by recovering the global vector of variables (IV.36). We refer to this as "sequential linear system". A desirable thing is to preserve its structure also when working in parallel with multiple processes.
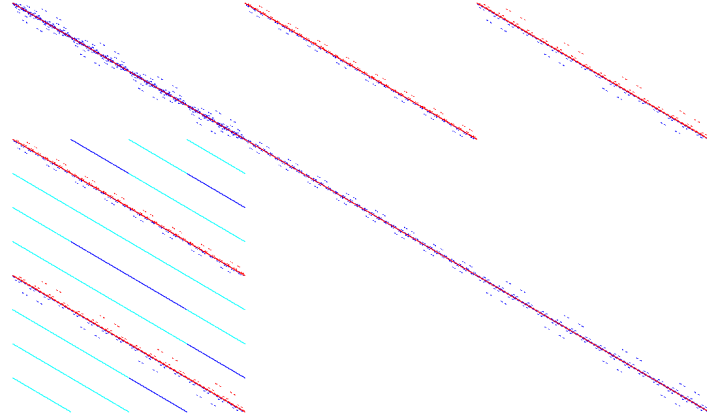
Figure IV.3: Structure of the global matrix **C** on a VolOctree mesh in the uniform case.

Let l be the number of sub-domains assigned to l processes. The global number of nodes is k: we have that the local number of nodes (namely the nodes owned by each process) is $j = k/l$. For simplicity we analyze the case where k is a multiple of l. The idea is then to define l sub-problems and l local vectors of variables, as follows

$$
\begin{aligned}
\boldsymbol{z}_{loc} =[& \rho_0^{n+1},\ \rho_1^{n+1},\ ...,\ \rho_j^{n+1}, \\
& (\rho u_1)_0^{n+1},\ ...,\ (\rho u_1)_j^{n+1}, \\
& (\rho u_2)_0^{n+1},\ ...,\ (\rho u_2)_j^{n+1}, \\
& ... \\
& (\rho e)_0^{n+1},\ ...,\ (\rho e)_j^{n+1}, \\
& (v_1)_0^{n+1},\ ...,\ (v_1)_j^{n+1}, \\
& ... \\
& (v_8)_0^{n+1},\ ...,\ (v_8)_j^{n+1}, \\
& (w_1)_0^{n+1},\ ...,\ (w_1)_j^{n+1}, \\
& ... \\
& (w_8)_0^{n+1},\ ...,\ (w_8)_j^{n+1}]
\end{aligned}
\tag{IV.37}
$$

If $l = 1$ (only one process is present) then we have that $j = k$ and that $\boldsymbol{z}_{loc} \equiv \boldsymbol{z}$. The global matrix **C** of (IV.35) is then created with the PETSc library by using the MATMPIAIJ matrix format, which uses the CRS storage for sparse matrices. Thanks to the variables ordering (IV.37), the matrix partitioning, which is automatically done by PETSc, directly corresponds to the grid partitioning. Due to this, each process has to solve a matrix with the same structure of the global matrix **C**, depicted in Fig. IV.3. To clarify how the PETSc partitioning works, an example is illustrated in Fig. IV.4, where 4 threads are used. For more details we refer to the PETSc manual [11].

For all the numerical results, the linear system is solved by adopting a global flexible GMRES due to the asymmetry of matrix **C**. The default GMRES solver inside PETSc is preconditioned with ILU(0) for the uniprocess case and with the block Jacobi method for the multiprocess case.
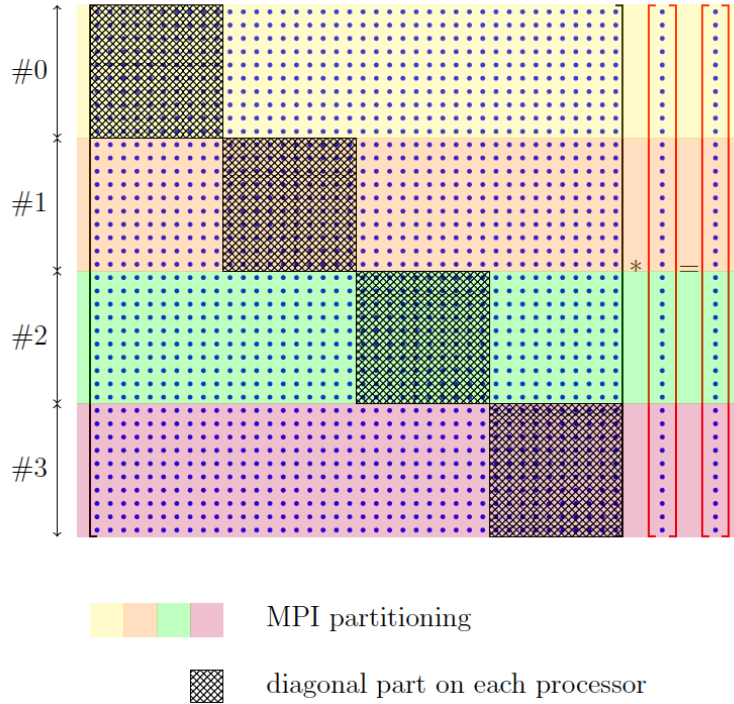
Figure IV.4: Partitioning for the PETSc MATMPIAIJ format with 4 processes.

IV.4 Numerical results on uniform grids

In this section we conduct several validations of the 2D all-speed scheme on uniform grids. As a first step, the behavior of the scheme in the low Mach regime is assessed on the standard Gresho vortex test. Then, some cases of propagating waves inside compressible materials are analyzed.

IV.4.1 The Gresho vortex

We test the two dimesional all-speed scheme (IV.11) on the classical Gresho vortex test case [63, 85]. This vortex is a time-independent solution of the incompressible Euler equations where centrifugal forces are exactly balanced by pressure gradients. In the compressible setting it can be endowed with different maximum Mach numbers. The Gresho vortex is a standard test in literature, used to asses the quality of a numerical scheme in the low Mach regime. As anticipated in Section II.1.2, incompressible solutions should be recovered when setting up an incompressible flow as initial condition for the compressible Euler equations. Moreover, the scheme should recover pressure fluctuations that scale with the square of the Mach number of the flow.

A rotating vortex is positioned at the center $(0.5, 0.5)$ of the computational domain $[0, 1] \times [0, 1]$. The initial conditions are specified in terms of the radial distance $r = \sqrt{(x - 0.5)^2 + (y - 0.5)^2}$ in the form

$$\begin{cases} \rho(x, y, 0) = 1 \\ u_1(x, y, 0) = -u_\phi(r) \sin\phi \\ u_2(x, y, 0) = u_\phi(r) \cos\phi \end{cases}$$
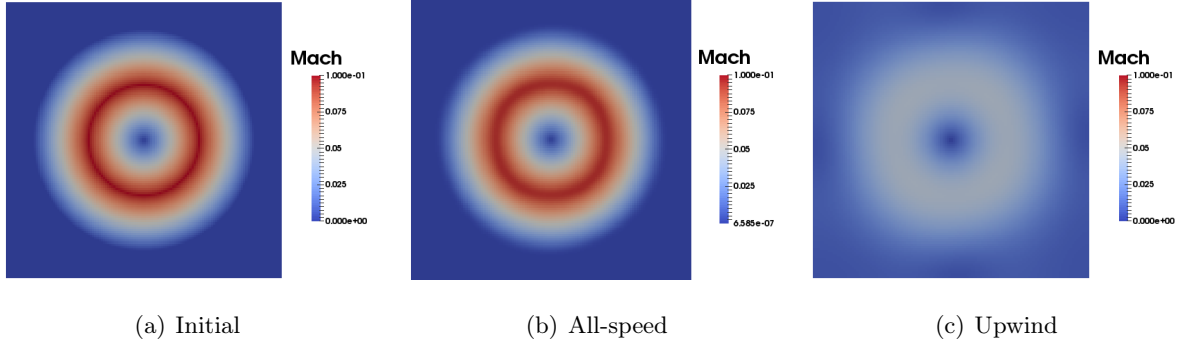
(a) Initial (b) All-speed (c) Upwind

Figure IV.5: Gresho vortex with $M_{max} = 10^{-1}$: initial condition and results at time $t = 1$ with the all-speed implicit scheme and with a upwind spatial discretization.

The rotation of the vortex is initiated by imposing a simple angular velocity distribution of

$$u_\phi(x, y, 0) = \begin{cases} 5r & 0 \leq r \leq 0.2 \\ 2 - 5r & 0.2 \leq r \leq 0.4 \\ 0 & r \geq 0.4 \end{cases}$$

The background pressure is adjusted such that it matches the maximum Mach number M_{max}:

$$p_0 = \frac{\rho(u_\phi)^2_{max}}{(\gamma M^2_{max})} = \frac{\rho}{(\gamma M^2_{max})} \tag{IV.38}$$

since the maximum velocity $(u_\phi)_{max} = 1$, which is reached in $r = 0.2$ The total pressure is then calculated by adding a dynamic pressure which balances the centrifugal forces:

$$p(x, y, 0) = \begin{cases} p_0 + \frac{25}{2}r^2 & 0 \leq r \leq 0.2 \\ p_0 + \frac{25}{2}r^2 + 4(1 - 5r - ln0.2 + lnr) & 0.2 \leq r \leq 0.4 \\ p_0 - 2 + 4ln2 & r \geq 0.4. \end{cases}$$

This pressure profile is arranged to be continuous and differentiable everywhere.

We follow the flow over one full revolution of the vortex in a perfect gas, which is completed at time $t = 1$. In the first case we set $M_{max} = 10^{-1}$: the initial condition in $t = 0$ is presented in Fig. IV.5(a). In Figs. IV.5(b) and IV.5(c), we compare the results obtained with the implicit all-speed scheme (IV.11) and with the implicit scheme where the spatial derivatives are discretized in the upwind manner (IV.10) respectively. We employ a uniform grid of 128×128 points and a material CFL constraint of $\nu_{mat} = 0.2$. A comparison with the initial Mach number distribution shows that the all-speed spatial discretization accurately preserves the shape of the vortex, due to the convex combination of upwind and centered fluxes. Instead, an upwind discretization of the fluxes is too diffusive for the targeted regime and thus the shape of the vortex is lost. We also plot the results obtained after 2 and 3 revolutions of the vortex in Fig. IV.6, confirming that the all-speed scheme is able to recover the correct incompressible solution also after long times.

The results obtained with $M_{max} = 10^{-2}$ and $M_{max} = 10^{-3}$ are reported in Fig. IV.7 (first and second row respectively). We compare the results at $t = 1$, after one full revolution, obtained
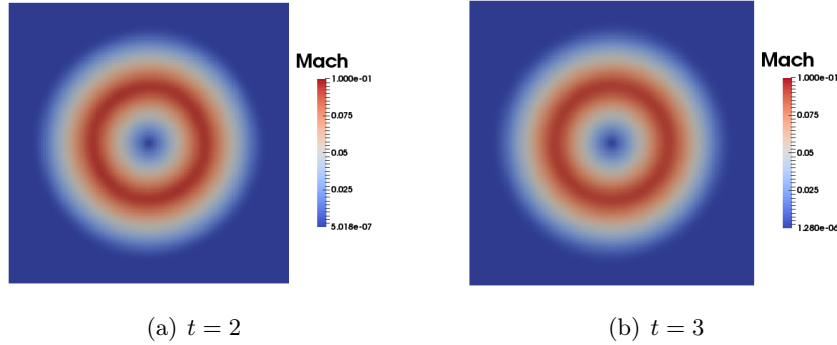
(a) $t = 2$ (b) $t = 3$

Figure IV.6: Gresho vortex with $M_{max} = 10^{-1}$: results at time $t = 2$ and $t = 3$ with the all-speed implicit scheme.

	$M_{max} = 10^{-1}$	$M_{max} = 10^{-2}$	$M_{max} = 10^{-3}$
explicit-upwind	0.652	0.355	0.273
all-speed	0.985	0.987	0.984

Table IV.1: Total kinetic energy $E_{kin,tot}$ $(t = 1)$ after one full revolution of the Gresho vortex relative to its initial value $E_{kin,tot}$ $(t = 0)$ for different maximum Mach numbers.

with the all-speed implicit scheme and with the upwind discretization (IV.10). It is evident that the upwind discretization of the fluxes provides an excessive numerical viscosity, which increases as the Mach number gets lower. The shape of the two vortices is completely diffused. On the contrary, the all-speed implicit scheme accurately preserves the initial vortex shape for both cases, besides a small noise probably due to directional splitting.

In Table IV.1, we report the total kinetic energy in the simulation domain at time $t = 1$ relative to the total kinetic energy at time $t = 0$ for the three tests. With the all-speed scheme, the kinetic energy reduces by about 1.5 per cent over one revolution of the vortex in our setup. However, this loss is independent of the Mach number of the flow. This is very much in contrast to conventional upwind spatial discretizations: we can observe in the first line of Table IV.1 that the dissipation rate of kinetic energy of such schemes consistently increases as the Mach number decreases.

We also perform a study on the pressure fluctuations, by computing $p_{fl} = (p_{max} - p_{min}) / p_{max}$ on the same grid at the end of the simulation (time $t = 1$) for different Mach numbers. These results are reported in Table IV.2 and they prove that with the all-speed spatial discretization, the pressure fluctuations scale exactly with M_{max}^2. Thus, the simulated flow is in the incompressible regime as described by the asymptotic analysis in Chapter II (in particular the formulation for the pressure fluctuations is reported in expression (II.16)). This is of course not the case when adopting an upwind spatial discretization, as observed in the first line of Table IV.2.
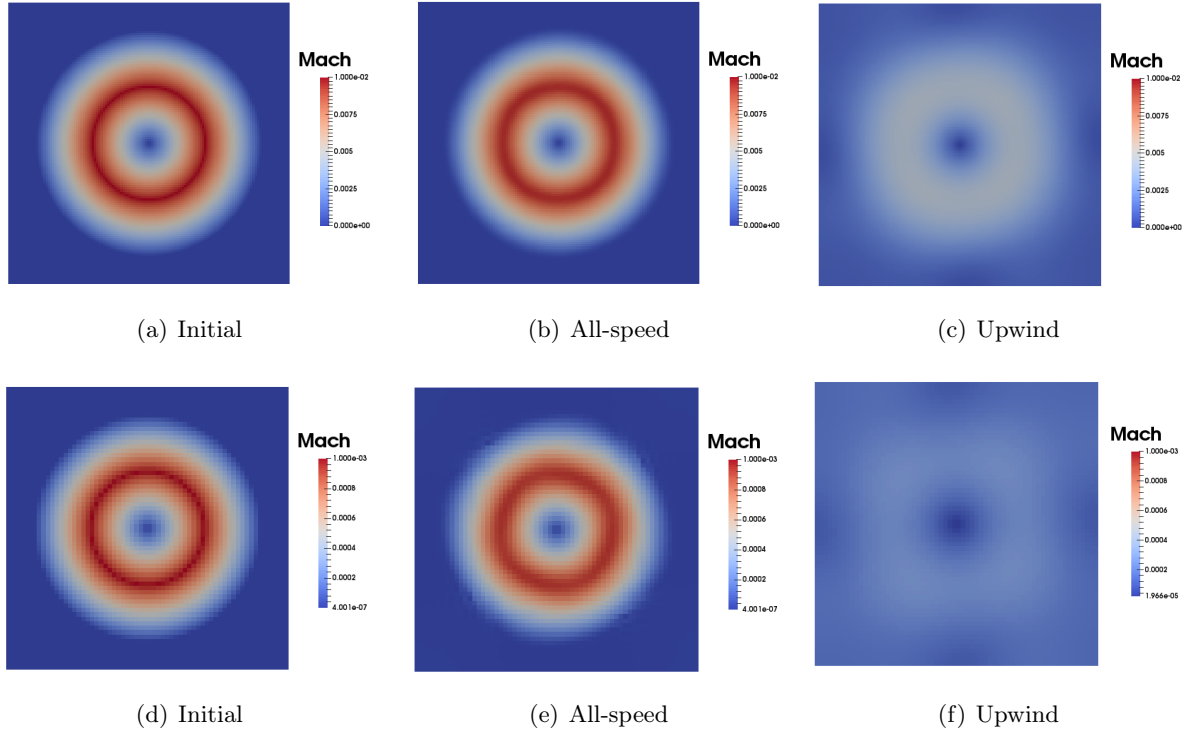
<table>
<tr><td align="center">(a) Initial</td><td align="center">(b) All-speed</td><td align="center">(c) Upwind</td></tr>
</table>

<table>
<tr><td align="center">(d) Initial</td><td align="center">(e) All-speed</td><td align="center">(f) Upwind</td></tr>
</table>

Figure IV.7: Gresho vortex with $M_{max} = 10^{-2}$ (first row) and with $M_{max} = 10^{-3}$ (second row): initial condition and results at time $t = 1$ with the all-speed implicit scheme and with the upwind spatial discretization.

	$M_{max} = 10^{-1}$	$M_{max} = 10^{-2}$	$M_{max} = 10^{-3}$
explicit-upwind	$3.37 \cdot 10^{-3}$	$3.43 \cdot 10^{-5}$	$1.86 \cdot 10^{-6}$
all-speed	$1.02 \cdot 10^{-2}$	$1.06 \cdot 10^{-4}$	$1.15 \cdot 10^{-6}$

Table IV.2: Global pressure fluctuations p_{fl} after one full revolution of the Gresho vortex for different maximum Mach numbers.

IV.4.1.1 Water Gresho vortex

We adapt the standard Gresho vortex test case to a water flow. It suffices to adjust the setting of the background pressure (IV.38) with the stiffened gas state law in the following way:

$$p_0 = \frac{\rho \, (u_\phi)^2_{max}}{(\gamma M^2_{max})} - p_\infty.$$

The density is set to $\rho = 1000 \mathrm{Kg/m}^3$ and the water parameters $\gamma = 4.4$ and $p_\infty = 6.8 \cdot 10^8$ are set inside the state law.

The results for $M_{max} = 10^{-1}$ and $M_{max} = 10^{-2}$ are reported in Figs. IV.8(a) and IV.8(b) at time $t = 1$, when the vortex has completed one rotation. The all-speed scheme is preserving the vortex shape also with the water state law.
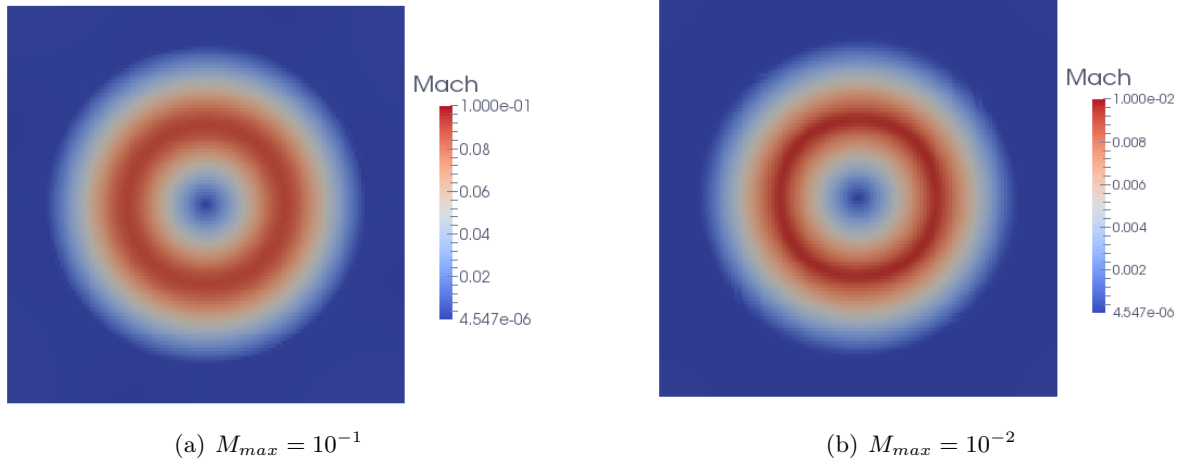
(a) $M_{max} = 10^{-1}$

(b) $M_{max} = 10^{-2}$

Figure IV.8: Water Gresho vortex with $M_{max} = 0.1$ (left) and $M_{max} = 0.01$: results at time $t = 1$ with the all-speed scheme.

IV.4.2 Travelling waves: Sod tubes

We perform some tests on travelling waves, by reproducing some of the tests presented in Chapter III. For tests 1, 2 and 3 the domain is a 1×1 square and it is initially divided into the left and the right region by $y + \frac{0.5}{a}x \leq \frac{0.5}{a}(0.5 + a)$, with $a = 0.06$. For test 4 the domain is a 2×2 square and it is initially divided into the left and the right region by $y + \frac{1}{a}x \leq \frac{1}{a}(1 + a)$, with $a = 0.1$.

Test	material	t_{end} (s)	ρ_L (Kg/m^3)	ρ_R (Kg/m^3)	$u_{1,L}$ (m/s)	$u_{1,R}$ (m/s)	$u_{2,L}$ (m/s)	$u_{2,R}$ (m/s)	p_L (Pa)	p_R (Pa)
1	biatomic gas	0.1644	1	0.125	0	0	0	0	1	0.1
2	biatomic gas	0.25	1	1	0	0.008	0	0	0.4	0.399
3	water	10^{-4}	10^3	10^3	0	15	0	0	10^8	$0.98 \cdot 10^8$
4	copper	$6 \cdot 10^{-5}$	$8.9 \cdot 10^3$	$8.9 \cdot 10^3$	0	0	0	100	10^9	10^5

Table IV.3: Parameters for the material waves test cases: initial state.

Test 1 and *test 2* are tubes filled with a biatomic perfect gas with $\gamma = 1.4$. The first test is a standard Sod shock tube, with Mach number around 0.9 on the contact wave. The second test is a low Mach gas tube, with a Mach number $M \simeq 6 \cdot 10^{-3}$ on the material wave. In the density profiles in Fig. IV.9 the material wave is kept sharp due to the all-speed convex combination.

Test 3 deals with an almost incompressible flow, since the tube is filled with water at almost constant pressure. The Mach number on the material wave is $M \simeq 2.5 \cdot 10^{-3}$. In Fig. IV.10 we compare the result obtained with an upwind spatial discretization and the all-speed spatial discretization. It is evident that with a standard upwind scheme the material wave is diffused.

Test 4 is a copper tube and due to copper intrinsic properties, the acoustic Mach number and the elastic Mach number are of the same order. In particular, in this simulation we have $M \simeq M_\chi \simeq \mathcal{O}\left(10^{-3}\right)$ on the material wave. The results for the pressure and the density profiles are shown in Fig. IV.11 where it is evident that the all-speed scheme is keeping the material wave sharp.
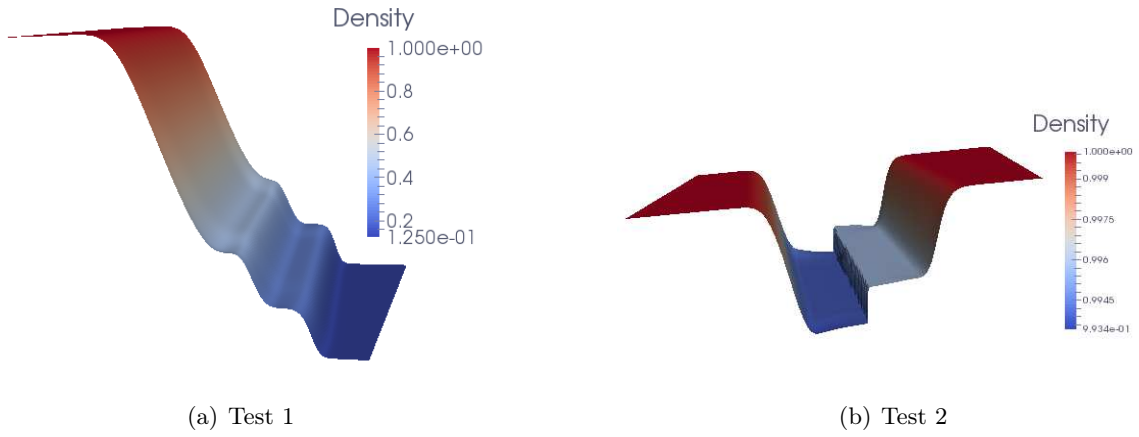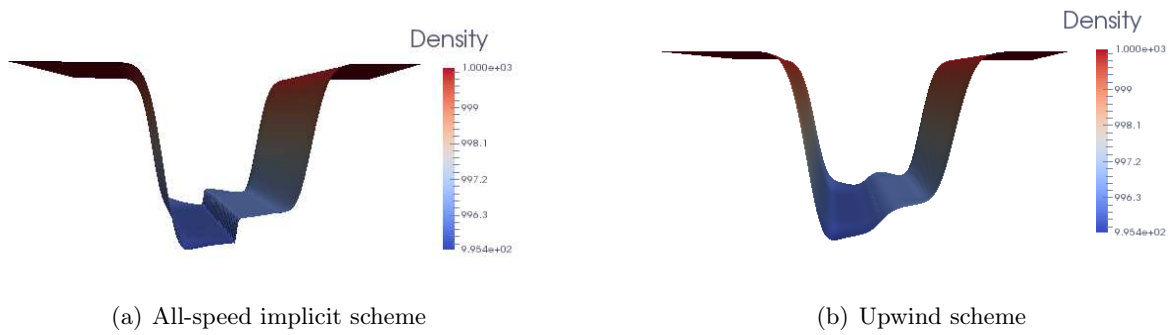
(a) Test 1

(b) Test 2

Figure IV.9: Tests 1 and 2: biatomic gas tubes.

(a) All-speed implicit scheme

(b) Upwind scheme

Figure IV.10: *Test 3*: stiffened gas tube. Comparison between the upwind scheme and the all-speed scheme.
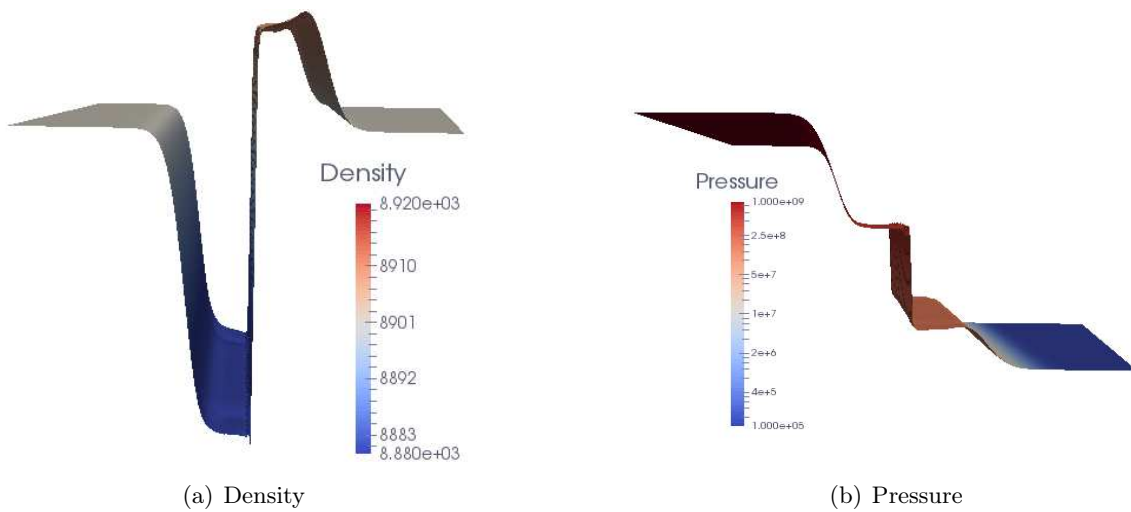

(a) Density

(b) Pressure

Figure IV.11: *Test 4*: copper tube: pressure and density profiles.

IV.5 Adaptive mesh refinement

Modelling multi-scale physical phenomena requires the capability of describing geometrical features of different sizes and strong variations in a small portion of the computational domain. In order to reduce the computational costs, the discretization of the solution can be done by using non-conforming hierarchical meshes, as anticipated in Section IV.3. Specifically, the adpative mesh refinement (AMR) techinque consists in adapting the accuracy of the solution within certain regions of interest in a dynamic fashion, during the time the solution is being calculated [17]. Octree-meshes allow a strong reduction of the number of degrees of freedom where the problem exhibit smooth behavior and also a strongly localized increase of information in areas needing more accuracy.

In the present work, non-conforming hierarchical meshes are employed to discretize the solution thanks to the Bitpit library. The hierarchical nature of the grid makes mesh generation, adaptivity and partitioning very efficient and with a low-memory footprint.

IV.5.1 Linear octrees and the Bitpit library

Octrees are a hierarchical data structure based on the principle of recursive decomposition of space, which is done into equal parts on every level. Each internal node has exactly four children (quadtree) for 2D problems, and eight children (octree) for 3D problems. Here we focus on quadtree meshes, that are defined in a square, as can be observed in Fig. IV.12. As anticipated above, we base the generation of the Cartesian mesh on the library Bitpit, where the data structure is based on a linear quadtree [57], namely only the leafs of the tree structure are stored. This linear data structure is easily dispatched to a distributed memory architecture and in Bitpit parallel communications are limited to only the first layer of neighboring cells. As detailed in Section IV.3, this constraint is perfectly in line with the stencil needed by our numerical scheme.
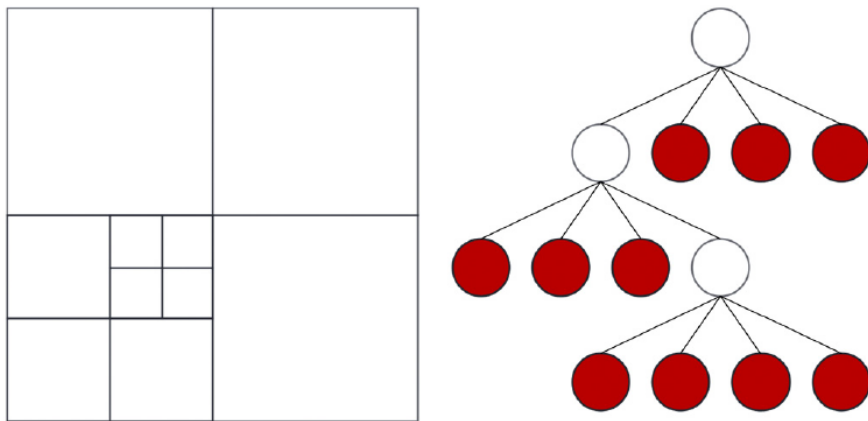

Figure IV.12: Decomposition of a squared domain and corresponding quadtree.

We report a brief description of the data structure, more details can be found in [108, 107]. In the linear quadtree structure, every cell may be the parent of four children. The root cell is the base of the tree and it usually represents the entire domain before the discretization. The

level of a cell is defined starting from zero for the root cell and by adding one every time a group of descendant children is appended. Hierarchical grids are defined graded (or balanced) if the levels of all neighboring cells do not differ by more than one, allowing for a gradual refinement by increments of two.

The quadtree data structure in Bitpit is based on the following requirements:

1. efficient access to neighboring cells

2. efficient access to cell positions and their levels

3. efficient access to stored data

To this end, a Z-order index is assigned to every cell (see Fig. IV.2).

IV.5.2   Refinement criteria

In literature, several techniques have been exploited in order to decide where to locally refine or coarsen the mesh. Most of them are based on the use of local error indicators, such as, for example, discrete gradients and discrete curvature [10], interpolation error [18], residuals of the numerical solution [73] or of the entropy [116, 8]. In the present work we adopt the numerical entropy production as our refinement criterion. This was introduced in [104] for central schemes and extended in [105] to unstaggered finite volume schemes of arbitrary order. Our main motivation in choosing the numerical entropy production lies in the fact that this quantity is naturally available for any system of conservation laws with an entropy inequality and in both fluid dynamics and non-linear elasticity it has a well defined physical meaning. Moreover, the entropy production of a scheme scales as the truncation error in the regular regions and its behavior allows to distinguish between contact discontinuities and shocks.

IV.5.2.1   Numerical entropy production

An effective adaptive algorithm has to be driven by an indicator able to provide a robust a posteriori measure of the local error and also to recognize the qualitative structure of the flow, to pivot the grid adaptivity. This indicator is built on the fact that it is well known that solutions of initial value hyperbolic problems may loose their regularity even if the initial data are smooth, developing shock waves. In this case the solution must be understood in the weak sense and the uniqueness of the solution is lost. In order to restore uniqueness, the system must be completed with an entropy inequality, characterizing the unique admissible weak solution. Thus, we will consider hyperbolic systems possessing an entropy-entropy flux pair, that is we assume there exist a convex function $\eta\left(\boldsymbol{\psi}\right)$ and a corresponding entropy flux $\boldsymbol{\zeta}\left(\boldsymbol{\psi}\right)$ which satisfies the compatibility condition $\nabla^{T}\eta J\left(\boldsymbol{\psi}\right) = \nabla^{T}\boldsymbol{\zeta}$ (see [122, 43]). Then it is well known that entropy solutions must satisfy, in the weak sense for all entropies, the entropy inequality

$$\partial_t\eta + \nabla_x \cdot \boldsymbol{\zeta} \leq 0. \tag{IV.39}$$

Then the indicator is constructed by considering the entropy pair $(\eta, \boldsymbol{\zeta})$ and integrating the entropy inequality (IV.39) with the finite volume scheme used to integrate the hyperbolic system we need to solve. Thus in our case we employ a first order implicit scheme for time integration

[3]. Having the entropy flux $\boldsymbol{\zeta} = (\zeta_1, \zeta_2)$, we get then the following numerical entropy production in every cell:

$$S_{ij}^{n+1} = \eta\left(\boldsymbol{\psi}_{ij}^{n+1}\right) - \eta\left(\boldsymbol{\psi}_{ij}^{n}\right) + \frac{\Delta t}{\Delta x_1}\left(\zeta_{1;i+1/2,j}^{n+1} - \zeta_{1;i-1/2,j}^{n+1}\right) + \frac{\Delta t}{\Delta x_2}\left(\zeta_{2;i,j+1/2}^{n+1} - \zeta_{2;i,j-1/2}^{n+1}\right),$$
(IV.40)

where $\zeta_{1;i+1/2,j}$ is the first component of numerical entropy flux. We compute this flux at the interface according to the all-speed scheme we use to integrate our system of conservation laws. Our scheme is equivalent to a Lax-Friedrichs scheme with a numerical viscosity modulated with the Mach number. Thus we have:

$$\zeta_{1;i+1/2,j}^{n+1} = \frac{1}{2}\left(\zeta_{1;i+1,j}^{n+1} + \zeta_{1;i,j}^{n+1}\right) - \frac{\sqrt{a_{max}}f(M_{loc})}{2}\left(\eta_{i+1,j}^{n+1} - \eta_{i,j}^{n+1}\right)$$
(IV.41)

In the numerical experiments, we build the entropy pair on the physical entropy of the Euler system, as follows:

$$\eta(\boldsymbol{\psi}) = -\rho\log\left(\frac{p + p_\infty}{\rho^\gamma}\right), \quad \boldsymbol{\zeta}(\boldsymbol{\psi}) = \eta(\boldsymbol{\psi})\,\mathbf{u}.$$

Puppo and Semplice [105] have shown for one dimensional problems that, if the solution is locally smooth, $S_{ij}^{n+1} = \mathcal{O}(h^r)$ with r equal to the order of the scheme. On the other hand, $S_{ij}^{n+1} = \mathcal{O}(1)$ if there is a contact discontinuity and $S_{ij}^{n+1} = \mathcal{O}(1/h)$ if there is a shock in the considered cell.

IV.5.2.2   AMR algorithm

We start from a uniform coarse grid of $2^d \times 2^d$ grid points. This grid is associated to the minimum level $L_{min} = d$ of the quadtree data structure. At every refinement, each cell of the grid may be replaced by four children, as described in the previous section. Let L_{max} be the maximum refinement level allowed for a grid.

At the end of every time step, the following procedure is implemented:

1. the quantity S_{ij}^n is computed in every cell with scheme (IV.40);

2. if $S_{ij}^n > S_{ref}$ and if the level of refinement of cell C_{ij} does not equal L_{max} then the cell is marked for refinement; this cell is thus split into four children and cell averages in the newly created cells are set by taking the cell average of the "ancestor";

3. if $S_{ij}^n < S_{coa}$ and if the level of refinement of cell C_{ij} does not equal L_{min} then the cell is marked for coarsening; the 4 children are replaced by the ancestor cell and the cell average in the ancestor is set by taking the mean of the cell averages of the four children;

4. the time step Δt is computed with the chosen CFL constraint using the smallest cell size Δx of the grid.

IV.5.3 2D Riemann problems

The code has been tested on two dimensional Riemann problems [78, 114]. The 2D Euler equations of gas-dynamics are solved for a Riemann problem with initial data:

$$
(p, \rho, u_1, u_2)(x, y, t = 0) = \begin{cases} (p_1, \rho_1, u_{1,1}, u_{2,1}), & \text{if } x > 0.5 \text{ and } y > 0.5 \\ (p_2, \rho_2, u_{1,2}, u_{2,2}), & \text{if } x < 0.5 \text{ and } y > 0.5 \\ (p_3, \rho_3, u_{1,3}, u_{2,3}), & \text{if } x < 0.5 \text{ and } y < 0.5 \\ (p_4, \rho_4, u_{1,4}, u_{2,4}), & \text{if } x > 0.5 \text{ and } y < 0.5. \end{cases} \tag{IV.42}
$$

The Riemann problem is classified according to the combination of the four elementary waves used to define it. Let $\overrightarrow{R}$ and $\overrightarrow{S}$ be forward moving rarefaction and shock respectively and let $\overleftarrow{R}$ and $\overleftarrow{S}$ the corresponding backward moving waves. Let $\overrightarrow{C}$ be a contact wave.

IV.5.3.1 Uniform grid

We start by performing some tests on uniform Cartesian grids. All the uniform simulations are carried out with a grid of 256×256 points (namely $L_{min} = L_{max} = 8$) and an acoustic CFL constraint of 0.9.

Acoustic waves

As a first step, we test our scheme on four different configurations involving only acoustic waves, i. e. shocks and/or rarefactions.

Configuration 1. Four forward moving rarefaction waves (isentropic flow): $\overrightarrow{R}_{21}$, $\overrightarrow{R}_{32}$, $\overrightarrow{R}_{34}$, $\overrightarrow{R}_{41}$.

$$
\begin{array}{cc cc}
p_2 = 0.4 & \rho_2 = 0.5197 & p_1 = 1 & \rho_1 = 1 \\
u_{1,2} = -0.7259 & u_{2,2} = 0 & u_{1,1} = 0 & u_{2,1} = 0
\end{array}
$$

$$
\begin{array}{cc cc}
p_3 = 0.0439 & \rho_3 = 0.1072 & p_4 = 0.15 & \rho_4 = 0.2579 \\
u_{1,3} = -0.7259 & u_{2,3} = -1.4045 & u_{1,4} = 0 & u_{2,4} = -1.4045
\end{array}
$$

Configuration 2. Four rarefaction waves (isentropic flow): $\overrightarrow{R}_{21}$, $\overleftarrow{R}_{32}$, $\overleftarrow{R}_{34}$, $\overrightarrow{R}_{41}$.

$$
\begin{array}{cc cc}
p_2 = 0.4 & \rho_2 = 0.5197 & p_1 = 1 & \rho_1 = 1 \\
u_{1,2} = -0.7259 & u_{2,2} = 0 & u_{1,1} = 0 & u_{2,1} = 0
\end{array}
$$

$$
\begin{array}{cc cc}
p_3 = 1 & \rho_3 = 1 & p_4 = 0.4 & \rho_4 = 0.5197 \\
u_{1,3} = -0.7259 & u_{2,3} = -0.7259 & u_{1,4} = 0 & u_{2,4} = -0.7259
\end{array}
$$

(a) configuration 1 ($t = 0.2$)

(b) configuration 2 ($t = 0.2$)

(c) configuration 3 ($t = 0.3$)

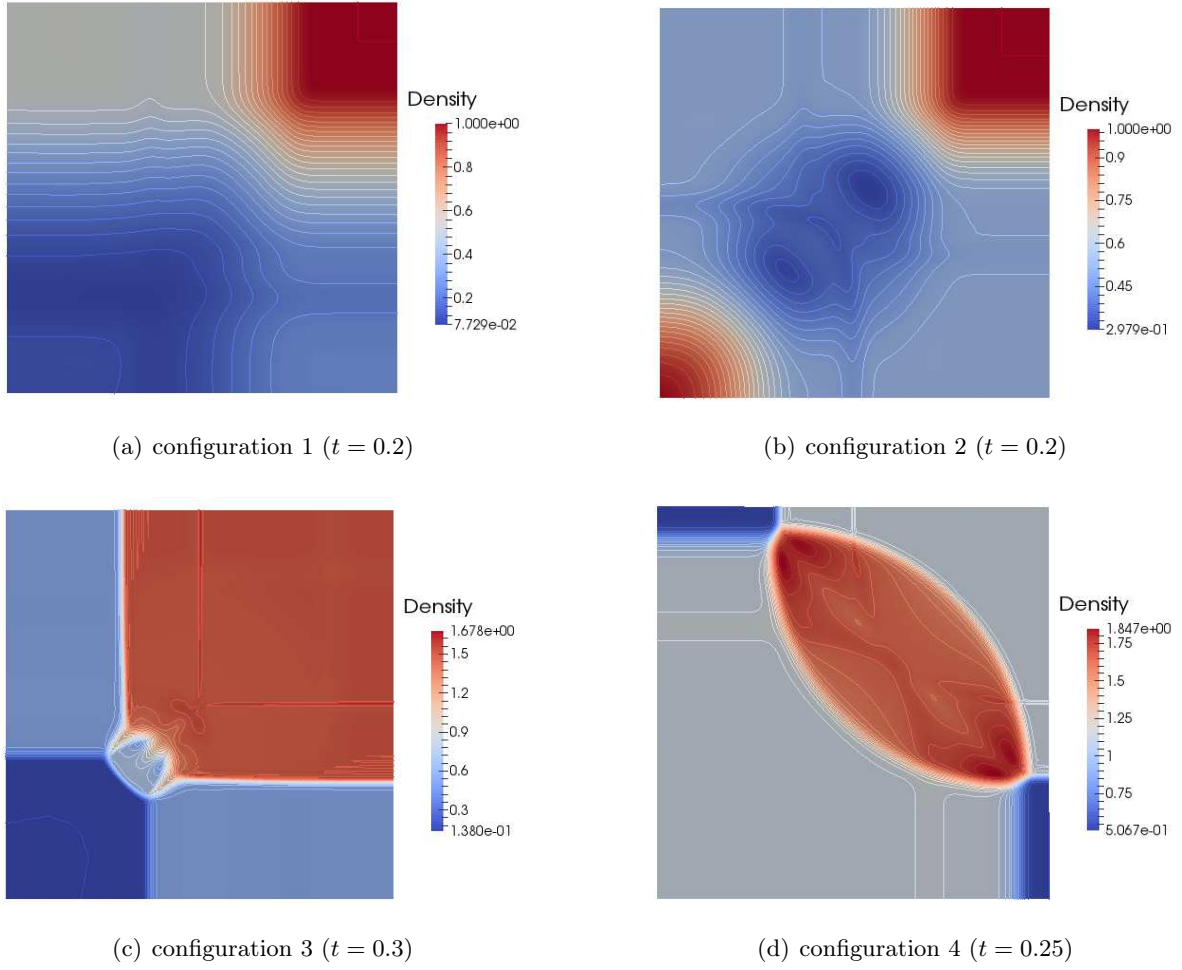(d) configuration 4 ($t = 0.25$)

Figure IV.13: 4 configurations of 2D Riemann problems involving only acoustic waves.

Configuration 3. Four backward moving shocks: $\overleftarrow{S}_{21}$, $\overleftarrow{S}_{32}$, $\overleftarrow{S}_{34}$, $\overleftarrow{S}_{41}$.

$$p_2 = 0.3 \quad \rho_2 = 0.5323 \qquad p_1 = 1.5 \quad \rho_1 = 1.5$$
$$u_{1,2} = 1.206 \quad u_{2,1} = 0 \qquad u_{1,1} = 0 \quad u_{2,1} = 0$$

$$p_3 = 0.029 \quad \rho_3 = 0.138 \qquad p_4 = 0.3 \quad \rho_4 = 0.5323$$
$$u_{1,3} = 1.206 \quad u_{2,3} = 1.206 \qquad u_{1,4} = 0 \quad u_{2,4} = 1.206$$

Configuration 4. Four shocks: $\overleftarrow{S}_{21}$, $\overrightarrow{S}_{32}$, $\overrightarrow{S}_{34}$, $\overleftarrow{S}_{41}$.

$$p_2 = 0.35 \quad \rho_2 = 0.5065 \qquad p_1 = 1.1 \quad \rho_1 = 1.1$$
$$u_{1,2} = 0.8939 \quad u_{2,2} = 0 \qquad u_{1,1} = 0 \quad u_{2,1} = 0$$

$$p_3 = 1.1 \quad \rho_3 = 1.1 \qquad p_4 = 0.35 \quad \rho_4 = 0.5065$$
$$u_{1,3} = 0.8939 \quad u_{2,3} = 0.8939 \qquad u_{1,4} = 0 \quad u_{2,4} = 0.8939$$

In Fig. IV.13 the results for the four configurations are presented. Our scheme is able to accurately reproduce the solution of the Riemann problems. The chosen grid is coarser than the

ones used in [78, 114] and we are anyway able to obtain results that are comparable with the two cited articles.

Problems involving contact waves

Now we test the scheme on two problems where also contact waves occur. For these tests we compare the results obtained with the proposed all-speed scheme (IV.11) and the results obtained with the upwind spatial discretization (IV.10).
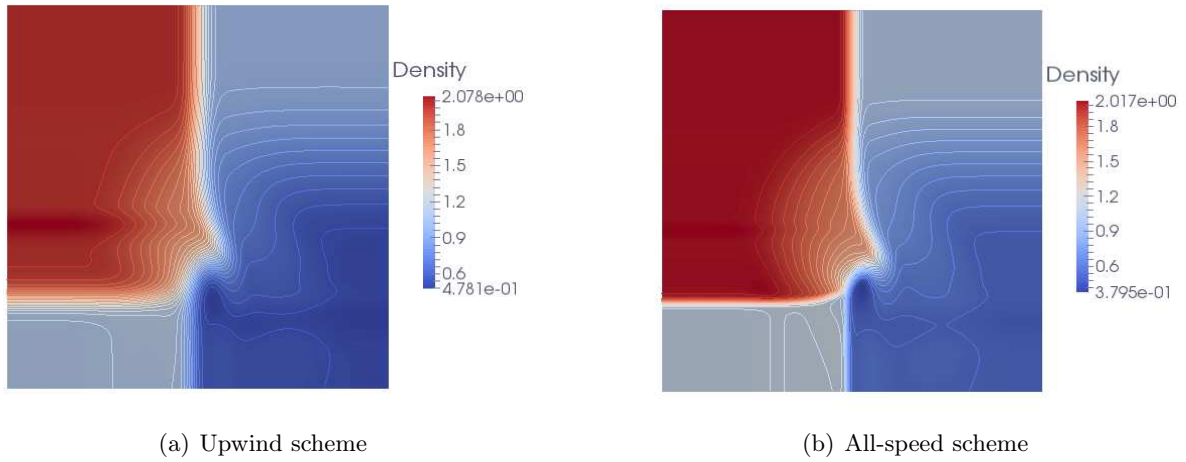

(a) Upwind scheme

(b) All-speed scheme

Figure IV.14: 2D Riemann problem with contact waves $t = 0.3$: comparison between upwind and all-speed spatial discretizations.

Configuration 5. Two contact waves, one left moving shock and one right moving rarefaction: C_{21}, $\overleftarrow{S}_{32}$, C_{34}, $\overrightarrow{R}_{41}$.

$$p_2 = 1 \quad \rho_2 = 2 \quad p_1 = 1. \quad \rho_1 = 1$$
$$u_{1,2} = 0 \quad u_{2,2} = -0.3 \quad u_{1,1} = 0 \quad u_{2,1} = -0.4$$

$$p_3 = 0.4 \quad \rho_3 = 1.0625 \quad p_4 = 0.4 \quad \rho_4 = 0.5197$$
$$u_{1,3} = 0 \quad u_{2,3} = 0.2145 \quad u_{1,4} = 0 \quad u_{2,4} = -1.1259$$

In Fig. IV.14 we plot the density contours lines (30 contours: from 0.53 to 1.98). On the chosen grid of 256×256 points, we employ a material constraint on the time step $\nu_{mat} = 0.3$, which is equivalent for this test to an acoustic constraint $\nu_{ac} = 0.9$. It is evident that the all-speed property helps in keeping sharp the two waves occuring in the bottom left part of the domain. On these two waves (a shock and a contact wave) the Mach number is of the order of $8 \cdot 10^{-3}$. The small vortex in the center is more accurately captured by the all-speed scheme. The vortex is here resolved not as accurately as in [78, 114] because here we are using a less refined grid.

Configuration 6. Two contact waves, one left moving rarefaction and one left moving shock:

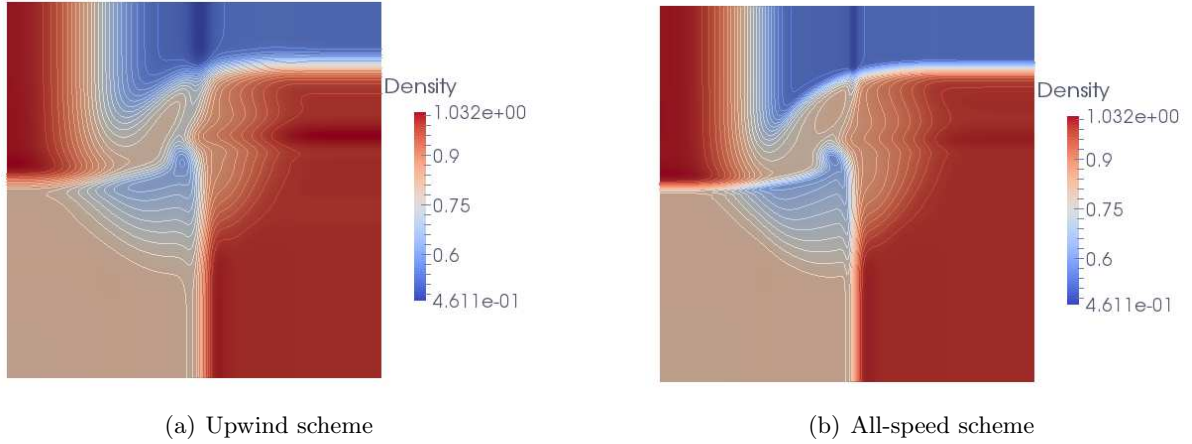(a) Upwind scheme

(b) All-speed scheme

Figure IV.15: 2D Riemann problem with contact waves $t = 0.2$: comparison between upwind and all-speed discretizations.

$\overleftarrow{R}_{21}, C_{32}, C_{34}, \overrightarrow{S}_{41}$.

$$p_2 = 1 \quad \rho_2 = 1.0222 \qquad p_1 = 0.4 \quad \rho_1 = 0.5313$$
$$u_{1,2} = -0.6179 \quad u_{2,2} = 0.1 \qquad u_{1,1} = 0.1 \quad u_{2,1} = 0.1$$

$$p_3 = 1 \quad \rho_3 = 0.8 \qquad p_4 = 1 \quad \rho_4 = 1$$
$$u_{1,3} = 0.1 \quad u_{2,3} = 0.1 \qquad u_{1,4} = 0.1 \quad u_{2,4} = 0.8276$$

In Fig. IV.15 we plot the density contours lines (24 contours: from 0.53 to 0.99) obtained on a grid of 256×256 points with a material CFL condition $\nu_{mat} = 0.3$. The comparison between the upwind scheme and the all-speed scheme confirms that the all-speed property helps in keeping the contact waves (bottom and right waves) sharper, due to a smaller numerical viscosity.

IV.5.3.2 Numerical entropy

We analyze the numerical entropy production for the Riemann *configuration 5* presented above.

In Fig. IV.16, we show the behavior of the numerical entropy production of the implicit scheme with the upwind spatial discretization (IV.10) and with the all-speed spatial discretization (IV.8). As expected, the all-speed scheme produces less numerical entropy with respect to the upwind scheme, especially on the two contact waves.

In Fig. IV.17 the numerical entropy of the all speed scheme is plotted for different refinements of the uniform grid. It is evident that with the progressive refinement of the grid, the entropy decreases on all waves except for the shock, as it has been proved in [105].

IV.5.3.3 Adaptive grids

We test the AMR algorithm on the 2D Riemann problems involving 2 contact discontinuities, a shock and a rarefaction (configurations 5 and 6). We set for all simulations the minimum
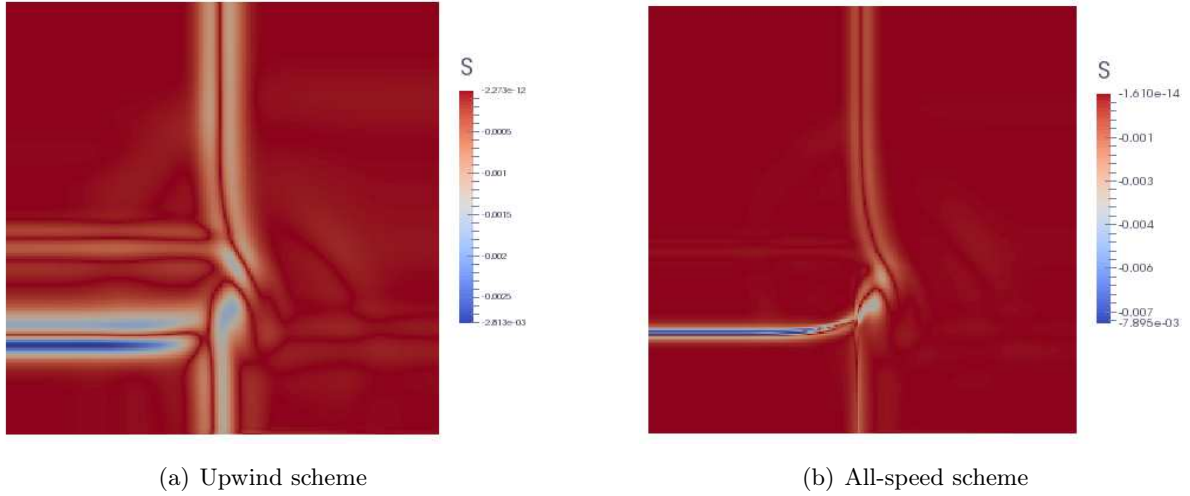
(a) Upwind scheme

(b) All-speed scheme

Figure IV.16: Numerical entropy production for *configuration 5* (see Fig. IV.14): comparison between upwind and all-speed discretizations (256×256 grid points).

(a) 128×128 grid points

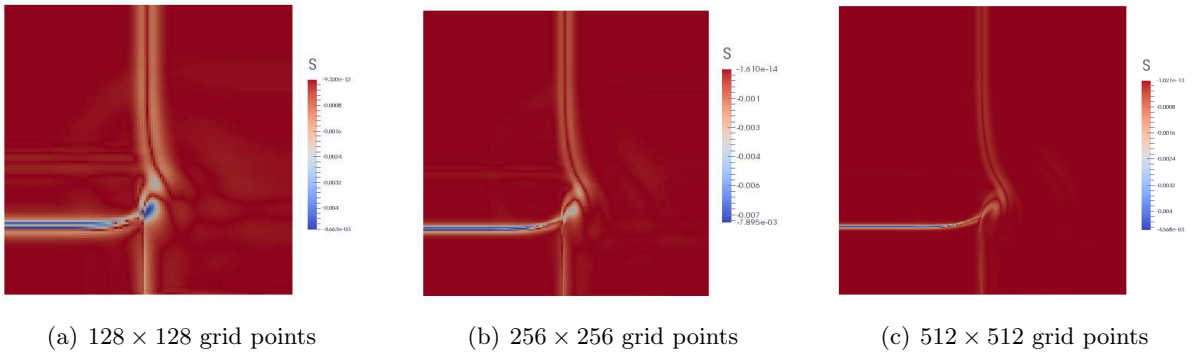(b) 256×256 grid points

(c) 512×512 grid points

Figure IV.17: Numerical entropy production for *configuration 5* of the 2D Riemann problems (see Fig. IV.14): comparison between upwind and all-speed discretizations.

level of refinement $L_{min} = 5$ (namely a uniform grid of 32×32 grid points) and we enforce a material CFL constraint $\nu_{mat} = 0.3$. The threshold on the numerical entropy production are set to $S_{ref} = 0.002$ and $S_{coa} = 0.0001$.

For *configuration 5* we conduct five simulations by changing the maximum level of refinement: L_{max} goes from 6 to 10, having only have one level of refinement with $L_{max} = 6$, whereas with $L_{max} = 10$ we have 4 levels of refinement. The hierarchical Cartesian grids from $L_{max} = 6$ to $L_{max} = 9$ at time $t = 0.3$ are reported in Fig. IV.18. We observe that the entropy criterion is pivoting the AMR in the correct way, since the refinement levels are set where the 4 waves occur. The fact that the areas of refinement are quite large is due to the order one error of the proposed scheme. The density and pressure solutions for the different maximum levels of refinement are plotted in Figs. IV.19 and IV.20.
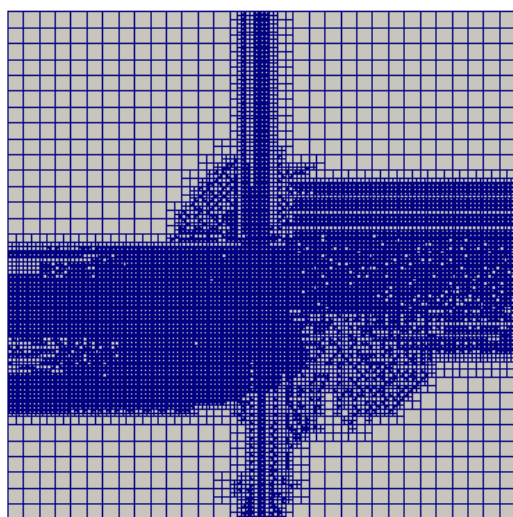
In Fig. IV.21 we compare the density profile obtained with a uniform grid built with $L_{min} = L_{max} = 10$, which gives 1,048,576 cells and the density obtained with the AMR by setting $L_{min} = 5$ and $L_{max} = 10$, which gives a total number of cells of 146,578 at the end of the simulation. The solution structure, the different waves and the small vortex in the center are
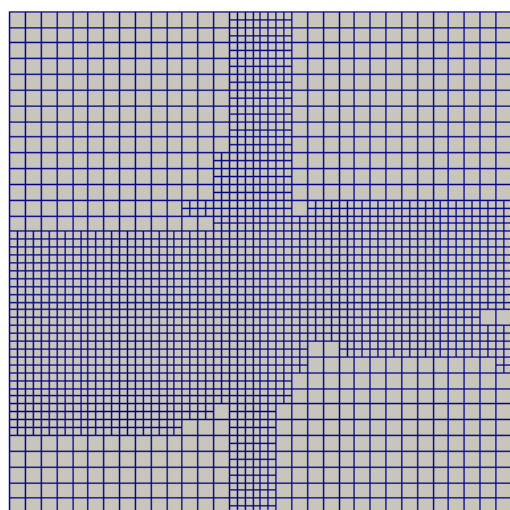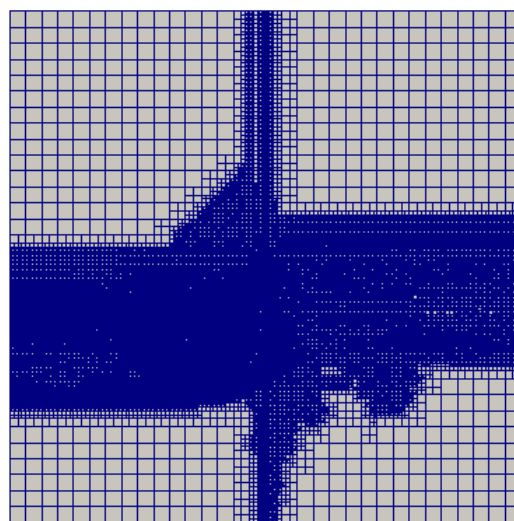
(a) $L_{max} = 6$
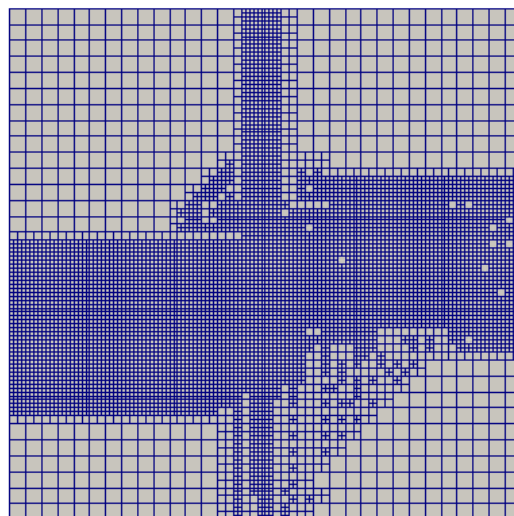
(b) $L_{max} = 7$

(c) $L_{max} = 8$

(d) $L_{max} = 9$

Figure IV.18: *Configuration 5*: grids for the 2D Riemann problem at time $t = 0.3$, obtained with a $L_{min} = 5$ and with different L_{max} ($L_{max} = 6$: 3916 cells, $L_{max} = 7$: 10030 cells, $L_{max} = 8$: 22918 cells, $L_{max} = 9$: 68251 cells).

accurately approximated for both grids, gaining a very similar precision. However, it is evident that with the AMR technique the computational effort is reduced, since the number of degrees of freedom is consistently reduced (of about one order of magnitude).

The results of *configuration 6* are reported in Fig. IV.22. We conduct simulations by changing L_{max} from 6 to 9: once again the entropy criterion is correctly conducting the refinement of the grid. The density plots confirm an accurate approximation of the solution.
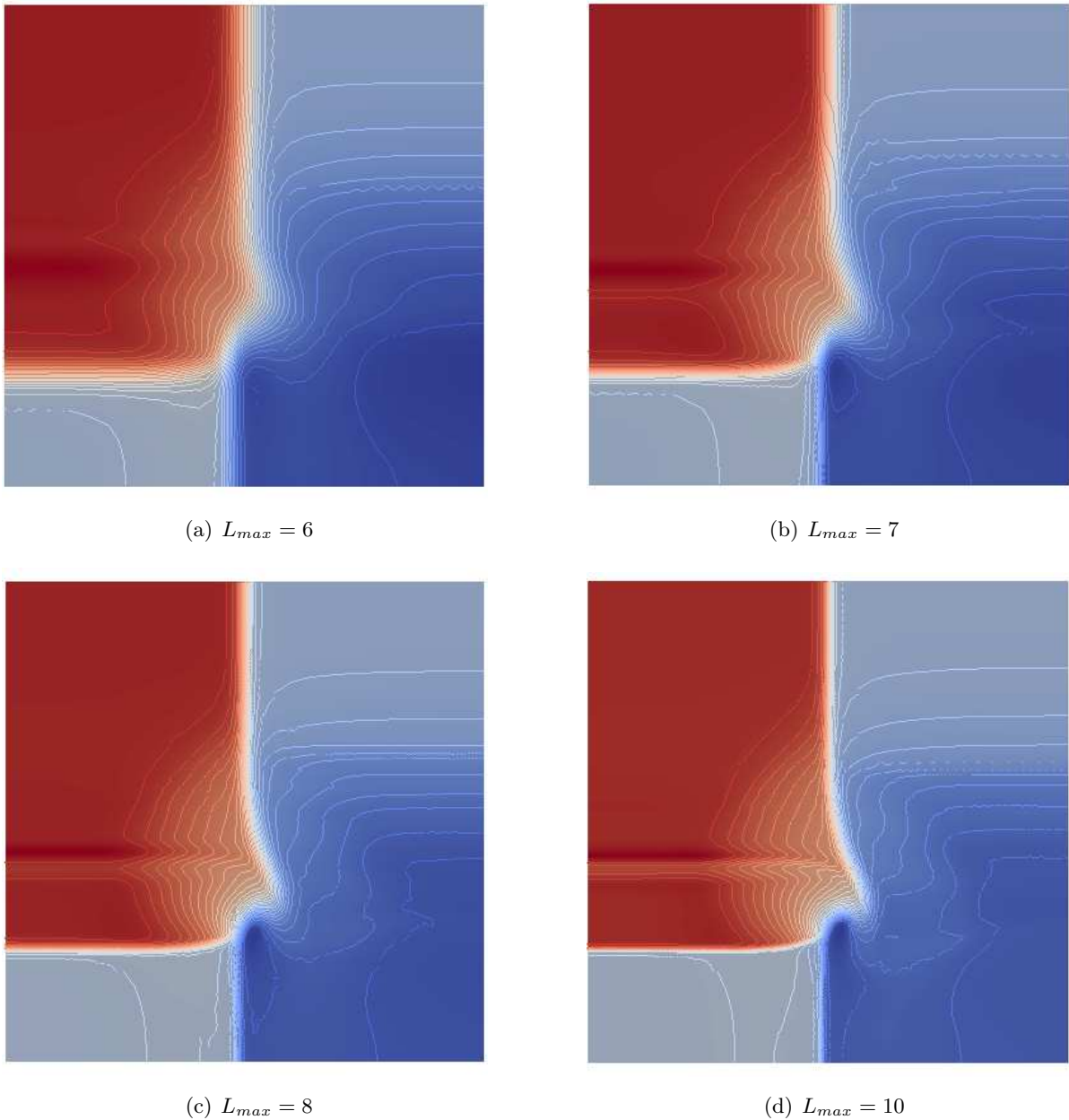
(a) $L_{max} = 6$

(b) $L_{max} = 7$

(c) $L_{max} = 8$

(d) $L_{max} = 10$

Figure IV.19: *Configuration 5*: density for the 2D Riemann problem at time $t = 0.3$, obtained with a $L_{min} = 5$ and with different L_{max}.

IV.6   Preliminary conclusions

In this chapter the all-speed relaxation scheme has been extended to two dimensional problems. A proof of the asymptotic preserving property of the scheme has been proposed. The correct behavior of the scheme in low Mach regimes has been assessed with the Gresho vortex test case. Moreover, we have analyzed problems related to the high computational costs of numerical simulations. Two solutions to reduce these costs have been proposed: the first one is the parallelization of the code and the second one is the use of hierarchical adaptive grids. In the future, a third method will be explored, in order to reduce the computational times mainly re-
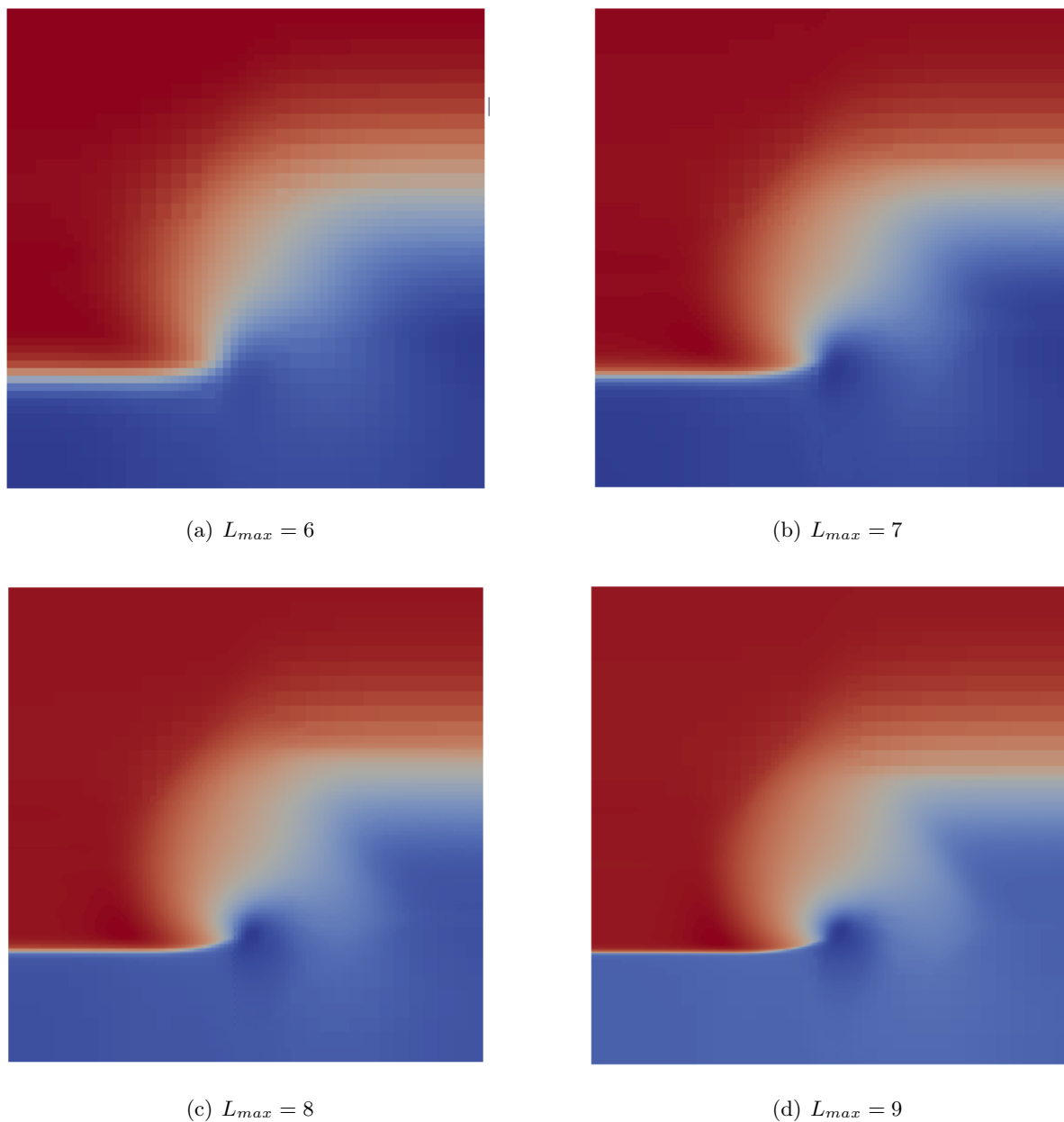
(a) $L_{max} = 6$

(b) $L_{max} = 7$

(c) $L_{max} = 8$

(d) $L_{max} = 9$

Figure IV.20: *Configuration 5*: pressure for the 2D Riemann problem at time $t = 0.3$, obtained with a $L_{min} = 5$ and with different L_{max}.

lated to the linear system solution. Preconditioning techniques may be adopted to decrease the number of iterations needed to reach convergence, by taking into account the specific structure of the assembled matrices.

This chapter concludes the part of the thesis devoted to the derivation of all-speed schemes that solve mono-material problems, namely problems with domain fully filled by only one compressible material. We now want to address the solution of multi-material flows. This can be done in the Eulerian framework that we have introduced, by proposing suitable numerical methods to approximate physical interfaces. This topic will the main object of the two following chapters.
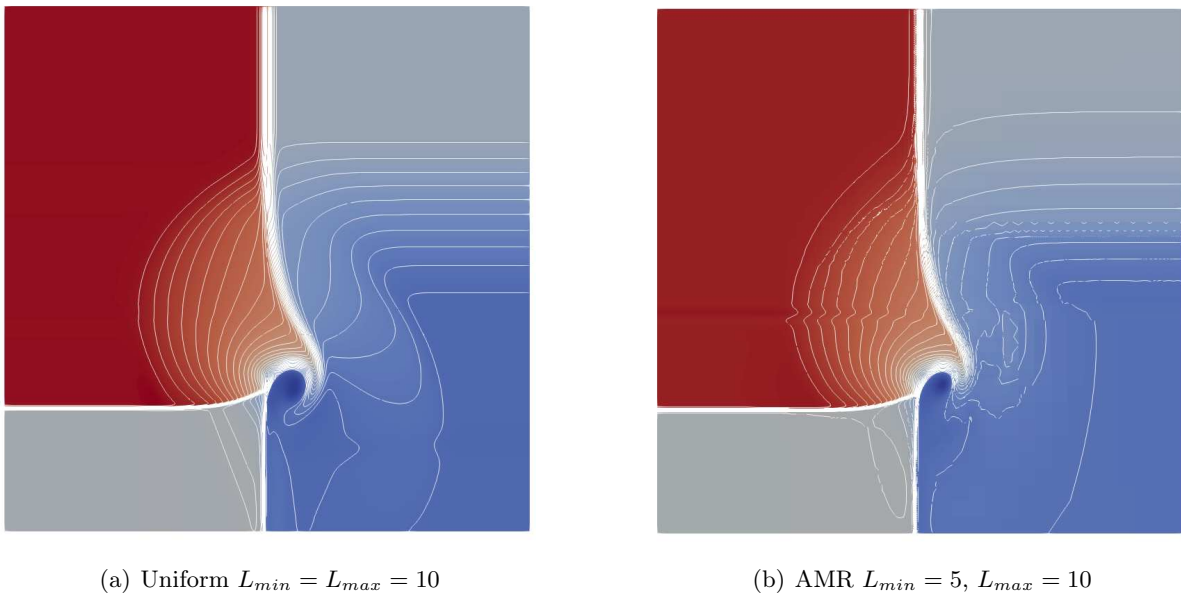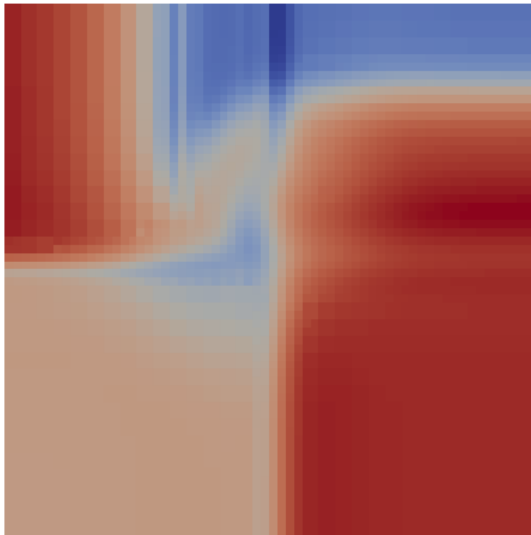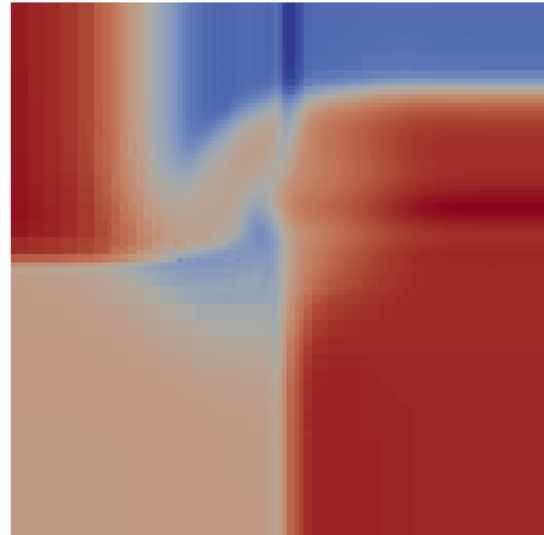
(a) Uniform $L_{min} = L_{max} = 10$
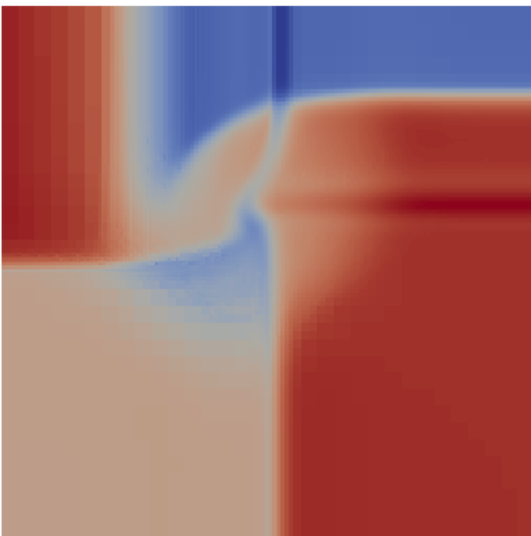
(b) AMR $L_{min} = 5$, $L_{max} = 10$

Figure IV.21: *Configuration 5*: density for the 2D Riemann problem at time $t = 0.3$. Comparison between uniform (number of cells: 1,048,576) and AMR grids (number of cells: 146,578).
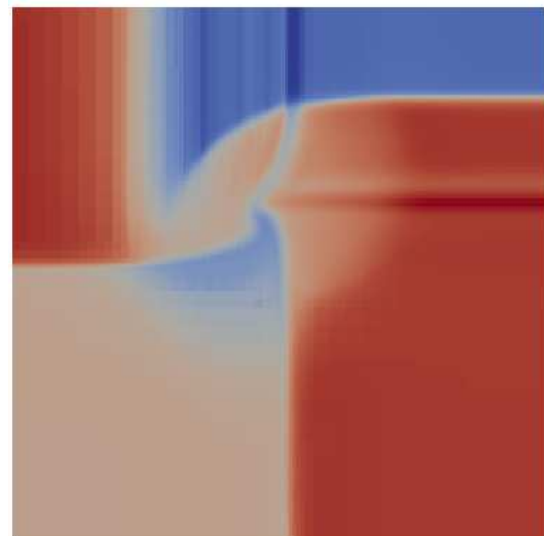
(a) $L_{max} = 6$

(b) $L_{max} = 7$

(c) $L_{max} = 9$

(d) $L_{max} = 10$

Figure IV.22: *Configuration 6*: density for the 2D Riemann problem at time $t = 0.2$, obtained with a $L_{min} = 5$ and with different L_{max}.

Chapter V

Numerical methods for multi-material interfaces

This chapter is devoted to the study of multi-material flows in domains with physical interfaces separating different compressible materials. We briefly revise the numerical methods proposed in literature, focusing on diffused and sharp interface methods. In the framework of a sharp interface treatment, we propose a novel implicit method with the derivation of ad hoc equilibrium conditions. This method exploits the relaxation all-speed scheme in the bulk of the flow and it couples it with an implicit treatment of the equilibrium interface conditions.

We focus on one dimensional problems. As a first step, we propose an implicit treatment of moving boundaries and walls conditions, namely the velocity of the wall is externally imposed. In literature, several explicit-upwind schemes have been extended to the simulation of moving boundaries in the fully compressible regime. In the present work, we are able to approach the approximation of moving walls also when the Mach number tends to zero, thanks to the use of the all-speed implicit framework. Thus, also the boundary treatment has to be implicit and has to preserve the asymptotic behavior of the solution.

The second step consists in introducing a multi-material method, by considering the interface between the two materials as a moving wall. The equilibrium conditions at the multi-material interface are imposed via extrapolations, as in immersed boundary methods. Therefore, the evolution of the material discontinuity is sharp by construction. To our knowledge, this is one of the first fully implicit scheme to deal with moving interfaces in compressible and weakly compressible non-viscous flows.

V.1   State of the art

Physical phenomena involving different materials can be multiphase flows, fluid-structure inter-action with large deformation and impacts. Multi-material flows consist in considering media with constitutive laws that can be extremely different. Due to these differences, oscillations at the material interfaces can easily arise (we refer the reader to the seminal works of Abgrall[5] and Fedkiw et al. [55]). In this section we briefly review the main techniques that have been proposed in literature to model physical interfaces and solve problems involving different media.

We can distinguish two categories: the treatment with a diffuse-interface, namely the inter-

face in included in a small region with non zero width, and the treatment with a sharp interface, namely the interface is numerically considered as a discontinuity. In the following sections we briefly revise the two methodologies.

V.1.1 Diffuse-interface methods

The diffuse-interface approach was introduced by Karni [72] and Abgrall and collaborators [5, 111]. This method is robust and is able to avoid the formation of oscillations, thanks to an interface that corresponds to an artificial mixture of the two fluids. The interface is allowed to diffuse on a small number of computational cells and a mixture model is given for this transition region.

In the equations, the interface is usually represented by a changing in the volume (or mass) fraction of each medium, α_1 for one and $\alpha_2 = 1 - \alpha_1$ for the other one. This technique is justified by the fact that at the small scale the interface between the two fluids is actually a mixture of their molecules. The numerical diffusion of the scheme can thus be associated to the molecular diffusion. The main difficulty of these methods consists in defining thermodynamic laws that are physically, mathematically and numerically consistent in the transition region. The diffuse-interface models have to accurately describe both the pure phases and their interaction at the interface.

For example, in Allaire et al. [7] a diffuse-interface method for multi-fluid problems has been developed. It consists in replacing the continuity equation with two conservation equations for the mass fractions $\alpha_k \rho_k$ of each fluid. In the model, a transport equation for the volume fraction α_1 has also to be added. This method is able to simulate interactions between fluids with very different properties without oscillations.

Another example is proposed in the work of Saurel [111], which is a non-equilibrium model, namely $p_1 \neq p_2$, where p_1 and p_2 are the pressures of fluid 1 and fluid 2 respectively. This model avoids numerical difficulties such as the computation of shock waves in the case of non-conservative equations. The equilibrium is retrieved with a relaxation step on the pressures, in a three-steps algorithm: resolution of the hyperbolic system, relaxation on the pressures and update of the internal energies. It has proved to be robust and accurate, but the interface is diffused and its width grows with time evolution. Moreover, this model increases the number of equations that need to be solved and some of them are not in conservative form. The method presented in [111] has then been adapted by Favrie and Gavriliyuk [53] to model fluid/solid interfaces. The system of equations reads as follows:

$$
\begin{cases}
\partial_t E^\beta + (\nabla_x E^\beta)\mathbf{u} + (\nabla \mathbf{u})^\mathsf{T} E^\beta = 0 \\
\partial_t (\alpha_g \rho_g) + \nabla \cdot (\alpha_g \rho_g \mathbf{u}) = 0 \\
\partial_t (\rho \mathbf{u}) + \nabla \cdot (\rho \mathbf{u} \otimes \mathbf{u} - (\alpha_s \sigma_s + \alpha_g \sigma_g)) = 0 \\
\partial_t (\alpha_g \rho_g \varepsilon_g) + \nabla \cdot (\alpha_g \rho_g \varepsilon_g \mathbf{u}) + \alpha_g \sigma_g : \nabla \mathbf{u} = -p_I \mu_0 (p_g - p_s) \\
\partial_t (\alpha_s \rho_s \varepsilon_s) + \nabla \cdot (\alpha_s \rho_s \varepsilon_s u) + \alpha_s \sigma_s : \nabla \mathbf{u} = -p_I \mu_0 (p_s - p_g)
\end{cases}
$$

where the subscripts $_s$ and $_g$ indicate the solid and fluid quantities respectively, α is the volume fraction, $\rho = \alpha_g \rho_g + \alpha_s \rho_s$ is the total mass, u the velocity field, σ the stress tensor ($\sigma_g = -p_g$), ε the internal energy, $\mu_0 > 0$ is a constant, E^β is a vector representing the deformation, depending

on α_s and p the pressure, $p_I = \frac{\rho_g c_g p_s + \rho_s c_s p_g}{\rho_g c_g + \rho_s c_s}$ is the pressure at the interface which can be obtained with the linearized Riemann problem, with c being the sound speed. The conservation of mass for the solid phase can be find by rewriting the first equation in this system. However, in the pure fluid phase or if the shear modulus tends to zero, the system loses the hyperbolicity property. In order to avoid this problem, a part of each material is represented in the other phase. This model has also been extended to include plasticity in [52].

Other diffused-interface methods have been recently proposed by Dumbser for free-surface flows in [58] and also for linear elasticity equations in [123].

The main advantage of diffuse-interface methods consists in the fact that only one scheme is implemented for the two materials and for the mixture. In this perspective, the exact positions of the interface is not known, since it lies in the transition region. Then, the introduction of methods for the interface tracking is not required when implementing a diffuse-interface method. However, these models often increase the number of equations to be solved and introduce equations that are not always in conservative form. The other fact to be noticed is that the width of the interfaces is due to the numerical diffusion, which increases with time evolution.

V.1.2   Sharp interface methods

The interface can also be considered as a contact discontinuity, especially in presence of inter-actions such as solid/solid and solid/fluid, or also between two non-miscible fluids. The main difficulty of the sharp treatment is due to the need of knowing the interface position and of reconstructing of the interface conditions. Lagrangian models such as the ones proposed by Sco-vazzi et al. in [115] and by Russo and Fazio in [54] and Arbitrary-Lagrangian–Eulerian (ALE) models [59, 77, 23] naturally fall in this framework. However, here we focus on the description of Cartesian methods that introduce a level set for the interface tracking, including ghost fluid methods and Riemann solvers, where the interface is seen as an immersed boundary.

Ghost fluid methods

The ghost fluid method has been introduced by Fedkiw et al. in [55] and Abgrall in [6] to model multiphase flows with sharp interfaces on Cartesian meshes. In every cell of the domain both the real fluid and a "ghost fluid" are considered. In practice, only a layer of cells is necessary in the neighbourhood of the interface and its size depends on the stencil of the chosen numerical method to compute the numerical fluxes. In the case of 1D Euler equations, three quantities need to be extrapolated. Since pressure and normal velocity are continuous through the interface, they are taken in the ghost fluid equal to their value in the real fluid in each cell. The third quantity to be defined is the entropy, which is instead discontinuous and then it is extrapolated from the other side of the interface.

Then, the Euler system is solved inside each fluid independently and a level set method is used to associate each cell to the correct material. With this technique, the numerical fluxes at the interface are different from the left and from the right part of the domain. This means that the scheme is locally non conservative.

Other variants and extensions of the ghost fluid method have been proposed in several works. In the works of Barton et al. [13, 14] and previously in the work of Liu [87] the ghost fluid

method has been extended for the description of solid/solid and solid/fluid interfaces. Other works concerning the ghost fluid method can be found in [131, 110].

Multi-material HLLC methods

Immersed boundary methods were originally proposed in the work of Peskin [100, 101] to solve fluid-structure interaction problems on grids that do not conform to the surface of the body (other references may be found in [69, 88]). The treatment of multi-material interfaces as immersed boundaries is a possible choice in constructing multi-material methods that keep the material interface sharp. With these methods, the contact discontinuity can arbitrarily cross the grid and the transmission conditions are applied via interpolations/extrapolations.

In this category falls the HLLC sharp interface scheme developed by Iollo and collaborators [62, 44], where the interface is captured by a level-set function. In order to keep separated and to not mix the two materials, two numerical flows are computed at the interface. The scheme uses the HLLC Riemann solver to compute these numerical fluxes. The continuity of the normal velocity and of the normal component of the stress tensor are preserved. The choice of such a solver allows to impose the transmission conditions directly on the physical interface.

This method is stable and accurate for the simulation of interactions between materials with very different properties. The scheme is comparable to a standard HLLC solver in terms of computational time. The main advantage of this method with respect to the ghost fluid method is the fact that it is simpler as it does not require the storage of any additional variables or equation of state relative to a ghost fluid to treat the material interface, nor the solution of additional Riemann problems, each relative to a different material at the interface.

V.1.3   Multi-material implicit scheme

When simulating the propagation of waves in heterogeneous compressible media, these phenomena can be affected by drastic changes in the speed of sound or in the speed of elastic waves. This is related to the different local stiffness of the considered materials. In this thesis, we are concerned with the numerical simulation of multi-material flows characterized by different regimes. These can be caused by heterogeneity of the problem and by high differences in the waves propagation velocity. Standard multi-material schemes developed for the simulation of compressible flows may fail when approaching the low Mach number limit. Upwind discretizations provide an excessive numerical viscosity on the slow waves when the Mach number tends to zero, as discussed in Section II.3. The other issue in adopting standard explicit methods for low Mach flows is related to the need of extremely small time stepping. For such schemes a CFL condition has to be imposed on the fastest wave speed to have stability. Thus, the time step of compressible codes becomes extremely small as the incompressible regime gets closer, requiring an increasingly large computational time.

We are able to overcome the problems mentioned above by coupling an implicit treatment of the interface with the all-speed relaxation scheme proposed in Chapter III for the simulation of compressible materials, including elastic solids. We are interested in an all-speed treatment to accurately approximate moving boundaries and multi-material interfaces in the weakly compressible and low Mach regimes. For this reason, the treatment of the boundary and of the

interface must be fully implicit. The general implicit relaxation framework is written in the following way in one dimension:

$$
\begin{cases}
\dfrac{\boldsymbol{\psi}_i^{n+1} - \boldsymbol{\psi}_i^n}{\Delta t} + \dfrac{\mathbf{v}_{i+1/2}^{n+1} - \mathbf{v}_{i-1/2}^{n+1}}{\Delta x} = 0 \\[4mm]
\dfrac{\boldsymbol{v}_i^{n+1} - \boldsymbol{v}_i^n}{\Delta t} + \mathbf{A}\dfrac{\boldsymbol{\psi}_{i+1/2}^{n+1} - \boldsymbol{\psi}_{i-1/2}^{n+1}}{\Delta x} = \dfrac{1}{\eta}\left(\mathbf{F}\left(\boldsymbol{\psi}_i^{n+1}\right) - \mathbf{v}_i^{n+1}\right)
\end{cases}
\tag{V.1}
$$

This is modified at the wall/interface with specific conditions that will be derived and it is coupled with the all-speed spatial discretizations of the advective operator introduced in Chapter III.

In the same spirit of immersed boundary methods, the physical interface is considered as a boundary or a wall moving inside the domain. Hence, we firstly solve problems with walls moving at a prescribed velocity, which is externally imposed and thus known at all times. Some examples can be the piston problem or beam elongations/compressions. Next, a multi-material scheme is derived. The interface between the two materials is treated as a moving wall and equilibrium boundary conditions are derived and implicitly imposed, by extrapolating the quantities of interest to impose the correct behaviour at the physical interface. The conditions are imposed implicitly, inside discretization (V.1) and they are coupled with the all-speed spatial discretization in the bulk of the flow. Moreover, we avoid demanding stability constraints on Δt in low Mach flows. Due to the immersed boundary framework, the evolution of the material discontinuity is sharp by construction. This method has been proposed in a recently submitted paper [4]. The detailed derivation of the model is the object of the next section.

## V.2 Implicit method for walls and interfaces in 1D

We introduce a general framework to model both walls moving at prescribed velocity and physical interfaces where the velocity is dictated by the flow. Once again, the 1D computational domain $[0, L]$ of length L is divided into N cells $C_i = \left[x_{i-1/2}, x_{i+1/2}\right]$ $i = 1, .., N$, letting $\Delta x = x_{i+1/2} - x_{i-1/2}$ be the grid spacing. $\mathbf{w}_i$ denotes the approximate cell average of a quantity $\mathbf{w}$ in the cell C_i and $\mathbf{w}_{i+1/2}$ denotes the approximate point value of $\mathbf{w}$ at the cell interface $x = x_{i+1/2}$. Let the wall/interface be in position $x_k \leq x_B(t) < x_{k+1}$ at time t with material 1 on the left side of the domain $[0, x_B]$ and material 2 on the right side $[x_B, L]$.

We distinguish among *internal cells* (of each material) and *interface cells*. The internal cells are fully occupied by one specific material, the interface cells form a thin layer between the two materials. The interface cells have to be introduced since the moving wall/interface cannot in general be forced to coincide with the cell edges. As a result, the interface cells are partially filled with one material and partially with the other one. This can be inconvenient in a finite volume logic, because numerical solutions are represented in terms of the cell averages. We point out that in 1D we have only one interface cell for each considered wall or physical interface.

In the present work, we assign to material 1 cell C_k and to material 2 cell C_{k+1}, as it is depicted in Fig. V.1(a). This means that the wall/interface is "artificially" set to coincide with the closest numerical interface, which is $x_{k+1/2}$ in Fig. V.1(a). This gives a numerical error of order $\mathcal{O}(\Delta x)$. Only when the wall/interface overcomes a cell center, this cell changes the material to which it is assigned. This approximation is consistent with the first order scheme (III.19).
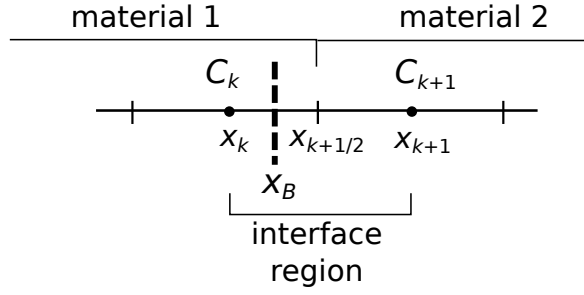
(a) Wall/Interface position
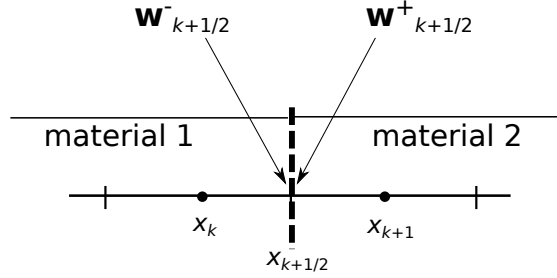
(b) Interface values

Figure V.1: Wall/interface position in the discretized domain and interface values at the numerical interface.

Since we are dealing with two different materials, we need to introduce two different *interface values* at $x_{k+1/2}$, one from the left and one from the right. For a generic variable $\mathbf{w}$, the interface value at the left of the interface (from material 1) will be $\mathbf{w}_{k+1/2}^-$ and the value at the right of the interface (from material 2) will be $\mathbf{w}_{k+1/2}^+$, as depicted in Fig. V.1(b). We have then

$$\left(\boldsymbol{\psi}_{k+1/2}\right)^- \neq \left(\boldsymbol{\psi}_{k+1/2}\right)^+ \text{ and } \left(\mathbf{v}_{k+1/2}\right)^- \neq \left(\mathbf{v}_{k+1/2}\right)^+. \tag{V.2}$$

Scheme (III.8) is therefore modified for cells k and $k+1$ by distinguishing among left and right interface values as follows:

$$\begin{cases} \dfrac{\boldsymbol{\psi}_k^{n+1} - \boldsymbol{\psi}_k^n}{\Delta t} + \dfrac{\left(\mathbf{v}_{k+1/2}^{n+1}\right)^- - \mathbf{v}_{k-1/2}^{n+1}}{\Delta x} = 0 \\[4mm] \dfrac{\mathbf{v}_k^{n+1} - \mathbf{v}_k^n}{\Delta t} + \mathbf{A} \dfrac{\left(\boldsymbol{\psi}_{k+1/2}^{n+1}\right)^- - \boldsymbol{\psi}_{k-1/2}^{n+1}}{\Delta x} = \dfrac{1}{\eta} \left(\mathbf{F}\left(\boldsymbol{\psi}_k^{n+1}\right) - \mathbf{v}_k^{n+1}\right), \end{cases} \tag{V.3}$$

$$\begin{cases} \dfrac{\boldsymbol{\psi}_{k+1}^{n+1} - \boldsymbol{\psi}_{k+1}^n}{\Delta t} + \dfrac{\mathbf{v}_{k+3/2}^{n+1} - \left(\mathbf{v}_{k+1/2}^{n+1}\right)^+}{\Delta x} = 0 \\[4mm] \dfrac{\mathbf{v}_{k+1}^{n+1} - \mathbf{v}_{k+1}^n}{\Delta t} + \mathbf{A} \dfrac{\boldsymbol{\psi}_{k+3/2}^{n+1} - \left(\boldsymbol{\psi}_{k+1/2}^{n+1}\right)^+}{\Delta x} = \dfrac{1}{\eta} \left(\mathbf{F}\left(\boldsymbol{\psi}_{k+1}^{n+1}\right) - \mathbf{v}_{k+1}^{n+1}\right). \end{cases} \tag{V.4}$$

$\mathbf{v}_{k+1/2}^{n+1}$, $\mathbf{v}_{k+3/2}^{n+1}$ and the corresponding conservative variables are computed with the chosen scheme, which can be upwind (III.9), centered (III.14) or all-speed (III.18). The interface variables $\left(\mathbf{v}_{k+1/2}\right)^-$, $\left(\mathbf{v}_{k+1/2}\right)^+$, $\left(\boldsymbol{\psi}_{k+1/2}\right)^-$ and $\left(\boldsymbol{\psi}_{k+1/2}\right)^+$ need to be reconstructed with specific conditions that will be derived below (either moving wall conditions or multi-material interface conditions according to the physical problem). In all other cells C_i, $i \neq k, k+1$, scheme (III.19) is solved.

Since we are using a fully implicit scheme, it is more practical to avoid the introduction of ghost cells to impose wall and multi-material interface conditions. Ghost cells would consistently increase the dimension of the matrix and the memory use, especially in multi-dimensions. This explains why we work directly on the interface $x_{k+1/2}$ and we introduce left and right reconstructions to be used directly inside discretizations (V.3)-(V.4).

Specific conditions for reconstructing the interface values need to be derived. In this perspective, we firstly approach the numerical modeling of walls moving at an externally imposed velocity. In this case the interface velocity is known at all times, whereas the interface values of the other quantities need to be reconstructed. As a second step, we derive the conditions needed for the simulation of interfaces between different materials. In the latter case, the velocity of the interface is unknown, being dictated by the interaction between the two materials.

V.2.1 Conditions for moving walls with imposed velocity

We consider walls separating two media that do not interact. Problems that can be described by this framework are pistons in fluids that expand or compress according to the piston motion. In the case of solids, elongations or compressions of elastic beams can be simulated.

We now derive the numerical conditions that have to be imposed in order to reconstruct the interface values $\left(\mathbf{v}_{k+1/2}\right)^-$, $\left(\mathbf{v}_{k+1/2}\right)^+$, $\left(\boldsymbol{\psi}_{k+1/2}\right)^-$ and $\left(\boldsymbol{\psi}_{k+1/2}\right)^+$ for the case of a wall that moves with a prescribed velocity. Let u_1^* be the velocity imposed to the wall and known at all times. The position of the wall at time t^{n+1} is computed as $x_B\left(t^{n+1}\right) = x_B\left(t^n\right) + u_1^* \cdot \Delta t$.

In the case of Euler gas-dynamics equations, the density and the pressure are extrapolated from the left and from the right, having:

$$\begin{cases} \left(\rho_{k+1/2}^{n+1}\right)^- = \frac{3}{2}\rho_k^{n+1} - \frac{1}{2}\rho_{k-1}^{n+1} \\ \left(u_{k+1/2}^{n+1}\right)^- = u_1^*\left(t^{n+1}\right) \\ \left(p_{k+1/2}^{n+1}\right)^- = \frac{3}{2}p_k^{n+1} - \frac{1}{2}p_{k-1}^{n+1} \end{cases} \quad \text{and} \quad \begin{cases} \left(\rho_{k+1/2}^{n+1}\right)^+ = \frac{3}{2}\rho_{k+1}^{n+1} - \frac{1}{2}\rho_{k+2}^{n+1} \\ \left(u_{k+1/2}^{n+1}\right)^+ = u_1^*\left(t^{n+1}\right) \\ \left(p_{k+1/2}^{n+1}\right)^+ = \frac{3}{2}p_{k+1}^{n+1} - \frac{1}{2}p_{k+2}^{n+1}. \end{cases} \quad \text{(V.5)}$$

By considering the full Eulerian framework (I.44), we also need to extrapolate the backward characteristic $Y_{,1}^2$ from each material and to impose the transverse velocity of the wall u_2^*. Thus, to conditions (V.5), we add

$$\begin{cases} \left((Y_{,1}^2)_{k+1/2}^{n+1}\right)^- = \frac{3}{2}(Y_{,1}^2)_k^{n+1} - \frac{1}{2}(Y_{,1}^2)_{k-1}^{n+1} \\ \left(v_{k+1/2}^{n+1}\right)^- = u_2^*\left(t^{n+1}\right) \end{cases} \quad \text{and} \quad \begin{cases} \left((Y_{,1}^2)_{k+1/2}^{n+1}\right)^+ = \frac{3}{2}(Y_{,1}^2)_{k+1}^{n+1} - \frac{1}{2}(Y_{,1}^2)_{k+2}^{n+1} \\ \left(v_{k+1/2}^{n+1}\right)^+ = u_2^*\left(t^{n+1}\right). \end{cases}$$
$$\text{(V.6)}$$

Conditions (V.5)-(V.6) have to be formulated on the conservative and on the relaxation variables, n order to be included in (V.3)-(V.4) with the correct formulation. Conditions on the

momentum are easily imposed with u_1^* and the density extrapolations. For the energy, we use the pressure extrapolations and the state law. We apply a linearization to this non-linear part due to the implicit time discretization. The relaxation variables are written as

$$\begin{cases} \left(\mathbf{v}_{k+1/2}^{n+1}\right)^- = \mathbf{F}\left(\boldsymbol{\psi}_{k+1/2}^{n+1}\right)^- \\ \left(\mathbf{v}_{k+1/2}^{n+1}\right)^+ = \mathbf{F}\left(\boldsymbol{\psi}_{k+1/2}^{n+1}\right)^+, \end{cases} \tag{V.7}$$

where a linearization is applied to $\mathbf{F}(\boldsymbol{\psi})$. When linearizations are required, we employ the Taylor formula as for the stiff source, having $H\left(\boldsymbol{\psi}^{n+1}\right) = H\left(\boldsymbol{\psi}^n\right) + H'\left(\boldsymbol{\psi}^n\right)\left(\boldsymbol{\psi}^{n+1} - \boldsymbol{\psi}^n\right)$, where $H\left(\boldsymbol{\psi}^{n+1}\right)$ is a function of the conservative variables and $H'\left(\boldsymbol{\psi}^{n+1}\right)$ is its jacobian.

The model and the conditions derived above solve the case of *internal moving walls*, separating two non-interacting materials. Of course, the model can be easily adapted to the simulation of a *moving boundary wall*, where the focus is on the piston or the beam only, and the surrounding medium is not considered. In this case, the right part of the domain is considered empty.

Linear system for moving walls

By defining the vector containing the grid point values of conservative and relaxation variables as $\mathbf{w} = [\boldsymbol{\psi}, \mathbf{v}] \in \mathbb{R}^{N \cdot 2n}$ (N is the number of cells and n the number of conservative variables), the full linear problem can be written in the following way:

$$\mathbf{M}\left(\mathbf{w}^n, u_1^*, u_2^*\right) \mathbf{w}^{n+1} = \mathbf{r}\left(\mathbf{w}^n, u_1^*, u_2^*\right) \tag{V.8}$$

where $\mathbf{M} \in \mathbb{R}^{(N \cdot 2n) \times (N \cdot 2n)}$ and $\mathbf{r} \in \mathbb{R}^{N \cdot 2n}$. The matrix structure comes from the spatial discretization introduced in Sec. III.2 and from the linearized conditions. The matrix and the right hand side are both functions of the wall velocity u_1^* (and u_2^* when it is non zero). The two materials are not interacting with each other, hence the full system can be split into two sub-systems, each one associated to the corresponding material.

We divide the unknowns into $\mathbf{w}_{(1)} = \left[\boldsymbol{\psi}_{(1)}, \mathbf{v}_{(1)}\right] \in \mathbb{R}^{k \cdot 2n}$ (unknowns in cells C_i, $i = 1, ...k$ associated to material 1) and $\mathbf{w}_{(2)} = \left[\boldsymbol{\psi}_{(2)}, \mathbf{v}_{(2)}\right] \in \mathbb{R}^{(N-k) \cdot 2n}$ (unknowns in cells C_i, $i = k, ...N$ associated to material 2. Then we solve

$$\begin{cases} \mathbf{M}_{(1)}(\mathbf{w}_{(1)}^n, u_1^*, u_2^*)\mathbf{w}_{(1)}^{n+1} = \mathbf{r}_{(1)}(\mathbf{w}_{(1)}^n, u_1^*, u_2^*) \\ \mathbf{M}_{(2)}(\mathbf{w}_{(2)}^n, u_1^*, u_2^*)\mathbf{w}_{(2)}^{n+1} = \mathbf{r}_{(2)}(\mathbf{w}_{(2)}^n, u_1^*, u_2^*), \end{cases}$$

where $\mathbf{M}_{(1)} \in \mathbb{R}^{(k \cdot 2n) \times (k \cdot 2n)}$ and $\mathbf{M}_{(2)} \in \mathbb{R}^{((N-k)2n) \times ((N-k)2n)}$. The size of the two sub-systems varies with k every time the wall overcomes a cell center.

V.2.2 Conditions for multi-material interfaces

We now approach the case of a physical interface separating two interacting materials. The interface can be seen as a moving wall and thus treated with the framework introduced above. However, in this case the velocity of the wall is dictated by the flow and thus it is one of the unknowns of the problem. Therefore, equilibrium conditions have to be added to account for

the interactions between the two materials and to recover the correct velocity of the interface. Due to this, the system cannot be split into two different sub-systems associated to the two materials.

It is physically required that the forces are balanced at the multi-material interface. For simplicity, we start by reasoning on gas/gas interactions. In this case, a force balancing simply corresponds to a pressure balancing, namely $p^-_{k+1/2} = p^+_{k+1/2}$. By using the state law of perfect gases, one gets:

$$\left(\gamma^- - 1\right) \left((\rho e)^-_{k+1/2} - \frac{1}{2}\rho^-_{k+1/2} \left(u^*_1\right)^2\right) = \left(\gamma^+ - 1\right) \left((\rho e)^+_{k+1/2} - \frac{1}{2}\rho^+_{k+1/2} \left(u^*_1\right)^2\right), \qquad \text{(V.9)}$$

where γ^- and γ^+ are the heat ratios for material 1 and material 2 respectively and u^*_1 is the unknown velocity of the interface.

The balancing relation (V.9) could be used to find u^*_1 and to close the system for the moving wall (V.8). However, the matrix of the full moving wall system depends on u^*_1 itself. Moreover, in (V.9) $\rho^\pm_{k+1/2}$ and $(\rho e)^\pm_{k+1/2}$ are unknowns because the scheme is implicit. This procedure would then require an fixed point iteration to find the correct interface velocity at every time step.

In order to avoid this problem, trasmission conditions at interface are imposed in terms of velocity and pressure via interpolations, as in immersed boundary methods [101]. This means that we enforce in our scheme continuity of velocity and pressure across the interface for fluid-dynamics problems. Specifically, this is done by computing a mean of the values on the left and on the right of the interface for continuous quantities. Instead, other quantities such as density and energy may be discontinuous and then we extrapolate from each material (left and right). Hence, for fluid/fluid interactions we compute the mean for pressure and velocity in the following way:

$$\begin{cases} \left(u^{n+1}_{k+1/2}\right)^- = \left(u^{n+1}_{k+1/2}\right)^+ = \frac{1}{2}\left(u^{n+1}_k + u^{n+1}_{k+1}\right) \\ \left(p^{n+1}_{k+1/2}\right)^- = \left(p^{n+1}_{k+1/2}\right)^+ = \frac{1}{2}\left(p^{n+1}_k + p^{n+1}_{k+1}\right) \end{cases} \qquad \text{(V.10)}$$

This way, the balancing (V.9) at the interface is automatically taken into account by the scheme. Other quantities such as density and energy may be discontinuous across the interface, hence we compute them with an extrapolation from each material (left and right) as for the moving wall case (V.5), having

$$\begin{cases} \left(\rho^{n+1}_{k+1/2}\right)^- = \frac{3}{2}\rho^{n+1}_k - \frac{1}{2}\rho^{n+1}_{k-1} \\ \left(\rho^{n+1}_{k+1/2}\right)^+ = \frac{3}{2}\rho^{n+1}_{k+1} - \frac{1}{2}\rho^{n+1}_{k+2}. \end{cases} \qquad \text{(V.11)}$$

We extend the interface treatment also to the simulation of solid/solid and fluid/solid interactions. The multi-material conditions are enforced on the full Eulerian system (I.44), where the stress tensor σ takes the role that pressure has in gas-dynamics. When dealing with an interface between two elastic solids, normal and tangential stress are continuous across the contact discontinuity. Moreover, also both velocity components are continuous. Instead, in the case where at least one of the materials is a fluid, namely $\chi = 0$ on one side, the tangential stress σ^{21} vanishes at the interface and thus the transverse velocity can be discontinuous.

Interface conditions to be imposed for every kind of interaction (fluid/fluid, solid/solid and solid/fluid) consist in the left/right extrapolation of the density $(\rho^{n+1}_{k+1/2})^\pm$ and of the backward

characteristics $((Y_{,1}^2)_{k+1/2}^{n+1})^{\pm}$ as in (V.11). Then, conditions $((u_1)_{k+1/2}^{n+1})^- = ((u_1)_{k+1/2}^{n+1})^+$ and $(\sigma_{k+1/2}^{11})^- = (\sigma_{k+1/2}^{11})^+$ are imposed with the mean computation (V.10). To these relations, we need to add conditions on the remaining variables, distinguishing the two following cases

1. solid/solid interface: $(\sigma_{k+1/2}^{21})^- = (\sigma_{k+1/2}^{21})^+$ and $((u_2)_{k+1/2}^{n+1})^- = ((u_2)_{k+1/2}^{n+1})^+$ are computed with the mean as in (V.10), since they are continuous functions across the interface;

2. solid/fluid interface: we impose that . The transverse velocity $((u_2)_{k+1/2}^{n+1})^{\pm}$ is discontinuous and then it is computed with the left/right extrapolation as in (V.5).

We point out that the interface conditions are written on primitive variables, to impose the continuity of u_1 and σ^{11}. These relations need to be transferred on the conservative variables $\boldsymbol{\psi}$ and on the relaxation variables enforcing (V.7), in order to include them inside the relaxation scheme (V.3)-(V.4). The relation between primitive and conservative variables is non-linear, therefore a linearization (III.12) could be used in order to handle the non linearities. This linearization, as previously observed, corresponds to one iteration of the Newton method. The linearization itself is usually enough, however, for cases when the Mach number gets of order one or for wave patterns with shocks that are close to the interface, running the Newton sub-iteration is required to recover the correct speed and position of the interface.

In what follows, we will refer to the scheme (III.19)-(V.3)-(V.4) with the multi-material conditions derived above as "multi-material all-speed scheme". As for ghost-fluid methods, the scheme is locally non-conservative, but it is consistent since $(\mathbf{v}_{k+1/2})^-$, $(\mathbf{v}_{k+1/2})^+$, $(\boldsymbol{\psi}_{k+1/2})^-$ and $(\boldsymbol{\psi}_{k+1/2})^+$ are regular enough functions of the states to the left and to the right of the interface. In the numerical tests section V.3.2 we show this consistency, by correctly predicting shock speeds and positions. Indeed, the number of cell interfaces for which a non-conservative numerical flux is employed is always negligible compared to the total number of mesh cells.

Multi-material algorithm

We summarize the multi-material scheme algorithm applied at each time step. Let the interface be in position $x_B(t^n)$ at time t^n, having $x_k \leq x_B(t^n) \leq x_{k+1}$. We remark that we always impose a material CFL condition, thus the physical interface can cross at most one cell interface at each time step. Hence, the following procedure is implemented from time t^n to time t^{n+1}:

1. the physical interface is advected, by computing its position with the velocity at the previous time step as follows:

$$x_B(t^{n+1}) = x_B(t^n) + \frac{(u_1)_k^n + (u_1)_{k+1}^n}{2}\Delta t.$$

2. the new position is located on the grid by finding the cell index $\overline{k}$ such that $x_{\overline{k}} \leq x_B(t^{n+1}) \leq x_{\overline{k}+1}$. We distinguish two cases:

   - $\overline{k} = k$ (the multi-material interface has not overcome a cell center in the advection from time t^n to time t^{n+1}). In this case the cells occupied by material 1 and the ones occupied by material 2 are the same as they were at time t^n.

- $\overline{k} \neq k$ (the multi-material interface at time t^{n+1} has overcome one cell center with respect to time t^n, either having $\overline{k} = k - 1$ or $\overline{k} = k + 1$). We examine the case $C_{\overline{k}} = C_{k+1}$ (forward-moving interface). This cell at time t^{n+1} is assigned to a different material with respect to time t^n.

  Values of the quantities in cell $C_{\overline{k}}$ are needed at time t^n to assemble the matrix of the implicit scheme. In this cell, values at time t^n are known for material 2, but are now needed for material 1. We "correct the initial condition" at the interface cell by creating fictitious values at time t^n for the cell that has changed material at time t^{n+1}. To do this, we simply extrapolate the quantities from the material in expansion. In the case of fluids we impose:

$$
\begin{cases}
\rho_{\overline{k}}^n = \frac{3}{2}\rho_k^n - \frac{1}{2}\rho_{k-1}^n \\
u_{\overline{k}}^n = \frac{1}{2}\left(u_k^n + u_{k+1}^n\right) \\
p_{\overline{k}}^n = \frac{1}{2}\left(p_k^n + p_{k+1}^n\right).
\end{cases}
$$

3. with all the computed quantities (interface position, assignment of the cells to the corresponding material, fictitious old values), we assemble the linear system associated to scheme (III.19)-(V.3)-(V.4), with the derived reconstructions for the interface conditions. Then the linear system is solved to obtain all variables at time t^{n+1}.

V.3   Numerical validations

We present different tests for a moving wall: pistons and beam elongations are analyzed in different regimes. The multi-material scheme is then used for the simulations of flows in Sod tubes with fluid/fluid, solid/solid and solid/fluid interactions. The numerical results show convergence of the proposed multi-material scheme. A comparison of different discretizations (upwind, centered and all-speed) of the advective operator in the bulk of the flow is carried out. It is observed that the moving wall condition can be accurately imposed with our numerical model no matter how the spatial derivatives are discretized away from boundaries/interfaces. The ability of the multi-material scheme in accurately approximating the physical interface is also proved by several tests in weakly compressible regimes.

We remark that in the low Mach limit, the all-speed spatial discretization produces an accurate resolution of material waves occurring independently of walls and interfaces, as analyzed in Chapter III. This is the main reason for introducing the wall/interface model inside an all-speed implicit framework.

V.3.1   Moving walls with imposed velocity

The moving wall model is here validated with simulations of gas pistons and beams elongations. In all the simulations we apply at the left boundary of the domain homogeneous Neumann boundary conditions and the final times are taken sufficiently small so that no waves reach the left end.

| **Test** | L | $x_B(0)$ | $x_{disc}(0)$ | t_{end} | ρ_1 | ρ_2 | $(u_1)_1$ | $(u_1)_2$ | p_1 | p_2 | u_1^* |
	(m)	(m)	(s)	(Kg/m^3)	(Kg/m^3)	(m/s)	(m/s)	(Pa)	(Pa)	(m/s)
1	1	0.5	-	0.2	1	-	0	-	1	-	0.5
2	2	1.75	-	0.9	1	-	0	-	1	-	0.01
3	2.2	2	0.5	0.6	1	1	0	0.008	0.4	0.399	0.008
4	1	0.9	0.5	0.2	4/3	1	35/99	0	1.5	1.499	$0.5 \cdot \pi cos\left(10\pi t\right)$

Table V.1: Parameters for the gas pistons: initial state (subscripts: $_1$ for left chamber and $_2$ right chamber), initial position of the wall $x_B(0)$, of the initial discontinuity $x_{disc}(0)$ and imposed velocity u_1^*. A biatomic gas with $\gamma = 1.4$ fills the entire domain.

(a) Velocity

(b) Pressure

(c) Density
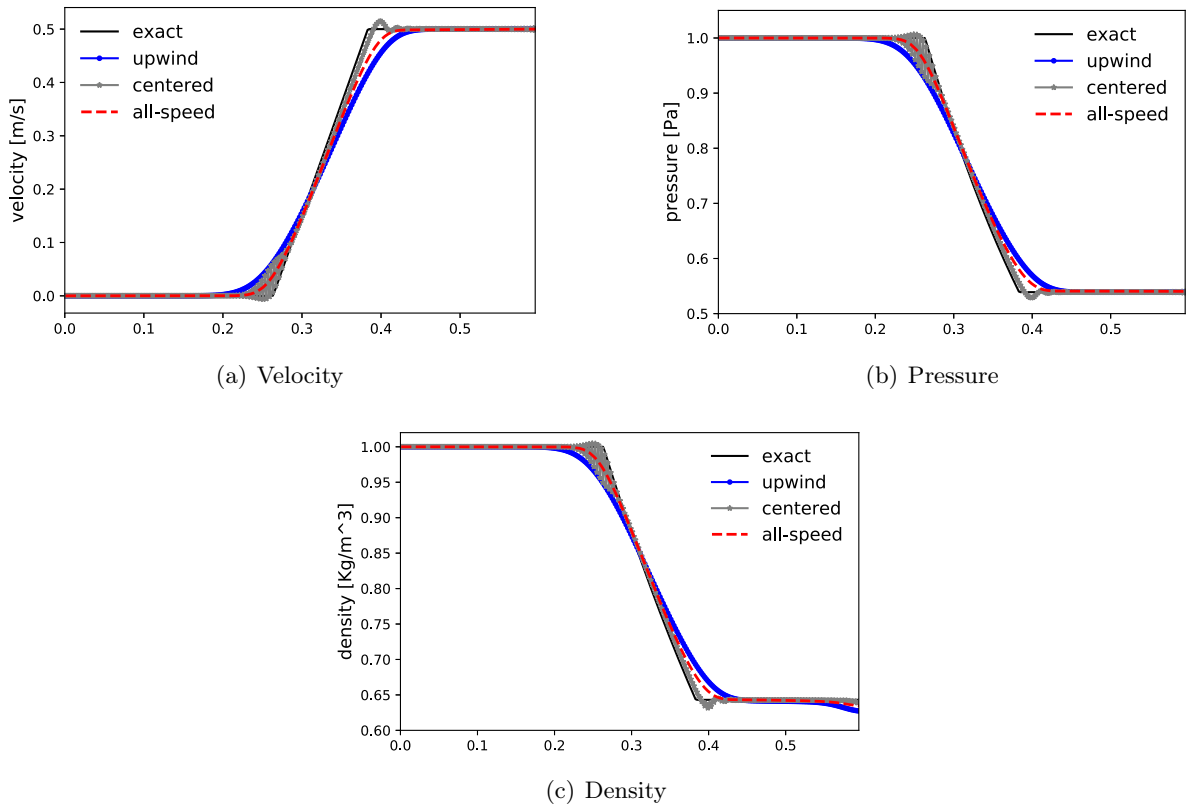
Figure V.2: *Test 1*: gas piston ($\Delta x = 2 \cdot 10^{-3}$ and $\Delta t = 8 \cdot 10^{-4}$). Comparison of the three spatial discretizations.

V.3.1.1 Gas pistons

We present four gas piston problems in different regimes, the piston being a moving boundary. The initial state, the initial position of the wall $x_B(0)$ and the velocity u_1^* imposed at the wall are reported in Table V.1. A biatomic gas with $\gamma = 1.4$ fills the entire domain. In tests 1, 2 and 3 the imposed velocity is constant in time, whereas in test 4 we study a piston with a sinusoidal trajectory to see expansion and compression. Test 3 and 4 present a discontinuity in the gas chamber at $x_{disc}(0) = 0.5$.

Test 1 and 2 are two piston problems in a pipe containing a biatomic gas. The initial gas density and pressure are taken constant in space. The pistons move with an imposed constant velocity u_1^* and consequently the gas expands with a rarefaction wave moving to the

left. We compare the results obtained with the implicit moving wall conditions coupled with three different spatial discretizations away from the boundaries (upwind, centered and all-speed schemes) for two regimes given by taking two different values of u_1^*. In *test 1* we impose $u_1^* = 0.5$m/s, yielding to subsonic but fully compressible flow with a Mach number on the piston of order $M \simeq 0.4$. After 0.2 s the piston has moved from $x_B(0) = 0.5$ to $x_B(t_{end}) = 0.6$. In Fig. V.2 we observe that the correct profiles are recovered. The upwind discretization suffers from the overheating problem on the density profile (entropy errors occuring at the interface may cause overshoots on the density and on the temperature: see [56]). The overheating disappears when reducing numerical diffusion, thus the centered discretization is the one with the smallest overheating spike. However, the centered scheme is oscillatory on the acoustic waves. Thus, the all-speed scheme proves to be the best choice among the three, preventing oscillations and reducing the overheating problem. It also reduces the diffusion on the head and tail of the rarefaction with respect to the upwind scheme. For this simulation we employ $\Delta x = 2 \cdot 10^{-3}$ and $\Delta t = 8 \cdot 10^{-4}$, which corresponds to $\nu_{mat} = 0.2$ and $\nu_{ac} = 0.9$. In fact, to resolve the rarefaction wave an acoustic CFL constraint has to be enforced.
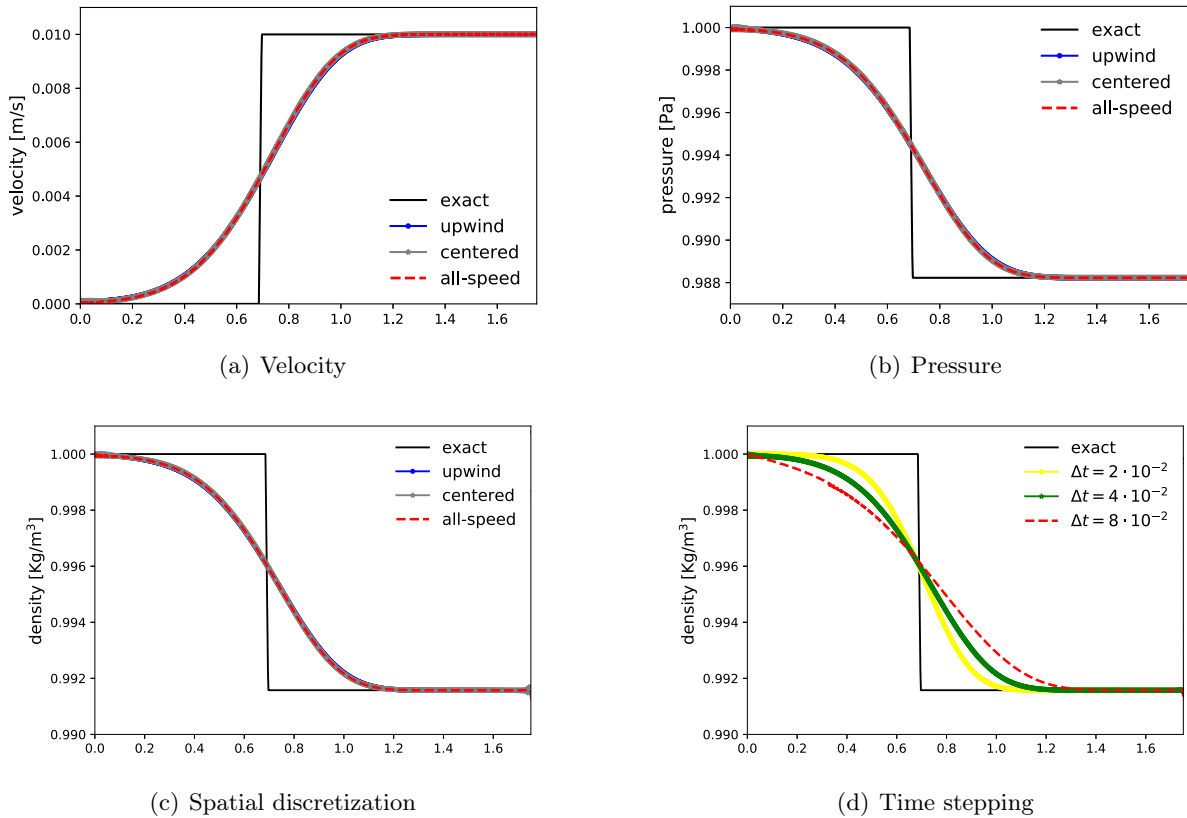

(a) Velocity

(b) Pressure

(c) Spatial discretization

(d) Time stepping

Figure V.3: *Test 2*: Low Mach gas piston ($\Delta x = 2 \cdot 10^{-3}$). Panel (a): comparison of the three spatial discretizations ($\Delta t = 4 \cdot 10^{-2}$ given by $\nu_{mat} = 0.2$). Panel (b): all-speed scheme for different time steps ($\Delta t = 2 \cdot 10^{-2}$, $\Delta t = 4 \cdot 10^{-2}$, $\Delta t = 8 \cdot 10^{-2}$, respectively given by $\nu_{mat} = 0.1$, $\nu_{mat} = 0.2$, $\nu_{mat} = 0.4$).

With *test 2*, instead, we study the low Mach regime, by imposing $u_1^* = 0.01$m/s. The Mach number on the piston is $M \simeq 0.8 \cdot 10^{-3}$. The rarefaction wave has a small amplitude and is

	(a) *Test 1*			(b) *Test 2*	
Δx	Error	Rate	Δx	Error	Rate
$8 \cdot 10^{-3}$	$1.0992 \cdot 10^{-3}$	-	$8 \cdot 10^{-3}$	$6.5869 \cdot 10^{-4}$	-
$4 \cdot 10^{-3}$	$4.7752 \cdot 10^{-4}$	1.15	$4 \cdot 10^{-3}$	$5.5646 \cdot 10^{-4}$	0.59
$2 \cdot 10^{-3}$	$2.3808 \cdot 10^{-4}$	1.002	$2 \cdot 10^{-3}$	$3.4784 \cdot 10^{-4}$	0.79
$1 \cdot 10^{-3}$	$1.2004 \cdot 10^{-4}$	0.99	$1 \cdot 10^{-3}$	$1.6824 \cdot 10^{-4}$	1.03

Table V.2: Mass conservation errors for tests 1 and 2 at the end of the simulations.

very fast if compared to the material wave (piston motion). At the end of the simulation the piston has moved from $x_B(0) = 1.75$ to $x_B(t_{end}) = 1.76$, namely it has crossed 5 cells in the chosen grid. In Fig. V.3(c), we compare the profiles obtained for the three different schemes and with time step $\Delta t = 4 \cdot 10^{-2}$ (which is given by imposing $\nu_{mat} = 0.2$ on the chosen grid). The rarefaction is smeared because the time step is too large to resolve acoustic waves. We can observe that the three schemes behave in a similar manner, only the centered scheme develops some small oscillations on the density profile at the wall. In Fig. V.3(d) we compare the results obtained with the all-speed scheme (III.19) with moving wall conditions for different time steps. The mass conservation errors obtained with the all speed scheme for tests 1 and 2 are reported in Table V.2. As expected, these errors are relatively small and decrease as the mesh is refined, exhibiting the numerical convergence of order one for test 1 and of almost order one for test 2.
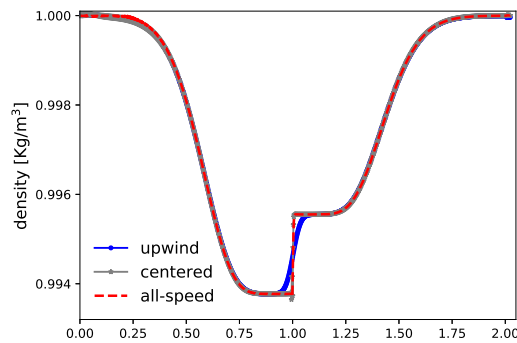

Figure V.4: *Test 3*: Low Mach gas piston with contact discontinuity ($\Delta x = 2 \cdot 10^{-3}$, $\Delta t = 5 \cdot 10^{-2}$ given by $\nu_{mat} = 0.2$).

The results of the first two tests have shown that the implicit scheme with the upwind and with the all-speed scheme behave in a very similar manner. We now perform a simulation of a piston problem with a discontinuity in the middle of the gas chamber $x_{disc}(0) = 0.5$ (*test 3*). *Test 3* is a Riemann problem in a gas piston, which results in a low Mach flow containing a contact discontinuity. A small pressure ratio and a small velocity on the right are imposed, which is the velocity of the piston too. The Mach number on the contact discontinuity is $M \simeq 6 \cdot 10^{-3}$. In Fig. V.4 it is evident the all-speed scheme is able to keep the contact discontinuity sharper than the upwind scheme, because it provides the correct numerical viscosity on the material wave. This test shows that the all-speed discretization is necessary in the low Mach regime for the approximation of material waves that are not "reconstructed" with wall conditions. At the

end of the simulation the piston position is $x_B\left(t_{end}\right) = 2.0048$ (crossing 4 cells on the chosen grid) and the contact discontinuity position is $x_{disc}\left(t_{end}\right) = 1.0027$ (crossing 2 cells).

(a) $t = 0.05$: $x_B = 0.95$

(b) $t = 0.1$: $x_B = 0.9$
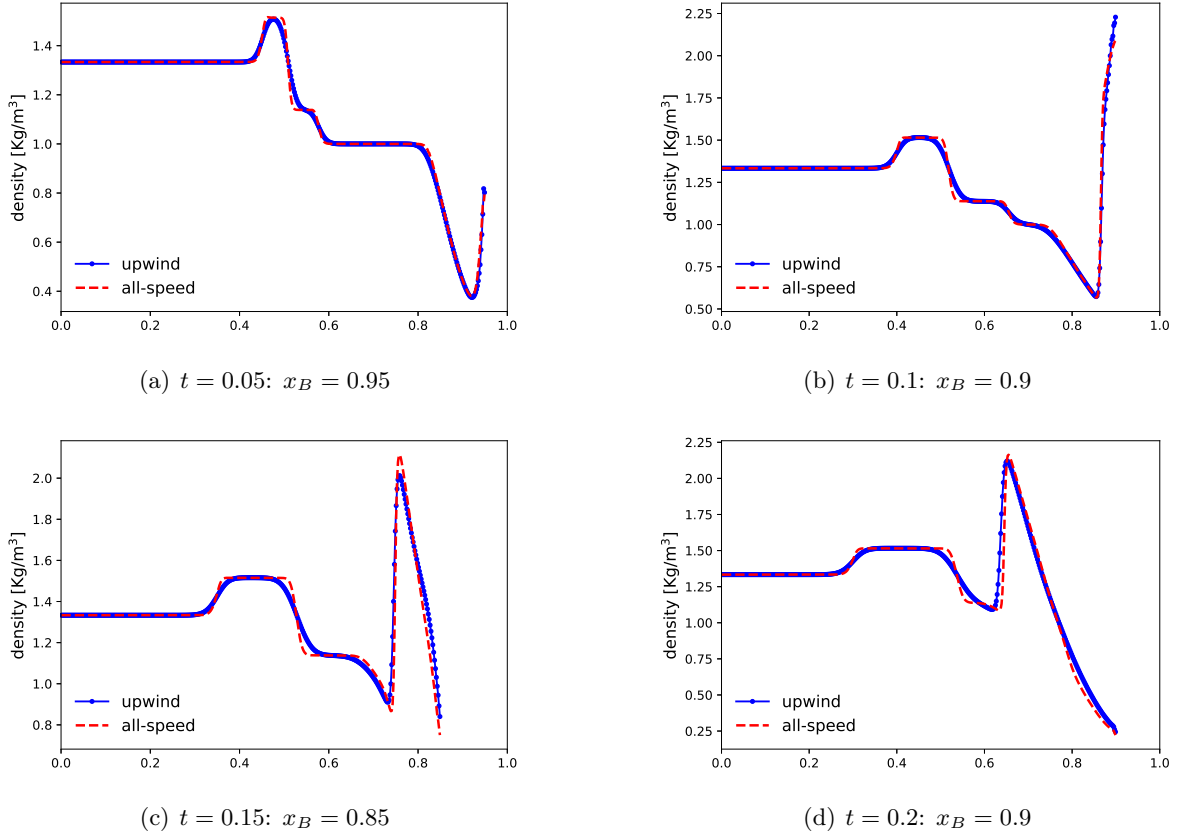
(c) $t = 0.15$: $x_B = 0.85$

(d) $t = 0.2$: $x_B = 0.9$

Figure V.5: *Test 4*: density profiles obtained with the upwind and all-speed spatial discretizations ($\Delta x = 2 \cdot 10^{-3}$ and $\Delta t = 4.9 \cdot 10^{-4}$).

With *test 4* we study a gas tube with a moving boundary wall oscillating around $x_B(0) = 0.9$ with a time-dependent velocity $u_1^*\left(t\right) = 0.5 \cdot \pi cos\left(10\pi t\right)$ (see [36] for a similar test). The initial data correspond to a right moving wave, initially positioned in $x_{disc} = 0.5$, with a small pressure ratio applied. The moving boundary generates shocks and rarefaction waves that interact with the incoming wave, creating a complicated solution structure. This test shows that a sinusoidal piston trajectory is well resolved in both expansion and compression phases. In Figs. V.6 and V.5 we compare velocity and density profiles obtained with the upwind and all-speed spatial discretizations at different times: at time $t = 0.05$ seconds the wall position is in $x_B = 0.95$ (maximum expansion) and at time $t = 0.15$ seconds in $x_B = 0.85$ (maximum compression). The all-speed scheme keeps the waves structure slightly sharper with respect to the upwind scheme, because the convex combination (III.17) is able to moderate the numerical viscosity. For this test we employ an acoustic CFL condition $\nu_{ac} = 0.9$ in order to resolve all the waves occurring during the simulation.
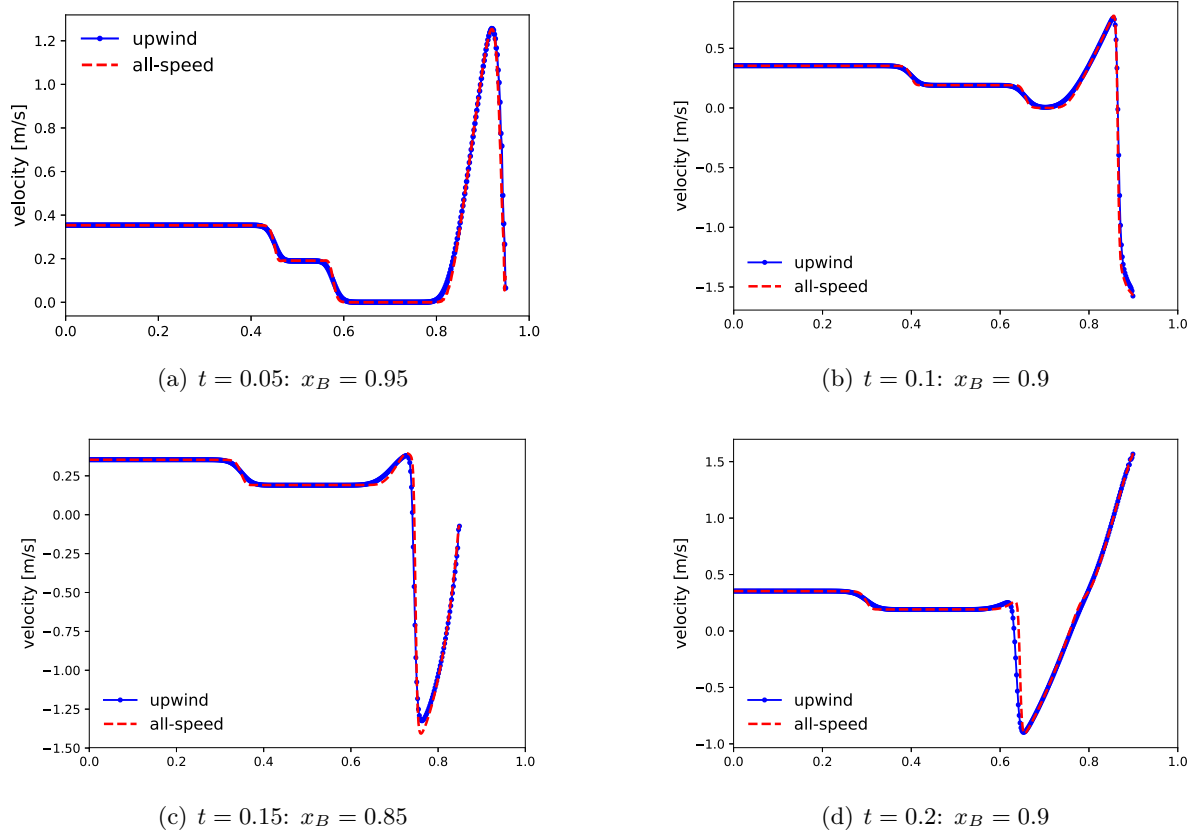
(a) $t = 0.05$: $x_B = 0.95$

(b) $t = 0.1$: $x_B = 0.9$

(c) $t = 0.15$: $x_B = 0.85$

(d) $t = 0.2$: $x_B = 0.9$

Figure V.6: *Test 4*: velocity profiles obtained with the upwind and all-speed spatial discretizations ($\Delta x = 2 \cdot 10^{-3}$ and $\Delta t = 4.9 \cdot 10^{-4}$).

Test	L (m)	$x_B(0)$ (m)	t_{end} (s)	ρ_1 (Kg/m^3)	ρ_2 (Kg/m^3)	$(u_1)_1$ (m/s)	$(u_1)_2$ (m/s)	p_1 (Pa)	p_2 (Pa)	u_1^* (m/s)
5	1	0.6	0.0001	8900	1	0	0	$5 \cdot 10^5$	10^5	500
6	2	1.75	$2.5 \cdot 10^{-4}$	8900	50	0	0	$5 \cdot 10^9$	10^5	25

Table V.3: Parameters for the two materials tests (copper/gas): initial state (subscripts: $_1$ for copper on the left and $_2$ for a biatomic gas on the right), initial position of the wall $x_B(0)$ and imposed velocity u_1^*.

V.3.1.2 Copper beams

Tests 5 and 6 simulate the elongation of two copper beams surrounded by a perfect gas. The initial state is reported in Table V.3 for the two tests. An external velocity is applied at the right boundary of the beam:

- $u_1^* = 500$m/s for test 5, giving a subsonic but fully compressible regime in copper ($M^- \simeq 0.14$) and a Mach number of order 1 in the gas side. The right boundary of the beam moves from $x_B(0) = 0.6$ to $x_B(t_{end}) = 0.65$;

- $u_1^* = 25$m/s for test 6, with a Mach number around $5.5 \cdot 10^{-3}$ on the copper side of the interface and of order 1 in the gas. The right boundary of the beam moves from
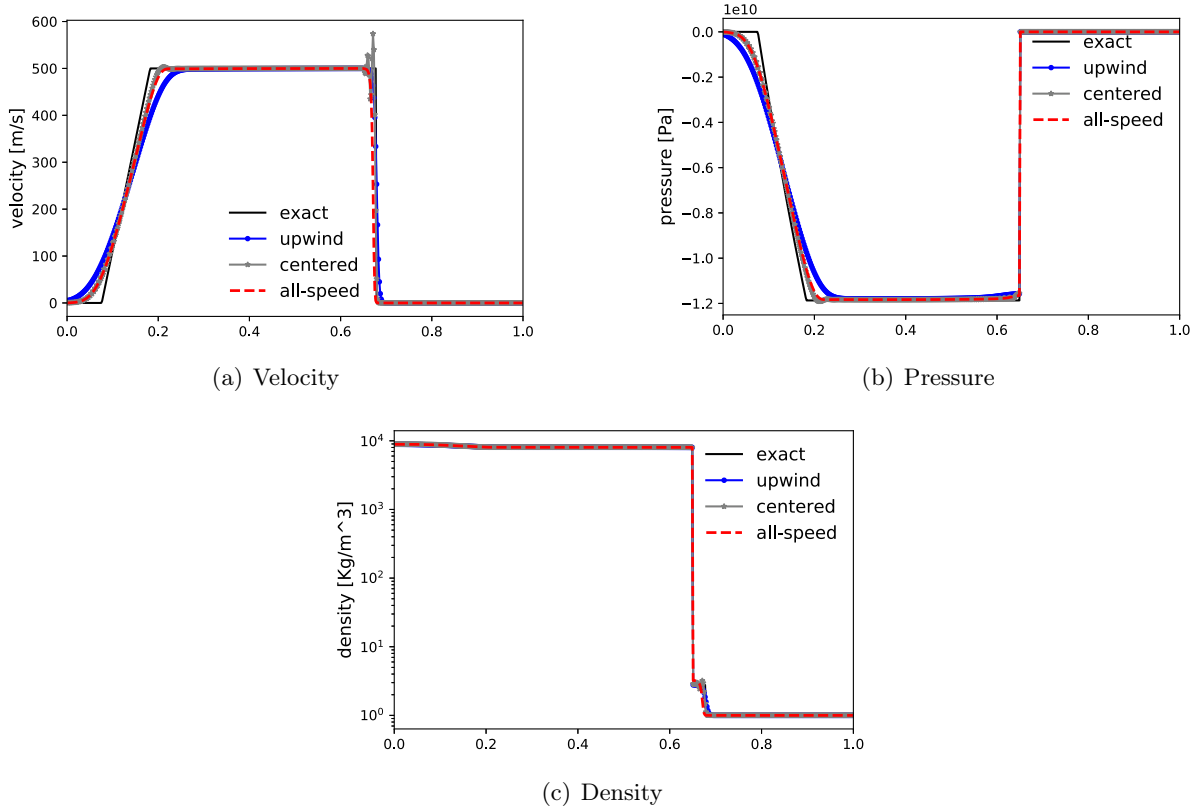
(a) Velocity

(b) Pressure

(c) Density

Figure V.7: *Test 5*: copper-gas beam elongation ($\Delta x = 2 \cdot 10^{-3}$ and $\Delta t = 8 \cdot 10^{-7}$).

$x_B(0) = 1.75$ to $x_B(t_{end}) = 1.756$, namely it crosses 3 cells on the chosen grid.

Copper is deformed in the normal direction (elongation), with a rarefaction wave moving to the left. The gas is compressed and a shock moving to the right occurs. In Figs. V.7 and V.8, the correct solution is recovered for both simulations. The moving boundary is accurately modeled and corresponds to the discontinuity on the density profile. As expected, the centered scheme is oscillatory on the acoustic waves, especially on the shocks. For both simulations we use $\Delta x = 2 \cdot 10^{-3}$ and we impose $\nu_{mat} = 0.2$. This gives a time step $\Delta t = 8 \cdot 10^{-7}$ for test 5 (which is equivalent to impose $\nu_{ac} = 0.9$) and $\Delta t = 1.6 \cdot 10^{-5}$, for test 6. In this latter case, the rarefaction wave is under-resolved because it is consistently faster than the wall, whose velocity dictates the large time step.

	(a) *Test 5*			(b) *Test 6*	
Δx	Error	Rate	Δx	Error	Rate
$8 \cdot 10^{-3}$	$3.5812 \cdot 10^{-4}$	-	$8 \cdot 10^{-3}$	$2.9575 \cdot 10^{-3}$	-
$4 \cdot 10^{-3}$	$2.5702 \cdot 10^{-4}$	0.69	$4 \cdot 10^{-3}$	$1.5401 \cdot 10^{-3}$	0.96
$2 \cdot 10^{-3}$	$1.7305 \cdot 10^{-4}$	0.74	$2 \cdot 10^{-3}$	$5.7029 \cdot 10^{-4}$	1.35
$1 \cdot 10^{-3}$	$1.1183 \cdot 10^{-4}$	0.77	$1 \cdot 10^{-3}$	$2.7520 \cdot 10^{-4}$	1.03

Table V.4: Mass conservation errors for tests 5 and 6 at the end of the simulations.

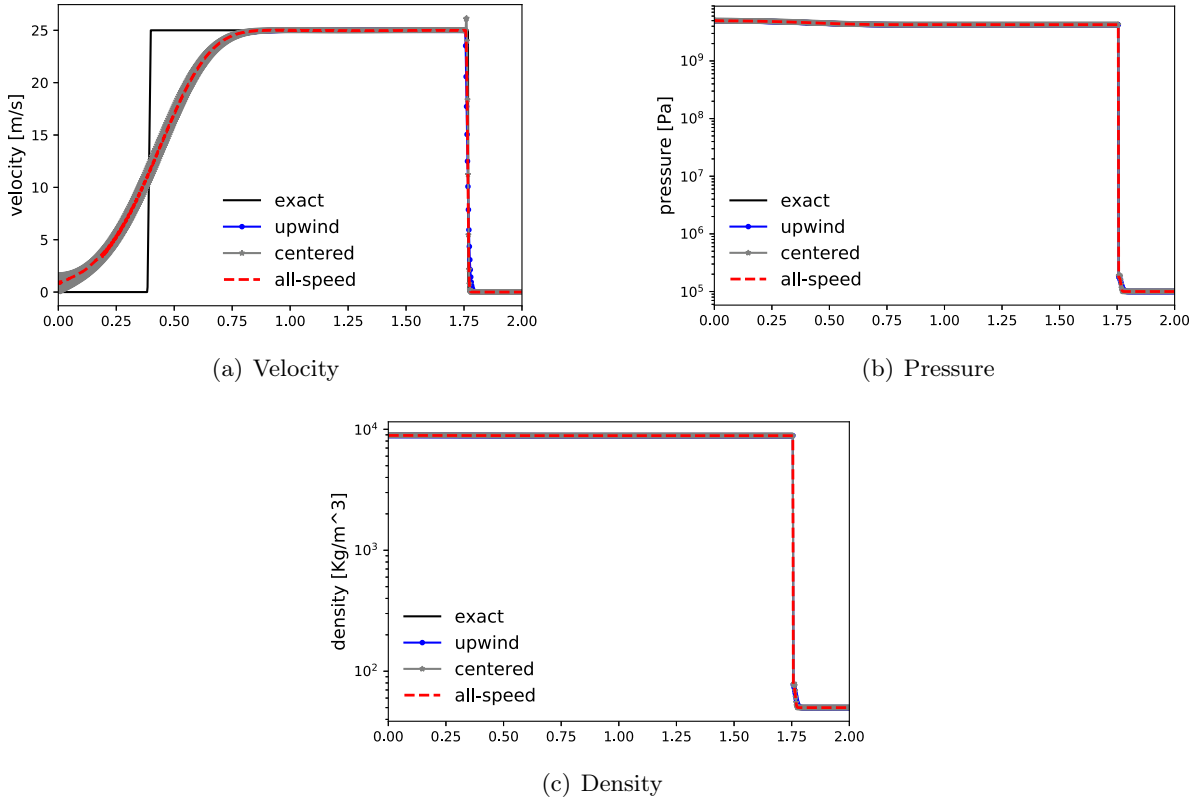(a) Velocity

(b) Pressure

(c) Density

Figure V.8: *Test 6*: low Mach copper-gas beam elongation ($\Delta x = 2 \cdot 10^{-3}$ and $\Delta t = 1.6 \cdot 10^{-5}$).

The mass conservation errors for the copper beam for the two tests are reported in Table V.4. The mass conservation is guaranteed, with a convergence of roughly order one.

V.3.2 Multi-material interfaces

We validate the multi-material all-speed scheme introduced in Sec. V.2.2 by presenting fluid/fluid, solid/solid and solid/fluid Sod tube problems. The tests are conducted for different regimes: the Mach numbers of the multi-material interface are reported in Tables V.5 and V.7. In some cases we need to distinguish between the Mach number on the left of the interface, which we call M^-, and the Mach number on the right M^+. The initial condition and the physical parameters of the test cases are described in Tables V.6 and V.8, where L is the length of the tube and $x_B(0)$ is the initial position of the interface. For all test cases we use homogeneous Neumann boundary conditions.

V.3.2.1 Fluid/fluid

We perform numerical validations on fluid/fluid interaction problems. The first tests are conducted with a progressive refinement of the grid, in order to validate the spatial convergence of the implicit multi-material method. Then we carry out a comparison with the mono-material all-speed relaxation scheme introduced in Chapter III, for low Mach interfaces separating chambers filled with the same material (gas-gas and water-water). In the last section, three different dis-

cretizations of the advective operator are compared for water/gas problems in different regimes (upwind, centered and all-speed).

Test	Materials	Regime	γ_1	γ_2	$p_{\infty,1}$ (Pa)	$p_{\infty,2}$ (Pa)
7	gas-gas	$M \simeq 0.9$	1.4	1.4	0	0
8	gas-gas	$M \simeq 6 \cdot 10^{-3}$	1.4	1.6	0	0
8.1	gas-gas	$M \simeq 6 \cdot 10^{-3}$	1.4	1.4	0	0
9 and **9.1**	water-water	$M \simeq 2.5 \cdot 10^{-3}$	4.4	4.4	$6.8 \cdot 10^8$	$6.8 \cdot 10^8$
10	water-gas	$M^- \simeq 0.035;\ M^+ \simeq 0.13$	4.4	1.4	$6.8 \cdot 10^8$	0
11	water-gas	$M^- \simeq 6.5 \cdot 10^{-3};\ M^+ \simeq 0.027$	4.4	1.4	$6.8 \cdot 10^8$	0

Table V.5: Parameters for the fluid/fluid test cases: materials and regime on the interface.

Test	L (m)	$x_B(0)$ (m)	t_{end} (s)	ρ_1 (Kg/m^3)	ρ_2 (Kg/m^3)	$(u_1)_1$ (m/s)	$(u_1)_2$ (m/s)	p_1 (Pa)	p_2 (Pa)
7: gas-gas	1	0.5	0.1644	1	0.125	0	0	1	0.1
8: gas-gas	1	0.5	0.25	1	1	0	0.008	0.4	0.399
8.1: gas-gas	400	200	150	1	1	0	0.008	0.4	0.399
9: water-water	1	0.5	10^{-4}	10^3	10^3	0	15	10^8	$0.98 \cdot 10^8$
9.1: water-water	400	200	0.095	10^3	10^3	0	15	10^8	$0.98 \cdot 10^8$
10: water-gas	1	0.7	$2.4 \cdot 10^{-4}$	1000	100	0	0	10^8	10^7
11: water-gas	400	200	0.095	1000	50	0	25	$5 \cdot 10^7$	$2.5 \cdot 10^7$

Table V.6: Parameters for the fluid/fluid test cases: initial state (material 1 on the left and material 2 on the right) and initial position of the interface $x_B(0)$.

Grid refinement

We perform three tests with different grid spacing, with the aim of showing that the all-speed scheme (III.19) modified the multi-material conditions introduced in Sec. V.2.2 is convergent in different regimes.

Test 7 is a gas-gas Sod shock tube, with the same perfect gas everywhere in the tube. This is a mono-material test, thus the interface corresponds to the material wave. The Mach number on the material wave is around 0.9, hence we are dealing with a fully compressible regime. Fig. V.9 shows that the scheme is convergent to the exact solution and it is stable. Both the pressure and the velocity profile are continuous on the contact wave as expected. The correct velocity of the material wave is well approximated and consequently also its correct position is recovered. The density profile suffers from the overheating effect, due to the "wall conditions" imposition for the material wave approximation. This effect slowly decreases when refining the grid. The results are obtained with the enforcement of a material CFL condition $\nu_{mat} = 0.3$. For this test, the material condition corresponds to an acoustic CFL $\nu_{ac} = 0.9$ because we deal with a Mach number close to 1. This explains the accurate approximation of the acoustic waves.

Test 8 is a low Mach gas-gas Sod tube, with two different adiabatic constants γ. In the tube, a small pressure ratio and a small velocity on the right are imposed. Both gases are expanding in

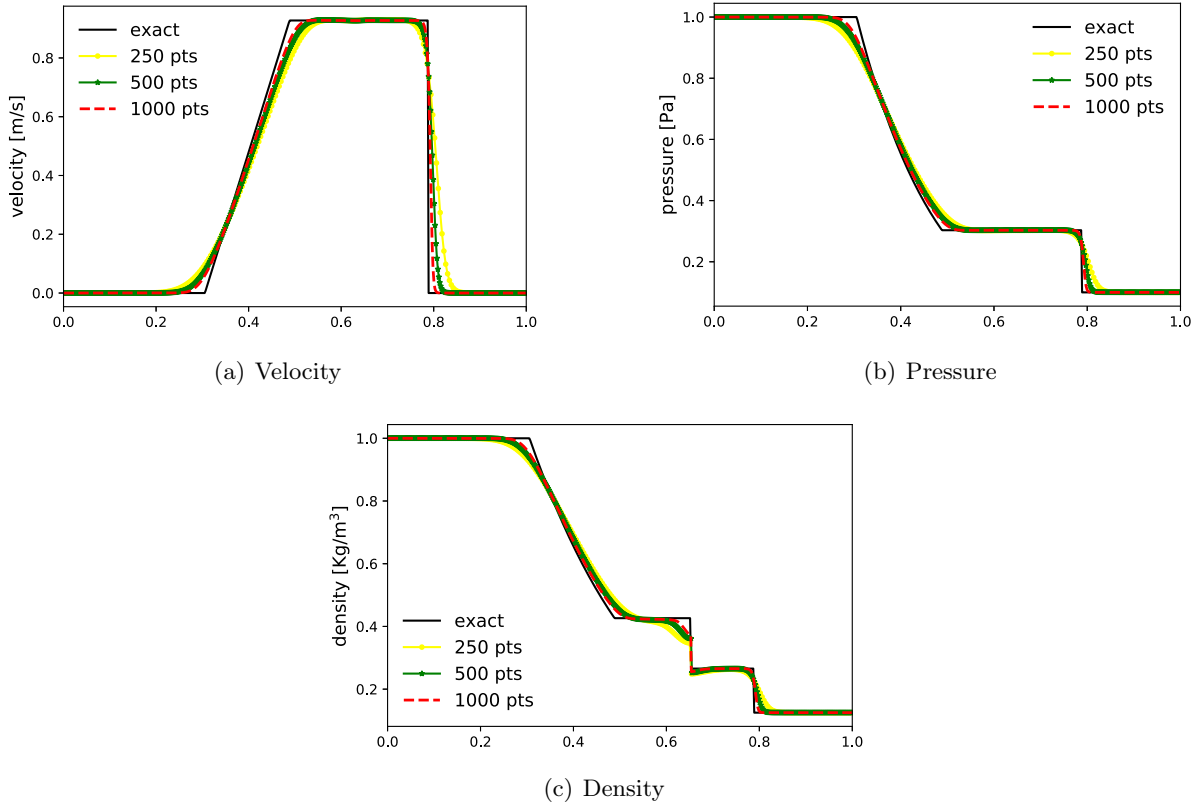(a) Velocity

(b) Pressure

(c) Density

Figure V.9: *Test 7*: gas-gas tube, results obtained with the all-speed multi-material scheme for an increasing number of points with $\nu_{mat} = 0.3$.

the two directions with two small rarefaction waves. The interface between the two gases moves very slowly if compared to the acoustic waves (the Mach number on the interface is $M \simeq 6 \cdot 10^{-3}$). After 0.25s, the interface has only moved from $x_B(0) = 0.5$ to $x_B(t_{end}) = 0.5012$, namely it has crossed 1 cell for a grid spacing $\Delta x = 10^{-3}$. In Fig. V.10 we observe that he interface is kept sharp and its correct position and velocity are reproduced. The acoustic waves are smoothed due to the choice of a material constraint on the time step $\nu_{mat} = 0.2$.

Test 9 is a water-water low Mach tube where a very small pressure ratio is imposed. The Mach number on the interface (which here corresponds to the material wave) is around $2.5 \cdot 10^{-3}$. The contact wave moves from $x_B(0) = 0.5$ to $x_B(t_{end}) = 0.5008$m. Fig. V.11 shows that the material wave is sharp and its correct position and speed are accurately captured. Once again, the acoustic waves are smoothed due to the choice of a material time step obtained with $\nu_{mat} = 0.2$.

Comparison with mono-material schemes

We compare the results of the multi-material scheme (in its upwind and all-speed versions) with the mono-material all-speed relaxation scheme introduced in Chapter III. Of course, this can be done only if the interface separates chambers filled with the same material, namely the interface corresponds to a material wave. We focus on low Mach material waves, propagating at slow velocity.
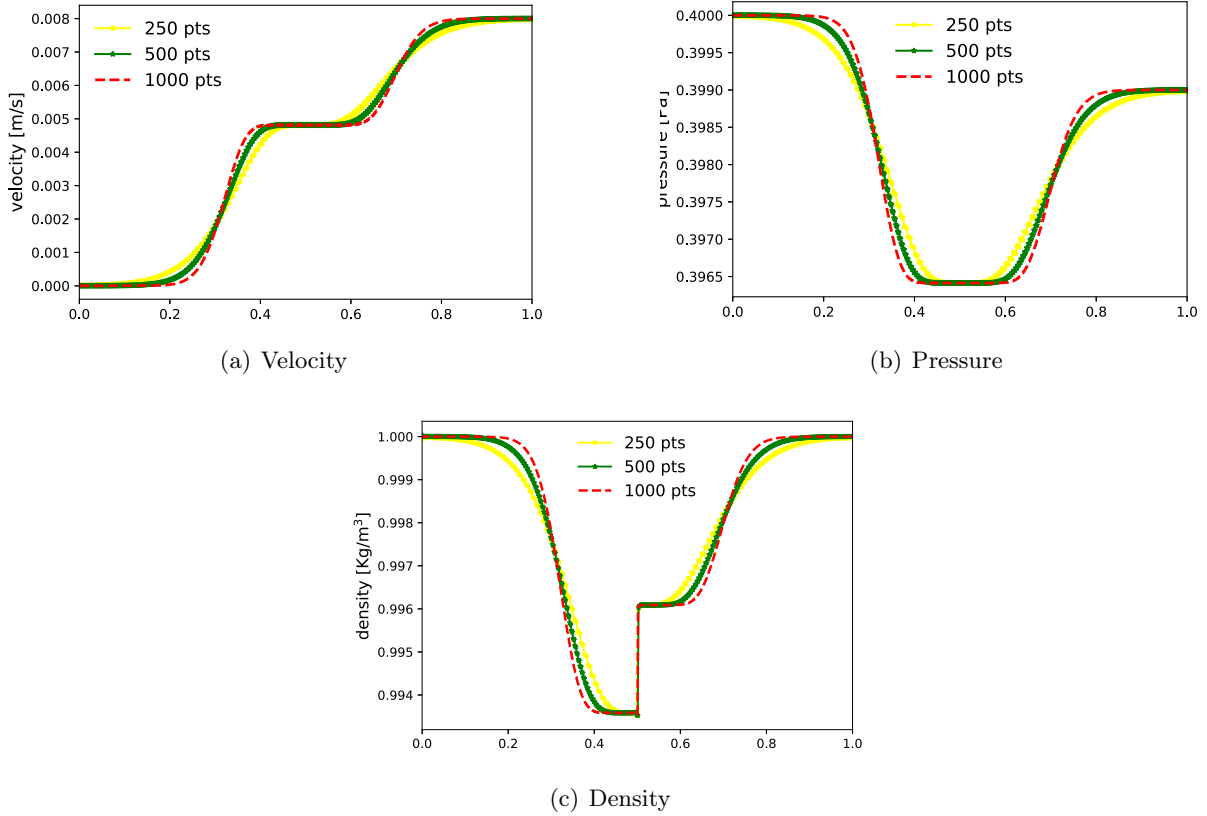
(a) Velocity

(b) Pressure

(c) Density

Figure V.10: *Test 8*: low Mach gas-gas tube (two different gases). Results obtained with the all-speed multi-material scheme for an increasing number of points with $\nu_{mat} = 0.2$.

In Fig. V.12 we plot a zoom on the density for *tests 8.1 and 9.1*. These tests are low Mach tubes filled with perfect gas and water respectively. A small pressure ratio and small velocity on the right are applied. For test 8.1 the material wave is initially in $x_B(0) = 200$ and after 150 seconds it is in $x_B(t_{end}) = 200.71$, namely for a grid spacing $\Delta x = 10^{-1}$ it crosses 7 cells. For test 9.1, after 0.095 seconds the material wave is in $x_B(t_{end}) = 200.76$, namely for a grid spacing $\Delta x = 10^{-1}$ it crosses 8 cells. The curves in Fig. V.12 are obtained with a standard mono-material explicit-upwind scheme (yellow), with the mono-material all-speed scheme (green), and with the implicit multi-material schemes (blue and red). As already discussed in Chapter III, the mono-material all-speed scheme is superior in accurately capturing material waves in the low Mach regime with respect to a standard explicit-upwind scheme. With the multi-material model (no matter how the spatial derivatives are discretized) the material wave is kept sharper with respect to the mono-material scheme, since it is treated as an interface. This comes from the fact that we are introducing a "material wave reconstruction", whereas a mono-material scheme produces a "material wave approximation".

Comparison of the spatial discretizations

By using the general implicit discretization (V.1), we compare the results obtained with the three discretizations of the advective part in the bulk of the flow (upwind (III.9), centered (III.14) and
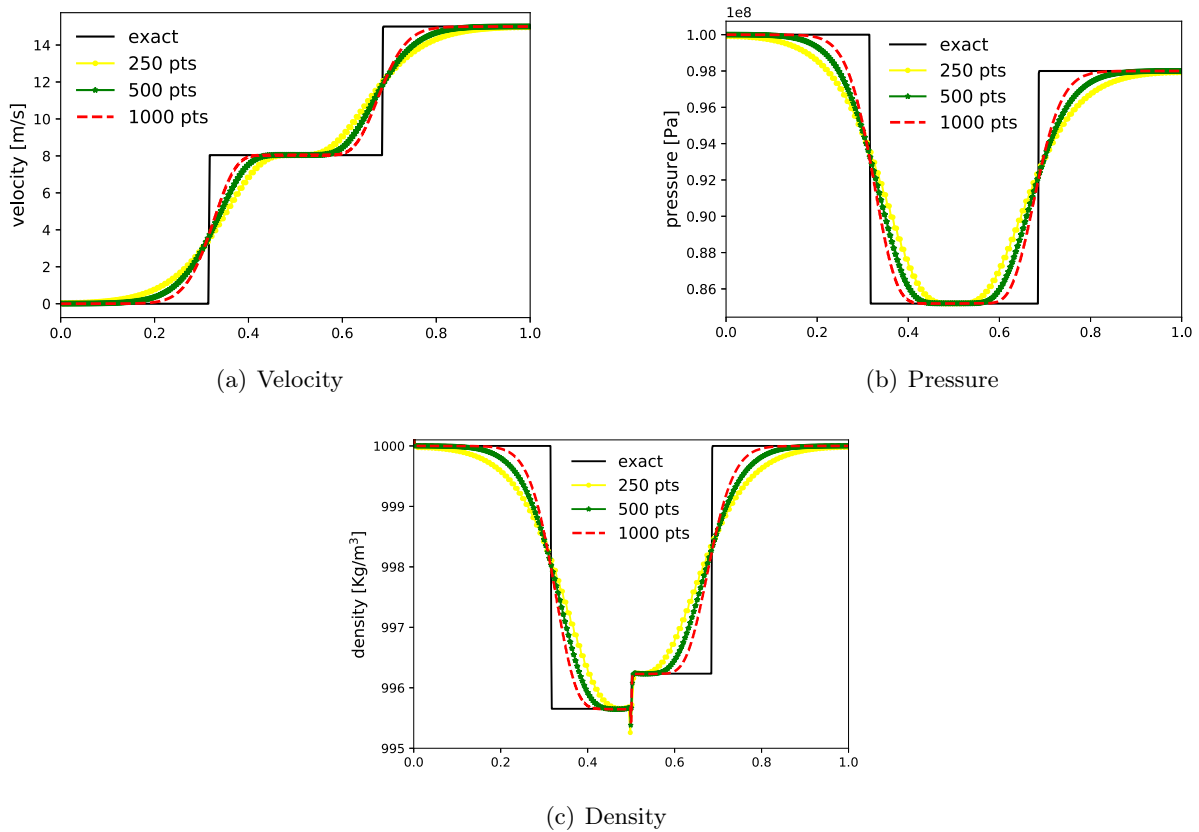
117

(a) Velocity

(b) Pressure

(c) Density

Figure V.11: *Test 9*: water-water tube, results obtained with the all-speed multi-material scheme for an increasing number of points with $\nu_{mat} = 0.2$.

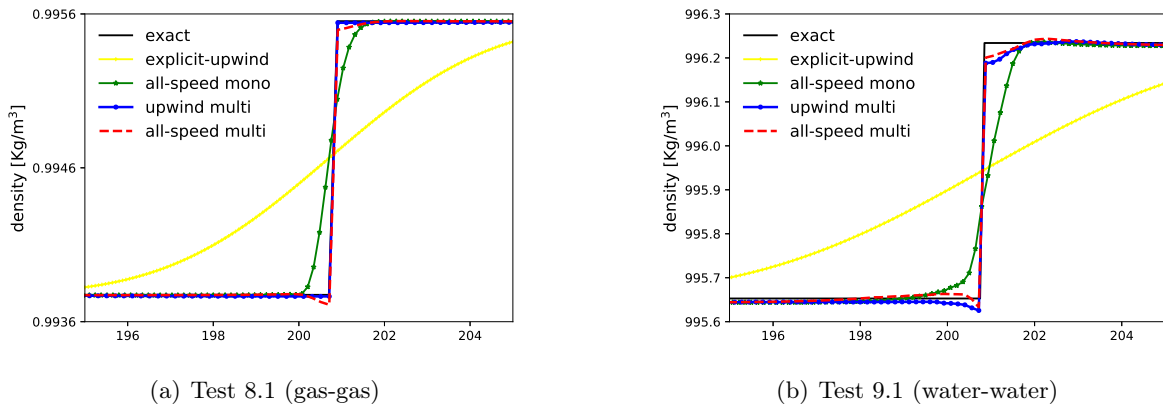
(a) Test 8.1 (gas-gas)

(b) Test 9.1 (water-water)

Figure V.12: *Test 8.1* in panel (a) and *test 9.1* in panel (b): low Mach gas-gas and water-water tubes (zoom on the material wave in the density profile). Comparison of the multi-material schemes (upwind and all-speed) with the "mono-material" all-speed scheme and a standard explicit-upwind scheme.

all-speed (III.18) discretizations). Each one of the three schemes employs the implicit multi-material interface conditions described in Sec. V.2.2.

Test 10 is a water-air shock tube. The interface is initially in $x_B(0) = 0.7$ and moves to

(a) Velocity

(b) Pressure

(c) Density
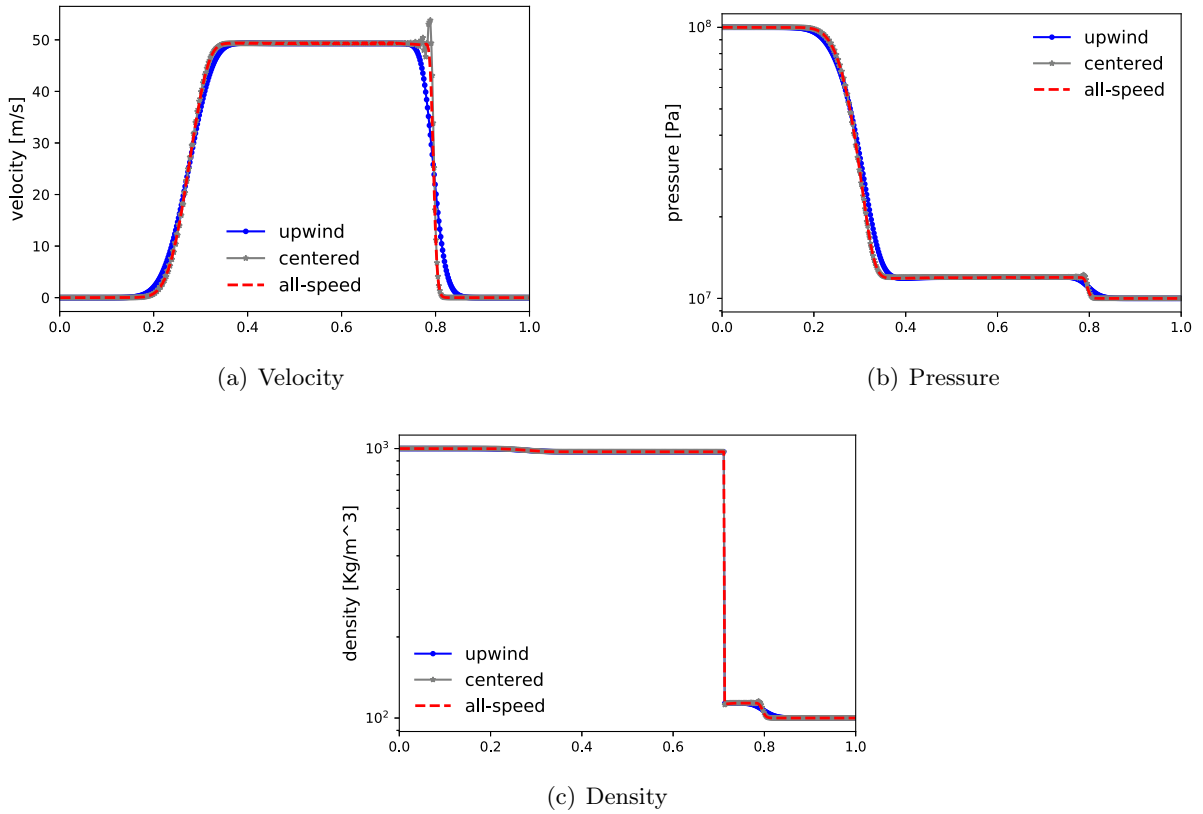
Figure V.13: *Test 10*: water-gas tube, results obtained with the three spatial discretizations modified with the multi-material interface conditions.

$x_B(t_{end}) = 0.712$. It means that for a grid spacing $\Delta x = 2 \cdot 10^{-3}$ it overcomes 12 cell centers. We are dealing with a "multi-regime" test. In fact, on the left of the interface (water side) we have $M^- \simeq 0.035$, instead on the right (gas side) $M^+ \simeq 0.13$. Thus, we have a weakly compressible regime in water and a fully compressible subsonic regime in the gas. The water is expanding with a rarefaction, which moves to the left very fast if compared to the velocity of the interface. A shock occurs in the gas due to compression. We observe that all the three density profiles in Fig. V.13 keep the interface sharp and recover the correct speed and position. However, due to the presence of different regimes, the all-speed scheme is the most accurate on the acoustic waves. Due to the local Mach number combination, it provides the correct numerical viscosity on each wave.

Test 11 is a low Mach water-air tube. The regime is everywhere low Mach, with a lower Mach number on the left side ($M^- \simeq 6.5 \cdot 10^{-3}$ and $M^+ \simeq 0.027$). The interface moves very slowly, hence we consider a long integration in time. For this simulation we enforce $\nu_{mat} = 0.2$, giving a time step $\Delta t = 8 \cdot 10^{-4}$ on a grid spacing $\Delta x = 10^{-1}$. The interface is initially in $x_B(0) = 200$ and at the end of the simulation it is in $x_B(t_{end}) = 201.103$, namely it crosses 11 cells. In Fig. V.14 we can observe that the interface is kept sharp even after long times (see the zoom on the density in Fig. V.14(d)) and its velocity and position are accurately approximated. The other two waves are smoothed due to the use of a material constraint on the time step.
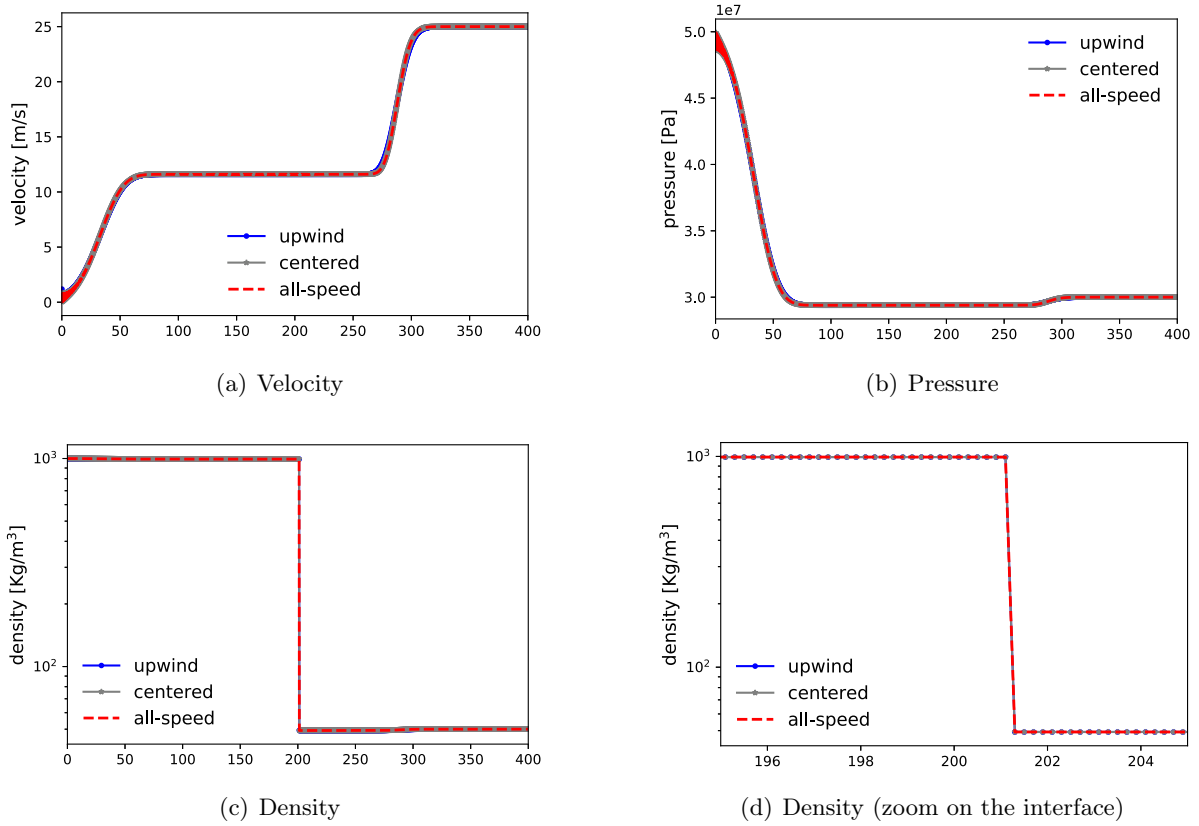
(a) Velocity

(b) Pressure

(c) Density

(d) Density (zoom on the interface)

Figure V.14: *Test 11*: water-gas low Mach tube, results obtained with the three spatial discretizations modified with the multi-material interface conditions.

V.3.2.2 Solid/solid

Test	Materials	Regime	γ_1	γ_2	$p_{\infty,1}$ (Pa)	$p_{\infty,2}$ (Pa)	χ_1 (Pa)	χ_2 (Pa)
12	copper-copper	$M \simeq 0.14$	4.22	4.22	$3.42 \cdot 10^{10}$	$3.42 \cdot 10^{10}$	$5 \cdot 10^{10}$	$5 \cdot 10^{10}$
13	copper-copper	$M \simeq 2.6 \cdot 10^{-3}$	4.22	4.22	$3.42 \cdot 10^{10}$	$3.42 \cdot 10^{10}$	$5 \cdot 10^{10}$	$5 \cdot 10^{10}$
14	copper-gas	$M^- \simeq 2.5 \cdot 10^{-2}$; $M^+ \simeq 0.9$	4.22	1.4	$3.42 \cdot 10^{10}$	0	$5 \cdot 10^{10}$	0

Table V.7: Parameters for the solid/solid and solid/fluid test cases: materials and regime on the interface.

We study copper-copper interfaces, hence we have that $M_\chi \simeq M$ due to copper intrinsic properties $\mathcal{O}(\chi) = \mathcal{O}(p_\infty)$. This means that the speeds of shear and of longitudinal waves are of the same order of magnitude (see Section II.2). We present two copper-copper Sod tubes with shear, in two different regimes. With the first test we compare the three discretizations of the spatial derivatives and with the second we study the convergence by refining the grid.

In *test 12*, the Mach number at the interface is around 0.14, thus we are in the fully compressible regime. The interface is initially in $x_B(0) = 0.75$ and at the end of the simulation it is in $x_B(t_{end}) = 0.794$, namely for a grid spacing $\Delta x = 2 \cdot 10^{-3}$ it crosses 22 cells. Figs. V.15-V.16 show the results for the upwind, centered and all-speed discretizations of the spatial derivatives

Test	L	$x_B(0)$	t_{end}	ρ_1	ρ_2	$(u_1)_1$	$(u_1)_2$	$(u_2)_1$	$(u_2)_2$	p_1	p_2
	(m)	(m)	(s)	(Kg/m^3)	(Kg/m^3)	(m/s)	(m/s)	(m/s)	(m/s)	(Pa)	(Pa)
12: copper-copper	1.5	0.75	$5.6 \cdot 10^{-5}$	8900	8900	0	0	0	100	10^{11}	10^9
13: copper-copper	1	0.5	$5 \cdot 10^{-5}$	8900	8900	0	0	0	100	10^9	10^5
14: copper-gas	1	0.6	$8.7 \cdot 10^{-4}$	8900	50	0	0	0	0	$5 \cdot 10^9$	10^5

Table V.8: Parameters for the solid/solid and solid/fluid test cases: initial state (material 1 on the left and material 2 on the right) and initial position of the interface $x_B(0)$.

(a) Density   (b) Pressure
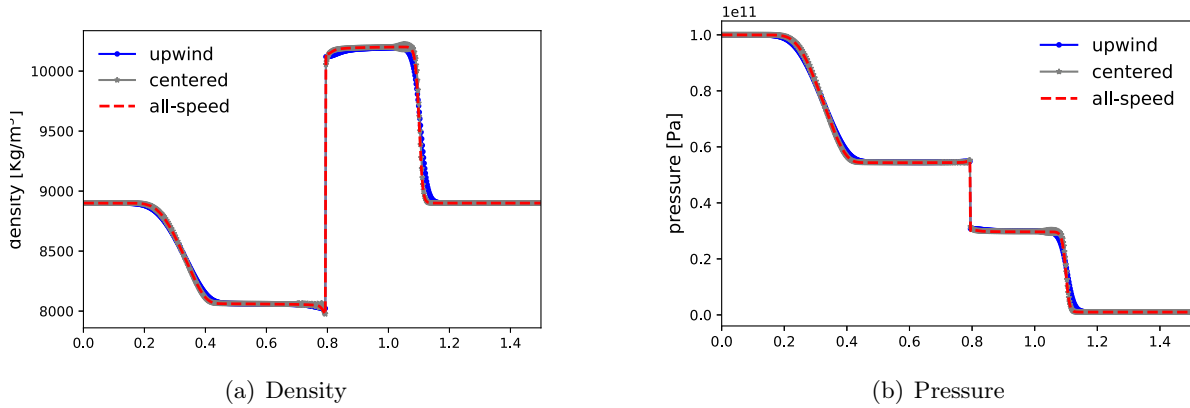
Figure V.15: *Test 12*: copper-copper tube, density and pressure obtained with the three spatial discretizations modified with the multi-material interface conditions.

away from the interface. We can observe that the interface stays sharp and its position and velocity are accurately captured. The centered scheme develops some oscillations on the material wave in the transverse velocity and the tangential stress profiles, which should be continuous at the interface. Small oscillations of the centered scheme are present also on the fast longitudinal waves, as expected. A small overheating effect is present on the density profile when employing the upwind scheme. These results are obtained for a grid spacing $\Delta x = 2 \cdot 10^{-3}$ and for a time step $\Delta t = 5 \cdot 10^{-7}$, given by a material constraint $\nu_{mat} = 0.2$.

Test 13 is a low Mach tube, with a Mach number at the interface around $2.6 \cdot 10^{-3}$. The interface is initially in $x_B(0) = 1$ and at the end of the simulation is in $x_B(t_{end}) = 1.001$. In Figs. V.17-V.18 we show the results obtained with the all-speed multi-material scheme for an increasing number of points. We can observe that the interface stays sharp and its position and velocity are accurately captured. The small spikes at the interface on the density and pressure profiles are due to the overheating effect related to the wall conditions. This is progressively reduced by refining the grid. These results are obtained by enforcing a constraint on the time step $\nu_{mat} = 0.2$. The material CFL condition is responsible for the smoothing of the longitudinal and shear waves, which are too fast to be accurately captured.

V.3.2.3 Solid/fluid

Test 14 is a shock tube containing copper at high pressure and air at atmospheric pressure. This test case is stiff because at the initial time, the pressure and density ratios are very large, since the copper is compressed. The results for an increasing number of grid points are plotted in Fig.
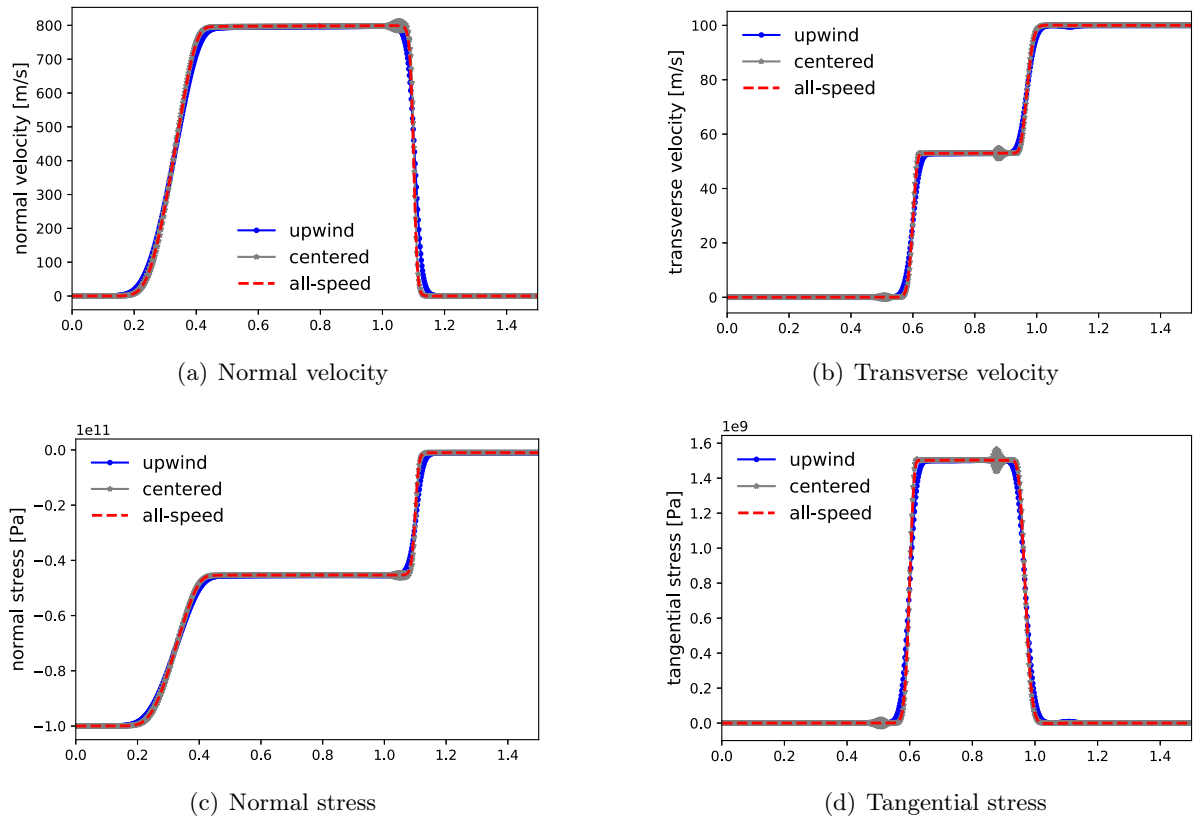
(a) Normal velocity

(b) Transverse velocity

(c) Normal stress

(d) Tangential stress

Figure V.16: *Test 12*: copper-copper tube, velocity field and stress tensor obtained with the three spatial discretizations modified with the multi-material interface conditions.
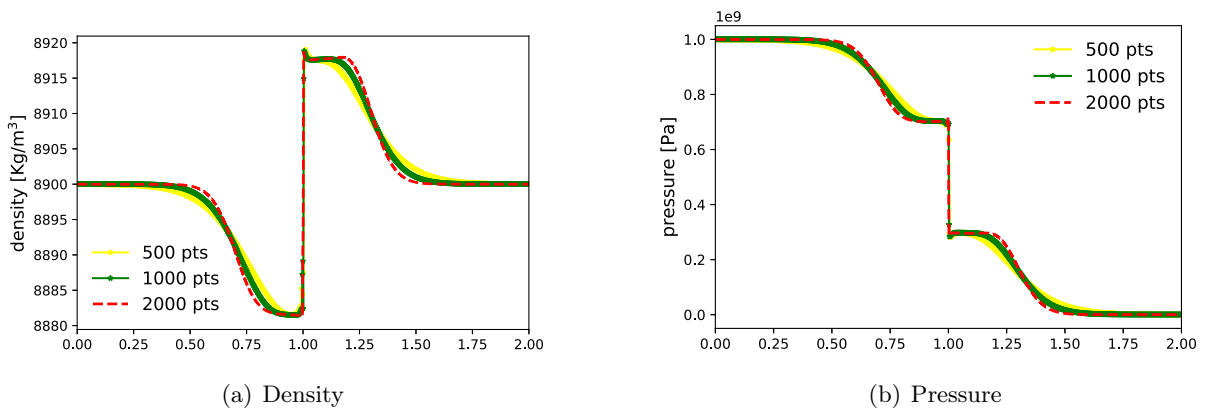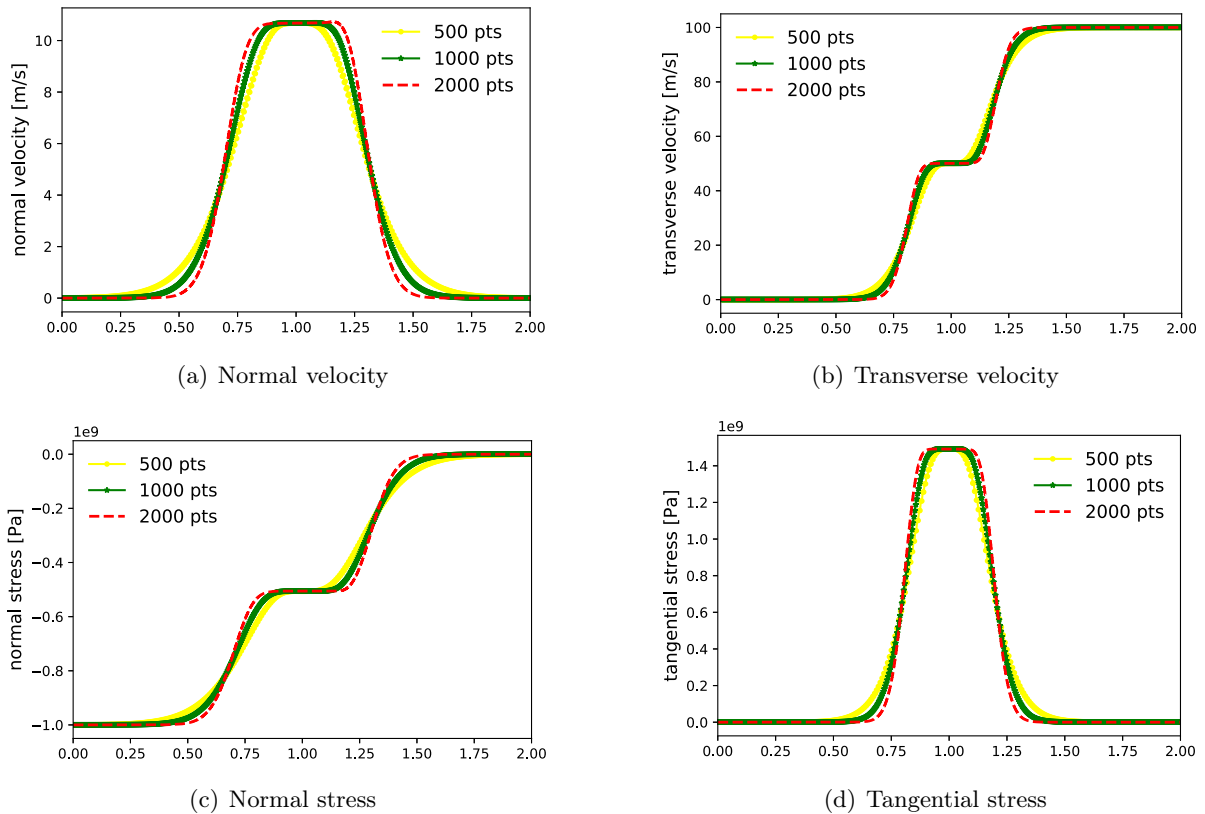

(a) Density

(b) Pressure

Figure V.17: *Test 13*: copper-copper low Mach tube, density and pressure obtained with the three spatial discretizations modified with the multi-material interface conditions.

V.19, where numerical convergence is observed. The normal velocity and the normal stress are continuous at the interface. The pressure and the density are discontinuous and we can see a shock wave transmitted in air. For these results, a local Newton subiteration to deal with the linearizations on the interface conditions is needed. As explained in Sec. V.2.2, this is due to highly non-linear wave pattern, with a shock wave occurring in the close neighbourhood of the

(a) Normal velocity

(b) Transverse velocity

(c) Normal stress

(d) Tangential stress

Figure V.18: *Test 13*: copper-copper low Mach tube, velocity field and stress tensor obtained with the three spatial discretizations modified with the multi-material interface conditions.

interface at Mach number of order 1.

V.4 Preliminary conclusions

In this chapter, we have proposed a completely implicit numerical method for moving boundaries and multi-material interfaces. The main purpose of the present method is the simulation of weakly compressible and low Mach multi-material flows. Moving walls are accurately solved and multi-material interfaces are kept sharp, accurately capturing their position and velocity. The scheme is able to deal with fluid/fluid, fluid/solid and solid/solid interfaces, as illustrated by the numerical tests. The multi-material model is validated on compressible and weakly compressible flows, adopting away from the boundaries the all-speed scheme proposed in the first part of thesis.

In the next chapter, the numerical method is extended to solve multi-material flows in two dimensions. The interface will be described with a level set function, coherently with the adopted fully Eulerian approach and the multi-material interface conditions will be extended in 2D.
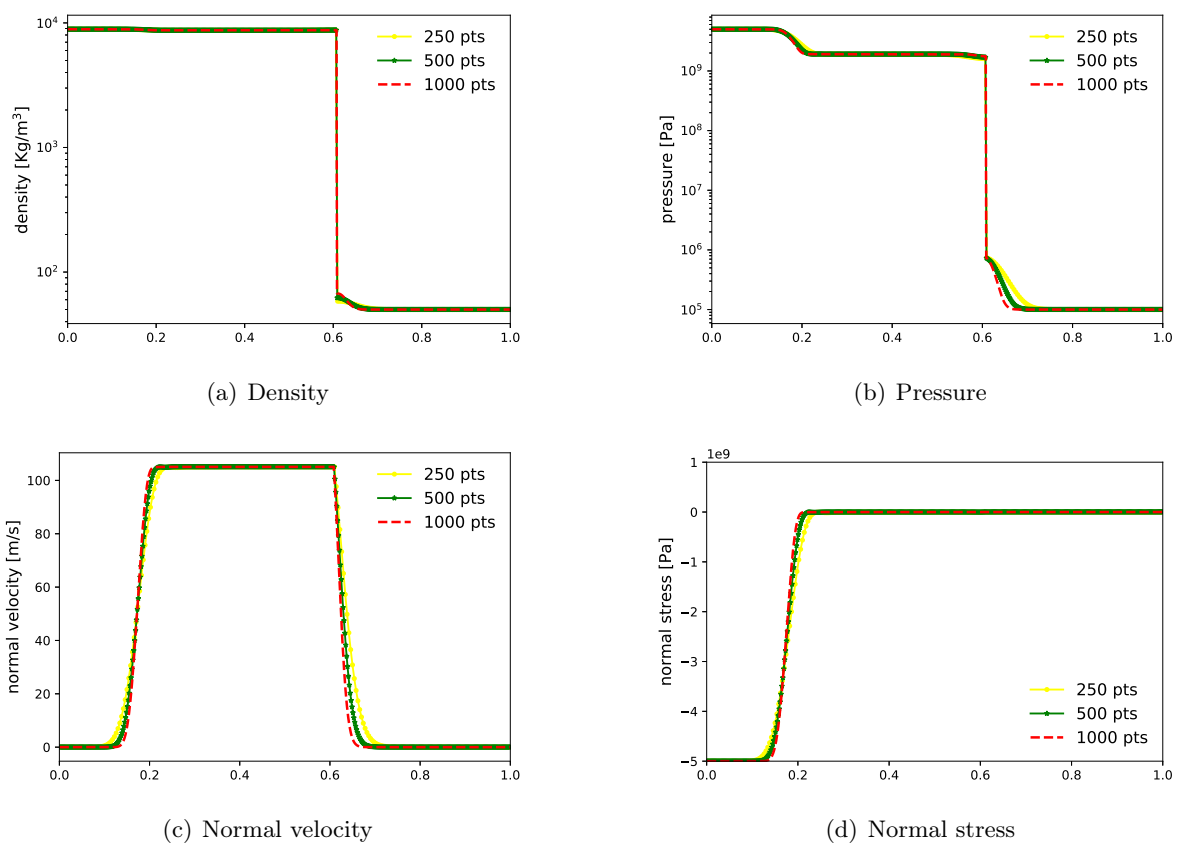
(a) Density

(b) Pressure

(c) Normal velocity

(d) Normal stress

Figure V.19: *Test 14*: copper-gas tube, results obtained with the multi-material all-speed scheme for an increasing number of points.

Chapter VI

Multi-material flows in two dimensions

This chapter is devoted to the extension of the implicit multi-material model to two dimensional problem. In the case of simulations on Cartesian grids, the mesh is not adapted to the geometry of the interfaces separating two different media. Therefore, a level set function is introduced in order to track the interface position on Cartesian grids. For the level set advection, we adopt a second order accurate semi-Lagrangian method, due to the constraints of the parallel communications in the Bitpit library. The level set is initialized as a distance function and identifies the contour of an object. The materials that are present in the computational domain are identified by a marker function.

Some simulations are presented in order to validate the two dimensional multi-material code, including a shock-bubble interaction and a low speed impact.

VI.1   The level set method

The level set method was initially introduced by Osher and Sethian [97] to track moving interfaces. This method allows to represent a curve in $\mathbb{R}^2$ or a surface in $\mathbb{R}^3$ without an explicit parametrization of both. Moreover, the level set method allows the coalescence and the division of fronts.

A function φ is defined in the way that its zero level $\varphi = 0$ corresponds to the interface that has to be tracked in the domain. One can also compute the interface normal $\mathbf{n}$ and its curvature κ in the following way

$$\mathbf{n} = \frac{\nabla \varphi}{|\nabla \varphi|} \ \text{ and } \ \kappa = \nabla \cdot \mathbf{n}. \tag{VI.1}$$

Generally, the function φ is taken as a signed distance function, where the sign changes from the left to the right of the interface (we refer the reader to Fig. VI.1(a), where the zero contour of a level set function is depicted on a computational grid). Letting Ω be an object with boarder Γ, then the level set function φ can be defined as

$$\varphi\left(x, t\right) = \begin{cases} -|x - \Gamma| \text{ if } x \in \Omega \\ |x - \Gamma| \text{ if } x \notin \Omega \end{cases} \tag{VI.2}$$

This is a signed distance function that satisfies the property $|\nabla \varphi| = 1$.

The level set function φ defines the contour of an object that can move inside inside the computational domain and that can be deformed in a multi-material perspective. Thus, the level set function is transported with the velocity field $\mathbf{u}$ of the considered flow. The following advection equation has then to be solved

$$\partial_t \varphi + \mathbf{u} \cdot \nabla \varphi = 0. \tag{VI.3}$$

This equation advects the zero isoline of the function φ by reproducing the movements and deformations of the considered material interface.

If the velocity field is non-uniform, the function φ can rapidly loose its signed distance function property during the numerical integration of equation (VI.3) and it may become distorted. This fact can introduce some numerical problems where the gradients of the function φ are very stiff. In order to restore the signed distance function property, a possible solution is the use of the Eikonal equation $|\nabla \varphi| = 1$, which can be solved with a fast-marching method, as proposed by Sethian in [117]. Another possible option can be the implementation of a reinitialization method, by solving the reinitialization equation

$$\partial_\tau \varphi + S(\varphi_0)(|\nabla \varphi| - 1). \tag{VI.4}$$

This is traditionally iterated for a few steps in fictitious time τ to steady state in order to reinitialize a level set function φ_0 into the signed distance function φ. Here $S(\varphi_0)$ is a smoothed sign function. The reinitialization method was firstly introduced by Sussman et al. in [120, 119] and then a subcell-fix technique that consistently improves the resolution of equation (VI.4) was proposed by Russo and Smereka in [109].

VI.1.1 Numerical integration of the level set

In Sections IV.3 and IV.5.1, the constraints due to the code parallelization in the Bitpit library have been presented. We remind the reader that these are mainly related to the fact that parallel communications are limited to only the first layer of neighboring cells (see Fig. IV.1). This implies that the stencil used in the numerical integration of the level set transport equation (VI.3) is restricted and thus the spatial interpolation limits the precision of the scheme.

In order to solve the level set advection on Cartesian grids that are based on quadtrees, we implement a semi-lagrangian method which consists in a second order Runge-Kutta time integration and in a biquadratic interpolation in space. We remark that we cannot use cubic or higher order interpolations due to the parallel communications constraint. In this first attempt of solving multi-material problems in 2D, only uniform grids are used, but the extension of the proposed method to the use of adaptive grids is straightforward.

VI.1.1.1 A second order accurate semi-Lagrangian method

The basic idea of semi-lagrangian methods is the reconstruction of the solution by numerically integrating the advection equation along characteristic curves, starting from any point x_i of the computational grid. The solution in a generic point x_i is computed by coupling an ODE method, which is used to find the upwind points with respect to the grid nodes, and an interpolation method, in order to compute the solution at those nodes. Semi-Lagrangian methods have been

widely studied in literature and some references for advection problems can be found in [51, 90, 130] and references therein.

The Lagrangian form of the level set transport equation (VI.3) reads

$$
\begin{cases}
\dfrac{D\varphi}{Dt} = 0 \\
\dfrac{Dx}{Dt} = \mathbf{u}\left(x, t\right),
\end{cases}
$$

where we are noting as $D \cdot /Dt$ the material derivative. The second equation solution gives the characteristics lines. In the semi-Lagrangian approach, at every time step, a discrete set of particles arriving at the grid points is tracked backward over a single time step along its characteristic up to its departure points, namely we have $\varphi^{n+1}\left(x^{n+1}\right) = \varphi^n\left(x_d\right)$. Here x^{n+1} is any grid node and x_d is the corresponding departure point from which the characteristic curve originates. As in [93, 130], we adopt the second order mid-point method for locating the departure point:

$$
\begin{aligned}
\widehat{x} &= x^{n+1} - \frac{\Delta t}{2} \cdot \mathbf{u}^n\left(x^{n+1}\right) \\
x_d &= x^{n+1} - \Delta t \cdot \mathbf{u}^{n+1/2}\left(\widehat{x}\right).
\end{aligned}
\tag{VI.5}
$$

This is is a second order Runge Kutta method (RK2). The velocity at the mid-time step $t^{n+1/2}$ is defined by a linear combination of the velocities at the two previous time steps, namely $\mathbf{u}^{n+1/2} = 3/2\mathbf{u}^n - 1/2\mathbf{u}^{n-1}$.

In general, the points $\widehat{x}$ and x_d do not coincide with grid points. Therefore, one needs an interpolation procedure to define both $\mathbf{u}^{n+1/2}\left(\widehat{x}\right)$ and $\varphi^n\left(x_d\right)$. In this sense, we adopt a two dimensional quadratic Lagrangian interpolation. The full biquadratic basis is defined as follows

$$
\left\{1, x, y, xy, x^2, y^2, x^2y, xy^2, x^2y^2\right\}
\tag{VI.6}
$$

and it covers a stencil of nine cells. In the cases of an adaptive grid, at a T-junction in a level jump, this stencil may be reduced. Thus, also the basis has to be reduced, by preserving its symmetry in the following ways

$$
\begin{aligned}
&\left\{1, x, y, xy, x^2, y^2, x^2y, xy^2\right\} \\
&\left\{1, x, y, xy, x^2, y^2, x^2y^2\right\},
\end{aligned}
$$

according to the number of cells of the considered stencil.

As proved by Falcone and Ferretti in their seminal work [51], the accuracy of a general semi-lagrangian method has the following formulation

$$
\mathcal{O}\left(\Delta t^k + \frac{\Delta x^{p+1}}{\Delta t}\right),
\tag{VI.7}
$$

where k is the accuracy of the time integration method and p is the degree of the interpolant, namely $p+1$ is the order of accuracy of the chosen interpolation procedure. For example, this means that the simplest semi-Lagrangian scheme with linear interpolation is equivalent to the classical first order upwind scheme. In our case, with the RK2 time integration (VI.5) and the

biquadratic interpolation (VI.6) that has an overall accuracy of $p + 1 = 3$, the error estimate (VI.7) becomes

$$\mathcal{O}\left(\Delta t^2 + \frac{\Delta x^3}{\Delta t}\right) \simeq \mathcal{O}\left(\Delta x^2\right),$$

where the last simplification is due to the enforcement of the CFL constraint.

VI.2   Multi-material model in two dimensions

The multi-material model derived in Chapter V is easily extended to two dimensional problems, with the introduction of a level function to track the interface. This is done as explained in the previous section. Our approach falls into the category of a sharp interface treatment (see Section V.1.2), which is an extension to multi-material flows of "immersed boundary" methods. The interface is considered as a contact discontinuity, which can arbitrarily cross the grid cells and the transmission conditions are applied via interpolations.

The multi-material interface conditions derived in Sec. V.2.2 can be applied to two dimensional problems once again in a "direction by direction" approach. We here write these conditions focusing on direction x_1, the same considerations will apply to an interface along direction x_2. Let $C_{k,j}$ and $C_{k+1,j}$ be two contiguous cells sharing the interface $x_{k+1/2,j}$ and let the two cells be filled by different materials. The normal velocity u_1 and the normal component of the stress tensor σ^{11} are continuous, whereas the density is discontinuous through the multi-material interface. We compute all the quantities of interest with averages and extrapolations side by side as in the 1D model. Since the proposed interface treatment is implicit, all the equilibrium conditions are written at time t^{n+1}, as in 1D. This is due to the fact that our goal is to solve weakly compressible and low Mach flows. The conditions read as follows:

$$\begin{cases} \left(\sigma_{k+1/2,j}^{11,n+1}\right)^- = \left(\sigma_{k+1/2,j}^{11,n+1}\right)^+ = \dfrac{\left(\sigma_{k,j}^{11}\right)^{n+1} + \left(\sigma_{k+1,j}^{11}\right)^{n+1}}{2} \\[2mm] \left((u_1)_{k+1/2,j}^{n+1}\right)^- = \left((u_1)_{k+1/2,j}^{n+1}\right)^+ = \dfrac{(u_1)_{k,j}^{n+1} + (u_1)_{k+1,j}^{n+1}}{2} \\[2mm] \left(\rho_{k+1/2,j}^{n+1}\right)^- = \rho_{k,j}^{n+1}; \qquad \left(\rho_{k+1/2,j}^{n+1}\right)^+ = \rho_{k+1,j}^{n+1}, \end{cases}$$

where we are restricting the extrapolation to the first layer of cells. For the other quantities of interest, we distinguish three different cases:

1. *fluid/fluid interface*: the tangential stress is equal to zero and the transverse velocity is discontinuous, then we set

$$\begin{cases} \left(\sigma_{k+1/2,j}^{21,n+1}\right)^- = \left(\sigma_{k+1/2,j}^{21,n+1}\right)^+ = 0 \\[2mm] \left((u_2)_{k+1/2,j}^{n+1}\right)^- = (u_2)_{k,j}^{n+1}; \quad \left((u_2)_{k+1/2,j}^{n+1}\right)^+ = (u_2)_{k+1,j}^{n+1} \end{cases}$$

2. *solid/solid interface*: the transverse velocity in this case is continuous as the tangential stress

$$\begin{cases} \left(\sigma_{k+1/2,j}^{21,n+1}\right)^- = \left(\sigma_{k+1/2,j}^{21,n+1}\right)^+ = \dfrac{\sigma_{k,j}^{21} + \sigma_{k+1,j}^{21}}{2} \\[2mm] \left((u_2)_{k+1/2,j}^{n+1}\right)^- = \left((u_2)_{k+1/2,j}^{n+1}\right)^+ = \dfrac{(u_2)_{k,j}^{n+1} + (u_2)_{k+1,j}^{n+1}}{2} \end{cases} \qquad \text{(VI.8)}$$

3. *solid/fluid interface*: if one of the materials is a fluid, then inside this latter the tangential stress is zero, hence $\left(\sigma^{21}_{k+1/2,j}\right)^{-} = \left(\sigma^{21}_{k+1/2,j}\right)^{+} = 0$. The transverse velocity is instead discontinuous and then extrapolated from the two media as in (VI.8).

The geometrical quantities $Y^i_{,2}$ of the two materials must not be "mixed", especially in the case of a solid/fluid interface. First of all, the tensor $[\nabla Y]$ is not useful inside fluids. Secondly, the backward characteristics Y can be discontinuous at the multi-material interface. The fluid slips on the solid, thus we compute these values via extrapolations from each side as follows:

$$\left(\left(Y^i_{,2}\right)^{n+1}_{k+1/2,j}\right)^{-} = \left(Y^i_{,2}\right)^{n+1}_{k,j} \text{ and } \left(\left(Y^i_{,2}\right)^{n+1}_{k+1/2,j}\right)^{+} = \left(Y^i_{,2}\right)^{n+1}_{k+1,j}.$$

This extrapolation is necessary since it is required that the information on the gradients arrives only from the material corresponding to each side of the interface.

Once again, the interface conditions are derived on primitive variables. However, inside the full relaxation scheme we need to compute interface values of the conservative variables $\boldsymbol{\psi}$ and of the relaxation variables $\mathbf{v} = \mathbf{F}(\boldsymbol{\psi})$ and $\mathbf{w} = \mathbf{G}(\boldsymbol{\psi})$. This is dealt with the usual linearization of the interface conditions with respect to the conservative variables, as explained in Chapter V. Of course, as detailed for one dimensional problems, when solving fully compressible flows and/or flows where shocks interacting with the multi-material interfaces, a Newton sub-iteration is required to accurately recover the correct speed and position of the interface. In these case, the simple linearization is not enough due to the highly nonlinear structure of the wave pattern.

VI.2.1 Representation of the materials in the code

In order to identify which material is filling every cell of the computational mesh, we study the sign of the level set function. We define a marker function M that covers the entire discretized domain, such that

$$M(i,j) = \begin{cases} 1 \text{ if } \varphi(x_i, y_j) \geq 0 \\ 0 \text{ otherwise} \end{cases} \tag{VI.9}$$

Here (i,j) are the indexes of cell C_{ij} in two dimensions and $\varphi(x_i, y_j)$ is the value of the level set function in the center of this cell. Then, the value of M in the considered cell is accordingly associated to material 1 ($M = 1$) or to material 2 ($M = 0$). This is illustrated in Fig. VI.1, where we show a simple example with a level set function for a circle. The zero isoline is plotted and the corresponding marker M is built. Here, the circle is filled by material 1 and material 2 is the surrounding medium.

The marker function (VI.9) is used to determine the material filling a grid cell but also to determine if a cell is an interface cell or not. This implies that the marker is used in the code to choose if the numerical fluxes at a cell interface have to be computed with the multi-material conditions introduced above, or with the all speed spatial discretization (IV.8) in the case of a numerical interface separating two cells of the same material. In our first order approximation, the normal to the physical interface "locally" corresponds to the normals to the cell interfaces in directions x_1 and x_2. This approximation allows to avoid the computation of the normal of the level set function (VI.1). This way a reinitialization procedure is not strictly required. On the other hand, in this approximation the physical interfaces are somehow "pixelated". As expected, the more the mesh is refined, the less the pixelation effect is prominent.

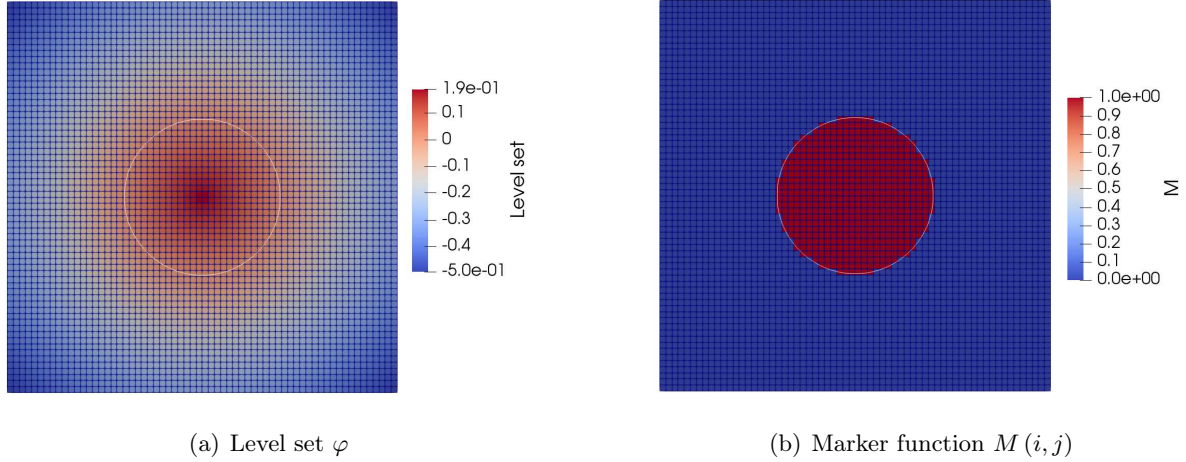(a) Level set φ

(b) Marker function $M(i,j)$

Figure VI.1: Grid and level set function for a circle (left panel). The zero isoline is depicted in white. Marker function $M(i,j)$ given the level set (right panel).

VI.2.2 Two-dimensional multi-material algorithm

The multi-material algorithm for two dimensional simulations follows the same logic of the one introduced in Section V.2.2 for one dimensional problems, except for the fact that we need to add the solution of the level set equation.

We summarize the algorithm steps from time t^n to time t^{n+1}:

1. advection of the level set function with the semi-Lagrangian method introduced in Section VI.1.1. In the integration of the transport equation (VI.3), the velocity field $\mathbf{u}$ is given by the velocity field computed at the previous time step t^n. In the mid-time step $t^{n+1/2}$ of the Runge Kutta scheme, the velocity is approximated as a linear combination of the velocities at the two previous time steps, namely $\mathbf{u}^{n+1/2} = 3/2\mathbf{u}^n - 1/2\mathbf{u}^{n-1}$;

2. update of the marker function (VI.9) by evaluating the level set φ^{n+1} in every cell and update the cells that have changed material by assigning "fictitious old states" through extrapolations from their neighbors;

3. setting of the interface conditions at all numerical interfaces via linearizations. The global linear system is assembled and solved with the GMRES method of PETSc, obtaining all the conservative and relaxation variables at time t^{n+1}.

Special care has to be devoted to step 2 of the algorithm: after the level set advection, its zero contour may cross some cell centers of the grid. In this case, these cells change the materials they are assigned to in the algorithm. Therefore, one needs to "build" a fictitious state at the previous time step that is associated to the new material, as done in 1D. We illustrate an example in Fig. VI.2, where we see that one cell changes material and needs this special treatment. The cells in blue correspond to $M = 1$ and the white ones to $M = 0$. The zero contour of the level set φ^{n+1} is represented here by the blue line. Cell $C_{i,j}$ changes material right after the level set advection, becoming a blue cell. Its state at time t^n was referring to the white material, hence we need to substitute it with a t^n fictitious state that is instead associated

to the blue material. This is done in order to prescribe a correct initial condition when building the linear system. This fictitious state is computed as the mean of the state $\boldsymbol{\psi}^-$ (computed via averages and extrapolations between cells $C_{i-1,j}$-$C_{i,j}$) and the state $\boldsymbol{\psi}^+$ (computed via averages and extrapolations between cells $C_{i,j+1}$-$C_{i,j}$).

The CFL condition on the time step may be acoustic or material, limiting Δt with the fastest characteristic speed or with the material velocity, respectively. Either ways, the interface corresponding to the zero contour cannot cross more than one cell at every time step.
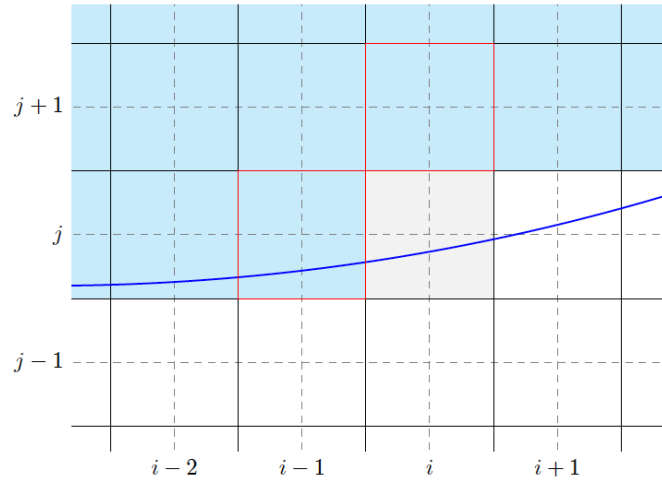
Figure VI.2: Scheme for the update of the cells. The blue line is the zero contour of the level set. The grey cell changes material (from white to blue). The cells with the red edges are used for the computation of the fictitious old state of the grey cell.

VI.3 Numerical simulations

In this section, some preliminary numerical results are presented, to validate the two dimensional multi-material scheme of the previous section. We solve the proposed problems on uniform grids to test the quality of the algorithm. We remark that the level set resolution with the semi-Lagrangian scheme of Section VI.1.1 has a lower accuracy if compared to previous works such as [62, 44], where a WENO interpolation of order 5 is adopted.

VI.3.1 Shock-bubble interaction

Test	Media	ρ (Kg/m^3)	u_1 (m/s)	p (Pa)	γ	p_∞ (Pa)
1	Air (pre-shock)	1.225	0	101325	1.4	0
	Air (post-shock)	1.6861	-156.26	250638	1.4	0
	Helium	0.228	0	101325	1.648	0

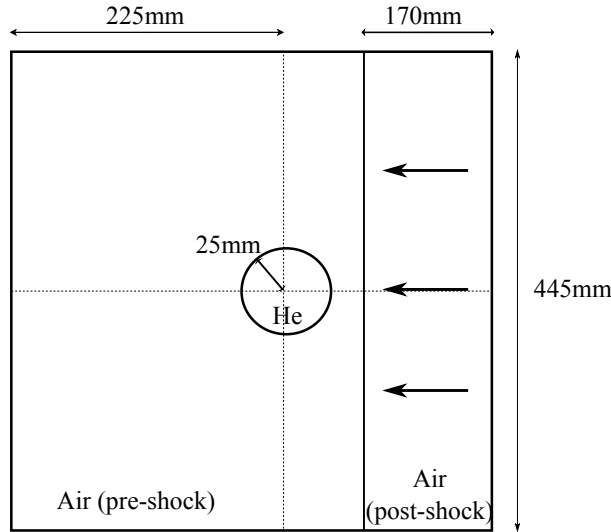**Table VI.1:** Parameters for the shock-bubble interaction test case.

Figure VI.3: Sketch of the computational domain for test 1 (helium bubble in air).

We solve a shock-bubble interaction test that is characterized by an interface separating two fluids. We point out that the surface tension is not taken into account in our model, so the solution is not physically relevant when the interface presents a high curvature. The interface may present instabilities that are related to the mesh size since the bubble splitting happens when a structure becomes smaller than the size of a computational cell. The boundary conditions are homogeneous Neumann boundary conditions at all four edges of the squared computational domain.

This test simulates the propagation of a right moving shock characterized by a Mach number $M_{shock} = 1.22$. The shock propagates in air through a helium bubble. The two gases have the same state law but they are characterized by a different adiabatic constant γ. This test case has been initially proposed in [106]. The initial configuration and the physical parameters are reported in Table VI.1, where we have that the helium bubble is contaminated with 28% of air. On Fig. VI.3, a sketch of the initial domain is drawn. We have chosen the initial conditions reported in [89, 62] for comparison purposes.

The results are plotted in Figs. VI.4-VI.5, showing the density at different times. The computation is performed on a uniform grid of 1024×1024 cells. The simulation is in good agreement with literature results (see [89, 62]), where the same problem was solved with standard explicit codes for fully compressible flows. We can observe that the shock propagates faster in the helium bubble than in air and that the reflection of the shock inside the bubble presents the typical patterns. Then, the bubble is deformed and the two chambers are linked by a small filament. The last picture in Fig. VI.5(b) shows that the level set is very fragmented. This is mainly due to the fact that the adopted second order semi-Lagrangian method is only second order accurate and that no reinitialization procedure is implemented. The improvement of the accuracy on the level set integration is currently under investigation. Another possible cause for the fragmentation may be the fact that the surface tension of the bubble is not taken into account in the model.
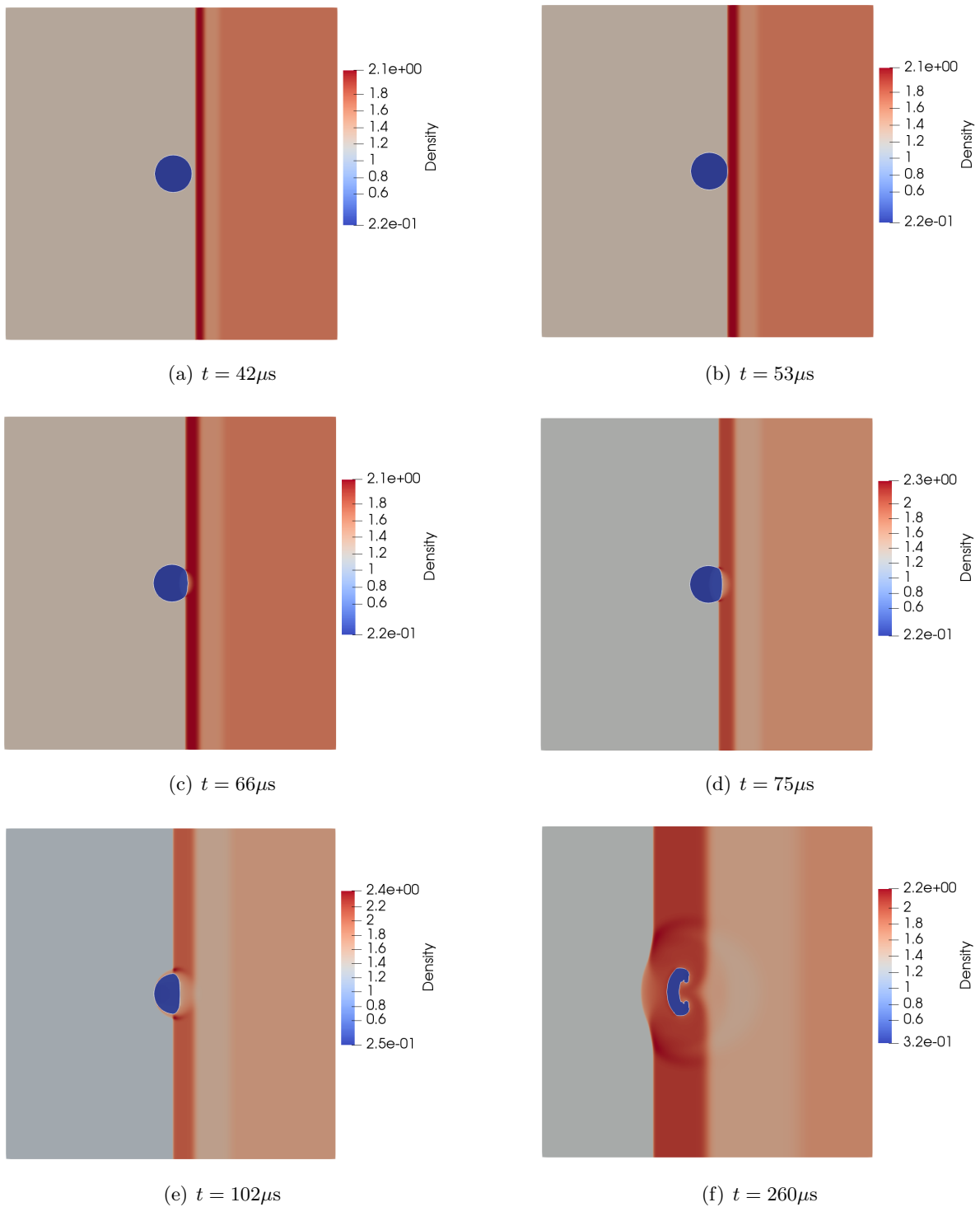
(a) $t = 42\mu$s

(b) $t = 53\mu$s

(c) $t = 66\mu$s

(d) $t = 75\mu$s

(e) $t = 102\mu$s

(f) $t = 260\mu$s

Figure VI.4: *Test 1*: density and zero contour of the level set for different time steps.

VI.3.2   Solid/fluid interfaces and impacts

In this section, we analyze two test cases on solid/gas interfaces: the first test consists in a simple advection of a copper ball in air (it can be seen as a projectile advection) and the second is an impact at low speed. These validations are meant to show the ability of the proposed numerical

(a) $t = 445\mu s$

(b) $t = 674\mu s$
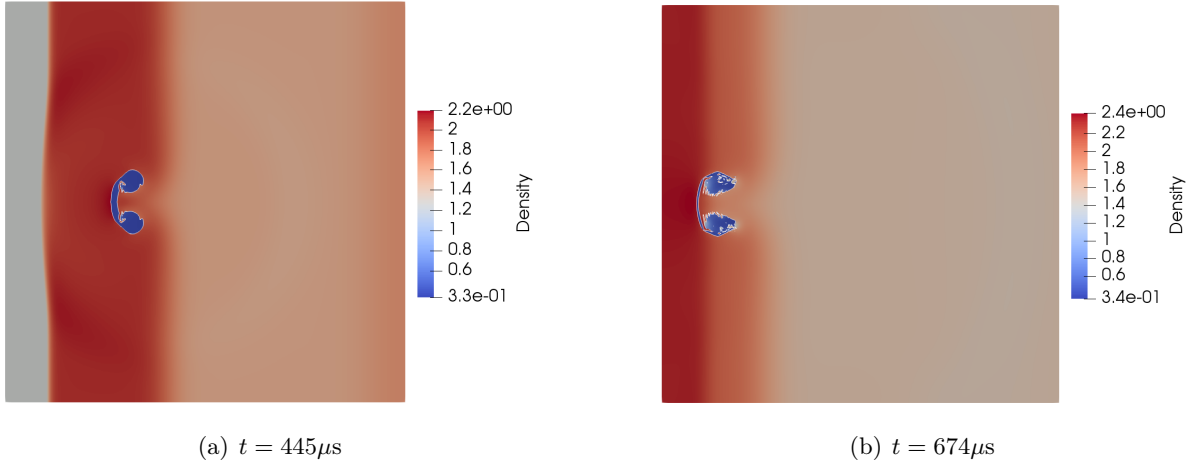
Figure VI.5: *Test 1*: density and zero contour of the level set for different time steps.

Test	Media	ρ (Kg/m^3)	u_1 (m/s)	u_2 (Pa)	p	γ (Pa)	p_∞	chi
2	Copper	8900	50	0	10^5	4.22	$3.42 \cdot 10^{10}$	$5 \cdot 10^{10}$
	Air	50	0	0	10^5	1.4	0	0
3	Copper (plate)	8900	0	0	10^5	4.22	$3.42 \cdot 10^{10}$	$5 \cdot 10^{10}$
	Copper (projectile)	8900	50	0	10^5	4.22	$3.42 \cdot 10^{10}$	$5 \cdot 10^{10}$
	Air	1.2	0	0	10^5	1.4	0	0

Table VI.2: Parameters for the solid/fluid interface test cases.

method to solve different problems concerning solid/fluid interfaces at low speed, however they have to be considered as preliminary results, as it will clarified in what follows.

We begin presenting a very simple test that consists in the advection of a ball of copper of radius $r = 0.15$m surrounded by a perfect biatomic gas. The gas is at rest and the copper ball normal velocity is initialized at 50 m/s. The pressure is uniform in the whole domain. This test case is a first validation of the solid/gas code, by simulating an advection of a solid continuum immersed in a perfect gas. The results are shown in Fig. VI.6 on a computational squared domain $[0, 1] \times [0, 1]$ meters, which is discretized with a grid of 512×512 cells. Here we plot the zero level set contour of the initial condition (time $t = 0$) and for three different times: $t = 0.45$ms, $t = 0.9$ms and the final time $t = 2.25$ms. The density and the velocity fields are shown at the final time. As expected, the center of the ball has moved along the normal direction x_1 of 22.5, 45 and 112.5 millimeters with respect to the initial position at the three time snapshots.

As a last case, we show the results of the simulation of the impact of a 50 m/s copper projectile on a copper plate immersed in air. Similar test cases at higher speeds have been performed in [62, 53] with multi-material explicit solvers for fully compressible flows. We expect to observe a deformation that is similar but slower with respect to the ones shown in these papers. The computational domain is a square $[-0.5, 0.5] \times [-0.5, 0.5]$ and the initial configuration with the initial state are reported in Fig. VI.7 and in Table VI.2. We start the simulation
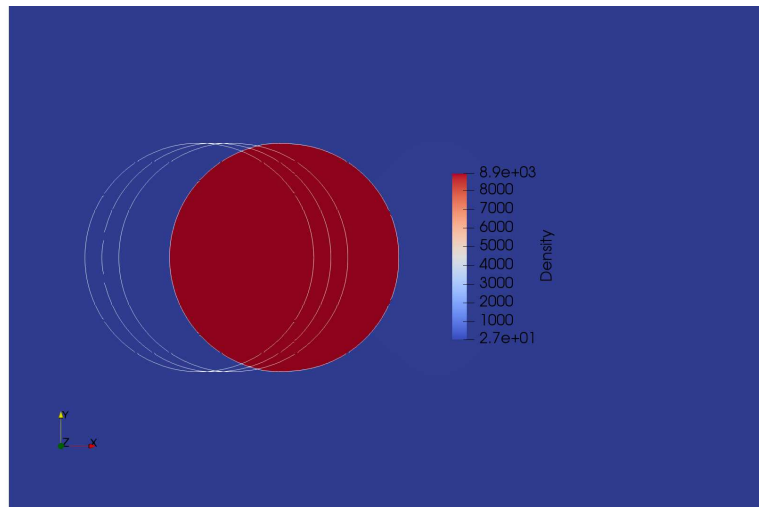
(a) Density
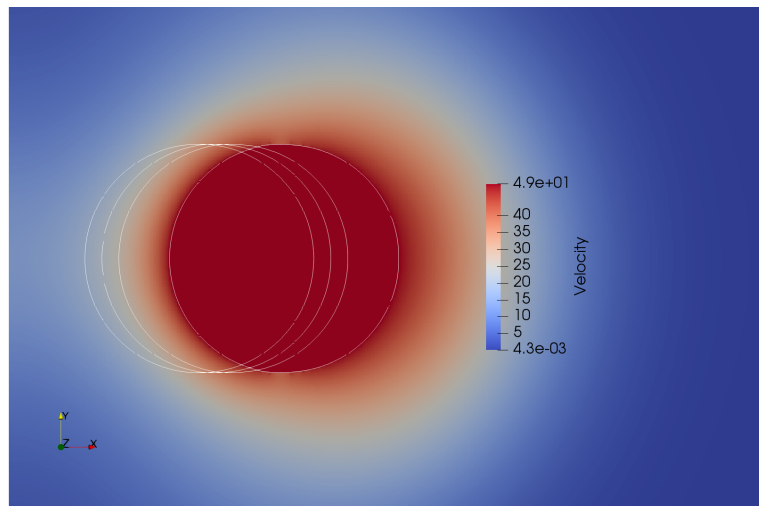
(b) Velocity

Figure VI.6: *Test 3*: density and velocity distributions at time $t = 2.25$ms. Zero level set contours plotted at the initial state $t = 0$ and at three different times $t = 0.45$ms, $t = 0.9$ms and $t = 2.25$ms.

when the projectile has already impacted the plate, i. e. they are adjacent at initial time. Homogeneous Neumann conditions are imposed at the boundaries and the chosen computational grid is 512×512 cells.

In Fig. VI.8 we report the results at four different time steps, by plotting the density profile and the zero contour. As expected, the elastic material is deformed while the projectile enters in the plate and the plate is shifted to the right. We can observe that some oscillations are present on the zero contour, especially at the up and down boarders of the plate. This simulation has to be considered a first attempt in the solution of slow speed impacts. The level set is lacking precision in its resolution, especially due to the geometry with corners. Some improvements regarding the level set are required, including a higher order scheme for the advection and also a reinitialization procedure that can help smoothing the oscillations. Moreover, sometimes
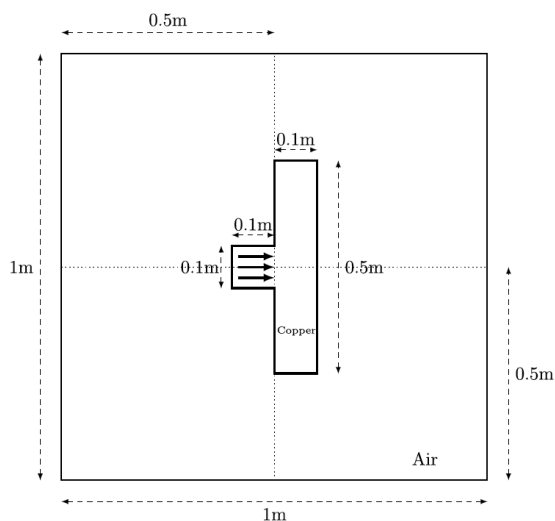
Figure VI.7: Sketch of the initial configuration for the impact test 3 (copper-air interaction).

negative oscillations are observed in the pressure function occurring in the gas domain near the interface of the plate. This may be related to the fact that the Newton subiteration used in the linearization of the interface conditions is stopped before convergence. Another reason may be related to the backward characteristics reconstruction: those are not usually solved in fluid dynamics and they might be responsible for the spurious oscillations in the pressure. The thorough investigation of these numerical oscillations will be carried out in order to improve these results.

VI.4   Preliminary conclusions

In this chapter we have proposed a two dimensional extension of the multi-material implicit method of Chapter V. The 2D extension is based on the introduction of a level set function in order to track the interface that separates the different materials of the domain. The level set transport equation is integrated with a semi-Lagrangian second order method. Especially when significant deformations are studied, a higher order resolution would be recommended.

Nevertheless, the proposed simulations have shown that the implicit equilibrium conditions coupled with the all-speed scheme away from boundaries are able to resolve shock-bubble interactions and low speed impacts. The results can be improved by further refining the grid and by working on the level set method. To reduce the high computational costs, the adaptive mesh refinement proposed in Chapter IV will be implemented also for in multi-material code.
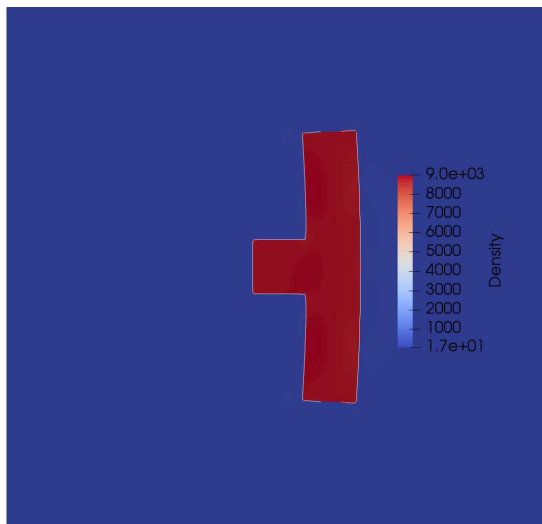
(a) $t = 104.7\mu$s
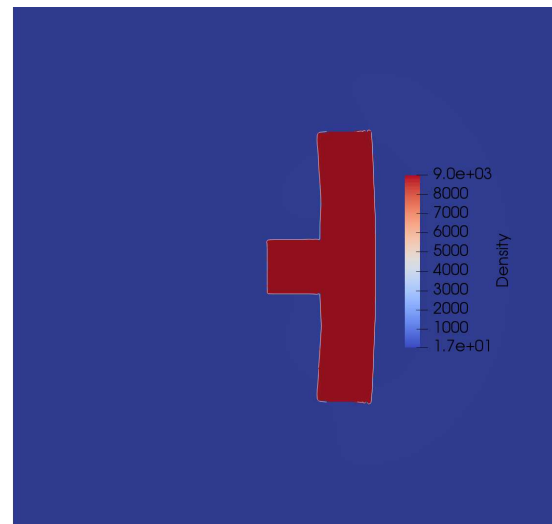
(b) $t = 523.5\mu$s
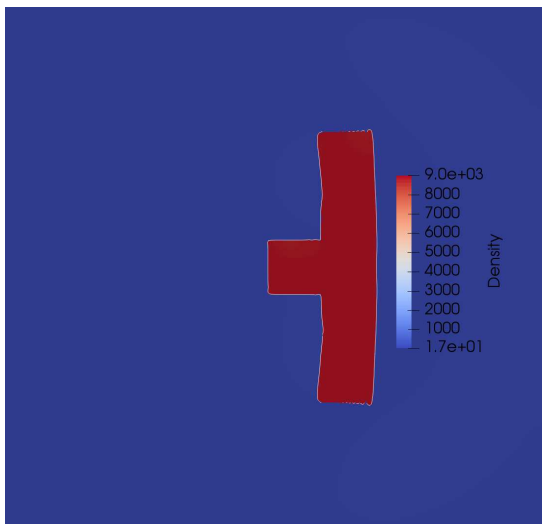
(c) $t = 1.047$ms

(d) $t = 1.779$ms

Figure VI.8: *Test 3*: density and zero contour of the level set for different time steps.

Conclusions

In the present thesis, we have proposed novel numerical methods to solve flows of compressible materials, including fluids and elastic solids, in different regimes. Moreover, the resolution of multi-material flows with physical interfaces has been approached.

In this spirit, we have introduced a model that describes the evolution of compressible fluids and solids with a unique system of conservation laws, in the Eulerian framework. This monolithic model is closed by a general state law which is able to identify the specific medium with the choice of suitable parameters that are specified for the different materials. In the case of fluids, the state law reduces to a thermodynamic EOS which includes perfect gas, Van der Waals gas and stiffened gas (liquids), while for elastic solids the EOS includes also a hyperelastic law that accounts for finite deformations.

Within this framework, we have studied the low Mach limits that can occur in both fluid dynamics and elastic deformations. Specifically, through the non-dimensionalization of the monolithic Eulerian model proposed in Chapter II, three different scales have been identified: the advection scale, the acoustic scale and the elastic scale. With the introduction of the standard acoustic Mach number and of an "elastic" Mach number, we have been able to analyze two different low Mach limits. The first limit occurs when both acoustic and elastic waves are consistently faster with respect to the flow velocity, i. e. both Mach numbers tend to zero. This can happen for example in a slow deformation of a copper bar, due to the material intrinsic properties. The second limit is verified when only the acoustic waves are faster with respect to both the flow velocity and the shear waves, namely the acoustic Mach number is much smaller than the elastic Mach.

This analysis has been the starting point for the numerical solution of the Eulerian model at all speeds. We have proposed a novel numerical scheme to solve fluid flows and elastic deformations in the fully compressible regime and also in the two low Mach regimes. The scheme is based on an implicit version of the Jin-Xin relaxation, which allows to linearize the advective operator at the continuous level. The linearity of the transport operator is one of the main advantages in the construction of the scheme, since the introduction of complex Riemann solvers is avoided. This property is twofold: on one hand, implicit time integrators are easily implemented, avoiding acoustic stability constraints on the time step which would dramatically increase the computational effort if the Mach numbers are small. On the other hand, the direct dependence of the transport operator on the state law is lost: the EOS appears only in the diagonal terms. Thus, the non linearities of the implicit scheme are decoupled and the scheme structure is the same for all the considered materials. The spatial discretization consists in a Mach dependent convex combination of upwind and centered schemes, in order to recover the

correct numerical viscosity in each regime. We are able to adopt centered discretizations without stability constraints thanks to the implicit integration in time.

In two dimensions, the relaxation is performed direction by direction, allowing for a straightforward extension. This method is easily parallelizable on Cartesian grids. We have developed a parallel code that uses the PETSc library [11] to solve the assembled linear system and the Bitpit library [50] for the generation of the mesh. Thanks to Bitpit, we have proposed an extension of the numerical scheme to discretizations on hierarchical adaptive grids based on quadtrees. The adaptive mesh refinement is pivoted by an entropy criterion, easily adapted to the implicit all-speed framework.

The second part of the thesis is devoted to the numerical simulation of multi-material flows in low Mach regimes. A numerical method that treats the physical interfaces as immersed boundaries has been proposed and validated. The interface is seen as a moving boundary that arbitrarily crosses the computational grid and implicit equilibrium conditions are imposed via extrapolations, thus the interface is sharp by construction. The implicit framework is important in order to resolve multi-material flows in the weakly compressible and low Mach regimes. For two dimensional multi-material simulations, a level set function has been introduced in order to track the interface position, coherently with the fully Eulerian framework. A higher order numerical integration of the level set transport equation is still under investigation, therefore the two dimensional simulations of the last chapter still have to be considered as preliminary results.

Perspectives

The perspectives and future developments of the present thesis are different.

The relaxation all-speed scheme derived in Chapter III is globally first order accurate, in both time and space. For the moment, we have adopted a second order version only to solve the analyzed nozzle flow test cases (see Section III.3.1), since no shock waves or discontinuities have to be approximated. The scheme will be extended to higher orders in the future, including cases with discontinuous solutions. The idea is to adopt a CWENO interpolation of order three, in order to get a centered spatial discretization (the CWENO interpolation has been the focus of several works in literature [82, 83, 42] and it can also be adapted to quadtree grids [116]).

As already anticipated at the end of Chapter IV, another line of research consists in deriving preconditioners for the linear system associated to the proposed implicit scheme. The computational effort in fact is mainly related to the linear system resolution. Therefore, the derivation of ad-hoc preconditioners will consistently reduce the computational times, since the number of the iterations required for the linear solver to converge will be decreased.

The use of adaptive grids in the mono-material code has allowed to reduce the number of degrees of freedom and consequently the computational times, by maintaining the required precision in areas of interest. The implementation of the multi-material scheme on adaptive grids, will thus increase the resolution of the multi-material interfaces, by adaptively refining in the neighbourhood of the interfaces. The entropy criterion that we have introduced and adopted in the simulations of Chapter IV can still be employed. Of course, in addition the zero contour of the level-set identifies the regions of interest for the refinement.

This work can be seen as a step towards the simulation of cases of engineering interest

whose focus is a deformation that is much slower with respect to the other propagating waves. An example of such simulations can be a crash test, which can be considered as a low speed impact. During the crash, fast acoustic waves rapidly propagate forward and backward in air, but their resolution is not necessary. The proposed numerical method is then a good candidate for numerically simulate this kind of tests: on one hand the method has proved to be accurate in approximating material waves at all speeds. On the other hand, the use of large time steps avoids the resolution of acoustic waves and considerably reduces the computational effort.

Bibliography

[1] E Abbate, A Iollo, and G Puppo. An all-speed relaxation scheme for gases and compressible materials. *Journal of Computational Physics*, 351:1–24, 2017.   p. 5, 25, 32, 63

[2] E Abbate, A Iollo, and G Puppo. A relaxation scheme for the simulation of low Mach number flows. In *International Conference on Finite Volumes for Complex Applications*, pages 227–235. Springer, 2017.   p. 32, 63

[3] E Abbate, A Iollo, and G Puppo. An asymptotic-preserving all-speed scheme for fluid dynamics and non linear elasticity. *Submitted*, 2018.   p. 67, 86

[4] E Abbate, A Iollo, and G Puppo. An implicit scheme for moving walls and multi-material interfaces in weakly compressible materials. *Communications in Computational Physics*, Accepted for publication, 2018.   p. 101

[5] R Abgrall. How to prevent pressure oscillations in multicomponent flow calculations: a quasi conservative approach. *Journal of Computational Physics*, 125(1):150–160, 1996.   p. 97, 98

[6] R Abgrall and S Karni. Computations of compressible multifluids. *Journal of computational physics*, 169(2):594–623, 2001.   p. 99

[7] G Allaire, S Clerc, and S Kokh. A five-equation model for the simulation of interfaces between compressible fluids. *Journal of Computational Physics*, 181(2):577–616, 2002.   p. 98

[8] T Altazin, M Ersoy, F Golay, D Sous, and L Yushchenko. Numerical investigation of bb-amr scheme using entropy production as refinement criterion. *International Journal of Computational Fluid Dynamics*, 30(3):256–271, 2016.   p. 85

[9] A Ambroso, C Chalons, F Coquel, and T Galié. Relaxation and numerical approximation of a two-fluid two-pressure diphasic model. *ESAIM: Mathematical Modelling and Numerical Analysis*, 43(6):1063–1097, 2009.   p. 36

[10] C Arvanitis and A Delis. Behavior of finite volume schemes for hyperbolic conservation laws on adaptive redistributed spatial grids. *SIAM Journal on Scientific Computing*, 28(5):1927–1956, 2006.   p. 85

[11] S. Balay, S. Abhyankar, M.F. Adams, J. Brown, P. Brune, K. Buschelman, L. Dalcin, V. Eijkhout, W.D. Gropp, D. Kaushik, M.G. Knepley, D.A. May, L. Curfman

McInnes, K. Rupp, P. Sanan, B.F. Smith, S. Zampini, and H. Zhang. PETSc users manual. Technical Report ANL-95/11 - Revision 3.8, Argonne National Laboratory, 2017.
p. 63, 76, 77, 140, 161, 171

[12] W Barsukow, P VF Edelmann, C Klingenberg, F Miczek, and F K Röpke. A numerical scheme for the compressible low-Mach number regime of ideal fluid dynamics. *Journal of Scientific Computing*, 72(2):623–646, 2017.
p. 30

[13] P T Barton and D Drikakis. An Eulerian method for multi–component problems in non–linear elasticity with sliding interfaces. *Journal of Computational Physics*, 229(15):5518–5540, 2010.
p. 5, 99

[14] P T Barton, B Obadia, and D Drikakis. A conservative level–set based method for compressible solid/fluid problems on fixed grids. *Journal of Computational Physics*, 230(21):7867–7890, 2011.
p. 5, 99

[15] M Ben-Artzi and J Falcovitz. *Generalized Riemann problems in computational fluid dynamics*, volume 11. Cambridge University Press, 2003.
p. 52

[16] G. Benison and E. Rubin. A time-dependent analysis for quasi-one-dimensional, viscous, heat conducting, compressible Laval nozzle flows. *Journal of Engineering Mathematics*, 5(1):39–49, 1971.
p. 45

[17] M J Berger and P Colella. Local adaptive mesh refinement for shock hydrodynamics. *Journal of computational Physics*, 82(1):64–84, 1989.
p. 84

[18] M J Berger and R J LeVeque. Adaptive mesh refinement using wave-propagation algorithms for hyperbolic systems. *SIAM Journal on Numerical Analysis*, 35(6):2298–2316, 1998.
p. 85

[19] S Boscarino, P G LeFloch, and G Russo. High-order asymptotic-preserving methods for fully nonlinear relaxation problems. *SIAM Journal on Scientific Computing*, 36(2):A377–A395, 2014.
p. 36

[20] S Boscarino and G Russo. On a class of uniformly accurate IMEX Runge–Kutta schemes and applications to hyperbolic systems with relaxation. *SIAM Journal on Scientific Computing*, 31(3):1926–1945, 2009.
p. 36, 38

[21] S Boscarino and G Russo. Flux-explicit IMEX Runge–Kutta schemes for hyperbolic to parabolic relaxation problems. *SIAM Journal on Numerical Analysis*, 51(1):163–190, 2013.
p. 38

[22] S Boscarino, G Russo, and L Scandurra. All Mach number second order semi-implicit scheme for the Euler equations of gas dynamics. *Journal of Scientific Computing*, pages 1–35, 2017.
p. 32

[23] W Boscheri, M Dumbser, and R Loubère. Cell centered direct Arbitrary-Lagrangian-Eulerian ADER-WENO finite volume schemes for nonlinear hyperelasticity. *Computers & Fluids*, 134:111–129, 2016.
p. 99

[24] F. Bouchut. *Nonlinear stability of finite volume methods for hyperbolic conservation laws: And well-balanced schemes for sources.* Springer Science & Business Media, 2004.   p. 36

[25] F Bouchut, C Klingenberg, and K Waagan. A multiwave approximate riemann solver for ideal mhd based on relaxation. i: theoretical framework. *Numerische Mathematik*, 108(1):7–42, 2007.   p. 36

[26] R E Caflisch, S Jin, and G Russo. Uniformly accurate schemes for hyperbolic systems with relaxation. *SIAM Journal on Numerical Analysis*, 34(1):246–281, 1997.   p. 36

[27] F Cavalli, G Naldi, G Puppo, and M Semplice. High-order relaxation schemes for nonlinear degenerate diffusion problems. *SIAM Journal on Numerical Analysis*, 45(5):2098–2119, 2007.   p. 38

[28] A. Chalabi and Y. Qiu. Relaxation schemes for hyperbolic conservation laws with stiff source terms: Application to reacting Euler equations. *Journal of scientific computing*, 15(4):395–416, 2000.   p. 36

[29] C. Chalons, F. Coquel, and C. Marmignon. Well-balanced time implicit formulation of relaxation schemes for the Euler equations. *SIAM Journal on Scientific Computing*, 30(1):394–415, 2008.   p. 36

[30] C Chalons and J Coulombel. Relaxation approximation of the Euler equations. *Journal of Mathematical Analysis and Applications*, 348(2):872–893, 2008.   p. 36

[31] C Chalons, M Girardin, and S Kokh. Large time step and asymptotic preserving numerical schemes for the gas dynamics equations with source terms. *SIAM Journal on Scientific Computing*, 35(6):A2874–A2902, 2013.   p. 31

[32] C Chalons, M Girardin, and S Kokh. An all-regime Lagrange-projection like scheme for the gas dynamics equations on unstructured meshes. *Communications in Computational Physics*, 20(1):188–233, 2016.   p. 31

[33] C Chalons, M Girardin, and S Kokh. An all-regime Lagrange-projection like scheme for 2D homogeneous models for two-phase flows on unstructured meshes. *Journal of Computational Physics*, 335:885–904, 2017.   p. 32

[34] S Chapman and T G Cowling. *The mathematical theory of non-uniform gases: an account of the kinetic theory of viscosity, thermal conduction and diffusion in gases.* Cambridge university press, 1970.   p. 36

[35] G Chen, C D Levermore, and T Liu. Hyperbolic conservation laws with stiff relaxation terms and entropy. *Communications on Pure and Applied Mathematics*, 47(6):787–830, 1994.   p. 35

[36] A Chertock and A Kurganov. A simple Eulerian finite-volume method for compressible fluids in domains with moving boundaries. *Communications in Mathematical Sciences*, 6(3):531–556, 2008.   p. 111

[37] A J Chorin. A numerical method for solving incompressible viscous flow problems. *Journal of Computational Physics*, 2(1):12–26, 1967. p. 30

[38] P G Ciarlet. *Élasticité tridimentionelle*. Masson, Paris, 1985. p. 12

[39] F Coquel and B Perthame. Relaxation of energy and approximate riemann solvers for general pressure laws in fluid dynamics. *SIAM Journal on Numerical Analysis*, 35(6):2223–2249, 1998. p. 36

[40] F. Cordier, P. Degond, and A. Kumbaro. An asymptotic-preserving all-speed scheme for the Euler and Navier–Stokes equations. *Journal of Computational Physics*, 231(17):5685–5704, 2012. p. 20, 31

[41] G. Cottet, E. Maitre, and T. Milcent. Eulerian formulation and level set models for incompressible fluid-structure interaction. *ESAIM: Mathematical Modelling and Numerical Analysis*, 42(3):471–492, 2008. p. 5, 11

[42] I Cravero, G Puppo, M Semplice, and G Visconti. Cool weno schemes. *Computers & Fluids*, 169:71–86, 2018. p. 140

[43] C M Dafermos. The entropy rate admissibility criterion for solution of hyperbolic conservation laws. 1972. p. 85

[44] A. de Brauer, A. Iollo, and T. Milcent. A Cartesian scheme for compressible multimaterial models in 3d. *Journal of Computational Physics*, 313:121–143, 2016. p. 5, 13, 15, 100, 131

[45] P Degond and M Tang. All speed scheme for the low Mach number limit of the isentropic Euler equation. *arXiv preprint arXiv:0908.1929*, 2009. p. 19, 31

[46] S. Dellacherie. Analysis of Godunov type schemes applied to the compressible Euler system at low Mach number. *Journal of Computational Physics*, 229(4):978–1016, 2010. p. 19, 24, 28, 29, 40

[47] S Dellacherie, J Jung, P Omnes, and P-A Raviart. Construction of modified Godunov-type schemes accurate at any Mach number for the compressible Euler system. *Mathematical Models and Methods in Applied Sciences*, 26(13):2525–2615, 2016. p. 29, 40

[48] G Dimarco, R Loubère, and M Vignal. Study of a new asymptotic preserving scheme for the Euler system in the low Mach number limit. *SIAM Journal on Scientific Computing*, 39(5):A2099–A2128, 2017. p. 32

[49] M Dumbser, I Peshkov, E Romenski, and O Zanotti. High order ader schemes for a unified first order hyperbolic formulation of continuum mechanics: Viscous heat-conducting fluids and elastic solids. *Journal of Computational Physics*, 314:824–862, 2016. p. 5

[50] Optimad Engineering. Bitpit Web page. http://optimad.github.io/bitpit/modules/index.html, 2017. p. 63, 74, 140, 161, 171

[51] M Falcone and R Ferretti. Convergence analysis for a class of high-order semi-Lagrangian advection schemes. *SIAM Journal on Numerical Analysis*, 35(3):909–940, 1998. p. 127

[52] N Favrie and S L Gavrilyuk. Diffuse interface model for compressible fluid–compressible elastic–plastic solid interaction. *Journal of Computational Physics*, 231(7):2695–2723, 2012. p. 99

[53] N Favrie, S L Gavrilyuk, and R Saurel. Solid–fluid diffuse interface model in cases of extreme deformations. *Journal of Computational Physics*, 228(16):6037–6077, 2009. p. 5, 98, 134

[54] R Fazio and G Russo. Central schemes and second order boundary conditions for 1D interface and piston problems in Lagrangian coordinates. *Communications in Computational Physics*, 8(4):797–822, 2010. p. 99

[55] R P Fedkiw, T Aslam, B Merriman, and S Osher. A non-oscillatory Eulerian approach to interfaces in multimaterial flows (the ghost fluid method). *Journal of Computational Physics*, 152(2):457–492, 1999. p. 97, 99

[56] R P Fedkiw, A Marquina, and B Merriman. An isobaric fix for the overheating problem in multimaterial compressible flows. *Journal of Computational Physics*, 148(2):545–578, 1999. p. 109

[57] S F Frisken and R N Perry. Simple and efficient traversal methods for quadtrees and octrees. *Journal of Graphics Tools*, 7(3):1–11, 2002. p. 84

[58] E Gaburro, M J Castro, and M Dumbser. A well balanced diffuse interface method for complex nonhydrostatic free surface flows. *arXiv preprint arXiv:1806.04960*, 2018. p. 99

[59] S Galera, P Maire, and J Breil. A two–dimensional unstructured cell–centered multi–material ALE scheme using VOF interface reconstruction. *Journal of Computational Physics*, 229(16):5755–5787, 2010. p. 99

[60] S Godunov. Elements of continuum mechanics. *Nauka Moscow*, 1978. p. 9, 11, 158, 168

[61] S. Godunov and E. Romenskii. *Elements of continuum mechanics and conservation laws.* Springer Science & Business Media, 2013. p. 5, 9, 158, 168

[62] Y. Gorsse, A. Iollo, T. Milcent, and H. Telib. A simple Cartesian scheme for compressible multimaterials. *Journal of Computational Physics*, 272:772–798, 2014. p. 5, 13, 15, 16, 100, 131, 132, 134, 158, 168

[63] P Gresho. On the theory of semi-implicit projection methods for viscous incompressible flow and its implementation via a finite element method that also introduces a nearly consistent mass matrix. part 1: Theory. *International Journal for Numerical Methods in Fluids*, 11(5):587–620, 1990. p. 78

[64] H Guillard and A Murrone. On the behavior of upwind schemes in the low Mach number limit: II. Godunov type schemes. *Computers & fluids*, 33(4):655–675, 2004. p. 28

[65] H. Guillard and C. Viozat. On the behaviour of upwind schemes in the low Mach number limit. *Computers & fluids*, 28(1):63–86, 1999. p. 19, 20, 21, 28, 40

[66] J Haack, S Jin, and J Liu. An all-speed asymptotic-preserving method for the isentropic Euler and Navier-Stokes equations. *Communications in Computational Physics*, 12(04):955–980, 2012. p. 32

[67] C. Hirsch. *Numerical computation of internal and external flows: The fundamentals of computational fluid dynamics*. Butterworth-Heinemann, 2007. p. 41

[68] G. A Holzapfel. Nonlinear solid mechanics: a continuum approach for engineering science. *Meccanica*, 37(4):489–490, 2002. p. 12, 14, 158

[69] XY Hu, NA Adams, and G Iaccarino. On the HLLC Riemann solver for interface interaction in compressible multi–fluid flow. *Journal of Computational Physics*, 228(17):6572–6589, 2009. p. 100

[70] A Jameson and D Caughey. How many steps are required to solve the Euler equations of steady, compressible flow-In search of a fast solution algorithm. In *15th AIAA Computational Fluid Dynamics Conference*, page 2673, 2001. p. 46

[71] S. Jin and Z. Xin. The relaxation schemes for systems of conservation laws in arbitrary space dimensions. *Communications on Pure and Applied Mathematics*, 48(3):235–276, 1995. p. 32, 35, 36, 37, 38, 39, 66, 73, 160, 170

[72] S Karni. Multicomponent flow calculations by a consistent primitive algorithm. *Journal of Computational Physics*, 112(1):31–43, 1994. p. 98

[73] S Karni and A Kurganov. Local error analysis for approximate solutions of hyperbolic conservation laws. *Advances in Computational mathematics*, 22(1):79–99, 2005. p. 85

[74] S. Klainerman and A. Majda. Singular limits of quasilinear hyperbolic systems with large parameters and the incompressible limit of compressible fluids. *Communications on Pure and Applied Mathematics*, 34(4):481–524, 1981. p. 19, 30

[75] S. Klainerman and A. Majda. Compressible and incompressible fluids. *Communications on Pure and Applied Mathematics*, 35(5):629–651, 1982. p. 19, 30

[76] R. Klein. Semi-implicit extension of a Godunov-type scheme based on low Mach number asymptotics i: One-dimensional flow. *Journal of Computational Physics*, 121(2):213–237, 1995. p. 19, 30

[77] G Kluth and B Després. Discretization of hyperelasticity on unstructured mesh with a cell-centered Lagrangian scheme. *Journal of Computational Physics*, 229(24):9092–9118, 2010. p. 99

[78] A Kurganov and E Tadmor. Solution of two-dimensional riemann problems for gas dynamics without riemann problem solvers. *Numerical Methods for Partial Differential Equations*, 18(5):584–608, 2002. p. 87, 89

[79] N. Kwatra, J. Su, J. Grétarsson, and R. Fedkiw. A method for avoiding the acoustic time step restriction in compressible flow. *Journal of Computational Physics*, 228(11):4146–4161, 2009. p. 31

[80] R J LeVeque. *Numerical methods for conservation laws*, volume 132. Springer, 1992.
p. 6, 28, 43

[81] R.J. LeVeque and M. Pelanti. A class of approximate Riemann solvers and their relation to relaxation schemes. *Journal of Computational Physics*, 172(2):572–591, 2001.　　p. 36

[82] D Levy, G Puppo, and G Russo. Central weno schemes for hyperbolic systems of conservation laws. *ESAIM: Mathematical Modelling and Numerical Analysis*, 33(3):547–571, 1999.　　p. 140

[83] D Levy, G Puppo, and G Russo. Compact central weno schemes for multidimensional conservation laws. *SIAM Journal on Scientific Computing*, 22(2):656–672, 2000.　　p. 140

[84] X Li and C Gu. An all-speed Roe-type scheme and its asymptotic analysis of low Mach number behaviour. *Journal of Computational Physics*, 227(10):5144–5159, 2008.　　p. 30

[85] R Liska and B Wendroff. Comparison of several difference schemes on 1D and 2D test problems for the Euler equations. *SIAM Journal on Scientific Computing*, 25(3):995–1017, 2003.　　p. 78, 161, 171

[86] T. Liu. Hyperbolic conservation laws with relaxation. *Communications in Mathematical Physics*, 108(1):153–175, 1987.　　p. 35, 37, 64, 160, 170

[87] TG Liu, BC Khoo, and KS Yeo. Ghost fluid method for strong shock impacting on material interface. *Journal of Computational Physics*, 190(2):651–681, 2003.　　p. 99

[88] H Luo, R Mittal, X Zheng, S A Bielamowicz, R J Walsh, and J K Hahn. An immersed-boundary method for flow–structure interaction in biological systems with application to phonation. *Journal of computational physics*, 227(22):9303–9332, 2008.　　p. 100

[89] A Marquina and P Mulet. A flux-split algorithm applied to conservative models for multicomponent compressible flows. *Journal of Computational Physics*, 185(1):120–138, 2003.
p. 132

[90] A McDonald. Accuracy of multiply-upstream, semi-Lagrangian advective schemes. *Monthly Weather Review*, 112(6):1267–1275, 1984.　　p. 127

[91] G Métivier and S Schochet. The incompressible limit of the non-isentropic Euler equations. *Archive for rational mechanics and analysis*, 158(1):61–90, 2001.　　p. 19

[92] GH Miller and P Colella. A conservative three–dimensional Eulerian method for coupled solid–fluid shock capturing. *Journal of Computational Physics*, 183(1):26–82, 2002.　　p. 5

[93] C Min and F Gibou. A second order accurate level set method on non-graded adaptive cartesian grids. *Journal of Computational Physics*, 225(1):300–321, 2007.　p. 127, 164, 174

[94] G M Morton. *A computer oriented geodetic data base and a new technique in file sequencing.* International Business Machines Company New York, 1966.　　p. 75

[95] G Naldi and L Pareschi. Numerical schemes for hyperbolic systems of conservation laws with stiff diffusive relaxation. *SIAM Journal on Numerical Analysis*, 37(4):1246–1270, 2000.   p. 36

[96] S. Noelle, G. Bispen, K Arun, M. Lukacova-Medvidova, and C. Munz. An asymptotic preserving all Mach number scheme for the Euler equations of gas dynamics. *SIAM J. Sci. Comput*, 2014.   p. 32

[97] S Osher and J A Sethian. Fronts propagating with curvature-dependent speed: algorithms based on hamilton-jacobi formulations. *Journal of computational physics*, 79(1):12–49, 1988.   p. 125

[98] L. Pareschi and G. Russo. Implicit-explicit Runge-Kutta schemes and applications to hyperbolic systems with relaxation. *Journal of Scientific computing*, 25(1-2):129–155, 2005.   p. 38, 39

[99] I Peshkov and E Romenski. A hyperbolic model for viscous newtonian flows. *Continuum Mechanics and Thermodynamics*, 28(1-2):85–104, 2016.   p. 5

[100] C S Peskin. Numerical analysis of blood flow in the heart. *Journal of computational physics*, 25(3):220–252, 1977.   p. 100

[101] C S Peskin. The immersed boundary method. *Acta numerica*, 11:479–517, 2002.
                                                                     p. 100, 105, 163, 173

[102] B J Plohr and D H Sharp. A conservative Eulerian formulation of the equations for elastic flow. *Advances in Applied Mathematics*, 9(4):481–499, 1988.   p. 5

[103] B J Plohr and D H Sharp. A conservative formulation for plasticity. *Advances in Applied Mathematics*, 13(4):462–493, 1992.   p. 5

[104] G Puppo. Numerical entropy production for central schemes. *SIAM Journal on Scientific Computing*, 25(4):1382–1415, 2004.   p. 63, 85

[105] G Puppo and M Semplice. Numerical entropy and adaptivity for finite volume schemes. *Communications in Computational Physics*, 10(5):1132–1160, 2011.   p. 63, 85, 86, 90

[106] J J Quirk and S Karni. On the dynamics of a shock–bubble interaction. *Journal of Fluid Mechanics*, 318:129–163, 1996.   p. 132, 164, 175

[107] A Raeli. *Solution Of The Variable Coefficient Poisson Equation On Cartesian Hierarchical Meshes In Parallel: Applications To Phase Changing Materials*. PhD thesis, IMB-Institut de Mathématiques de Bordeaux, 2017.   p. 84

[108] A Raeli, M Bergmann, and A Iollo. A finite-difference method for the variable coefficient poisson equation on hierarchical cartesian meshes. *Journal of Computational Physics*, 355:59–77, 2018.   p. 84

[109] G Russo and P Smereka. A remark on computing distance functions. *Journal of Computational Physics*, 163(1):51–67, 2000.   p. 126

[110] S Sambasivan, A Kapahi, and HS Udaykumar. Simulation of high speed impact, penetration and fragmentation problems on locally refined cartesian grids. *Journal of Computational Physics*, 235:334–370, 2013.   p. 100

[111] R Saurel and R Abgrall. A multiphase Godunov method for compressible multifluid and multiphase flows. *Journal of Computational Physics*, 150(2):425–467, 1999.   p. 98

[112] S Schochet. Fast singular limits of hyperbolic pdes. *Journal of differential equations*, 114(2):476–512, 1994.   p. 24

[113] S. Schochet. The mathematical theory of low Mach number flows. *Mathematical Modelling and Numerical Analysis*, 39(3):441–458, 2005.   p. 19

[114] C Schulz-Rinne, J Collins, and H Glaz. Numerical solution of the riemann problem for two-dimensional gas dynamics. *SIAM Journal on Scientific Computing*, 14(6):1394–1414, 1993.   p. 87, 89

[115] G Scovazzi, M A Christon, T JR Hughes, and J N Shadid. Stabilized shock hydrodynamics: I. A Lagrangian method. *Computer Methods in Applied Mechanics and Engineering*, 196(4):923–966, 2007.   p. 99

[116] M Semplice, A Coco, and G Russo. Adaptive mesh refinement for hyperbolic systems based on third-order compact weno reconstruction. *Journal of Scientific Computing*, 66(2):692–724, 2016.   p. 85, 140

[117] J A Sethian. A fast marching level set method for monotonically advancing fronts. *Proceedings of the National Academy of Sciences*, 93(4):1591–1595, 1996.   p. 126

[118] I. Suliciu. On the thermodynamics of rate-type fluids and phase transitions. i. Rate-type fluids. *International journal of engineering science*, 36(9):921–947, 1998.   p. 36

[119] M Sussman, E Fatemi, P Smereka, and S Osher. An improved level set method for incompressible two-phase flows. *Computers & Fluids*, 27(5-6):663–680, 1998.   p. 126

[120] M Sussman, P Smereka, and S Osher. A level set approach for computing solutions to incompressible two-phase flow. *Journal of Computational physics*, 114(1):146–159, 1994.   p. 126

[121] RC Swanson, E Turkel, and C-C Rossow. Convergence acceleration of Runge–Kutta schemes for solving the Navier–Stokes equations. *Journal of Computational Physics*, 224(1):365–388, 2007.   p. 46

[122] E Tadmor. Entropy stability theory for difference approximations of nonlinear conservation laws and related time-dependent problems. *Acta Numerica*, 12:451–512, 2003.   p. 85

[123] M Tavelli, M Dumbser, D E Charrier, L Rannabauer, T Weinzierl, and M Bader. A simple diffuse interface approach on adaptive cartesian grids for the linear elastic wave equations with complex topography. *arXiv preprint arXiv:1804.09491*, 2018.   p. 99

[124] E F Toro. *Riemann solvers and numerical methods for fluid dynamics: a practical introduction.* Springer Science & Business Media, 2013.   p. 28, 54

[125] E Turkel. Preconditioned methods for solving the incompressible and low speed compressible equations. *Journal of Computational Physics*, 72(2):277–298, 1987.   p. 30

[126] E Turkel and VN Vatsa. Local preconditioners for steady state and dual time-stepping. *Mathematical Modeling and Numerical Analysis, ESAIM: M2AN*, 39:515–536, 2005. p. 30

[127] B Van Leer, W Lee, and P Roe. Characteristic time-stepping or local preconditioning of the Euler equations. In *10th Computational Fluid Dynamics Conference*, volume 1, pages 260–282, 1991.   p. 30

[128] C Viozat. *Implicit upwind schemes for low Mach number compressible flows.* PhD thesis, Inria, 1997.   p. 30

[129] G B Whitham. *Linear and nonlinear waves*, volume 42. John Wiley & Sons, 2011.
                    p. 6, 37, 64

[130] D Xiu and GE Karniadakis. A semi-Lagrangian high-order method for Navier–Stokes equations. *Journal of computational physics*, 172(2):658–684, 2001.   p. 127, 164, 174

[131] X Zeng and C Farhat. A systematic approach for constructing higher-order immersed boundary and ghost fluid methods for fluid–structure interaction problems. *Journal of Computational Physics*, 231(7):2892–2923, 2012.   p. 100

List of Figures

List of Tables

Metodi numerici per flussi multi-regime in fluidodinamica ed elasticità non lineare

Introduzione

I flussi attraverso materiali comprimibili in domini eterogenei possono generare fenomeni complessi. In questa tesi ci occupiamo della simulazione numerica di questi flussi, proponendo metodi robusti e generali, in grado di risolvere problemi in materiali differenti (gas, liquidi e solidi elastici) e in regimi diversi. In questo senso, introduciamo un modello di tipo euleriano che descrive fluidi e solidi con lo stesso sistema di leggi di conservazione. La legge di stato che chiude il sistema caratterizza i materiali considerati, includendo i diversi comportamenti che si possono verificare attraverso questi mezzi.

Come in fluidodinamica classica, anche con il modello euleriano proposto si possono osservare regimi diversi. Per studiare questi regimi, introduciamo il numero di Mach acustico classico e un numero di Mach elastico, che aiutano nella distinzione delle possibili scale. Il limite low Mach in un solido elastico si può essere associato al concetto di deformazione piccola o lenta. Questo significa che l'onda materiale ha una velocità molto inferiore rispetto a tutte le altre onde, o a un sottoinsieme di queste. Uno degli obiettivi di questo lavoro è la costruzione di uno schema numerico che risolva con accuratezza tutti i regimi, dal comprimibile ai limiti low Mach individuati.

Per avere uno schema che sia sufficientemente generale da non cambiare la sua struttura in base al materiale considerato, adottiamo una tecnica di rilassamento dei flussi, che rende lineare l'operatore di trasporto. In questo modo, si possono integrare le equazioni nel tempo in modo implicito senza dover ricorrere a solutori di Riemann e si evitano condizioni restrittive sul passo di tempo. Inoltre, schemi centrati in spazio posso essere introdotti senza problemi di stabilità. La proprietà all-speed viene rispettata grazie a una combinazione di flussi centrati e upwind, in modo da ritrovare la corretta viscosità numerica nei diversi regimi. L'implementazione dello schema su griglie cartesiane è facilmente parallelizzabile, attraverso un metodo di decomposizione di domini.

La seconda parte della tesi èdedicata alla derivazione di metodi numerici per trattare le interfacce, in modo da poter risolvere flussi multi-materiale. Le interfacce vengono trattate in modo "sharp", come nei metodi di frontiere immerse: l'interfaccia viene considerata come una frontiera che può liberamente attraversare le celle del dominio. Le condizioni di equilibrio sono

imposte tramite estrapolazioni e sono integrate in implicito, per risolvere flussi anche in regimi a basso Mach ed evitare restrizioni onerose sul passo di tempo.

Modello Euleriano per l'elasticità

Introduciamo un modello euleriano monolitico, originariamente proposto da Godunov in [60, 61]. Siano $\Omega_0 \in \mathbb{R}^2$ la configurazione iniziale di un continuo e $\Omega_t \in \mathbb{R}^2$ la configurazione deformata al tempo t. Le caratteristiche inverse $Y(x,t)$ descrivono il continuo nel formalismo euleriano: per un tempo t e un punto $x \in \Omega_t$ la posizione del punto corrispondente $\xi \in \Omega_0$ è data da $Y : \Omega_t \times [0,T] \to \Omega_0, \ (x,t) \mapsto Y(x,t)$. Queste funzioni registrarano la deformazione di un solido. In particolare, data la dipendenza del tensore degli sforzi σ dal gradiente di $Y(x,t)$, la legge di conservazione che viene inserita nel modello euleriano è scritta come gradiente di $\partial_t Y + \mathbf{u} \cdot \nabla_x Y = 0$, dove $\mathbf{u}$ è il campo di velocità. Le altre equazioni del modello consistono nella conservazione della massa, della quantità di moto e dell'energia. Otteniamo quindi il seguente modello in 2D:

$$\begin{cases} \partial_t \rho + \nabla_x \cdot (\rho \mathbf{u}) = 0 \\ \partial_t (\rho \mathbf{u}) + \nabla_x \cdot (\rho \mathbf{u} \otimes \mathbf{u} - \sigma) = 0 \\ \partial_t ([\nabla_x Y]) + \nabla_x (u \cdot [\nabla_x Y]) = 0 \\ \partial_t (\rho e) + \nabla_x \cdot (\rho e \mathbf{u} - \sigma^T \mathbf{u}) = 0, \end{cases} \tag{IT.10}$$

dove ρ è la densità, e è l'energia totale per unità di massa, data dalla somma dell'energia cinetica e dell'energia interna per unità di massa ϵ. Il sistema viene chiuso con la legge di stato dell'iper-elasticità, che include comportamenti diversi tipici di gas, liquidi e solidi, con la seguente formulazione [62]:

$$\epsilon(\rho, s, [\nabla_x Y]) = \underbrace{\frac{\kappa(s)}{\gamma - 1} \left(\frac{1}{\rho} - b\right)^{1-\gamma} - a\rho + \frac{p_\infty}{\rho}}_{\text{general gas}} + \underbrace{\frac{\chi}{\rho} \left(\text{tr}\overline{B} - 2\right)}_{\text{neohookean solid}} . \tag{IT.11}$$

Qui $\gamma = c_p/c_v$ è la costante dei gas politropici, $\kappa(s) = exp((s-s_0)/c_v)$ con s_0 entropia di riferimento, a e b sono i coefficienti dei gas reali (modello di Van der Waals) e p_∞ una costante che descrive le forze intermolecolari. Infine, χ è il modulo elastico di taglio e $\overline{B} = [\nabla_x Y]^{-1} [\nabla_x Y]^{-T}/J$, con $J = det([\nabla_x Y]^{-1} [\nabla_x Y]^{-T})$ è il tensore sinistro di Cauchy Green normalizzato.

Dalla legge di stato (IT.11), si ottiene il tensore degli sforzi di Cauchy seguente (per la derivazione si rimanda a [68]):

$$\begin{cases} \sigma(\rho, s, [\nabla_x Y]) = -p(\rho, s)\mathbf{I} + 2\chi J^{-1} \left(\overline{B} - \frac{\text{tr}\overline{B}}{2} I\right) \\ p(\rho, s) = -p_\infty - a\rho^2 + k(s) \left(\frac{1}{\rho} - b\right)^{-\gamma}, \end{cases} \tag{IT.12}$$

dove $\mathbf{I}$ è la matrice identità e p è la pressione.

Limiti low Mach

Per semplicità, consideriamo il sistema Euleriano (IT.10) in 1D e escludiamo i gas di Van der Waals dall'analisi ($a = b = 0$). La velocità del suono viene definita in modo classico:

$$c\left(\rho, s, \nabla_x Y\right) = \sqrt{\left.\frac{\partial p}{\partial \rho}\right|_{s=const}} = \sqrt{\gamma k\left(s\right) \rho^{\gamma - 1}} = \sqrt{\frac{\gamma}{\rho}\left(p + p_\infty\right)}. \tag{IT.13}$$

Definiamo inoltre una velocità isocorica elastica nel modo seguente:

$$u_{iso} = \sqrt{\frac{2\chi}{\rho}}. \tag{IT.14}$$

Date le velocità (IT.13) e (IT.14), si possono definire due numeri di Mach diversi: il primo è il classico numero di Mach acustico della fluidodinamica

$$M = \frac{u_1}{c};$$

il secondo è un numero di Mach definito dal rapporto tra la velocità del flusso e la velocità elastica (IT.14):

$$M_\chi = \frac{u_1}{u_{iso}} = \sqrt{\frac{\rho u_1^2}{2\chi}}.$$

Date queste definizioni, procediamo adimensionalizzando il sistema per capire il comportamento nei vari regimi, usando c per scalare la pressione, $\overline{\chi}$ di riferimento per scalare il modulo elastico e una velocità normale di riferimento per scalare u_1 e u_2. Inserendo M e M_χ nell'adimensionalizzazione, si ottiene il seguente sistema euleriano 1D adimensionale:

$$\begin{cases} \partial_t \rho + \partial_x \left(\rho u_1\right) = 0 \\[2mm] \partial_t \left(\rho u_1\right) + \partial_x \left(\rho u_1^2\right) + \dfrac{\partial_x p}{M^2} - \dfrac{\chi}{2} \dfrac{\partial_x \left(1 - \left(Y_{,1}^2\right)^2 - \left(\rho/\rho_0\right)^2\right)}{M_\chi^2} = 0 \\[4mm] \partial_t \left(\rho u_2\right) + \partial_x \left(\rho u_1 u_2\right) + \chi \dfrac{\partial_x Y_{,1}^2}{M_\chi^2} = 0 \\[4mm] \partial_t \left(Y_{,1}^2\right) + \partial_x \left(u_1 Y_{,1}^2 + u_2\right) = 0 \\[4mm] \partial_t \left(\dfrac{1}{2}\rho u^2 + \dfrac{p + \gamma p_\infty}{M^2\left(\gamma - 1\right)} + \dfrac{\chi\left(tr\overline{B} - 2\right)}{2 M_\chi^2}\right) + \partial_x \left(\dfrac{1}{2}\rho|u|^3 + \dfrac{\gamma\left(p + \gamma p_\infty\right)}{M^2\left(\gamma - 1\right)} u_1\right) + \\[4mm] \dfrac{\chi}{2 M_\chi^2}\partial_x \left[\left(tr\overline{B} - 2 - \chi\left(1 - \left(Y_{,1}^2\right)^2 - \left(\rho/\rho_0\right)^2\right)\right) u_1 + 2\chi Y_{,1}^2 u_2\right] = 0. \end{cases} \tag{IT.15}$$

Il concetto di regime low Mach in un solido elastico può essere associato ad una deformazione piccola (o lenta rispetto alle onde acustiche). Possiamo distinguere due limiti diversi:

1. *regime low Mach acustico-elastico*: $M \ll 1$ e $M_\chi \ll 1$. In (IT.15), sia i gradienti di pressione che le deformazioni elastiche introducono termini "stiff" nel sistema. Il fatto che $\mathcal{O}\left(M\right) \simeq \mathcal{O}\left(M_\chi\right)$ significa che $c \simeq u_{iso}$ e $p + p_\infty \simeq \chi$. In questo caso le onde longitudinali e le onde trasversali sono tutte considerevolmente più veloci dell'onda materiale;

2. *regime low Mach solo acustico*: $M \ll 1$ e $M \ll M_\chi$. In (IT.15) i gradienti di pressione sono gli unici termini dominanti e inoltre si ha che $c \gg |u_1|$ e $c \gg u_{iso}$ e dunque $p + p_\infty \gg \chi$. In questo caso le onde longitudinali sono molto più veloci di tutte le altre onde.

Schema all-speed di rilassamento

Con l'obiettivo di risolvere il sistema euleriano (IT.10) sia in regimi low Mach che in regimi completamente comprimibili, proponiamo uno schema "all-speed" implicito, basato sulla tecnica di rilassamento introdotta da Jin e Xin in [71]. Con questo metodo di rilassamento, i flussi vengono approssimati da nuove variabili (dette variabili di rilassamento) e dunque si costruisce un sistema il cui operatore di trasporto è lineare e le derivate spaziali non dipendono più dalla legge di stato. Questo è fondamentale nella costruzione di uno schema che mantenga la stessa struttura per risolvere flussi in materiali diversi.

Il sistema di leggi di conservazione (IT.10) può essere scritto nella seguente forma compatta:

$$\partial_t \boldsymbol{\psi} + \partial_{x_1} \mathbf{F}\left(\boldsymbol{\psi}\right) + \partial_{x_2} \mathbf{G}\left(\boldsymbol{\psi}\right) = 0, \qquad (IT.16)$$

dove $\boldsymbol{\psi}$ sono le variabili conservative, $\mathbf{F}\left(\boldsymbol{\psi}\right)$ e $\mathbf{G}\left(\boldsymbol{\psi}\right)$ sono i flussi nelle due direzioni. Introducendo i vettori di variabili di rilassamento "direzione per direzione" $\mathbf{v}$ e $\mathbf{w}$ che approssimano rispettivamente $\mathbf{F}\left(\boldsymbol{\psi}\right)$ e $\mathbf{G}\left(\boldsymbol{\psi}\right)$, si costruisce il seguente sistema di rilassamento

$$\begin{cases} \partial_t \boldsymbol{\psi} + \partial_{x_1} \mathbf{v} + \partial_{x_2} \mathbf{w} = 0 \\ \partial_t \mathbf{v} + \mathbf{A}_1 \partial_{x_1} \boldsymbol{\psi} = \dfrac{1}{\eta} \left(\mathbf{F}\left(\boldsymbol{\psi}\right) - \mathbf{v}\right) \\ \partial_t \mathbf{w} + \mathbf{A}_2 \partial_{x_2} \boldsymbol{\psi} = \dfrac{1}{\eta} \left(\mathbf{G}\left(\boldsymbol{\psi}\right) - \mathbf{w}\right), \end{cases} \qquad (IT.17)$$

dove $\eta > 0$ è il tasso di rilassamento e $\mathbf{A}_1$ e $\mathbf{A}_2$ sono matrici diagonali che devono essere scelte in modo da rispettare la condizione subcaratteristica [86]. Nel limite di rilassamento $\eta \to 0$, si ritrova il sistema originale (IT.16) e le variabili di rilassamento coincidono coi flussi.

Per derivare lo schema di rilassamento all-speed, ci poniamo in un contesto ai volumi finiti. Il sistema (IT.17) viene integrato in tempo in modo completamente implicito, dunque lo schema è incondizionatamente stabile. In questo modo, il passo di tempo $\Delta t = t_{n+1} - t_n$ viene scelto in base all'accuratezza che si vuole ottenere nella risoluzione delle diverse onde. Una condizione di tipo acustico su Δt permette una risoluzione accurata di tutte le onde, mentre un passo temporale più largo di tipo materiale permette di ridurre i tempi computazionali lasciando invariata l'accuratezza delle onde materiali, mentre le onde acustiche veloci vengono diffuse. I flussi non lineari a secondo membro vengono risolti con un metodo di Newton, tramite la linearizzazione

$$\mathbf{F}\left(\boldsymbol{\psi}^{n+1}\right) = \mathbf{F}\left(\boldsymbol{\psi}^n\right) + \mathbf{F}'\left(\boldsymbol{\psi}^n\right)\left(\boldsymbol{\psi}^{n+1} - \boldsymbol{\psi}^n\right), \qquad (IT.18)$$

dove lo Jacobiano $\mathbf{F}'\left(\boldsymbol{\psi}^n\right)$ (e quello per $\mathbf{G}\left(\boldsymbol{\psi}\right)$) è calcolato analiticamente.

La discretizzazione spaziale consiste in una combinazione convessa di flussi upwind e centrati. Lo schema centrato produce la corretta viscosità numerica nei regimi low Mach, mentre lo schema upwind evita la generazione di oscillazioni spurie nei regimi comprimibili. La combinazione è calcolata sulla base del Mach locale del flusso M_{loc}, ottenendo la viscosità numerica desiderata in ogni regime. Su una griglia cartesiana, dove Δx_l è il passo di griglia nella direzione x_l e $\Omega_{i,j}$ è il volume di controllo centrato in $(i\Delta x_1, j\Delta x_2)$, lo schema all-speed di rilassamento ha la seguente

formulazione

$$
\begin{cases}
\dfrac{\boldsymbol{\psi}_{ij}^{n+1} - \boldsymbol{\psi}_{ij}^{n}}{\Delta t} + \dfrac{1}{2\Delta x_1}\left(\mathbf{v}_{i+1,j}^{n+1} - \mathbf{v}_{i-1,j}^{n+1}\right) - \dfrac{f\left(M_{loc}\right)\mathbf{A}_1^{1/2}}{2\Delta x_1}\left(\boldsymbol{\psi}_{i+1,j}^{n+1} - 2\boldsymbol{\psi}_{ij}^{n+1} + \boldsymbol{\psi}_{i-1,j}^{n+1}\right) + \\[2mm]
\qquad\qquad \dfrac{1}{2\Delta x_2}\left(\mathbf{w}_{i,j+1}^{n+1} - \mathbf{w}_{i,j-1}^{n+1}\right) - \dfrac{f\left(M_{loc}\right)\mathbf{A}_2^{1/2}}{2\Delta x_2}\left(\boldsymbol{\psi}_{i,j+1}^{n+1} - 2\boldsymbol{\psi}_{ij}^{n+1} + \boldsymbol{\psi}_{i,j-1}^{n+1}\right) = 0 \\[3mm]
\dfrac{\mathbf{v}_{ij}^{n+1} - \mathbf{v}_{ij}^{n}}{\Delta t} + \dfrac{\mathbf{A}_1}{2\Delta x_1}\left(\boldsymbol{\psi}_{i+1,j}^{n+1} - \boldsymbol{\psi}_{i-1,j}^{n+1}\right) - \dfrac{f\left(M_{loc}\right)\mathbf{A}_1^{1/2}}{2\Delta x_1}\left(\mathbf{v}_{i+1,j}^{n+1} - 2\mathbf{v}_{ij}^{n+1} + \mathbf{v}_{i-1,j}^{n+1}\right) = \\[2mm]
\qquad\qquad\qquad\qquad\qquad\qquad \dfrac{1}{\eta}\left(\mathbf{F}\left(\boldsymbol{\psi}_{ij}^{n+1}\right) - \mathbf{v}_{ij}^{n+1}\right) \\[3mm]
\dfrac{\mathbf{w}_{ij}^{n+1} - \mathbf{w}_{ij}^{n}}{\Delta t} + \dfrac{\mathbf{A}_2}{2\Delta x_2}\left(\boldsymbol{\psi}_{i,j+1}^{n+1} - \boldsymbol{\psi}_{j,i-1}^{n+1}\right) - \dfrac{f\left(M_{loc}\right)\mathbf{A}_2^{1/2}}{2\Delta x_2}\left(\mathbf{w}_{i,j+1}^{n+1} - 2\mathbf{w}_{ij}^{n+1} + \mathbf{w}_{i,j-1}^{n+1}\right) = \\[2mm]
\qquad\qquad\qquad\qquad\qquad\qquad \dfrac{1}{\eta}\left(\mathbf{G}\left(\boldsymbol{\psi}_{ij}^{n+1}\right) - \mathbf{w}_{ij}^{n+1}\right).
\end{cases}
\tag{IT.19}
$$

Qui abbiamo introdotto la funzione $f\left(M_{loc}\right) = \min\{1, M_{loc}\}$.

La risoluzione numerica di casi bidimensionali può essere computazionalmente onerosa, poiché stiamo adottando un'integrazione completamente in implicito e poiché il rilassamento aumenta il numero di variabili. L'implementazione dello schema su griglie cartesiane è facilmente parallelizzabile, tramite un metodo di decomposizione di domini. Questo viene fatto grazie al paradigma MPI, con l'uso di librerie sviluppate per il calcolo scientifico (PETSc [11] per la parte di algebra lineare e Bitpit [50] per la generazione della griglia). Un'ulteriore riduzione dei tempi computazionali viene ottenuta grazie all'uso di griglie adattive basate su qudtrees.

Risultati numerici

Analizziamo un test classico per la validazione in regimi low Mach di schemi numerici, ovvero il vortice di Gresho [85]. Questo vortice è inizializzato con una soluzione stazionaria di Eulero incomprimibile, che deve essere mantenuta uguale a se stessa nel tempo. In Fig. IT.9(a) viene mostrata la condizione iniziale di un vortice di Gresho con $M_{max} = 0.1$. Uno schema numerico in grado di approssimare con accuratezza regimi a basso Mach, deve preservare la struttura iniziale del vortice. Questo si verifica utilizzando lo schema all-speed (IT.19), come si può osservare in Fig. IT.9(b). Qui mostriamo il risultato ottentuto al tempo $t = 1$, cioè quando il vortice ha compiuto una rotazione completa: la corretta viscosità numerica dello schema mantiene il vortice con la sua forma iniziale. Lo stesso vortice, se risolto con uno schema classico esplicito-upwind viene completamente diffuso, come si osserva in Fig. IT.9(c).

Presentiamo ora una validazione dello schema nel caso di approssimazione di onde materiali. Consideriamo un tubo di Sod di rame (parametri: $\chi = 5 \cdot 10^{10}$Pa, $p_\infty = 3.42 \cdot 10^{10}$Pa, $\gamma = 4.22$) rappresentativo del limite low Mach acustico-elastico, con $M \simeq 2.6 \cdot 10^{-3}$ e $M_\chi \simeq 3.15 \cdot 10^{-3}$ sull'onda materiale. Inizialmente, il rame a sinistra è a riposo e con una pressione più alta, mentre a destra viene applicata una velocità tangenziale. In Fig. IT.10 sono riportati i profili di pressione e di densità ottenuti con uno schema esplicito-upwind con passo temporale Δt acustico (in rosso), confrontati con i risultati ottenuti con lo schema all-speed (IT.19) con Δt acustico (nero) e con due diversi Δt materiali (blu e verde). Osserviamo che lo schema all-speed risolve accuratamente tutte le 5 onde con Δt dato da una condizione CFL acustica, invece passi di tempo materiali sono troppo grandi per seguire le onde longitudinali e di taglio. Tuttavia è
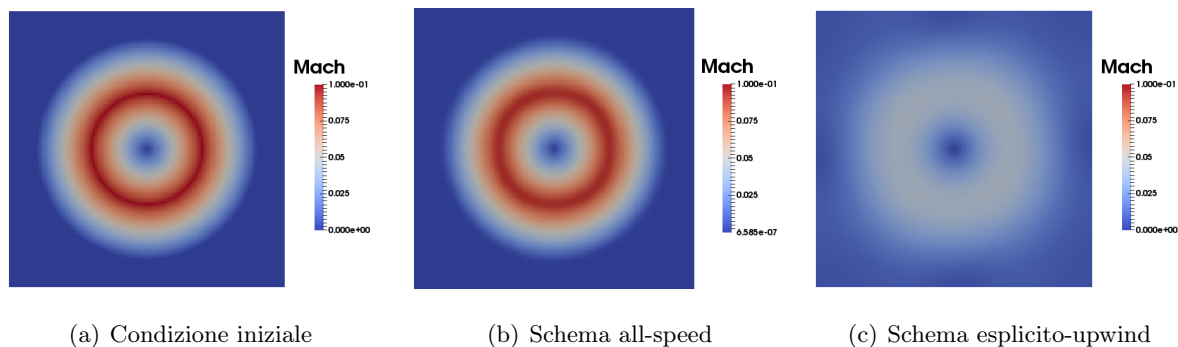
(a) Condizione iniziale   (b) Schema all-speed   (c) Schema esplicito-upwind

Figure IT.9: Vortice di Gresho con $M_{max} = 10^{-1}$: condizione iniziale e risultati al tempo $t = 1$ ottenuti con lo schema all-speed (IT.19) e con uno schema classico esplicito-upwind.
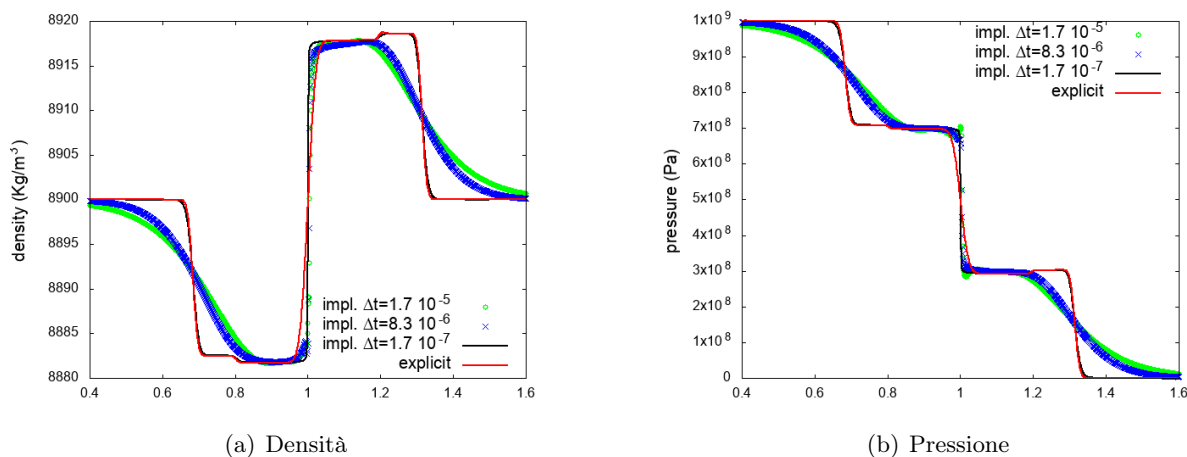

(a) Densità   (b) Pressione

Figure IT.10: Profili di densità e pressione ottenuti con lo schema all-speed di rilassamento con Δt differenti (2000 punti di griglia sul dominio 1D $[0,2]$). Condizioni CFL: $\Delta t = 1.7 \cdot 10^{-5}$ dato da $\nu_{mat} = 0.3$, $\Delta t = 8.3 \cdot 10^{-6}$ da $\nu_{mat} = 0.15$, $\Delta t = 1.7 \cdot 10^{-7}$ da $\nu_{ac} = 0.9$.

evidente che lo schema all-speed implicito è in grado di approssimare con maggiore accuratezza rispetto a uno schema upwind la discontinuità di contatto, grazie alla limitata viscosità numerica. Inoltre, l'accuratezza dell'approssimazione dell'onda materiale da parte dello schema all-speed è indipendente dal passo temporale scelto.

Metodo numerico per problemi multi-materiale

Abbiamo introdotto un modello Euleriano con una formulazione sufficientemente generale da rappresentare diversi materiali comprimibili. Inoltre, abbiamo proposto uno schema all-speed che non dipende dalla legge di stato e dunque conserva la stessa forma nella risoluzione di fluidi e solidi. Con queste premesse, ci dedichiamo ora alla risoluzione di problemi di tipo eterogeneo, ovvero domini in cui sono presenti materiali comprimibili diversi. Questo implica la necessità di derivare metodi numerici per il trattamento delle interfacce fisiche.

Deriviamo quindi un metodo per descrivere interfacce fisiche in modo "sharp", ponendoci in un caso 1D per semplicità. Il dominio $[0, L]$ è diviso in N celle $C_i = \left[x_{i-1/2}, x_{i+1/2} \right]$ $i = 1, .., N$

(a) Posizione dell'interfaccia
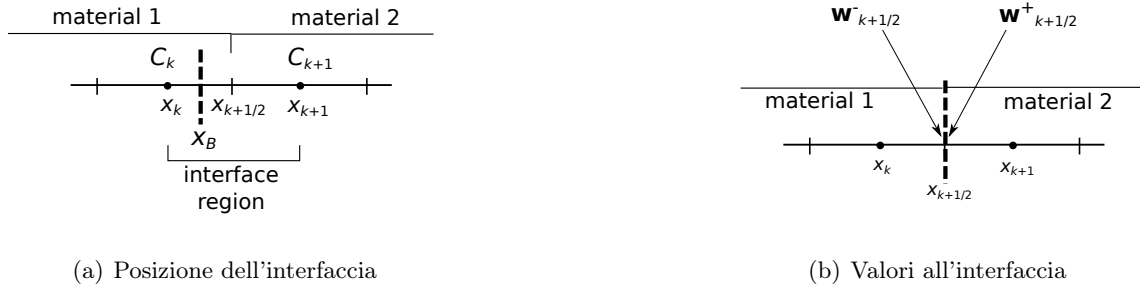
(b) Valori all'interfaccia

Figure IT.11: Posizione dell'interfaccia nel dominio discretizzato.

di ampiezza $\Delta x = x_{i+1/2} - x_{i-1/2}$. L'interfaccia al tempo t è in posizione $x_k \leq x_B(t) < x_{k+1}$, con il materiale 1 in $[0, x_B]$ e il materiale 2 in $[x_B, L]$. Introduciamo un'approssimazione per cui la cella C_k è assegnata al materiale 1 e la cella C_{k+1} al materiale 2, come mostrato in Fig. IT.11(a). Questo significa che l'interfaccia fisica coincide artificialmente con l'interfaccia numerica più vicina, $x_{k+1/2}$ in Fig. V.1(a). Inoltre, per una generica variabile $\mathbf{w}$, distinguiamo due diversi valori in $x_{k+1/2}$: $\mathbf{w}_{k+1/2}^-$ che viene da sinistra ed è relativo al materiale 1 e $\mathbf{w}_{k+1/2}^+$ che viene da destra ed è relativo al materiale 2, come mostrato in Fig. IT.11(b). Le variabili conservative di interfaccia $(\boldsymbol{\psi}_{k+1/2})^{\pm}$ e di rilassamento devono essere ricostruite con specifiche condizioni di equilibrio. In tutte le altre celle del dominio C_i, $i \neq k, k+1$ viene risolto lo schema all-speed (IT.19).

In particolare, le condizioni di equilibrio fisico all'interfaccia sono imposte in implicito al tempo t^{n+1}, con l'obiettivo di costruire un metodo che risolva problemi multi-materiale in regimi debolmente comprimibili e low Mach. Esse devono contenere il bilancio delle forze all'interfaccia e, nei casi di fluidodinamica, sono imposte tramite estrapolazioni in termini di continuità della pressione e della velocità, come nei metodi di frontiere immerse [101]. In generale, calcoliamo le quantità continue all'interfaccia tramite una media dei valori a destra e sinistra, mentre per le quantità discontinue, come la densità, adottiamo un'estrapolazione dalla parte dal materiale corrispondente (sinistra/destra). Per interazioni fluido/fluido imponiamo dunque le seguenti condizioni:

$$
\begin{cases}
\left(u_{k+1/2}^{n+1}\right)^- = \left(u_{k+1/2}^{n+1}\right)^+ = \frac{1}{2}\left(u_k^{n+1} + u_{k+1}^{n+1}\right) \\
\left(p_{k+1/2}^{n+1}\right)^- = \left(p_{k+1/2}^{n+1}\right)^+ = \frac{1}{2}\left(p_k^{n+1} + p_{k+1}^{n+1}\right) \\
\left(\rho_{k+1/2}^{n+1}\right)^- = \frac{3}{2}\rho_k^{n+1} - \frac{1}{2}\rho_{k-1}^{n+1} \qquad \text{and} \qquad \left(\rho_{k+1/2}^{n+1}\right)^+ = \frac{3}{2}\rho_{k+1}^{n+1} - \frac{1}{2}\rho_{k+2}^{n+1}.
\end{cases}
\tag{IT.20}
$$

Quando si studiano interazioni con solidi elastici, bisogna invece imporre la continuità delle componenti normali del tensore degli sforzi σ e del campo di velocità, sempre col calcolo della media. La densità e le caratteristiche $Y_{,j}^i$, invece, vengono estrapolate da sinistra e da destra come in (IT.20), essendo discontinue. Se l'interazione considerata è di tipo solido/solido, imponiamo anche la continuità di σ^{21} e di u_2 con il calcolo della media. Nel caso di un'interazione solido/liquido, la componente trasversale di σ viene invece posta uguale a zero all'interfaccia, ovvero $((\sigma_{k+1/2}^{21})^{n+1})^- = ((\sigma_{k+1/2}^{21})^{n+1})^+ = 0$ e la velocità tangenziale u_2 è calcolata con l'estrapolazione da sinistra e da destra.

Le condizioni di interfaccia proposte sono derivate sulle variabili primitive, per poter imporre la continuità di σ^{11} e di u_1. Queste relazioni devono essere riportate sulle variabili conservative $\boldsymbol{\psi}$ e su quelle di rilassamento, per includere il modello di interfaccia nello schema. La relazione tra variabili primitive e conservative è non lineare ed essendo scritta in implicito, è risolta con un metodo di Newton, nello spirito di ciò che è stato introdotto per il termine non lineare (IT.18) del sistema di rilassamento.

L'interfaccia fisica in problemi monodimensionali è trasportata, calcolando la sua posizione tramite la velocità al passo precedente:

$$x_B\left(t^{n+1}\right) = x_B\left(t^n\right) + \frac{(u_1)_k^n + (u_1)_{k+1}^n}{2}\Delta t.$$

Per problemi bidimensionali, invece, coerentemente con l'approccio euleriano, introduciamo una funzione level-set φ, il cui contorno di livello zero corrisponde all'interfaccia. Generalmente, φ viene scelta come una funzione distanza, il cui segno cambia da sinistra a destra dell'interfaccia. Sia Ω un oggetto con frontiera Γ, la funzione level set φ può essere definita nel modo seguente:

$$\varphi(x,t) = \begin{cases} -|x-\Gamma| \text{ if } x \in \Omega \\ |x-\Gamma| \text{ if } x \notin \Omega \end{cases}$$

φ rappresenta il contorno di un oggetto che può muoversi ed essere deformato, quindi essa viene trasportata dal campo di velocità $\mathbf{u}$ del flusso nel modo seguente:

$$\partial_t\varphi + \mathbf{u} \cdot \nabla\varphi = 0.$$

Risolviamo questa equazione di trasporto con un metodo semi-lagrangiano, basato su una integrazione in tempo di tipo Runge-Kutta di ordine 2 e su una interpolazione di tipo biquadratico in spazio [93, 130].

Risultati numerici

Analizziamo il caso di un tubo di Sod che contiene rame ad alta pressione a sinistra e gas a pressione atmosferica a destra. In Fig. IT.12 sono riportati i risultati di questa interazione solido/fluido per un numero crescente di punti di griglia. Come ci si apsetta, la velocità normale u_1 e lo sforzo normale σ^{11} sono continui all'interfaccia. Invece, la densità e la pressione sono discontinue e inoltre si osserva un'onda di shock che si propaga nel gas. L'interfaccia è risolta correttamente e in modo "sharp", senza lo sviluppo di oscillazioni spurie.

Passando a un caso bidimensionale, risolviamo un'interazione shock-bolla. Qui viene simulata la propagazione di un'onda di shock che si muove verso destra, il cui numero di Mach è $M_{shock} = 1.22$. Lo shock colpisce una bolla di elio e le passa atraverso, deformandola. I due gas sono caratterizzati dalla stessa legge di stato, ma da una diversa costante γ. Questo caso test è stato per la prima volta proposto in [106] e i risultati ottenuti in Fig. IT.13 sono in buon accordo con la letteratura. Si può notare che la risoluzione della level set, dopo tempi lunghi, risulta poco accurata. In futuro verranno utilizzati schemi di ordine più alto per incrementare la precisione della risolzione del contorno.
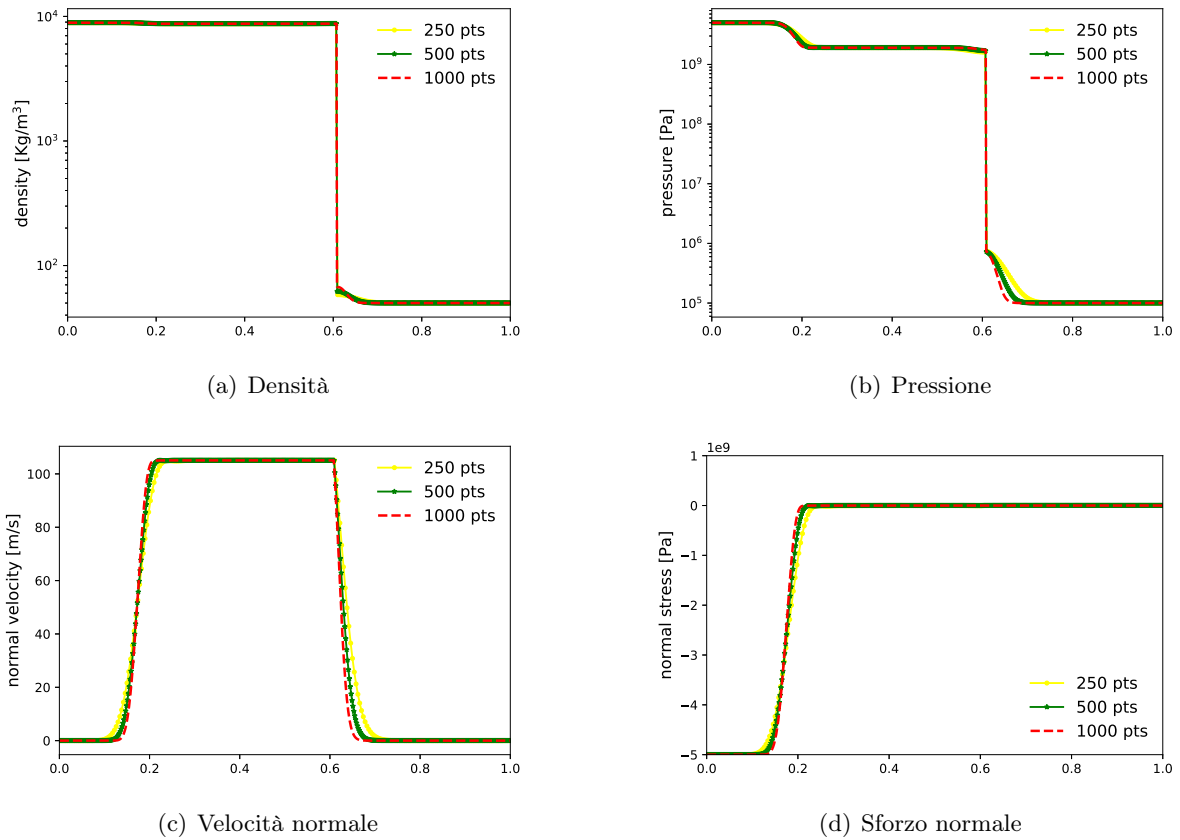
(a) Densità   (b) Pressione

(c) Velocità normale   (d) Sforzo normale

Figure IT.12: Tubo di Sod rame-gas: risultati ottenuti con le condizioni multi-materiali implicite per un numero crescente di punti di griglia.

(a) $t = 75\mu s$ (b) $t = 260\mu s$ (c) $t = 445\mu s$
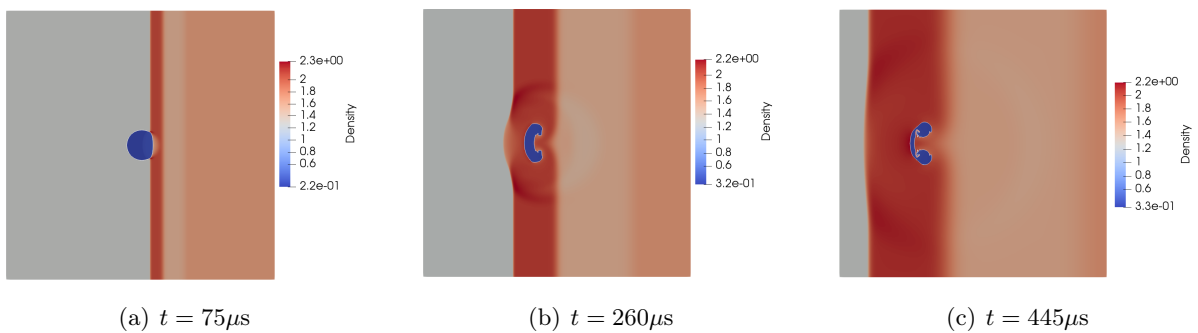
Figure IT.13: Interazione shock-bolla (aria-elio): densità e contorno zero della level set per tre diversi istanti temporali.

Conclusione

In questa tesi abbiamo proposto metodi numerici per la simulazione di materiali differenti sia in regimi totalmente comprimibili che nei limiti a basso Mach. Il modello euleriano introdotto descrive fluidi e solidi elastici con le stesse equazioni. Dunque, il concetto di regime low Mach è stato esteso anche alle deformazioni elastiche. Abbiamo proposto uno schema all-speed implicito basato su una tecnica di rilassamento. Questo schema migliora in modo consistente i risultati

ottenuti con metodi standard espliciti-upwind nei casi in cui il numero di Mach del flusso diventa piccolo. Abbiamo inoltre proposto un metodo numerico per trattare le interfacce fisiche in implicito, con l'obiettivo di risolvere flussi multi-materiale a basse velocità. L'implementazione del codice bidimensionale è stata sviluppata in parallelo, per essere risolta su strutture HPC.

Le prospettive di questo lavoro riguardano lo sviluppo di schemi di ordine più alto sia per la discretizzazione dei flussi, che per quella della funzione level-set che rappresenta l'interfaccia. Inoltre, la soluzione su griglie adattive, finora esplorata solo nei casi con un solo materiale, permetterà di limitare i costi computazionali anche per problemi multi-materiali.

Méthodes numériques pour des écoulements multi-régimes en fluidodynamique et élasticité non-linéaire

Introduction

Les écoulements dans des matériaux compressibles en domaines hétérogènes peuvent générer des phénomènes complexes. Dans cette thèse on s'occupe de simuler numériquement ces écoulements, en proposant des méthodes robustes et générales pour résoudre des problèmes dans des matériaux différents (gas, liquides et solides élastiques) dans des régimes différents. Dans ce sens, on introduit un modèle eulérian qui décrit les fluides et les solides avec le même système de lois de conservation. La lois d'état qui ferme le système caractérise les matériaux considérés, y compris les comportements qui peuvent se vérifier en traversant ces médiums.

Comme en fluidodynamique classique, aussi si on utilise ce modèle eulérian on peut observer des régimes différents. Pour étudier ces régimes, on introduit le nombre de Mach acoustique standard et de plus un nombre de Mach élastique. Ces deux nombres aident à distinguer le échelles possibles. La limite bas Mach dans un solide élastique peut être associée au concept de déformation pétite ou lente. Ceci signifie que l'onde matérielle a une vitesse beacoup plus faible par rapport à toutes les autres ondes ou à un sous-ensemble de celles-la. L'objectif est la construction d'un schéma numérique pour résoudre avec précision touts les régimes, du compressible aux limites bas Mach analysées.

Pour avoir un schéma général suffisammant à ne pas changer sa structure selon le matériel considéré, on adopte une technique de relaxation des fluxes, qui rend linéaire l'opérateur de transport. Grâce à cette linéarité, on peut integrer en temps les équations en façon implicite, sans avoir besoin des solveur de Riemann. Avec cette discrétization en temps, on évite des conditions réstrictives sûr le pas de temps et de plus on peut utiliser des schémas centrés en éspace sans problèmes de stabilité. La propriété all-speed est réspécté grâce à une combinaison des fluxes centrés et upwind. Comme ça on rétrouve la viscosité numérique correcte dans chanque régime. L'implémentation du schéma sûr des mailles cartesiennes est facilement parallelisable avec une méthode de décomposition des domaines.

La deuxième partie de la thèse est dédiée à la dérivation de méthodes numériques pour traiter les interfaces, avec l'objectif de résoudre des écoulements multi-matériaux. Les interfaces sont

traitées en façon "sharp", comme pour la méthode des frontières immergées: l'interface est donc vu comme une frontière qui peut traverser les mailles du domaine. Les conditions d'équilibre sont imposées avec des extrapolations et sont intégré en implicite, pour résoudre les écoulements aussi dans les régimes bas Mach et pour éviter des restrictions onéreuses sûr le pas de temps.

Modèle eulérian pour l'élasticité

On introduit un modèle eulérian monolithique, initialement proposé par Godunov in [60, 61]. $\Omega_0 \in \mathbb{R}^2$ est la configuration initial d'un continuum et $\Omega_t \in \mathbb{R}^2$ est la configuration déformé au temps t. Les caractéristiques rétrogrades $Y(x,t)$ décrivent le continuum en formalisme eulérian: pour un temps t et un point $x \in \Omega_t$, la position du point correspondant $\xi \in \Omega_0$ est donnée par: $Y : \Omega_t \times [0,T] \to \Omega_0, \ (x,t) \mapsto Y(x,t)$. Ces fonctions enregistrent la déformation d'un solide dans le modèle. Notamment, comme le tenseur des contraintes σ dépend du gradient de $Y(x,t)$, la loi de conservation est écrite avec le gradient de $\partial_t Y + \mathbf{u} \cdot \nabla_x Y = 0$, où $\mathbf{u}$ est le champ de vitesse. Les autres équations sont la conservation de la masse, de la quantité de mouvement et de l'énergie. On obtien donc le modèle 2D suivant:

$$\begin{cases} \partial_t \rho + \nabla_x \cdot (\rho \mathbf{u}) = 0 \\ \partial_t (\rho \mathbf{u}) + \nabla_x \cdot (\rho \mathbf{u} \otimes \mathbf{u} - \sigma) = 0 \\ \partial_t ([\nabla_x Y]) + \nabla_x (u \cdot [\nabla_x Y]) = 0 \\ \partial_t (\rho e) + \nabla_x \cdot (\rho e \mathbf{u} - \sigma^T \mathbf{u}) = 0, \end{cases} \tag{FR.21}$$

où ρ est la densité, e est l'énergie totale par unité de masse et est donnée par la somme de l'énergie cinétique et de l'énergie interne ϵ. Le système est fermé avec la loi d'état hyper-élastique, qui inclut les comportements différents des gaz, des liquides et des solide, avec la formulation suivante [62]:

$$\epsilon(\rho, s, [\nabla_x Y]) = \underbrace{\frac{\kappa(s)}{\gamma - 1} \left(\frac{1}{\rho} - b \right)^{1-\gamma} - a\rho + \frac{p_\infty}{\rho}}_{\text{general gas}} + \underbrace{\frac{\chi}{\rho} \left(\text{tr} \overline{B} - 2 \right)}_{\text{neohookean solid}} . \tag{FR.22}$$

Ici $\gamma = c_p/c_v$ est la constante des gaz polytopiques, $\kappa(s) = exp((s - s_0)/c_v)$ avec s_0 entropie de référence, a et b sont les coéfficients des gaz réels (modèle de Van der Waals) et p_∞ est une constante qui décrit le forces intermoléculaires. Enfin, χ est le modul élastique de cisaillement et $\overline{B} = [\nabla_x Y]^{-1} [\nabla_x Y]^{-T}/J$, avec $J = det([\nabla_x Y]^{-1} [\nabla_x Y]^{-T})$ est le tenseur gauche de Cachy-Green normalisé.

Le tenseur des contraintes de Cauchy est donc donné par

$$\begin{cases} \sigma(\rho, s, [\nabla_x Y]) = -p(\rho, s) \mathbf{I} + 2\chi J^{-1} \left(\overline{B} - \frac{\text{tr}\overline{B}}{2} I \right) \\ p(\rho, s) = -p_\infty - a\rho^2 + k(s) \left(\frac{1}{\rho} - b \right)^{-\gamma}, \end{cases} \tag{FR.23}$$

où $\mathbf{I}$ est l'identité et p est la pression.

Les limites bas Mach

Pour simplifier la notation, on considère le système eulérian (FR.21) en 1D et on exclus les gaz de Van der Waals de l'analyse ($a = b = 0$). On définit la vitesse du son en manière classique:

$$c\left(\rho, s, \nabla_x Y\right) = \sqrt{\left.\frac{\partial p}{\partial \rho}\right|_{s=const}} = \sqrt{\gamma k\left(s\right)\rho^{\gamma-1}} = \sqrt{\frac{\gamma}{\rho}\left(p + p_\infty\right)}. \qquad (FR.24)$$

De plus, on définit une vitesse isocorique élastique de la manière suivante:

$$u_{iso} = \sqrt{\frac{2\chi}{\rho}}. \qquad (FR.25)$$

Avec le deux vitesses (FR.24) et (FR.25) on peut définir deaux nombres de Mach: le prémier est le nombre de Mach acoustique de la fluidodynamique

$$M = \frac{u_1}{c};$$

le deuxième est un nombre de Mach définit par le rapport entre la vitesse de l'écoulement et la vitesse élastique (FR.25):

$$M_\chi = \frac{u_1}{u_{iso}} = \sqrt{\frac{\rho u_1^2}{2\chi}}.$$

On continue en adimensionalisant le système pour comprendre le comportement dans les différents régimes et on utilise c pour adimensionaliser la pression, $\overline{\chi}$ de référence pou adimensionaliser le module élastique de cisaillement et une vitesse normale de référence pour adimensionaliser u_1 et u_2. Le système eulérian adimensionnel 1D est le suivant:

$$\begin{cases} \partial_t \rho + \partial_x\left(\rho u_1\right) = 0 \\[2mm] \partial_t\left(\rho u_1\right) + \partial_x\left(\rho u_1^2\right) + \frac{\partial_x p}{M^2} - \frac{\chi}{2}\frac{\partial_x\left(1 - \left(Y_{,1}^2\right)^2 - \left(\rho/\rho_0\right)^2\right)}{M_\chi^2} = 0 \\[3mm] \partial_t\left(\rho u_2\right) + \partial_x\left(\rho u_1 u_2\right) + \chi\frac{\partial_x Y_{,1}^2}{M_\chi^2} = 0 \\[3mm] \partial_t\left(Y_{,1}^2\right) + \partial_x\left(u_1 Y_{,1}^2 + u_2\right) = 0 \\[3mm] \partial_t\left(\frac{1}{2}\rho u^2 + \frac{p + \gamma p_\infty}{M^2\left(\gamma-1\right)} + \frac{\chi\left(tr\overline{B} - 2\right)}{2M_\chi^2}\right) + \partial_x\left(\frac{1}{2}\rho|u|^3 + \frac{\gamma\left(p + \gamma p_\infty\right)}{M^2\left(\gamma-1\right)}u_1\right) + \\[3mm] \frac{\chi}{2M_\chi^2}\partial_x\left[\left(tr\overline{B} - 2 - \chi\left(1 - \left(Y_{,1}^2\right)^2 - \left(\rho/\rho_0\right)^2\right)\right)u_1 + 2\chi Y_{,1}^2 u_2\right] = 0. \end{cases} \qquad (FR.26)$$

Le concept de régime bas Mach dans un solide élastique peut être associé à une déformation pétite ou lente par rapport aux ondes acoustiques. On peut distinguer deux limites différentes:

1. *régime bas Mach acoustique-élastique*: $M \ll 1$ et $M_\chi \ll 1$. Dans (FR.26), soit les gradients de pression que le déformations élastiques introduisent des termes raides dans le systèmes. Comme on a dans cette limite que $\mathcal{O}\left(M\right) \simeq \mathcal{O}\left(M_\chi\right)$, on verifie que $c \simeq u_{iso}$ et $p + p_\infty \simeq \chi$. Dans le cas présent, les ondes longitudinaux et les ondes de cisaillement sont toutes considérablement plus rapides par rapport à l'onde matérielle;

2. *régime bas Mach seulement acustique*: $M \ll 1$ et $M \ll M_\chi$. Dans (FR.26) le gradients de pression sont prédominants sûr les autres partie du système et de plus on verifie que $c \gg |u_1|$ et $c \gg u_{iso}$, donc on a $p + p_\infty \gg \chi$. Dans ce cas, les onde longitudinaux sont considérablement plus rapides par rapport à toutes les autres ondes.

Schéma all-speed de relaxation

On a l'objectif de résoudre le système eulérian (FR.21) soit dans les régimes bas Mach que dans des régimes totalement compressibles. Dans cet ésprit, on propose un schéma "all-speed" implicite, qui se base sûr la technique de relaxation introduite par Jin e Xin dans le papier [71]. Avec cette méthode de relaxation, les flux sont approximés avec des nouvelles variables (variables de relaxation) et on construit un système dont l'operateur de transport est linéaire. Donc, les dérivées spatielles ne dépendent pas de la lois d'état. Ceci est fondamental pour la construction d'un schéma qui conserve la même structure pour résoudre des écoulements des matériaux différents.

Le système de lois de conservation (FR.21) peut être écrit sous forme compacte comme

$$\partial_t \boldsymbol{\psi} + \partial_{x_1} \mathbf{F}(\boldsymbol{\psi}) + \partial_{x_2} \mathbf{G}(\boldsymbol{\psi}) = 0,$$

où $\boldsymbol{\psi}$ sont les variables conservatives, $\mathbf{F}(\boldsymbol{\psi})$ et $\mathbf{G}(\boldsymbol{\psi})$ sont les fluxes dans les deux diréctions. En introduisant les vecteurs des variables de relaxation "direction par direction" $\mathbf{v}$ e $\mathbf{w}$ qui approximent respectivement $\mathbf{F}(\boldsymbol{\psi})$ et $\mathbf{G}(\boldsymbol{\psi})$, on construit le système de relaxation suivant

$$\begin{cases} \partial_t \boldsymbol{\psi} + \partial_{x_1} \mathbf{v} + \partial_{x_2} \mathbf{w} = 0 \\ \partial_t \mathbf{v} + \mathbf{A}_1 \partial_{x_1} \boldsymbol{\psi} = \dfrac{1}{\eta}(\mathbf{F}(\boldsymbol{\psi}) - \mathbf{v}) \\ \partial_t \mathbf{w} + \mathbf{A}_2 \partial_{x_2} \boldsymbol{\psi} = \dfrac{1}{\eta}(\mathbf{G}(\boldsymbol{\psi}) - \mathbf{w}), \end{cases} \qquad \text{(FR.27)}$$

où $\eta > 0$ est le taux de relaxation et $\mathbf{A}_1$ et $\mathbf{A}_2$ sont des matrices diagonales qui doivent être choisies en réspectant la condition subcaractéristique [86]. Dans la limite de relaxation $\eta \to 0$, on rétrouve le système original (IT.16) et les variables de relaxation coincident avec les flux.

Dans un contexte de volumes finis, le système (FR.27) est intégré en temps en manière totalement implicite. Donc le schéma est stable sans conditions. Le pas de temps $\Delta t = t_{n+1} - t_n$ est choisi sûr la base de la précision souhaité pour les différentes ondes. Une condition de type acoustique sûr Δt permet une résolution précise de toutes les ondes. Par contre, un pas de temps plus large de type matériel permet de réduire les temps de calcul en guardant la précision sûr les ondes matérielles, mais les ondes acoustiques sont diffusées. Les fluxes non linéaires sont dans le seconde membre et sont résolus avec une méthode Newton, via la linearisation suivante:

$$\mathbf{F}(\boldsymbol{\psi}^{n+1}) = \mathbf{F}(\boldsymbol{\psi}^n) + \mathbf{F}'(\boldsymbol{\psi}^n)(\boldsymbol{\psi}^{n+1} - \boldsymbol{\psi}^n), \qquad \text{(FR.28)}$$

où le jacobien $\mathbf{F}'(\boldsymbol{\psi}^n)$ (et celui de $\mathbf{G}(\boldsymbol{\psi})$) est calculé analytiquement.

La discrétisation en éspace se compose d'une combinaison convexe de fluxes centrés et upwind. Le schéma centré fournit la viscosité numérique correcte pour les régimes bas Mach. Au contraire, le schéma upwind évite la génération des oscillations numériques dans les régimes

totalement compressibles.Cette combinaison est calculé sûr la base du nombre de Mach local M_{loc}. Comme ça on se donne la viscosité numérique qu'on veut dans chaque régime. Avec une maille cartesienne, où Δx_l est la taille de maille dans la diréction x_l et $\Omega_{i,j}$ est le volume de control centré en $(i\Delta x_1, j\Delta x_2)$, le schéma all-speed de relaxation prend la formulation suivante:

$$
\begin{cases}
\dfrac{\boldsymbol{\psi}_{ij}^{n+1} - \boldsymbol{\psi}_{ij}^n}{\Delta t} + \dfrac{1}{2\Delta x_1}\left(\mathbf{v}_{i+1,j}^{n+1} - \mathbf{v}_{i-1,j}^{n+1}\right) - \dfrac{f\left(M_{loc}\right)\mathbf{A}_1^{1/2}}{2\Delta x_1}\left(\boldsymbol{\psi}_{i+1,j}^{n+1} - 2\boldsymbol{\psi}_{ij}^{n+1} + \boldsymbol{\psi}_{i-1,j}^{n+1}\right) + \\
\qquad \dfrac{1}{2\Delta x_2}\left(\mathbf{w}_{i,j+1}^{n+1} - \mathbf{w}_{i,j-1}^{n+1}\right) - \dfrac{f\left(M_{loc}\right)\mathbf{A}_2^{1/2}}{2\Delta x_2}\left(\boldsymbol{\psi}_{i,j+1}^{n+1} - 2\boldsymbol{\psi}_{ij}^{n+1} + \boldsymbol{\psi}_{i,j-1}^{n+1}\right) = 0 \\
\dfrac{\mathbf{v}_{ij}^{n+1} - \mathbf{v}_{ij}^n}{\Delta t} + \dfrac{\mathbf{A}_1}{2\Delta x_1}\left(\boldsymbol{\psi}_{i+1,j}^{n+1} - \boldsymbol{\psi}_{i-1,j}^{n+1}\right) - \dfrac{f\left(M_{loc}\right)\mathbf{A_1}^{1/2}}{2\Delta x_1}\left(\mathbf{v}_{i+1,j}^{n+1} - 2\mathbf{v}_{ij}^{n+1} + \mathbf{v}_{i-1,j}^{n+1}\right) = \\
\qquad\qquad\qquad\qquad\qquad\qquad \dfrac{1}{\eta}\left(\mathbf{F}\left(\boldsymbol{\psi}_{ij}^{n+1}\right) - \mathbf{v}_{ij}^{n+1}\right) \\
\dfrac{\mathbf{w}_{ij}^{n+1} - \mathbf{w}_{ij}^n}{\Delta t} + \dfrac{\mathbf{A}_2}{2\Delta x_2}\left(\boldsymbol{\psi}_{i,j+1}^{n+1} - \boldsymbol{\psi}_{j,i-1}^{n+1}\right) - \dfrac{f\left(M_{loc}\right)\mathbf{A}_2^{1/2}}{2\Delta x_2}\left(\mathbf{w}_{i,j+1}^{n+1} - 2\mathbf{w}_{ij}^{n+1} + \mathbf{w}_{i,j-1}^{n+1}\right) = \\
\qquad\qquad\qquad\qquad\qquad\qquad \dfrac{1}{\eta}\left(\mathbf{G}\left(\boldsymbol{\psi}_{ij}^{n+1}\right) - \mathbf{w}_{ij}^{n+1}\right).
\end{cases}
\tag{FR.29}
$$

Ici on a introduit la fonction $f\left(M_{loc}\right) = \min\{1, M_{loc}\}$.

La résolution numérique des cas 2D est très coûteuse du point de vu computational, parce que on adopte une intégration en temps totalement implicite et parce la relaxation augmente le nombre de variables. L'implémentation du schéma sûr de mailles cartesiennes est facilement parallelisable avec une méthode de décomposition de domaines. Ceci est fait avec le paradigme MPI et avec de librairies développées pour le calcul scientifique (PETSc [11] pour la partie d'algèbre linéaire et Bitpit [50] pour la génération de la maille). Une réduction supplémentaire des temps de calcul est obténue grâce à l'utilisation de mailles adaptives basées sûr des quadtrees.

Résultats numériques

On étudie un test classique pour valider les schémas numériques dans le régime bas Mach: ceci c'est le vortex de Gresho [85]. Ce vortex est initialisé avec une solution stationaire d'Euler incompressible, qui doit être conservé égal à soi même pour chaque temps. En Fig. FR.14(a) on montre la condition initiale d'un vortex de Gresho avec $M_{max} = 0.1$. Un schéma numérique qui est capable de bien approximer les régimes bas Mach doit conserver cette structure initiale du vortex. Cette préservation se vérifie en utilisant le schéma all-speed (FR.29), comme on observe en Fig. FR.14(b). Ici on a le résultat obténu au temps $t = 1$, quand le vortex a accompli une rotation entière: la correcte viscosité numérique du schéma maintient le vortex avec sa forme initiale. Le même vortex résolu avec un schéma classique explicite-upwind est totalement diffusé, comme on voit en Fig. FR.14(c).

On approche maintenant la simulation des ondes matérielles. On considère un tube de Sod en cuivre (les paramètres sont: $\chi = 5 \cdot 10^{10}$Pa, $p_\infty = 3.42 \cdot 10^{10}$Pa, $\gamma = 4.22$) qui réprésent la limite ba Mach acoustique-élastique, avec $M \simeq 2.6 \cdot 10^{-3}$ et $M_\chi \simeq 3.15 \cdot 10^{-3}$ sûr l'onde de contact. Initialement, le cuivre à gauche est en arrêt et avec une pression plus importante, alors que à droite on a une vitesse tangentielle. En Fig. FR.15 on peut voir les profils de densité et pression obtenus avec un schéma explicite-upwind avec un pas de temps Δt acoustique (en rouge). On compare cette solution avec le résultats du schéma all-speed (FR.29) avec Δt acoustique (en

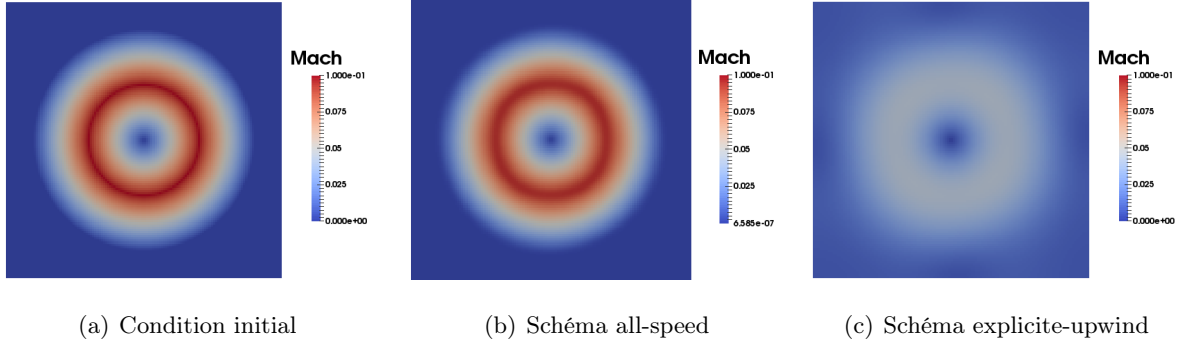(a) Condition initial   (b) Schéma all-speed   (c) Schéma explicite-upwind

Figure FR.14: Vortex de Gresho avec $M_{max} = 10^{-1}$: condition initiale et solutions au temps $t = 1$ obténues avec le schéma all-speed (FR.29) et avec un schéma classique explicite-upwind.
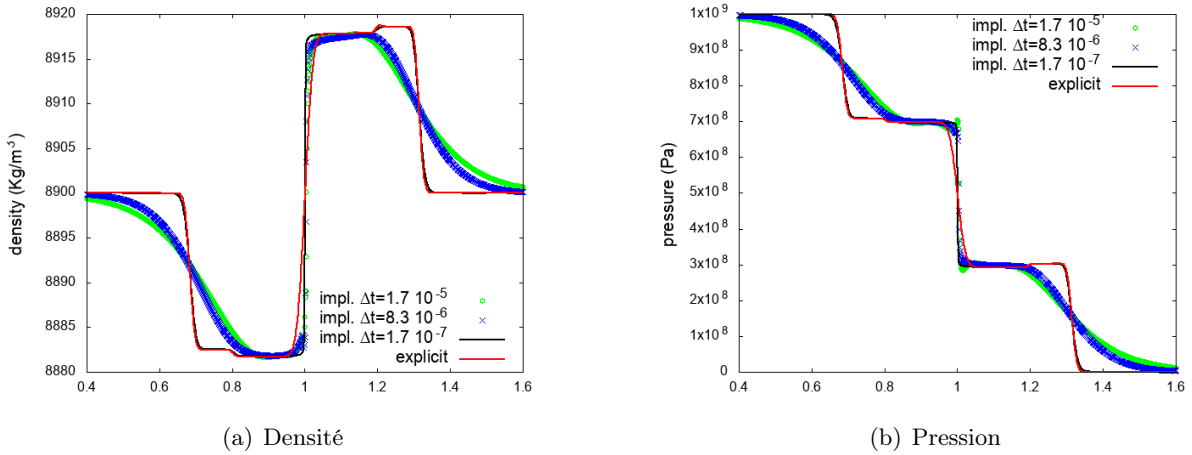

(a) Densité   (b) Pression

Figure FR.15: Profils de densité et pression obténus avec le schéma all-speed (FR.29) avec des Δt différents (2000 mailles sûr le domaine 1D $[0, 2]$). Conditions CFL: $\Delta t = 1.7 \cdot 10^{-5}$ obténu avec $\nu_{mat} = 0.3$, $\Delta t = 8.3 \cdot 10^{-6}$ avec $\nu_{mat} = 0.15$, $\Delta t = 1.7 \cdot 10^{-7}$ avec $\nu_{ac} = 0.9$.

noir) et avec deux Δt metériels (en bleu et vert). On observe que le schéma all-speed résout précisément toutes les 5 ondes avec Δt imposé d'une CFL acoustique. Par contre, les pas de temps matériels sont trop larges pour suivre les ondes longitudinaux et de cisaillement. Cependent, c'est clair que le schéma all-speed implicite est capable d'approximer plus précisément la discontinuité de contact par rapport à un schéma upwind, grâce à la limitation sûr la viscosité numérique. De plus, la précision de l'approximation de cette onde avec le schéma all-speed ne dépend pas du pas de temps utilisé.

Méthode numérique pour les écoulements multi-matériaux

On a introduit un modèle eulérian avec une formulation unique pour réprésenter des matériuax compressibles différents. De plus, on a proposé un chèmas all-speed qui ne dépend pas de la lois d'état et donc préserve la même formulation pour résoudre soit les fluides que les solides.

Avec ces arguments, on s'approche à la résolution des problèmes hétérogènes, c'est à dire des écoulements dans des domaines rémplis par des différents matériaux compressibles. Dans ces cas, on nécessite de dériver de méthodes numériques pour traiter les interfaces physiques.
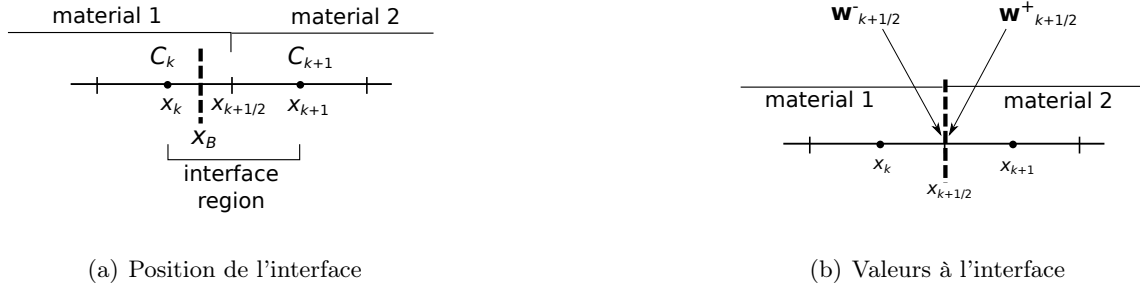

(a) Position de l'interface

(b) Valeurs à l'interface

Figure FR.16: Position de l'interface dans le domaine discretisé.

On propose donc une méthode pour décrire les interfaces en manière "sharp". Pour simplicité on se pose dans un cas 1D. Le domaine $[0, L]$ est divisé en N mailles $C_i = [x_{i-1/2}, x_{i+1/2}]$ $i = 1, .., N$ d'amplitude $\Delta x = x_{i+1/2} - x_{i-1/2}$. L'interface est en positions $x_k \leq x_B(t) < x_{k+1}$ au temps t, avec le matériau 1 en $[0, x_B]$ et le matériau 2 en $[x_B, L]$. On introduit une approximation en attribuant la maille C_k au matériau 1 et la mialle C_{k+1} au matériau 2, comme on montre en Fig. FR.16(a). Ca signifie que l'interface physique coincide artificiellement avec l'interface numérique la plus proche, c'est à dire $x_{k+1/2}$ en Fig. V.1(a). De plus, pour une variable $\mathbf{w}$, on distingue deux valeurs différents en $x_{k+1/2}$: $\mathbf{w}_{k+1/2}^-$ qui vient de gauche et se référe au matériau 1 et $\mathbf{w}_{k+1/2}^+$ qui vient de droite et se référe au matériau 2 (voir Fig. FR.16(b)). Les variables conservatives à l'interface $(\boldsymbol{\psi}_{k+1/2})^\pm$ et les variables de relaxation doivent être reconstruites avec des conditions d'équilibre spécifiques. Dans toutes les autres mailles du domaine C_i, $i \neq k, k+1$ on résout le schéma all-speed (FR.29).

En particulier, le conditions d'équilibre physique à l'interface sont imposées en implicite, dans le but de construire une méthode qui résout de problèmes multi-matériaux dans les régimes faiblement compressibles et bas Mach. Le conditions de transmission réspectent le bilan des forces à l'interface. En fluidodynamique, elles sont imposé en termes de continuité de la pression et de la vitesse avec des extrapolations, comme dans la méthode des frontières immergées [101]. En général, les quantités continues à l'interface sont calculées avec la moyenne de valeurs à droite et à gauche, par contre les quantités discontinues, comme la densité, sont calculées avec une extrapolation qui provient du matériau correspondant (gauche/droite). Donc, pour les intéractions fluide/fluide on impose les conditions suivantes:

$$\begin{cases} \left(u_{k+1/2}^{n+1}\right)^- = \left(u_{k+1/2}^{n+1}\right)^+ = \frac{1}{2}\left(u_k^{n+1} + u_{k+1}^{n+1}\right) \\ \left(p_{k+1/2}^{n+1}\right)^- = \left(p_{k+1/2}^{n+1}\right)^+ = \frac{1}{2}\left(p_k^{n+1} + p_{k+1}^{n+1}\right) \\ \left(\rho_{k+1/2}^{n+1}\right)^- = \frac{3}{2}\rho_k^{n+1} - \frac{1}{2}\rho_{k-1}^{n+1} \quad \text{and} \quad \left(\rho_{k+1/2}^{n+1}\right)^+ = \frac{3}{2}\rho_{k+1}^{n+1} - \frac{1}{2}\rho_{k+2}^{n+1}. \end{cases} \tag{FR.30}$$

Pour étudier les intéractions avec des solides élastiques, on doit imposer la continuité des composantes normales du tenseur de contraintes σ et du champ de vitesse, en calculant la moyenne. La densité et les caractéristiques rétrogrades $Y_{,j}^i$, par contre, sont extrapolées côté gauche et côté

droite comme en (FR.30), parce que elles sont discontinues. Si l'intéraction considérée est de type solide/solide, on impose aussi la continuité de σ^{21} et de u_2 avec la moyenne. Dans un cas d'intéraction solide/fluide, la composante trasversale de σ est posée egual à zero à l'interface, c'est à dire $((\sigma_{k+1/2}^{21})^{n+1})^- = ((\sigma_{k+1/2}^{21})^{n+1})^+ = 0$ et la vitesse tangentielle u_2 est calculé avec l'extrapolation gauche/droite.

Les conditions d'interface sont dérivées sûr les variables primitives, pour imposer la continuité de σ^{11} et de u_1. Ces rélations doivent être rapportées sûr les variables conservatives $\boldsymbol{\psi}$ et sûr celles de relaxation, pour inclure le modèle d'interface dans le schéma. La rélation entre variables primitives et conservatives est non linéaire et est en implicite. Donc, on résout ce problème avec une méthode de Newton, dans le même ésprit de ce qu'on a introduit pour le terme non linéaire (FR.28) du système de relaxation.

L'interface physique des problèmes 1D est transportée en calculant sa position avec la vitesse au pas de temps précédent:

$$x_B\left(t^{n+1}\right) = x_B\left(t^n\right) + \frac{(u_1)_k^n + (u_1)_{k+1}^n}{2}\Delta t.$$

Pour des problèmes 2D, dans l'approche eulérian, on introduit une fonction level set φ, dont le contour de niveau zero $\varphi = 0$ correspond à l'interface. En général, φ est choisie comme une fonction distance, dont le signe change du côté gauche au côté droite de l'interface. Si Ω est un objet de frontière Γ, la fonction level set φ peut être definie dans la manière suivante:

$$\varphi\left(x,t\right) = \begin{cases} -|x - \Gamma| \text{ if } x \in \Omega \\ |x - \Gamma| \text{ if } x \notin \Omega \end{cases}$$

φ représent le contour d'un objet qui peut se déplacer et aussi être déformé. Donc elle est transportée avec le champ de vitesse $\mathbf{u}$ du flux, selon l'équation suivante:

$$\partial_t\varphi + \mathbf{u} \cdot \nabla\varphi = 0.$$

On résout cette équation de transport avec une méthode semi-lagrangienne, qui est basée sûr une intégration en temps de type Runge-Kutta à l'ordre 2 et sûr une interpolation en éspace de type biquadratique [93, 130].

Résultats numériques

On étudie un tube de Sod qui contient du cuivre à haute pression à gauche et un gaz à pression atmosférique à droite. En Fig. FR.17 on montre les résultats de cette intéraction solide/fluide pour un nombre croissante des mailles. Comme attendu, la vitesse normale u_1 et le contrainte normale σ^{11} sont continus à l'interface. En revanche, la densité et la pression sont discontinues et de plus on voit une onde de choc qui se propage dans le gaz. L'interface est bien résolue en manière "sharp", sans développer des oscillations numériques.

On presente aussi un cas 2D, en simulant une intéraction choc-boulle. Ici on a une onde de choc qui se déplace vers la droite du domaine et son nombre de Mach est $M_{shock} = 1.22$. Le choc impacte une boulle d'helium et il passe travers la boulle, qui est déformé par ça. Les deux gaz sont décrits par la même loi d'étata, mais ils sont caractérisés par des constrantes γ différentes.

(a) Densité
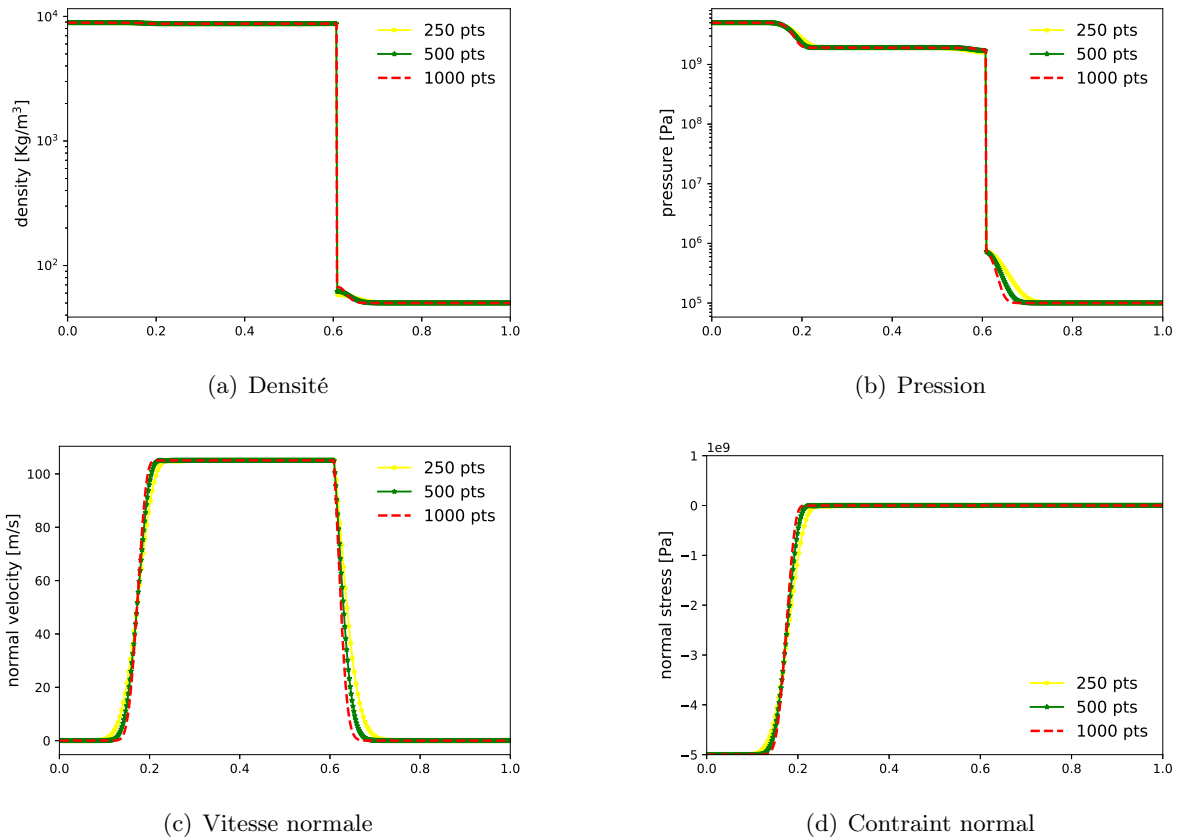
(b) Pression

(c) Vitesse normale

(d) Contraint normal

Figure FR.17: Tube de Sod gaz-cuivre: résultats obténus avec les conditions multi-matériaux implicites pour un nombre croissante des mailles.

(a) $t = 75\mu$s
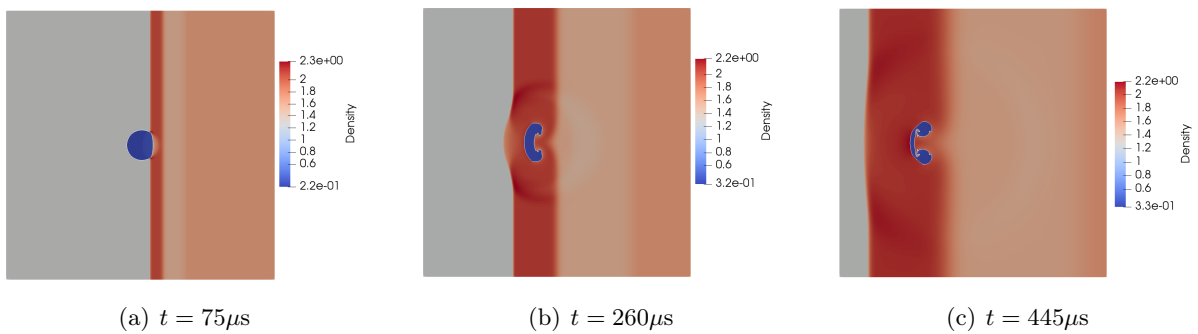
(b) $t = 260\mu$s

(c) $t = 445\mu$s

Figure FR.18: Intéraction choc-boulle (air-helium): densité et contour zéro de la level set pour trois temps différents.

Ce cas test a éeté proposé in [106] et les résultats obténus en Fig. FR.18 sont en bon accord avec la litérature. On observe que la résolution de la level set qui réprésent la boulle n'est pas suffisamment précis après des temps longs. Dans le futur on utilisera de schémas d'ordre plus élévé pour amélioré la précision du contour.

Conclusion

Dans cette thèse on a proposé des méthodes numériques pour simuler de matériaux différents soir en régimes totalement compressibles que dans la limite bas Mach. Le modèle eulérian introduit décrit les fluides et les solides élastiques avec les mêmes équations. Dans cet ésprit, le concept de régime bas Mach a été étendu aussi aux déformations élastiques. On a proposé un schéma all-speed implicite basé sûr une technique de relaxation. Ce schéma améliore considérablement les résultats obténus avec des méthodes classiques explicite-upwind dans les cas où le nombre de Mach dévient pétit. De plus, on a proposé une méthode numérique pour décrire les interfaces physiques en implicite, dans le but de résoudre des écoulements multi-matériaux à faible vitesse. L'implémentation du code bidimensionel a été dévéloppé en parallel pour être résolu sûr des structures HPC.

Les perspectives des ces travaux concernent le développement de schémas d'ordre élevé soit pour discretiser les écoulements que pour intégrer la level set qui réprésent l'interface. De plus, la solution sûr mailles adaptives a été éxploré que pour des problèmes avec un seul matériau. Celle-la nous permettera de limiter les coûts computationels aussi en l'utilisant pour les écoulements multi-matériaux.